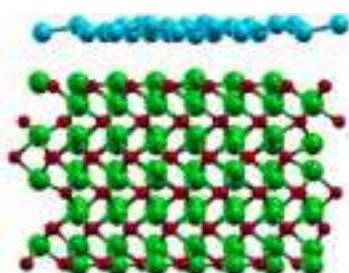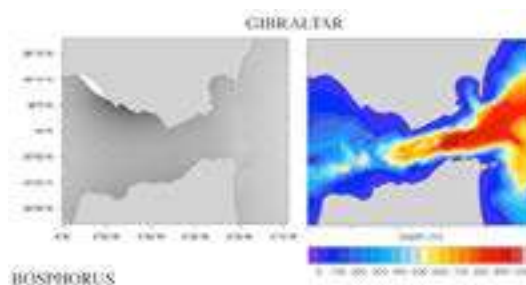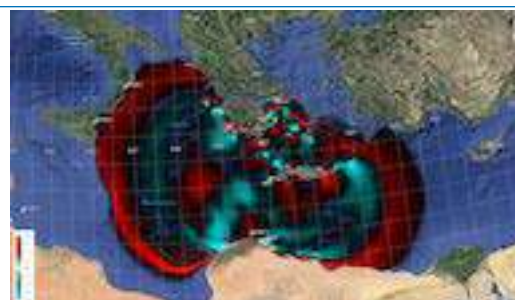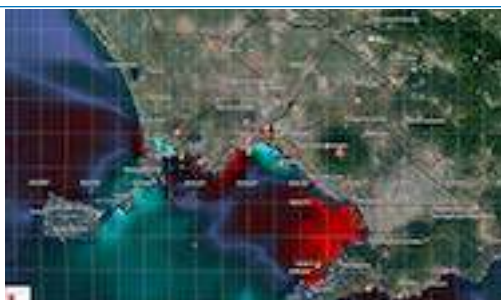# High Performance Computing on CRESCO infrastructure: research activities and results 2018

HIGH PERFORMANCE COMPUTING ON CRESCO INFRASTRUCTURE: RESEARCH ACTIVITY AND RESULTS 2018

December 2019

Contents

Foreword

During the year 2018, the CRESCO high performance computing clusters have provided 40 millions hours of "core" computing time, at a high availability rate, to about 140 users, supporting ENEA research and development activities in many relevant scientific and technological domains. In the framework of joint programs with ENEA researchers and technologists, computational services have been provided also to academic and industrial communities.

This report, the tenth of a series started in 2008, is a collection of 44 papers illustrating the main results obtained during 2018 using the CRESCO/ENEAGRID HPC facilities.

The significant number of contributions proves the importance of the HPC facilities in ENEA for the research community. The topics cover various fields of research, such as materials science, efficient combustion, climate research, nuclear technology, plasma physics, biotechnology, aerospace, complex systems physics, geophysical flow, renewable energies, environmental issues, HPC technology. The report shows the wide spectrum of applications of high performance computing, which has become an all-round enabling technology for science and engineering.

Since 2008, the main ENEA computational resources is located near Naples, in Portici Research Centre. This is a result of the CRESCO Project (Computational Centre for Research on Complex Systems), co-funded, in the framework of the 2001-2006 PON (European Regional Development Funds Program), by the Italian Ministry of Education, University and Research (MIUR).

The CRESCO Project provided the financial resources to set up the first HPC x86_64 Linux cluster in ENEA; a major computing installation for both the Italian and the International context: it ranked 126 in the HPC Top 500 June 2008 world list, with 17.1 Tflops and 2504 cpu cores. It was later decided to keep CRESCO as the name for all the Linux clusters in the ENEAGRID infrastructure, which integrates all ENEA scientific computing systems, and is currently distributed in six Italian sites.

CRESCO computing resources were later upgraded in the framework of PON 2007-2013 with the project TEDAT and the cluster CRESCO4, 100 Tflops computing power. In 2018 the ENEAGRID computational resources consist of more than 25000 computing cores (in production) and a raw data storage of about 3.2 PB.

In 2015 ENEA and CINECA, the main HPC institution in Italy, signed a collaboration agreement to promote joint activities and projects in HPC. In this framework, CINECA and ENEA participated successfully to a selection launched by EUROfusion, the European Consortium for the Development of Fusion Energy, for the procurement of a several PFlops HPC system, beating the competition of 7 other institutions. The new system MARCONI-FUSION started operation in July 2016 at 1 Pflops computation power level which has been increased to 5 Pflops in the summer of 2017 and thanks to a new awarded tender, the HPC services of MARCONI Fusion are being extended since 2023 with a power peak of 8 PFlops of conventional processors and 2 PFlops of accelerated co-processors.

The ENEA-CINECA agreement is a promising basis for the future development of ENEA HPC resources. A new CRESCO6 cluster of 1.4 Pflops has been installed in 2018 ranked 420th in November 2018 Top500 list. CRESCO6 has been a challenge in HPC co-design system thanks to implement a multi-fabric network able for working Infiniband and Omni-Path on a single GPFS cluster using the same storage systems of CRESCO data centre.

The success and the quality of the results produced by CRESCO stress the role that HPC facilities can play in supporting science and technology for all ENEA activities, national and international collaborations, and the ongoing renewal of the infrastructure provides the basis for an upkeep of this role in the forthcoming years.

Dipartimento Tecnologie Energetiche,
Divisione per lo Sviluppo Sistemi per l'Informatica e l'ICT - CRESCO Team

CRESCO HPC CLUSTERS EVOLUTION, USERS AND WORKLOADS 2008-2018

G.Bracco[1]*, S.Migliori[2], A.Quintiliani[2], F.Iannone[1], F.Ambrosino[3], G.Aprea[5],
A.Colavincenzo[3]†, P. D'Angelo[1], A.Funel[3], G.Guarnieri[3], A.Mariano[6], F.Palombi[1],
S.Pierattini[4], S.Podda[1], G.Ponti[3], G.Santomauro[3], D.Alderuccio[2], F.Beone[1], R.Bertini[5],
L.Bucci[7], B.Calosso[1], M.Caporicci[2], G.Caretto[7], M.Celino[5], M.Chinnici[5], D.De Chiara[3],
M.De Rosa[3], D.Di Mattia[1], M.Galli[8], D.Giammattei[3], S.Giusepponi[5], R.Guadagni[7],
M.Gusso[7], M.Marano[9], G.Mencuccini[2], M.Mongelli[2], P.Ornelli[8], S.Pecoraro[5],
A.Perozziello[1], F.Poggi[1], A.Rocchi[1], A.Santoro[1], A.Scalise[7], C.Scio[1], F.Simoni[1]

*DTE-ICT Division, CR.ENEA [1]Frascati,[2]Roma
Sede,[3]Portici,[4]Firenze,[5]Casaccia,[6]Bari,[7]Brindisi,[8]Bologna,[9]Trisaia*

ABSTRACT. Taking the opportunity of the first ten years of the CRESCO super-computer center, the paper illustrates the evolution of its HPC clusters and of its user community and computing workloads.

1 Introduction

The year 2018 marks the tenth anniversary of the CRESCO HPC (High Performance Computing) center at the ENEA Portici site near Naples and this is a good opportunity to illustrate the evolution of its HPC systems and make some considerations about its usage and results considering both the application domains and the involved user community.

ENEA (born as the Italian Nuclear Agency, CNRN/CNEN) has a long tradition in the HPC domain since the early '60s and the main computational resources were traditionally located in central and northern Italy, Ispra, Bologna, Casaccia and Frascati near Rome, following the distributed structure of the main ENEA research centers.

In 2006 ENEA participated successfully with the CRESCO project (Computation center for RESearch on COmplex systems) to the selection published by the Italian National Program for Research PON 2000-2006, supported by European Regional Development Funds dedicated to Southern Italy. The CRESCO project, based mostly in Portici, triggered a big step forward for HPC activity in ENEA and the present CRESCO HPC center [1] is the long-lasting offspring of that project. The results of two previous smaller projects in the early 2000s, CAMPUS and TELEGRID [2], both with computational resources also in Portici, helped in providing support to the CRESCO project approval.

Due to the variety of ENEA research and development fields, the application domains of its HPC systems are traditionally very diversified, from the original nuclear technology to nuclear plasma physics, climate analysis, combustion computational fluid dynamics, atmospheric pollution diffusion, computational chemistry, bioinformatics, a non exhaustive list. As a consequence, the choice of the HPC technology has been progressively oriented to general purpose systems capable to provide good performances for a wide range of different application codes.

---

*Corresponding author. E-mail: `giovanni.bracco@enea.it`.
†`now Accenture Italia,Milano.`

A key aspect of HPC is the very fast technological evolution so that the computational resources must be regularly updated to keep the state-of-the-art level and, as it will be described later, CRESCO HPC hardware has evolved along three generations in the last 10 years, with a two order of magnitude increase of the computing power.

Since the last '90 it has become clear that due to the availability of the high bandwidth WAN (wide area network) provided by GARR [3], the Italian National Research and Education Network, and the distributed structure of ENEA research sites, the optimal provision of HPC resources should go through the integration of all the systems in a unified infrastructure ENEAGRID [4] [5]. ENEAGRID was and still is based on a middleware composed of production level software components, as LSF (Platform Load Sharing Facility) for resource management, AFS (Andrew File System) as a common data area and a web based remote access tool as Citrix in the early days, later FreeNX and now Thinlinc. In the mid-2000s also IBM GPFS (General Parallel File System) now Spectrum Scale, was introduced in ENEAGRID to provide an high performance parallel file system, with WAN capability. This middleware provides a unified user environment and homogeneous access method for all ENEA researchers and facilitates the user migration along the fast hardware evolution.

The next section illustrates the technical characteristics of the CRESCO clusters and it is followed by a section providing information about the user community and the system workloads as provided by the accounting facilities, focussing the attention in both cases on the last 10 years evolution.

2 Cluster and Infrastructure Evolution

In the mid-2000s, most of the computational power of the ENEAGRID infrastructure was provided by IBM SP systems and the main site was Frascati, hosting the SP4 (IBM P4 690, 128 CPUs), and SP5 (IBM P5 575/595, 448 CPUs) clusters with a total of 2.2 TFlops. The arrival of CRESCO Project in 2008 made Portici the main location for the ENEA HPC resources in a new modern computing room with all the required services, 0.5 MW electrical power provision (protected by an uninterruptible power supply) and the air cooling systems. In 2013 the project TEDAT, from PON 2007-2013, supported the implementation of a second computer room with a dedicated cooling system.

In this way the operation overlaps of two generations of computing systems are easily attained on Portici site with a better and continuous service to users. This approach has been applied more than once in last 10 years and in the next subsections the evolution of the clusters installed on Portici site since 2008 up to 2018 are described.

In the same period some HPC resources have been installed as components of ENEAGRID in other ENEA sites, mainly in Frascati and Casaccia, and also these clusters are illustrated in a dedicated subsection. The Table 1 fully summarizes the ENEAGRID evolution in the last ten years and its content will be discussed in section 2.7 after a short description of the various clusters.

2.1 CRESCO1 and CRESCO2

The first cluster installed in 2008 in the new computer room ready to host the CRESCO clusters in Portici was the EFDA Gateway [6], a small cluster (3 racks) used as a developer platform by the Nuclear Fusion community as the HPC collaboration between ENEA and EUROFUSION [7] (EFDA at that time) dates back from the very beginning of CRESCO center settlement, see 2.5 for the later developments. The bulk of the computing resources for the CRESCO Project were the CRESCO1 and CRESCO2 clusters. CRESCO1 was dedicated to large memory applications and consisted of 42 nodes IBM X3850M2 (4 Intel Tigerton E7330 CPU 2.4 Ghz, 4 cores, 32 or 64 GB RAM). CRESCO2

Table 1: The available clusters in ENEAGRID ordered by elapsed time for each year, (the usage percentage of the most used cluster is shown), the total number of cores and the total computational power in TFlops

Year	Available Clusters	Total #Core	Total Peak Power (Tflops)
2008	CRESCO2 (57%), SP5,SP4,CRESCO1	3296	27.5
2009	CRESCO2 (90%), CRESCO1,SP5,SP4	3296	27.5
2010	CRESCO2 (86%), CRESCO1,SP5,SP4	3296	27.5
2011	CRESCO2 (81%), CRESCO1,SP5,CRESCOF,CRESCOC,SP4	4640	33.6
2012	CRESCO2 (84%), CRESCO1,CRESCOF,SP5,CRESCOC	4512	32.8
2013	CRESCO2 (63%), CRESCO3,CRESCOC,CRESCO1,CRESCOF,SP5	6528	52.2
2014	CRESCO4 (55%), CRESCO2,CRESCO3,CRESCOF,CRESCO1	10752	150.2
2015	CRESCO4 (82%), CRESCO3,CRESCO2,CRESCOF,CRESCO5	10752	169.6
2016	CRESCO4 (77%), CRESCO3,CRESCO5,CRESCOF,CRESCO2	8192	153.2
2017	CRESCO4 (79%), CRESCO3,CRESCO5,CRESCOF,CRESCO2	8192	154.2
2018	CRESCO4 (55%), CRESCO6,CRESCO5,CRESCOF,CRESCO3	26176	1508.5

was oriented to high scalability applications and consisted of 256 IBM HS21 blades (2 Intel Clovertown E5345, 2.33 Ghz, 4 cores, 16 GB RAM). Both clusters were interconnected by a CISCO DDR Infiniband fabric (552 ports) which provided access also to the IBM DCS9550 storage (180 TB raw), formatted in GPFS file system. Data backup was provided by an IBM TS3500 Tape Library. CRESCO2 ranked at the 126th place in the Top 500 list [8] in June 2008. The CRESCO computer room hosted a total of 23 racks, distributed in 3 rows. The cooling was provided by 5 CRAC (computer room air conditioning) air/gas units, for a total of 250 KW cooling power. Between 2010 and 2011 CRESCO2 cluster was expanded with additional 84 blades (Nehalem E5530 and Westmere E5620 CPUs) for a total of 2720 cores attaining 25 Tflops.

2.2 CRESCO3

In the first half of 2013, by combining the limited funding of the PON 2007-2013 research projects IT@CHA [9] and LAMRECOR[10], the cluster CRESCO3 was installed in the existing CRESCO computer room. It consisted of two racks with 84 nodes in 21 Supermicro Fat twin chassis, dual CPUs AMD Interlagos 6234 2.4 GHz, 64 GB RAM, 12 cores for a total of 2016 cores and 20 Tflops peak computing power. The nodes were interconnected by a 96 ports QDR 12800-040 Qlogic switch. A DDN S2A9900 provided 600 TB of raw data space, formatted in Spectrum Scale/GPFS filesystems. For rather small clusters as CRESCO3 the choice of AMD CPUs optimized the cost/performance ratio at that time, see also Section 2.6.

2.3 CRESCO4

Later in 2013 the more consistent funding of the PON 2007-2013 infrastructural project TEDAT [11] supported the procurement of the cluster CRESCO4 [12] in a new computer room with a dedicated cooling system (4 CRAC air-water units with free cooling capability). Only the electrical power supply was shared with the pre-existing computer room. CRESCO4 , still operating at this time, consists of 7

racks with 304 Supermicro nodes (assembled in 4U Fat twin chassis) dual Intel Sandy Bridge E5-2670, 2.6 GHz, 8 cores CPUS, 64 GB RAM connected by a 384 ports QDR 12800-180 Qlogic switch, for a total of 4864 cores and 100 TFlops peak power. The storage area was expanded with two DDN 7700/7700X storages (720 TB raw) shared with CRESCO3 cluster.

2.4 CRESCO5

In 2015 a new small cluster CRESCO5 was installed in the CRESCO4 computer room, with 42 Super-micro nodes (1 U twin chassis), dual CPUs Intel Haswell E5-2630v3, 2.4 GHz, 8 cores, 64 GB RAM, for a total of 672 cores and 24 TFlops. The cluster shared the QDR switch with CRESCO4 and was dedicated to applications with expensive licences as ANSYS, where the scalability was limited by the number of available licenses.

2.5 CRESCO6

In 2015 an agreement to promote joint activities and projects was signed between ENEA and CINECA, the main HPC institution in Italy [13]. In this framework, CINECA and ENEA participated successfully to a selection launched by EUROFUSION [7] for the procurement of a several PFlops HPC system. The new CINECA MARCONI-FUSION system started operation in 2016 at CINECA site in Bologna. In this context the role of ENEA Portici as one of Tier 1 Italian HPC sites was established and as a result the new CRESCO6 cluster was installed in 2018. The system consists of 8 racks for a total of 434 nodes (Lenovo SD530 8U chassis), dual CPUs Intel SKL 8160 2.1GHz, 24 cores, 192 GB RAM, for a total of 20832 cores. The nodes are interconnected by the Intel OmniPath (OPA) fabric configured in a fat-tree composed by 21 OPA 48 ports switches, with a 1:2 subscription. CRESCO6 ranked at the 420th place in the Top 500 list [8] in November 2018. CRESCO6 is installed in the computer room previously hosting CRESCO1, CRESCO2 and CRESCO3 clusters.

The room was completely reorganized in 2016-2017, by creating two different spaces, one for computing nodes and the other for storage and services and the installation of the new cluster was performed with a minimal downtime for the preexisting clusters. The storage area, shared with the previous clusters has been expanded with a new DDN7990 storage (1 PB raw). A new I/O server configuration has been implemented so that both the QDR and the OPA nodes have full access to all the available DDN storages (4 storages and 6 I/O servers), by taking advantage of GPFS/Spectrum Scale capability to operate in a mixed QDR/OPA fabric configuration.

2.6 Clusters outside Portici site

As already noted in the introduction to Section 2 the CRESCO project promoted Portici as the main ENEA HPC site while most of the previous computational resources were located in Frascati and Casaccia with some additions in the ENEA centers in Southern Italy (Trisaia, Brindisi and also Portici) from the TELEGRID and CAMPUS projects of the early 2000s. All these resources were integrated in ENEAGRID distributed infrastructure.

Taking advantage of that and with the aim to maintain significant local computational resources to users of the main ENEA centers, two clusters CRESCOC and CRESCOF, were installed in Casaccia and Frascati. As noted in Section 2.2 the choice of AMD CPUs optimized the cost performance ratio at that time. Casaccia CRESCOC cluster (2011) consists of 16 Supermicro nodes (1U Twin chassis),

dual AMD 2427 Istanbul CPUs, 2.2 GHz, 6 cores, for a total of 192 cores, interconnect by a DDR Infiniband fabric. Frascati CRESCOF cluster (2012) consists of 20 Gateway/Supermicro nodes (2U Fat twin chassis), dual AMD Magni-Cours 6174 CPUs, 2.2 GHz, 12 cores, for a total of 480 cores, interconnected by a Qlogic QDR fabric. The Frascati storage area is based on GPFS/Spectrum Scale, in WAN remote connection with Portici Spectrum/Scale GPFS cluster while Casaccia storage area is limited to AFS data space.

2.7 Discussion of the infrastructure evolution

Table 1 shows for each year the list of clusters open to users, together with the total number of available cores and the peak floating point computing power. The list of clusters for each year is ordered according to the usage, showing for the most used cluster the usage percentage in term of WCT (Wall Clock time). It can be seen that the largest cluster available in each year, CRESCO2 between 2008-2013) and later CRESCO4, takes most of the WCT with a clear increase in the transition years. In 2018 the arrival of CRESCO6 in the second half of the year reduces the fraction of CRESCO4. So users easily shift from old to new clusters, looking for high computational power.

In ten years the integrated computational power provided to users has increased of a factor greater than 50 and it exceeds now 1.5 Pflops, exploiting various opportunities in term of projects and agreements, with a strong effort of the CRESCO team along the years. Nevertheless, it must be remarked that this large increase does not match the general technological increase of HPC field: to gain in 2018 with CRESCO6 the same Top500 rank 126th of CRESCO2 in 2008, a factor 2 more computing power would have been required. In other words, from Table 1, it emerges that the time life of the main cluster has been 5-6 years, a period longer than the 3 years of the technological evolution of the HPC systems. This fact, from the user point of view, paradoxically turns out to have the positive effect to be able to concentrate on application results, in a rather stable computational context, without the need of continuous software upgrades.

A synergic effect between the HPC resources and the other ENEA information technology infrastructures has been the strategy of exploiting whenever possible the decommissioning of HPC clusters by reusing the servers as the bulk of the ENEA cloud farms, distributed in several ENEA sites. This has happened with CRESCO1, CRESCO3 and CRESCO5. Not so much with CRESCO2, as the blade technology was not flexible enough for reuse. Some of the CRESCO3 nodes (two chassis, 8 nodes, new NVIDIA GPUs) are now operating at the Italian Antarctic "Mario Zucchelli" Station at Terra Nova Bay and are mostly used for local image elaboration. ENEA is involved in the logistic and support activities of the Italian National Antarctic Program.

3 Usage and workloads

In Table 2 the main data about the usage of the ENEAGRID clusters in last decade are summarized. The usage data are provided by the accounting tool of LSF, the ENEAGRID resource manager. The next sections discuss the user characteristics and the applications workloads along the years.

3.1 Users Analysis

From Table 2 it emerges that the total number of ENEAGRID users in a year is in the range 130 to 350 according to the change in activities and collaboration of ENEA researchers while the number of real

Table 2: Yearly usage in the last decades for all ENEAGRID clusters. The table shows the WCT, the total number of users, the total number of intensive HPC users, the number of submitted jobs, the fraction of WTC of non ENEA users

Year	Wall Clock Time 10^6 core*hours	Total #Users	#Users with $>10^4$ core*hours	#Submitted jobs 10^3	Percentage external users
2008	4.6	257	34	2404.5	2.4
2009	13.9	350	63	620.7	14.0
2010	17.3	332	69	399.6	28.4
2011	19.8	267	71	301.4	39.6
2012	23.3	172	68	184.2	44.1
2013	30.0	183	85	217.6	26.5
2014	48.4	190	84	756.4	29.3
2015	46.6	167	83	162.7	33.8
2016	42.6	165	77	847.2	45.1
2017	34.1	134	72	571.3	24.6
2018	42.5	144	78	1321.6	17.0

HPC intensive users, with more than 10000 core hours, is rather stable in the range 70-80. Typically non intensive ENEAGRID users take advantage of only some of ENEAGRID resources, as they exploit the access to storage area for their own data management or make use of licensed serial applications in interactive sessions on front-end nodes.

The large number of non intensive users in the years 2008-2011 is due to users involved in ENEAGRID both by the EUROFUSION gateway, see Section 2.1, and by the so called "pool account" users implemented by the integration of some of ENEAGRID resources into EGEE, EGEE2, EGEE3 [14] GRID projects. In both cases the access to ENEAGRID resources was more a proof of concept than a real production approach.

The last column in Table 2 shows the percentage of the non ENEA usage of the yearly WCT. Non ENEA users can have access to ENEAGRID resources when involved in common activities with ENEA researchers in the framework of projects or in specific research and development activities. The involvement can change from year to year according to the life of the projects and the developments of the activities.

3.2 Applications Workloads

The first column in Table 2 shows the evolution of WCT along the years. The values increase both with the available number of cores, see Table 1, and with a progressive spread of utilization of HPC, especially in the first years of CRESCO clusters availability, when the user community was also increasing. The data are integrated over the year and so for example the startup of the large cluster CRESCO6 at the end of 2018 does not result in a significant increase of the used WCT.

If the WCT values of Table 2 are compared with the available core number of Table 1 the global utilization of all the systems appears to be typically in the range 50%:60% and it is higher (70%:80%) if the same evaluation is restricted only to the main cluster at the time, CRESCO2 between 2008-2013 e CRESCO4 between 2014-2018. Obviously the comparison includes also the effects due to the system downtimes, due to maintenance or incidents, and to the work regularity of the users. The lower utilization of secondary clusters is also correlated with their role: for example the target of CRESCO5, dedicated to expensive licenced codes, has been the optimization of the licence utilization while local

clusters as CRESCOF are dedicated to local user elaboration.

The number of yearly submitted jobs, see Table 2, shows strong variations of more than one order of magnitude along the years. This is due to the different kinds of system utilization approach according to different scenario of the research and development activities of the users. Some years have been dominated by a relative small number of large parallel jobs, other years by a large number of relatively small multicase jobs. The capability of the resource manager of ENEAGRID has demonstrated to easily support both operation modes.

References

[1] http://www.cresco.enea.it. The website is the user portal and contains also the references to the main projects that have supported CRESCO HPC Center development.

[2] http://www.telegrid.enea.it.

[3] http://www.garr.it.

[4] http://www.eneagrid.enea.it. The website contains information about ENEA HPC infrastructure architecture.

[5] Migliori S. et al. ENEA computing factory. In *Proceedings of the International Conference on Parallel and Distributed Processing Techniques and Applications, PDPTA 1999, June 28 - Junlly 1, 1999, Las Vegas, Nevada, USA*, pages 3037–3040, 1999.

[6] B.Guillerminet, F.Iannone, F.Imbeaux, G.Manduchi, A.Maslennikov, V.Pais, and P. Strand. Gateway: New high performance computing facility for efda task force on integrated tokamak modelling. *Fusion Engineering and Design*, 85(3-4):410–414, 2010.

[7] https://www.euro-fusion.org.

[8] http://www.top500.org.

[9] http://www.progettoitacha.it.

[10] http://www.lamrecor.it.

[11] http://www.eneagrid.enea.it/TEDATproject.

[12] Ponti G. et al. The role of medium size facilities in the HPC ecosystem: the case of the new CRESCO4 cluster integrated in the ENEAGRID infrastructure. In *International Conference on High Performance Computing & Simulation, HPCS 2014, Bologna, Italy, 21-25 July, 2014*, pages 1030–1033, 2014.

[13] https://www.cineca.it.

[14] http://eu-egee-org.web.cern.ch/eu-egee-org/index.html.

CRITICAL INFRASTRUCTURE PROTECTION
CRESCO6 TSUNAMI SIMULATIONS IN SOUTHERN ITALY

F.Iannone[1*], S.Migliori[2] and DTE-ICT-HPC team[2]

[1]*ENEA, DTE-ICT-HPC, via E.Fermi 45, 00044, Frascati,Rome,Italy*
[2]*ENEA, DTE-ICT, via Lungotevere Thaon de Ravel, Rome, Italy*

ABSTRACT. ENEA jointly INGV (National Institute Geophisical and Volcanology) is the Italian node of European Infrastructure Simulation and Analysis Centre aiming at establishing a collaborative, european-wide platform in the domain of Critical Infrastructure Protection (CIP), for supporting Operators and Public Authorities in better protecting assets and in enhancing their resilience with respect to all hazards. Tsunamis are among the natural hazards that can result in the largest number of victims per event as well as to damage or destruction critical infrastructure like power plant/grid, transport/information and communication networks. Therefore early warning tools can be provide about tsunami if there is enough distance between the seismic source and the coast.

1 Introduction

Industrial facilities and critical infrastructure are vulnerable to the impact of natural hazards such as: earthquakes and tsunamis. Tsunamis are among the most remarkable phenomena associated with events such as: strong earthquakes, volcanic eruptions and landslides and as the Mediterranean Sea characterized by high seismicity and significant volcanism, the geographical cost areas, where the people live, are highly vulnerable also far way from event source. Numerical simulations of tsunamis are useful in hazard analysis as tool for planning infrastructures development in costal areas. Furthermore they can adopted in early warning systems if they are enough fast to get out safety alarms for near sea inhabitants. This paper shows the feature of a software open source simulating tsunami scenarios and running on HPC cluster.

2 Numerical models

Because tsunamis begin as very long wavelength disturbances, they are commonly, and have been historically, modelled with the shallow water equations [*Glaister,1988*] a system of nonlinear hyperbolic PDEs described as follow:

$$\frac{\partial(z+h)}{\partial t} + \mathbf{\nabla} \cdot [\mathbf{v}(z+h)] = 0 \qquad (1)$$

$$\frac{\partial \mathbf{v}}{\partial t} + (\mathbf{v} \cdot \mathbf{\nabla})\mathbf{v} = -g\mathbf{\nabla}z + \boldsymbol{C} + \boldsymbol{F} \qquad (2)$$

where z is the water elevation above sea level, h is the water depth in a still ocean, $\mathbf{v}$ is the depth-averaged horizontal velocity vector, g is the gravity acceleration, $\boldsymbol{C}$ is the Coriolis force, and $\boldsymbol{F}$ represents bottom friction forces, for which we used the Manning's formula with a roughness coefficient of *0.05*. The equations were solved numerically by means of a finite volume method [*LeVeque, 2002*]. The boundary conditions as pure wave reflection at the solid boundary, by setting to zero the velocity component perpendicular to the coastline. In this way all tsunami kinetic energy is converted into potential energy at the coast. This is equivalent to the physical condition achieved when the wave reaches the maximum onshore inundation distance. Thus while the complex processes of inundation is not simulated (which are controlled by fine scale details of the nearshore topography), the predicted coastal wave

heights include wave shoaling in shallow waters and could be a rough proxy for the inundation effects.

2.1 GeoClaw

The numerical simulations have been carried out running GeoClaw on CRESCO6. It is an open source research code that uses high-resolution finite volume methods together with adaptive mesh refinement to tackle geophysical flow problems. In particular, this code has recently been used together with the shallow water equations to model tsunamis and dam-break foods [*Berger, 2011*]. The shallow water equations *(1)* and *(2)* have been numerically solved on a two-dimensional grid using adaptive mesh refinement (AMR) techniques in order to concentrate grid cells in regions of interest, and to follow such regions as the flow evolves. This is often the only efficient way to obtain results that have sufficient spatial resolution where needed without undue refinement elsewhere, such as regions the flow or wave has not yet reached or points distant from the study area.

The computational core of GeoClaw is written in Fortran and compiled with OpenMP on a single node of CRESCO6 equipped with 2xIntel Skylake CPUs with 24 cores each. A user interface written in Python is provided to simplify the setup of a single run, or of a series of runs as is often required for parameter studies, sensitivity studies, or probabilistic assessments of hazards. Python plotting tools are also provided for viewing the results in various forms, either on the dynamically changing set of adaptive grids or on a set of fixed grids, or in other forms such as gauge plots of depth vs. time at fixed spatial locations. The Python plotting tools have been parallelized with MPI tasks for each independent time frame on each core in order to speed-up the execution time.

3 Tsunami scenarios

The main aim of this work is to evaluate GeoClaw as tool for using in the early warning framework, able to safe humans life in case of tsunamis generated by natural disasters in the Mediterranean Sea such as: earthquakes and volcanic eruptions. Therefore three natural disasters are investigated by means numerical simulations using GeoClaw. The three scenarios have 2 different tsunami source: the first one is as sources: the earthquakes of the 365 AD in the island Crete area involving the whole Mediterranean East basin and the 1908 Messina Strait involving the costal areas of Calabria and Sicily; the second one is a volcanic eruption in the Campi Flegrei area, similar to 1538 Monte Nuovo eruption involving the Naples gulf.

3.1 Earthquakes in the Mediterranean Sea

The tsunamis simulations in the Mediterranean sea, caused by earthquakes: 365 AD Crete and 1908 Messina Strait, were carried out using as initial seawater elevation was assumed to be equal to the seismic vertical displacement of the sea bottom produced by a seismic fault computed through the Okada [*Okada*,1985,1992] analytical formulation. The initial velocity field was assumed to be identically zero. The seafloor topography was taken from the ETOPO1 bathymetric data set [*Smith*, 1997] with 1 arc-min of resolution. The seismic basic parameters used in the Okada model is shown in the table 1.

Table 1: Mediterranean Ses GeoClaw simulations. Seismic parameters for Okada model.

	LAT LOG	L/W [km]	D [km]	Slip [m]	Strike [deg]	Dip [deg]	Rake [deg]	M_w
365 AD Crete	35 23	130/86	5	17.5	314	35	90	8.5
1908 Messina Strait	38.09 15.58	56.7/18.5	1.1	1.5	355.8	38.6	270	7.16

The fig.1 shows the GeoClaw simulation of tsunami in the 365 AD Crete earthquake carried out over a 2D grid resolution using 3 levels of AMR: *L1=24 km, L2=12 km* and *L3=2 km*.
Output gauges have been set in the four towns: Crete,Derna, Catania and Catanzaro. The wall time of 1 hour simulation is 1675 sec.

720 s   2160 s   2880 s   3600 s

(a)

(b)
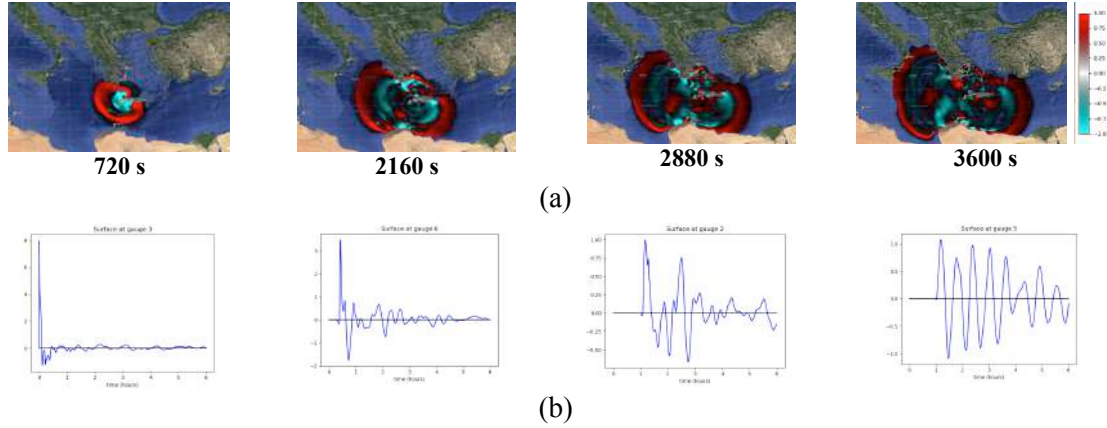
Fig.1: Mediterranean Sea: 356 AD Crete earthquake - tsunami simulation:
(a) 2D mapping of the height on level sea vs. time.
(b) Heights on level sea for gauges in : Crete, Derna, Catania and Catanzaro

The fig.2 shows the GeoClaw simulation of tsunami in the 1908 Messina Strait earthquake carried out over a 2D grid resolution using 3 levels of AMR: *L1=1.8 km, L2=912 m* and *L3=152 m*.
Four output gauges have been set in the towns: Messina,Catania,Paola and Milazzo. The wall time of the 2 hour simulation is 880 sec.

0 s   600 s   1200 s   1800 s

(a)

(b)
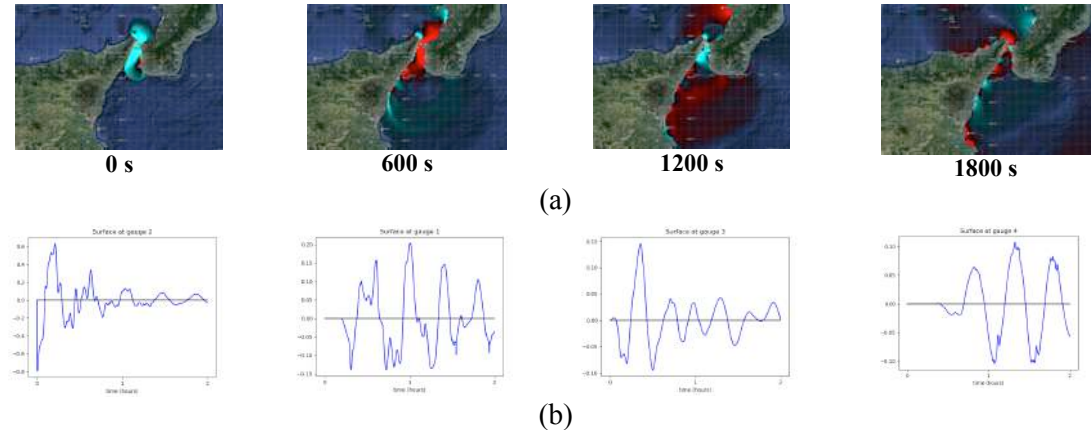
Fig.2: Mediterranean Sea: 1908 Messina Strait earthquake - tsunami simulation:
(a) 2D mapping of the height on level sea vs. time.
(b) Heights on level sea for gauges in : Messina, Catania, Paola and Milazzo

3.2 Monte Nuovo volcanic eruption

The 1538 eruption of Monte Nuovo erupted less than 0.1 km^3 of magma but substantially changed the morphology of the area and affected an area in the order of tens of square kilometres (fig.1a) [*Scandone,2002*]. Overall the eruption may be classified as a mild explosive eruption. The eruption was described by eyewitness: a suddenly ground uplift of 7 m was a precursor to the eruption and it caused rapidly the shoreline to push ahead as much as 300 m. The fig.1b shows a linear uplift field compatible with the witnesses that provide the displacement of the bathymetry for tsunami generation.

Fig.3a. The cone of Monte Nuovo was formed during the 1538 eruption of Campi Flegrei
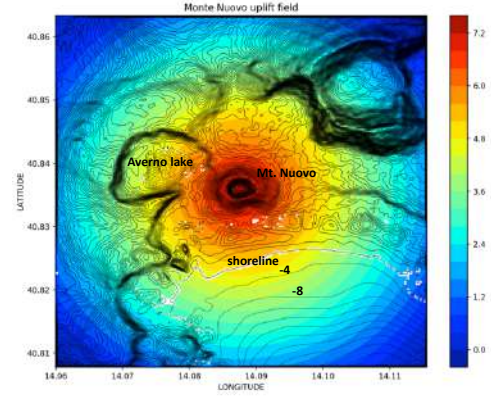
Fig.3b: Monte Nuovo linear uplift field as source of tsunami simulations.

The fig.4 shows the GeoClaw simulation of tsunami in the Monte Nuovo volcanic eruption carried out over a 2D grid 500x500 resolution using 3 levels of AMR: *L1=113.2m*, *L2=56.6 m* and *L3=9.4 m*. Four output gauges have been set in the towns: Pozzuoli, Naples, Portici and Sorrento. The wall time of the 4 hours of simulation is 3960 sec.

| 240 s | 480 s | 720 s | 1200 s |

(a)

(b)
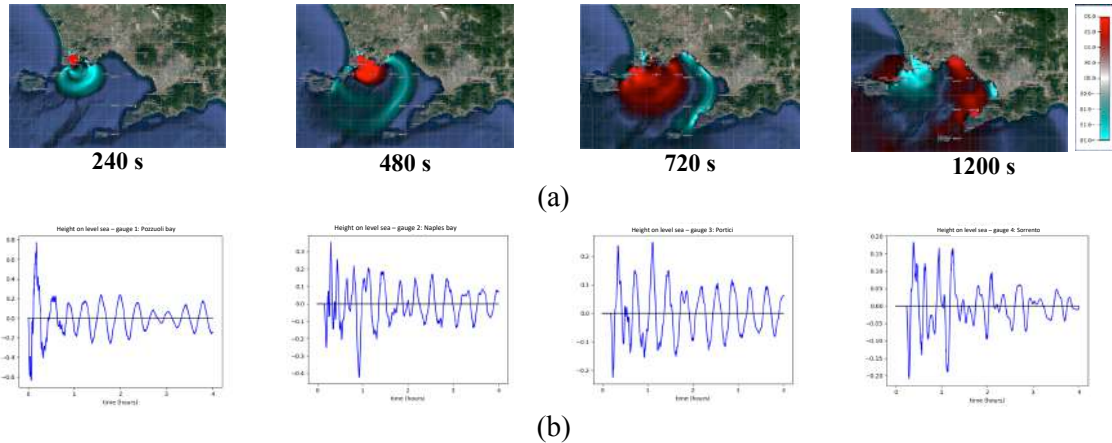
Fig.3: Monte Nuovo eruption - tsunami simulation:
(a) 2D mapping of the height on level sea vs. time.
(b) Heights on level sea for gauges in : Pozzuoli, Napoli, Portici and Sorrento

Table 2: Monte Nuovo eruption GeoClaw tsunami simulations. Wall Time vs. grid resolutions.

Grid	L1 res. [m]	L2 res. [m]	L3 res. [m]	Wall Time [s]
50×50	1132.2	566.1	94.4	144.8
100×100	566.1	283	47.2	241.5
500×500	113.2	56.6	9.4	3960

The fig.5 shows the output gauge of Sorrento in three different grid resolutions of the table 2, in order to evaluate the reliability of fast simulations on grid with low resolution. The reliability is quite good

16

for the first tsunami waves whilst it get worse on the successive waves. It means GeoClaw with grid low resolution is reliable on the early warning systems.
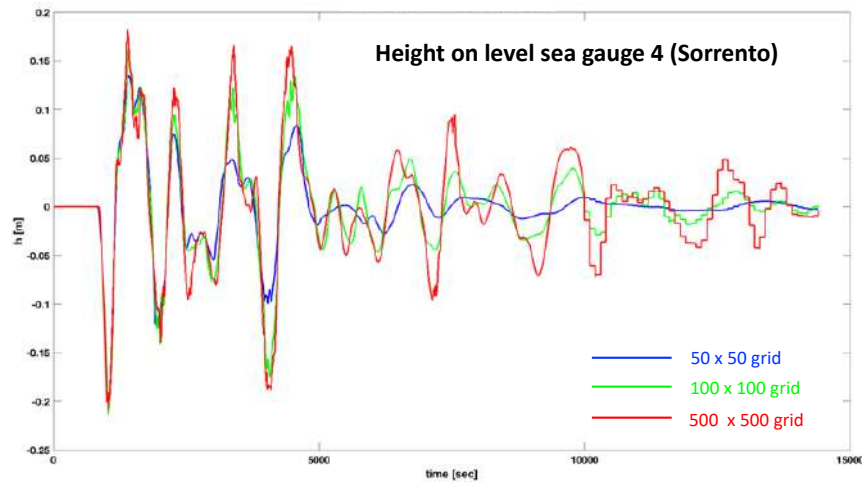
Fig.5: Reliability of GeoClaw simulations in different grid resolutions.

Conclusions

The GeoClaw open source software for tsunami numerical simulations, is available on CRESCO6 HPC cluster with the python tools for post-processing parallel tasks. In this way the graphic visualization of the simulations are quickly available for early warning systems.

References

[1] P. Glaister. *Approximate Riemann Solutions of the Shallow Water Equations*, J.Hydr. Research Vol. 26, No.3 (1988).

[2] R. J. LeVeque. *Finite Volume Methods for Hyperbolic Problems*. Cambridge University Press, 2002.

[3] Marsha J.Berger, David L.George, Randall J.LeVeque, Kyle T.Mandli, *The GeoClaw software for depth-averaged flows with adaptive refinement*. Advances in Water Resources Volume 34, Issue 9, September 2011, Pages 1195-1206.

[4] Okada, Y. (1985), Surface deformation due to shear and tensile faults in a half-space, Bull. Seismol. Soc. Am., 75, 1135–1154.

[5] Okada, Y. (1992), Internal deformation due to shear and tensile faults in a half-space, Bull. Seismol. Soc. Am., 82, 1018– 1040.

[6] Smith, W. H. F., and D. T. Sandwell (1997), Global sea floor topography from satellite altimetry and ship depth soundings, Science, 277, 1956–1962.

[7] R.Scandone,L.Giacomelli. *The reduction of volcanic risk in the Neapolitan area*. Journal of Research and Didactics in Geography (J-READING), 0, 1, Dec., 2012, pp. 25-33 DOI: 10.4458/1005-04.

REPORT ON THE PERFORMANCE ON THE CRESCO6 CLUSTER OF THE HYBRID OPENMP/MPI ORAC6.1 MOLECULAR DYNAMICS CODE

Piero Procacci[1]*, Guido Guarnieri[2]

[1]*Dipartimento di Chimica, Università di Firenze, Via della Lastruccia 3, I-50019 Sesto Fiorentino, Italy*

[2]*ENEA, Portici Research Centre, DTE-ICT-HPC, P.le E. Fermi, 1, I-80055 Portici (NA) (Italy)*

ABSTRACT. We present extensive benchmarks on the CRESCO6 (Enea, Portici) and Marconi/A1 (Cineca, Casalecchio) HPC platforms using the massively parallel OpenMP/MPI hybrid Molecular Dynamics code ORAC for binding free energy calculations in drug-receptor systems using the double annihilation fast switching alchemical technology.

1 Introduction

This report presents extensive performance data of the orac6.1 molecular dynamics (MD) code[1] on the CRESCO6 (Enea, Portici) and Marconi/A1 (Cineca, Casalecchio) HPC platforms. The ORAC6.0 program is a hybrid OpenMP/MPI code specifically designed for running simulation of complex systems on multi-cores NUMA architectures. The code is written in FORTRAN language and can be freely downloaded from the site http://www.chim.unifi.it/orac. The parallelism of the MD computation is done on two layers, based on i) an intra-node strong scaling algorithm for force decomposition implemented on a shared memory environment via OpenMP threading; ii) an intra- and inter-node weak scaling parallelization for replica exchange[2] (REM) and concurrent simulation of driven non equilibrium (NE) trajectories implemented via MPI. The total number of cores requested by a typical orac job is hence given by $N_{\text{cores}} = N_{\text{MPI}} \times N_{\text{threads}}$.

The present benchmark is aimed at comparing the CRESCO6 architecture[3] based on the Intel(R) Xeon(R) Platinum 8160 CPU 2.10GHz processor with respect to the Marconi Broadwell partition A1,[4] based on the Intel(R) Xeon(R) CPU E5-2697 v4 2.30GHz processor. The code has been compiled on both CRESCO6 and on Marconi/A1 with the Intel `ifort` compiler (ver 17.0.4). We used the processor specific options `-xCORE-AVX512` and `-xCORE-AVX2` on CRESCO6 and on Marconi/A1, respectively. Vectorization with `xCORE-AVX512` on CRESCO6 has been examined using the the compiler option `-qopt-report-phase=vec`.

This report is organized as follows. In section 2 we compare the performances of the orac6.1 code for the OpenMP layer only on the Marconi/A1 (Broadwell) and CRESCO6 (Skylake) platforms. In Section 3, we report on the performances of the orac6.1 on CRESCO6 for the MPI layer only. In the final section we report the results obtained on Marconi/A1 and on CRESCO6 for two typical production hybrid jobs for fast switching double annihilation[5, 6] computations, namely:

1) REM: A replica exchange simulation using a total 8 threads on the OpenMP layer and 96 MPI

---

*Corresponding author. E-mail: `procacci@unifi.it`.

instances for a total of 768 cores on CRESCO6 and 9 threads on the OpenMP layer and 64 MPI instances for a total of 576 cores on Marconi/A1. The system in both cases is the s45a mutant of streptavidin in complex with biotin (pdb code 1df8) for a total of 12830 atoms.

2) FNE: A non equilibrium alchemical annihilation for 720 concurrent trajectories on the MPI layer each running on 8 OpenMP threads for a total of 5760 cores on CRESCO6 and for 810 MPI trajectories each with 6 OpenMP threads on Marconi/A1 for a total of 4860 cores. The system in both cases is the structure of ricin chain bound with benzyl-(2-(2-amino-4-oxo-3,4-dihydropteridine-7-carboxamido)ethyl)carbamate (pdb code 4mx5) for a total of 25280 atoms.

2   Parallel efficiency on the OpenMP layer

In this section we compare the performances of the strong scaling part of the code up to 16 threads in the FNE annihilation stage. Results are reported in Figure 1. While speedup factors are found to be
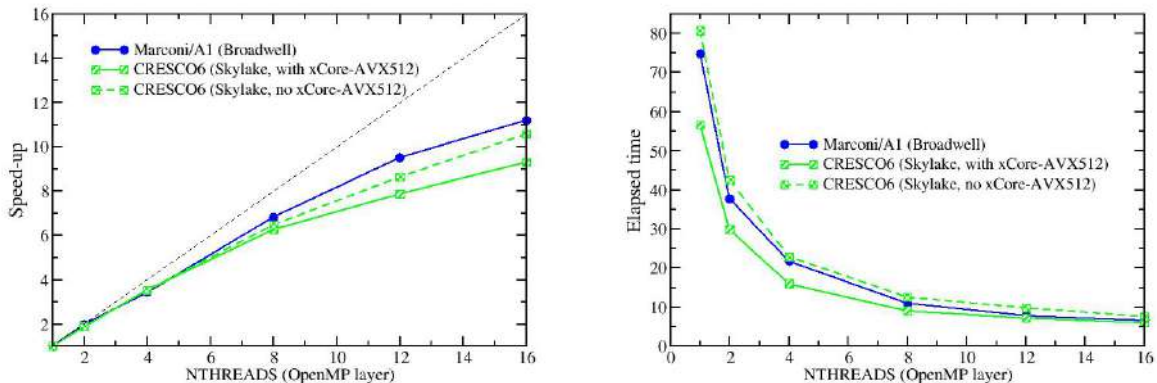
Figure 1: Speedup factors (left) and absolute timing per picosecond (right) of simulation of the 4mx5 system (25280 atoms, FNE stage) obtained on Marconi/A1 and CRESCO6 for the OpenMP parallel layer. The dotted black line in the right panel indicates ideal scaling.

slightly better on the Broadwell CPU (left panel), as far as elapsed times are concerned, the Skylake CPU appears to be more performing (right panel). The data for the elapsed time per picosecond clearly show the impact of the processor targeting option `xCORE-AVX512` for the Skylake based CRESCO6 cluster for low threads number. For serial execution, the vector compiled code is about 50% faster than the non vector code while with 16 threads the two codes have comparable performances.

3   Parallel efficiency on the MPI layer

In the Figures 3, we report the speed up ratio and parallel efficiency, *referred to the MPI layer only*, obtained for the REM stage (1df8 system) and for the FNE stage (4mx5 system) on CRESCO6. For the REM stage, we run a REM simulation lasting 1.0 ps. Simulations were run (using in all cases one OpenMP thread per trajectory) with 48, 96, 192, 384 and 768 communicating replicas each corresponding to a MPI process. Replica exchanges were attempted every 15 femtoseconds. All REM tests were
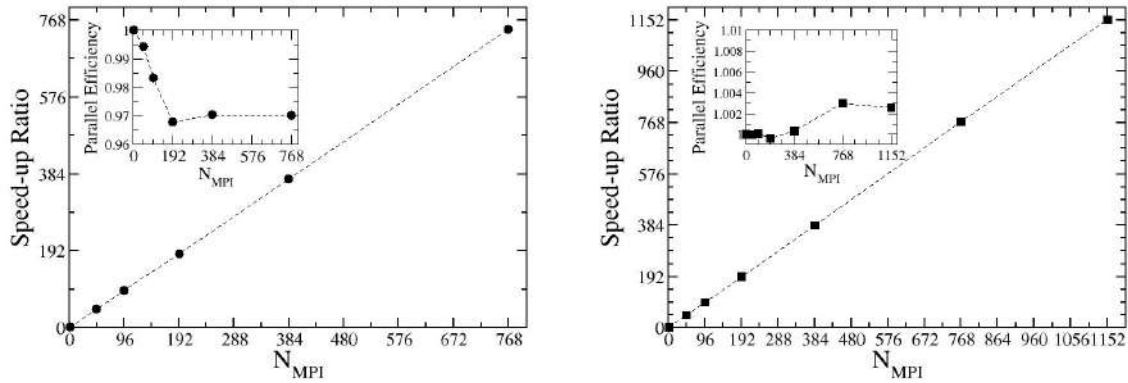
Figure 2: Performance test for the REM (left panel) and FNE)right panel) computational stages

completed in an elapsed time ranging form 31.9 seconds (1 replica) to 33.0 seconds (768 replicas).

For FNE , we launched NE trajectories lasting 1.0 ps. FNE parallel simulations were done producing 1, 48, 96, 192, 384, 576, 1152 independent non communicating trajectories, for a total simulation time ranging form 1 ps (1 FNE) to about 1 ns (1152 FNE). All FS-DAM tests were completed in an elapsed time ranging from 57.2 to 57.4 seconds. The performances on the MPI level are practically ideal for both the REM and FNE computational stages. While, expectedly, the embarrassingly parallel FNE computation exhibits no loss whatsoever of parallel efficiency (see the inset plot in the right panel of Figure 2), in the REM computation a minor efficiency loss can be barely appreciated with the 768 replicas simulation running at 97% of parallel efficiency (see the inset plot in the left panel Figure 1). This minor efficiency loss in REM is due to the communication overhead during replica exchange attempts. These are implemented each 15 fs (i.e. 67 attempts in total in the REM test) for all contiguous pairs of replicas and involve a `MPI_SEND` / `MPI_RECEIVE` couple of three double precision numbers (the so-called REST scale factors[1]) followed by an `MPI_BARRIER` on all MPI processes.

The ideal parallel efficiency of the REM and FNE stages on CRESCO6 has been observed on all tested HPC systems, including the Marconi/A1 partition, the CRESCO4 and CRESCO3 clusters.

4 Benchmark calculations for REM and FNE stages on the Marconi Broadwell and on the CRESCO6 Skylake platforms

In this section we report results on two typical FS-DAM production jobs on the CRESCO6 and Marconi/Broadwell clusters. The jobs on CRESCO6 were executed in the time window for CRESCO6 testing awarded by ENEA from 29 June to 1 July 2018. Jobs on Marconi were run in the spring 2018 in the framework of the PRACE project 2016163813 *DDFSDAM: Drug design for HPC systems: Fast Switching Double Annihilation Method (FS-DAM) at work.* Most of the parallelization in these production jobs is invested on the weak scaling (MPI) part (with basically ideal parallel efficiency) with few N_{threads} OpenMP instances (from 6 to 9) running in the intra-node shared memory environment. As shown in Table 1, such an hybrid setup allows to easily produce a total simulation time of the order of the microseconds using from few hundreds (REM) to few thousands (FNE) of cores. The parallel

	REM stage							
Platform	System	Atoms	N_{threads}	N_{MPI}	N_{cores}	τ_{sim}	τ_{Tot}	Elapsed/hours
CRESCO6	1df8	12830	8	96	768	3.6	345.6	**23.8**
Marconi/A1	1df8	12830	9	64	576	3.6	230.4	**19.2**

	FNE stage							
Platform	System	Atoms	N_{threads}	N_{MPI}	N_{cores}	τ_{sim}	τ_{Tot}	Elapsed/hours
CRESCO6	4mx5	25280	8	720	5760	0.72	518.6	**7.2**
Marconi/A1	4mx5	25280	6	810	4860	0.72	583.4	**11.4**

Table 1: Performances on the CRESCO6 and Marconi/A1 clusters for two FS-DAM production job using the orac6.0 hybrid OpenMP-MPI code. τ_{sim} and τ_{Tot} indicate, the simulation time in nanoseconds per (REM or FNE) trajectory and the total produced simulation time, respectively

setup for the two jobs reflects the different architecture of the CRESCO6 and Marconi/A1 nodes with 48 and 36 cores, respectively. The data reported in the Table show that Marconi is faster for the REM stage while it appears to be slower for the FNE computation. The reason for this outcome lies in the fact that, on CRESCO6, the FNE force routine involving the alchemical calculation, is fully vectorized while vectorization is incomplete for the more complex force REM routine.

We may conclude this report by stating that a careful code optimization/vectorization (diagnosed using the `-qopt-report-phase=vec` Intel compiler option) is essential for best performances on the CRESCO6 cluster. For example, for the fully vectorized FNE stage, based on the data given in Table 1, after threads re-normalization due to the architecture dependent hybrid parallelization, the CRESCO6 architecture appears to be about 30% faster than the Marconi/A1 HPC.

References

[1] Piero Procacci. Hybrid MPI/OpenMP Implementation of the ORAC Molecular Dynamics Program for Generalized Ensemble and Fast Switching Alchemical Simulations. *J. Chem. Inf. Model.*, 56(6):1117–1121, 2016.

[2] Y. Sugita and Y. Okamoto. Replica-exchange molecular dynamics method for protein folding. *Chem. Phys. Lett.*, 314:141–151, 1999.

[3] G. Ponti, F. Palombi, D. Abate, F. Ambrosino, G. Aprea, T. Bastianelli, F. Beone, R. Bertini, G. Bracco, M. Caporicci, B. Calosso, M. Chinnici, A. Colavincenzo, A. Cucurullo, P. Dangelo, M. De Rosa, P. De Michele, A. Funel, G. Furini, D. Giammattei, S. Giusepponi, R. Guadagni, G. Guarnieri, A. Italiano, S. Magagnino, A. Mariano, G. Mencuccini, C. Mercuri, S. Migliori, P. Ornelli, S. Pecoraro, A. Perozziello, S. Pierattini, S. Podda, F. Poggi, A. Quintiliani, A. Rocchi, C. Scio, F. Simoni, and A. Vita. The role of medium size facilities in the hpc ecosystem: the case of the new cresco4 cluster integrated in the eneagrid infrastructure. In *Proceeding of the International Conference on High Performance Computing & Simulation*, pages 1030–1033. Institute of Electrical and Electronics Engineers (IEEE), 2014.

[4] Consorzio Interuniversitario del Nord est Italiano Per il Calcolo Automatico (Interuniversity Consortium High Performance Systems) http://www.cineca.it (accessed 5 July 2018).

[5] Piero Procacci. I. dissociation free energies of drug-receptor systems via non-equilibrium alchemical simulations: a theoretical framework. *Phys. Chem. Chem. Phys.*, 18:14991–15004, 2016.

[6] Francesca Nerattini, Riccardo Chelli, and Piero Procacci. Ii. dissociation free energies in drug-receptor systems via nonequilibrium alchemical simulations: application to the fk506-related immunophilin ligands. *Phys. Chem. Chem. Phys.*, 18:15005–15018, 2016.

EFFECT OF BIDISPERSITY IN POLYMER CHAIN LENGTH ON THE POTENTIAL OF MEAN FORCE BETWEEN NANOPARTICLES IN A HOMOPOLYMER MATRIX

Gianmarco Munaò[1]*, Antonio De Nicola[2], Stefano Caputo[1], Greta Donati[1], Antonio Pizzirusso[1], Ying Zhao[3] and Giuseppe Milano[1,2]

[1]*Dipartimento di Chimica e Biologia, Università di Salerno, Via Giovanni Paolo II, 132, I-84084, Fisciano (SA), Italy.*

[2]*Department of Organic Materials Science, Yamagata University, 4-3-16 Jonan Yonezawa, Yamagata-ken 992-8510, Japan.*

[3]*Dalian Minzu University, Institute of Nano-Photonics, School of Physics and Materials Engineering, 116600, Dalian, China.*

ABSTRACT. Polymeric materials containing nanosized particles are experiencing an intensive investigation, mainly due to their improved physical properties which allow for many industrial applications. Here we present a hybrid particle-field molecular dynamic approach, well suited for guarantee an efficient relaxation of polymeric material with even high molecular weight. Such an approach is applied to silica-polystyrene nanocomposites, with silica nanoparticles (NPs) bare or grafted with polystyrene chains. By calculating the two-body potential of mean force (PMF) between ungrafted NPs, we show that a bidisperse distribution of polymer chains increases the strength of attraction, in comparison with a unimodal distribution. If the NPs are grafted, the effective interaction crucially depends on bidispersity and grafting density. Moreover, we estimate the three-particle contribution to the total PMF and its role in regulating the phase separation on the nanometer scale. In particular, the multi-particle contribution to the PMF is able to give an explanation of the complex experimental morphologies observed at low grafting densities. More in general, we propose this approach and the models utilized here for a molecular understanding of specific systems and the impact of the chemical nature of the systems on the composite final properties.

1 Introduction

A proper control of microscopic arrangements and interactions is crucial in order to design a polymer nanocomposite material with specific macroscopic properties. In this context, it has been largely proved [1, 2] that if the nanoparticles (NPs) embedded in the polymer matrix are grafted with polymer chains, they can be either well dispersed or arranged in nanoaggregates, the onset of a given morphology depending on both the ratio between the molecular weights of free and grafted polymer chains and the grafting density [3]. Since the interaction between the polymer chains is essential to lead the phase behavior of the composite, a desired morphology can be obtained also by properly tuning the the polydispersity of the polymer chains. Here we perform a simulation study of the two-body and

---

*Corresponding author. E-mail: gmunao@unisa.it.

three-body potential of mean force (PMF) between a pair of silica NPs (bare or grafted with PS chains) embedded in a PS matrix. We adopt the hybrid particle-field molecular dynamics approach [4] which has been recently employed to efficiently characterize, among others, nanocomposites [5, 6], polymer melts of high molecular weight [7] and including carbon nanotubes [8]. The advantage to use an hybrid approach relies on the possibility to significantly speed up the simulation times typically required to properly relax polymer nanocomposites [7]. This speed up is realized by decoupling the mutual particle-particle interactions and replacing them with a field representation. In the present work the grafting density and the polydispersity of both free and grafted polymer chains are varied, and realistic coarse-grained (CG) models are need, which have to account for the chemical detail of the system. In order to obtain accessible simulation times for a proper calculation of two- and three-body PMF we thus make use of CRESCO supercomputing resources.

2 Simulation protocol

The simulation approach that we adopt in the present work is based on a combination of a standard molecular dynamics (MD) approach and a self-consistent field (SCF) theory [9] for the calculation of non-bonded potentials. The resulting scheme is known as hybrid particle-field model [4]: in this approach, the Hamiltonian of a system of M molecules is split as:

$$\hat{H}(\Gamma) = \hat{H}_0(\Gamma) + \hat{J}(\Gamma) \tag{1}$$

where Γ represents a point in the phase space and the symbol $\hat{\ }$ indicates that a given quantity is a function of the microscopic state corresponding to Γ. In Eq. 1, $\hat{H}_0(\Gamma)$ is the Hamiltonian of a system with molecules experiencing only intramolecular (including intramolecular non bonded) interactions, whereas $\hat{J}(\Gamma)$ is the contribution due to the other non-bonded interactions. The latter can be calculated as an external potential $V(\mathbf{r})$ on single particles, which is due to the density field. The details of the derivation of $V(\mathbf{r})$ can be found elsewhere [4]. The mean field solution for the potential acting on a particle of type K at position $\mathbf{r}$, $V(\mathbf{r})$ is:

$$V_K(\mathbf{r}) = k_B T \sum_{K'} \chi_{KK'} \Phi_{K'}(\mathbf{r}) + \frac{1}{\kappa}(\sum_{K'} \Phi_{K'}(\mathbf{r}) - 1) \tag{2}$$

where k_B is the Boltzmann constant, T is the temperature, $\chi_{KK'}$ are the mean field parameters for the interaction of a particle of type K with the density field due to particles of type K' and the second term on the right-hand side of Eq. 2 is the incompressibility condition, κ being the compressibility. Also, $\Phi_K(\mathbf{r})$ and $\Phi_{K'}(\mathbf{r})$ are the density functions of the beads of type K and K', respectively, and normalized by the bulk density value ϕ_0. For the NP-PS interactions $\chi_{KK'} \times RT = 5.25$ kJ/mol (R being the gas constant), while for NP-NP and PS-PS interactions $\chi_{KK'} \times RT = 0$, in agreement with a previous MD-SCF study of the same model [5]. All simulations have been performed by means of the OCCAM code, whose details can be found in Ref. [10], and run in the *NVT* ensemble, with the temperature (fixed at 590 K) controlled by the Andersen thermostat and a time step of 4 fs. The density fields, with the corresponding derivatives, are calculated on a lattice obtained by dividing the simulation box into a grid of cells, whose spacing has been set to 1.18 nm. The density is calculated from particle positions and projected on the mesh according to a procedure described in Ref. [5]. The mesh is updated every 100 MD steps. The initial configurations have been built by using the Packmol program [11].

Table 1: Nanocomposite systems investigated for the calculation of the two-body potential of mean force. The grafting density ρ_g is in chains/nm^2. The box lengths are $L_x = 22$ nm, $L_y = L_z = 12.5$ nm. The chains length is given in number of beads.

ρ_g	No° of short grafted chains	No° of long grafted chains	Short grafted chains length	Long grafted chains length	No° of short free chains	No° of long free chains	Short free chains length	Long free chains length	BDI_g	BDI_f
0	0	0	0	0	1044	0	20	0	0	1
0	0	0	0	0	300	75	20	200	0	2.36
0	0	0	0	0	950	2	20	1000	0	5.14
0.1	0	5	0	80	995	0	20	0	1	1
0.1	0	5	0	80	840	23	20	200	1	2.36
0.1	0	5	0	80	100	19	20	1000	1	5.14
0.1	3	2	13	180	995	0	20	0	2.00	1
0.1	4	1	10	80	1005	0	20	0	2.36	1
0.1	4	1	5	80	1007	0	20	0	3.25	1
0.1	4	1	80	1000	903	0	20	0	2.94	1
0.5	0	25	0	80	854	0	20	0	1	1
0.5	0	25	0	80	187	69	20	200	1	2.36
0.5	0	25	0	80	84	16	20	1000	1	5.14
0.5	20	5	40	240	854	0	20	0	2.00	1
0.5	20	5	10	80	991	0	20	0	2.36	1
0.5	20	5	5	80	1001	0	20	0	3.25	1

3 Results

In order to highlight the effects due to the bidispersity on the effective interactions between the NPs we have introduced a bidispersity index (BDI) defined as:

$$BDI = M_w/M_n \tag{3}$$

where M_w and M_n are the weight average molecular weight and the number average molecular weight, respectively, and are defined as:

$$M_w = \frac{\sum_i N_i M_i^2}{\sum_i N_i M_i}; \qquad M_n = \frac{\sum_i N_i M_i}{\sum_i N_i} \tag{4}$$

where N_i and M_i indicate the number of chains with a given molecular weight and the number of beads belonging to each of these chains. The investigated systems are listed in Tab. 1. Upon computing the effective interactions between a pair of ungrafted NPs, we have found that the two-body PMF is remarkably attractive, this attraction increasing with the bidispersity of the free chains. The increase of the attraction can be ascribed to the layering of short and long free chains around the NP surface: when two NPs come in close contact, such a layering can no longer be realized and the entropic penalty causes the increase of the attraction between the NPs. The scenario becomes more complex for grafted NPs: under these conditions, we have found that for low grafting density ($\rho_g = 0.1$ chains/nm^2) the increase of both BDI_f and BDI_g increases the repulsion between the NPs. For higher grafting densities ($\rho_g = 0.5$ chains/nm^2) the repulsion increases with BDI_f but decreases with BDI_g. In addition, for
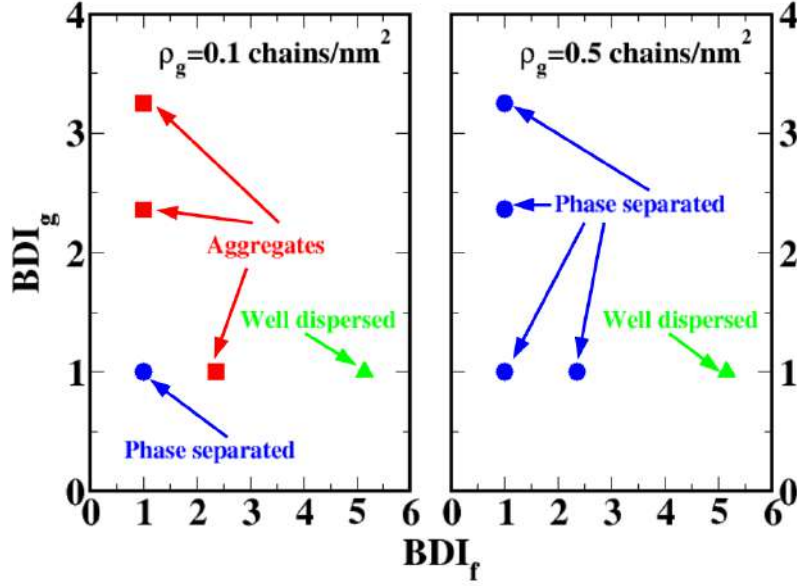
Figure 1: Schematic phase behavior of grafted nanoparticles as a function of bidispersity and grafting density. The diagram is drawn by considering the behavior of the two-body PMF and the second virial coefficient. Different colors and symbols identify phase separated ($B_2 < 0$), aggregated ($B_2 < 0$) and well dispersed ($B_2 > 0$) conditions.

$\rho_g = 0.1$ chains/nm^2 the PMF exhibits in some cases a short-range attraction followed by a long-range repulsion, this suggesting the possible existence of aggregates in the system. A further characterization of the phase behavior of the nanocomposite has been done by calculating the second virial coefficient B_2 from the PMF; in particular, it is known that positive values of B_2 indicate that repulsive contributions are dominant, whereas its negative values suggest a prevalence of attractive interactions [12]. A summarizing phase diagram showing the expected behavior of the system according to the PMF and B_2 is reported in Fig. 1.

The three-body PMF refines the two-body calculations, showing in particular that for ungrafted NPs the attraction is more attractive than in the two-body case, regardless the bidispersity. For $\rho_g = 0.1$ chains/nm^2 the three-body PMF predicts the existence of aggregates under conditions where the two-body PMF is only attractive, this agreeing with experimental [3] and numerical [13] studies of similar systems. The exhaustive study required for a fully relaxation of the system in a large variety of conditions has been possible thanks to the CRESCO Supercomputing resources, and for this purpose we have performed extensive molecular simulations on the CRESCO queues cresco4_h144, small_h144 and cresco6_h144. A computational study on the calculation of the two-body and three-body PMF between NPs in a monodisperse polymer matrix has been recently published on *Nanoscale* Journal (see Ref. [6]), in which we thank the HPC team of Enea (http://www.enea.it) for using the ENEAGRID and the HPC facilities CRESCO (http://www.cresco.enea.it) in Portici.

References

[1] Q. Lan, L. F. Francis, and F. S. Bates. Silica nanoparticle dispersions in homopolymer versus block copolymer. *J. Polym. Sci., Polym. Phys.*, 45:2284, 2007.

[2] D. Sunday, J. Ilavsky, and D. L. Green. A phase diagram for polymer-grafted nanoparticles in homopolymer matrices. *Macromolecules*, 45:4007, 2012.

[3] S. K. Kumar, N. Jouault, B. Benicewicz, and T. Neely. Nanocomposites with polymer grafted nanoparticles. *Macromolecules*, 46:3199, 2013.

[4] G. Milano and T. Kawakatsu. Hybrid particle-field molecular dynamics simulations for dense polymer systems. *J. Chem. Phys.*, 130:214106, 2009.

[5] A. De Nicola, T. Kawakatsu, F. Müller-Plathe, and G. Milano. Fast relaxation of coarse-grained models of polymer interphases by hybrid particle-field molecular dynamics: Polystyrene-silica nanocomposites as an example. *Eur. Phys. J. Special Topics*, 225:1817, 2016.

[6] G. Munaò, A. Pizzirusso, A. Kalogirou, A. De Nicola, T. Kawakatsu, F. Müller-Plathe, and G. Milano. Molecular structure and multi-body interactions in silica-polystyrene nanocomposites. *Nanoscale*, 10:21656, 2018.

[7] A. De Nicola, T. Kawakatsu, and G. Milano. Generation of well relaxed all atom models of large molecular weight polymer melts: A hybrid particle-continuum approach based on particle-field molecular dynamics simulations. *J. Chem. Theory Comput.*, 10:5651, 2014.

[8] Y. Zhao, M. Byshkin, Y. Cong, T. Kawakatsu, L. Guadagno, A. De Nicola, N. S. Yu, G. Milano, and B. Dong. Self-assembly of carbon nanotubes in polymer melts: Simulation of structural and electrical behaviour by hybrid particle-field molecular dynamics. *Nanoscale*, 8:15538, 2016.

[9] T. Kawakatsu. *Statistical Physics of Polymers*. Springer, Berlin, 2004.

[10] Y. Zhao, A. De Nicola, T. Kawakatsu, and G. Milano. Hybrid particle-field molecular dynamics simulations: Parallelization and benchmarks. *J. Comput. Chem.*, 33:868, 2012.

[11] L. Martinez, R. Andrade, E. G. Birgin, and J. M. Martinez. Packmol: A package for building initial configurations for molecular dynamics simulations. *J. Comput. Chem.*, 30:2157, 2009.

[12] J. P. Hansen and I. R. McDonald. *Theory of simple liquids,* 3rd Ed. Academic Press, New York, 2006.

[13] P. Akcora, H. Liu, S. K. Kumar, J. Moll, Y. Li, B. C. Benicewicz, L. S. Schadler, D. Acechin, A. Z. Panagiotopoulos, V. Pyramitsyn, V. Ganesan, J. Ilavsky, P. Thiyagarajan, R. H. Colby, and J. F. Douglas. Anisotropic self-assembly of spherical polymer-grafted nanoparticles. *Nat. Mater.*, 8:354, 2009.

FUNCTIONALIZATION OF PHOSPHORENE 2D MATERIAL: A COMPUTATIONAL INVESTIGATION

Andrea Ienco[1*], Gabriele Manca[1], Maurizio Peruzzini[1]

[1]*Consiglio Nazionale delle Ricerche - Istituto di Chimica dei Composti OrganoMetallici (CNR-ICCOM), Via Madonna del Piano 10, 50019 Sesto Fiorentino (FI), Italy e-mail: andrea.ienco@cnr.it*

ABSTRACT. Phosphorene is a 2D material and it can view as the all phosphorus counterpart of graphene. In our work, we have studied the non covalent functionalization of the phosphorene sheet with pyrene and pyren boronic derivatives. The solid state calculations using Density functional theory at PBE level, augmented with the D3 dispersion correction as implemented in CRYSTAL17 code, dismissed a possible covalent bond between the boron center and the phosphorus lone pairs, confirming the nature of non covalent functionalization. Our results helped to shed light on the NMR and spectroscopic experiments helping to understand better the remarkably stability toward oxidation in air of phosphorene/pyren boronic adducts.

1 Introduction

In the last century, chemistry has been able to exercise control in zero- and mono-dimensional architectures, molecules and polymers. [1] Nowadays with metal-organic frameworks or with some supramolecular architectures built using ad hoc building blocks, chemists started to obtain some control over three-dimensional objects. 2D materials are now the last frontier. They possess exceptional electronic and optical properties, with a *plethora* of potential astounding applications covering microelectronics, optoelectronics, medicine etc. Graphene due to the combination of structural and functional properties was the first protagonist in this field although its use in electronics has been hampered by the lack of a direct bandgap. [2] In the last few years, new 2D materials have been reported. One of them is phosphorene (see Scheme 1), the so called "graphene cousin". It is the mono-layer of layered black phosphorus, obtained by micro-mechanical or in solution exfoliation of the latter. Phosphorene features a direct bandgap, that can be largely tuned depending by the number of stacked layers, making it a very interesting material for electronic device. [3] The only drawback of the phosphorene is the low stability toward atmospheric oxygen and moisture, thus many efforts have been devoted toward the not covalent functionalization by covering the material with suitable substrate, although the covalent approach has been only marginally addressed.
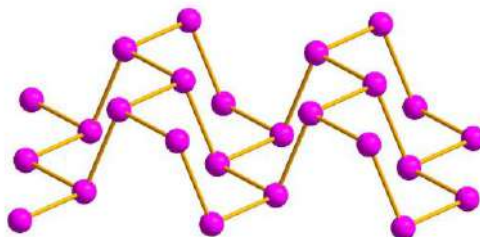
Scheme 1.

Our group worked on the subject in the last few years [3] and here we describe our contribution on non covalent functionalization of the phosphorene sheet with pyrene (Py) and pyren-boronic derivate namely Pyren-1-Boronic Acid (PBA) and 4,4,5,5-Tetramethyl-2-pyren-1-yl-1,3,2-dioxaborolane (PBE), as shown in Scheme 2. Only our computational work will be briefly discussed while the whole story has been recently published. [4] It is important to stress the contribution of our calculations to the understanding not only of the phosphorene/pyrene interactions but also for the interpretations of the results of NMR and spectroscopic data.

Py   PBA   PBE
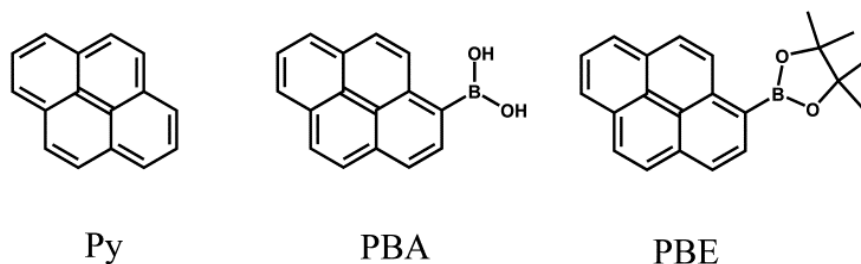
Scheme 2.

2 Computational Details

The bare and functionalized phosphorene surfaces have been fully optimized (atomic coordinates and cell constants) using the PBE-D3-DFT level of theory. [5, 6] The inclusion of the dispersion contribution allows a better description of the non-covalent interactions between the organic molecules and the phosphorene surfaces. For each atomic species, the local functions are linear combinations of Gaussian type functions (GTF) and in our calculations a triple zeta with polarizations basis set has been used. [7] Vibrational frequencies have been carried out in order to characterized the optimized geometries as true minima of potential energy surface. In the calculation a supercell of 64 phosphorus atoms has been adopted. For all the calculations CRYSTAL17 software package has been used. [8] Two different parallel versions of CRYSTAL17 are available. The first one *Pcrystal* (parallel crystal) is replicated-data versions of the serial *crystal* program. A massive parallel version, *MPPcrystal*, is available in case of large unit cell with large memory requirements, being able to well balance the computational loads on different cores. [9] Preliminary and test calculations showed that for our system the *Pcrystal* performances were adequate for the calculations. A typical run uses up to 256 processors on CRESCO4 cluster.

3 Results and Discussion

As interested in the covalent functionalization of the material, we wonder if the deposition of the boranes on the phosphorene surface may be successful. In this regards, we tried to simulate a covalent bond between the boron atom of PBA or PBE and the lone pair of a phosphorus atoms on the surface. In a previous work, [10] we have demonstrated the formation of strong P-B bond for a simple borane adduct as BH_3, in this case electronic and steric reasons ruled out the possibility to form such covalent interaction. So our interest switched to analyze the geometrical and electronic difference in the three different adducts.

The formation of the adducts is favored by -2.2 eV for phosphorene/Py and slightly larger in the case of PBA, and for PBE. The contribution of the non covalent interactions between the carbon and the phosphorus atoms is the main responsible for the large stabilization energies in the three adducts. The optimized geometries are illustrated in Figure 1. The effect of the interactions is clearly demonstrated

by the elongation of the C-C distances in the pyrene moieties. In the non-interacting molecule, the C-C distances are in between 1.35 and 1.42 Å, while, in the adducts, they are between 1.37 and 1.44 Å. On the other side, also the non-bonding intra channel P-P distances are somewhat shorter. In the bare phosphorene these distances are around 3.5 Å while in the adducts, especially in the channels below the pyrene moieties, are 0.2-0.3 Å shorter.
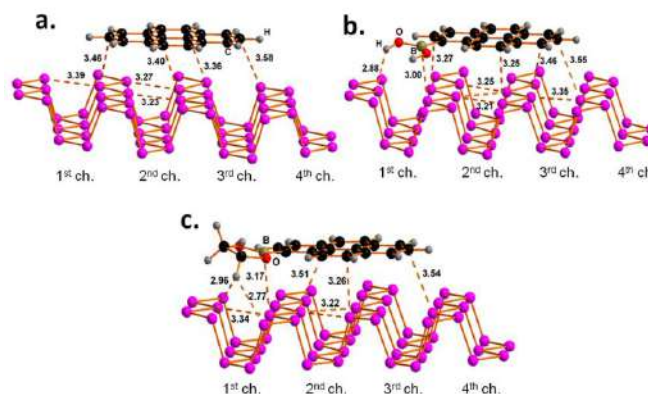
Figure 1. Optimized structure of the adducts of phosphorene with Py (a), PBA (b) and PBE (c). Adapted from *ACS Appl. Mater. Interfaces* **2019**, *11*, 22637−22647 reproduced under the ACS AuthorChoice License

From an electronic point of view, this behavior is consistent with some degree of electronic transfer from the phosphorus lone pairs into the C-C antibonding combinations of pyrene or of the PBA/PBE species. This can be easily visualized from the contribution of the total DOS of the PBA molecules as illustrated in Figure 2.
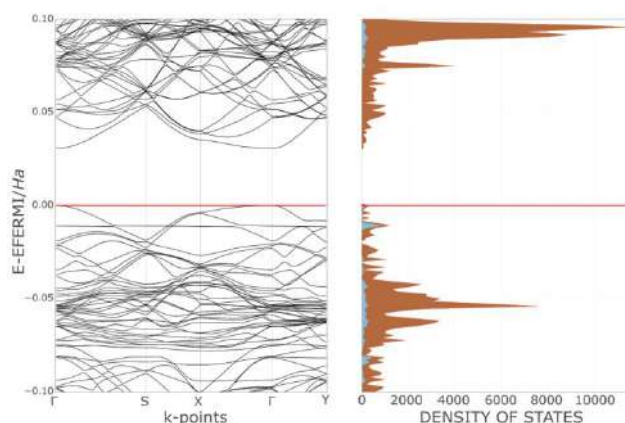
Figure 2. Band structure and Density of States (DOS) for the adduct between phosphorene and PBA. In the DOS plot, the contribution highlighted in blue is due to the PBA moiety. Figure from *ACS Appl. Mater. Interfaces* **2019**, *11*, 22637−22647 reproduced under the ACS AuthorChoice License

References

[1] R. Hoffmann. How Should Chemists Think? *Scientific American* **268**, pp. 66-73, (1993).

[2] K. S. Novoselov, A. K. Geim, S. V. Morozov, D. Jiang, Y. Zhang, S. V. Dubonos, I. V. Grigorieva, A. A. Firsov Electric Field Effect in Atomically Thin Carbon Films. *Science* **306**, pp. 666−669, (2004).

[3] M. Peruzzini, R. Bini, M. Bolognesi, M. Caporali, M. Ceppatelli, F. Cicogna, S. Coiai, S. Heun, A. Ienco, I. I. Benito, A. Kumar, G. Manca, E. Passaglia, D. Scelta, M. Serrano-Ruiz, F. Telesio, S. Toffanin, M. Vanni, A Perspective on Recent Advances in Phosphorene Functionalization and Its Applications in Devices. *Eur. J. Inorg. Chem.* **2019**, pp. 1476−1494, (2019).

[4] M. Bolognesi, S. Moschetto, M. Trapani, F. Prescimone, C. Ferroni, G., Manca, A. Ienco, S. Borsacchi, M. Caporali, M. Muccini, M. Peruzzini, M. Serrano-Ruiz, L. Calucci, M.A. Castriciano, S. Toffanin. Noncovalent Functionalization of 2D Black Phosphorus with Fluorescent Boronic Derivatives of Pyrene for Probing and Modulating the Interaction with Molecular Oxygen *ACS Appl. Mater. Interfaces* **11**, pp. 22637−22647, (2019)

[5] J. P. Perdew, K. Burke, M. Ernzerhof, Generalized Gradient Approximation Made Simple. *Phys. Rev. Lett.* **77**, pp. 3865−3868 (1996).

[6] S. Grimme, J. Antony, S. Ehrlich, H. Krieg, A Consistent and Accurate Ab Initio Parametrization of Density Functional Dispersion Correction (DFT-D) for the 94 Elements H-Pu. *J. Chem. Phys.* **132**, pp. 154104, (2010).

[7] M. F. Peintinger, D. V. Oliveira, T. Bredow, Consistent Gaussian Basis Sets of Triple-Zeta Valence with Polarization Quality for Solid-State Calculations. *J. Comput. Chem. 34*, pp. 451−459, (2013).

[8] (a) R. Dovesi, V. R. Saunders, C. Roetti, R. Orlando, C. M. Zicovich-Wilson, F. Pascale, B. Civalleri, K.; Doll, N. M. Harrison, I. J. Bush, P. D'Arco, M. Llunell, M. Causà, Y. Noël, L. Maschio, A. Erba, M. Rerat, S. Casassa, CRYSTAL17 User's Manual; University of Torino: Torino, (2017). (b) R. Dovesi, A. Erba, R. Orlando, C. M. Zicovich-Wilson, B. Civalleri, L. Maschio, M. Rerat, S. Casassa, J. Baima, S. Salustro, B. Kirtman. *WIREs Comput Mol Sci.* **8**, pp. e1360, (2018).

[9] R. Orlando, I. J. Bush, M. Delle Piane, P. Ugliengo, M. Ferrabone and R. Dovesi. A new massively parallel version of crystal for large systems onhigh performance computing architectures. *J. Comput. Chem.* **33**, pp. 2276–2284, (2012).

[10] A. Ienco, G. Manca, M. Peruzzini, C. Mealli Modelling Strategies for the Covalent Functionalization of 2D Phosphorene. *Dalton Trans. 47*, pp. 17243−17256, (2018).

PEPTIDE BOND DETECTION VIA GRAPHENE NANOGAPS: A PROOF OF PRINCIPLE STUDY

Giuseppe Zollo *, Tommaso Civitarese and Aldo Eugenio Rossini

Dipartimento di Scienze di Base e Applicate per l'Ingegneria- Sapienza Universitá di Roma, via A. Scarpa 14-16 00161 Rome- ITALY

ABSTRACT. In the context of the density functional theory atomistic modeling and non equilibrium Green function calculation, we show that, in the elastic regime of tunneling, glicyne based polypeptide chains translocating across a nano-gap between two semi-infinite graphene nano-ribbons leaves a specific transverse current signature for each peptide bond. Projected density of states and bond current analyses evidence that transmission occurs mainly through the closest α-carbons and side chains but a key role is also played by the partially resonant double bond of the peptide bond. The signal measured can be considered as a specific fingerprint of peptide bonds between small and neutral aminoacids with no polar/charge effects. On this basis, a newly conceived nano-device made of a graphene based array of nano-gap is proposed as a possible route to approach peptide sequencing with atomic resolution.

1 Introduction

Nano-science and physical phenomena at the nanoscale are being considered for a variety of applications including bio-molecule recognition and sequencing [1, 2, 3, 4, 5]. The protein case is challenging and the setup of newly conceived methods for fast and reliable amino-acid recognition is highly desirable to face the huge size of the human proteome [3, 4, 5, 6, 7, 8, 9, 10, 11, 12]. Compared to other schemes, the measurement of the transversal tunneling current across a gap seems to be particularly promising. The amino-acis (AAs) recognition can be attained, at least in principles, by measuring the tunneling current flowing through the gap during the peptide translocation, provided a bias is applied between the electrodes [11, 13]. This scheme, however, requires a controlled translocation dynamics of the peptide or the protein (in its primary structure state) that is still an open technological issue. Several proposals to employ nano-gaps for biomolecule sensing have been found in the recent literature [14, 13]. In this context, nano-gaps in "2D materials" are particularly appealing because of the expected sub-molecular resolution of the tunneling current and this is even more pronounced in the case of graphene due to its exceptional conduction properties and to its ideal 2D character that, in principles, allows the atomistic resolution sensing of biomolecules. Hence graphene nano-gap devices have been proposed as well [15, 16, 17, 18, 19]. Here we propose a nano-device, schematically shown in Fig. 1, that is constituted by an array of GNRs deposited onto a suitable solid substrate where a sub-nanometer nearly rectangular pore is fabricated exploiting the present capability of nanotechnology manufacturing techniques [3, 11, 20, 13, 21, 22] and the synthesis, by bottom-up strategies, of narrow GNRs [23, 24]. Of course there are still challenges to get the required extreme control at the atomistic scale and to control the bias [22]. For such a device, the rectangular shape of the pore imposes preferential AAs

---

*Corresponding author. E-mail: `giuseppe.zollo@uniroma1.it`.

configurations during translocation with the PBs chain at the center and the AAs side chains along the long side of the rectangular pore. Hence this implies that α-carbons and the PBs occupy the central nano-gap while the AAs side chains the adjacent ones so that, in principle, various transverse tunneling current signals could be collected for large residues while PBs and small residues signals could be measured at the central nano-gap. In the present study, as a fundamental step in the assessment of the
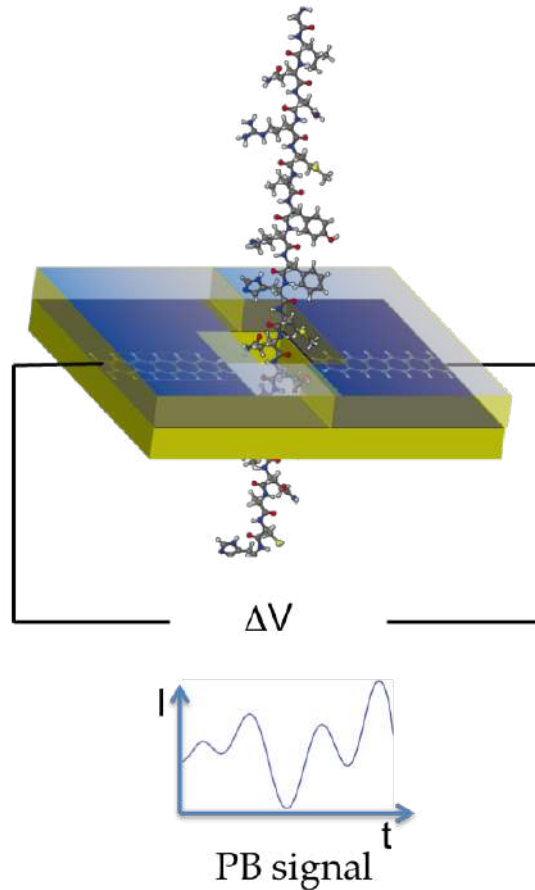
Figure 1: Drawing of the proposed nano-size device for amino-acids recognition

proposed device, we have focused on the PB recognition in a Gly homo-peptide by a single GNR in the context of NEGF-DFT (see below) elastic tunneling approach.

2 Theoretical methods

The atomistic model we adopted is basically made of two semi-infinite graphene nano-ribbons with zig-zag edges (ZGNR) and the peptide that translocates across the nano-gap. In our ideal sensing device the electrodes are made of two semi-infinite hydrogenated zig-zag GNRs (ZGNR) of the even type lying in the z direction with hydrogenated armchair pattern at the border and the distance between the

two semi-infinite ZGNRs is 5.0 Å. The ground sate of hydrogenated ZGNR is expected to have a gap due to spin interactions [25, 26] whereas the metallic spin unpolarized state has a larger energy. However it has been reported that the metallic unpolarized configurations is stable when a bias is applied and in presence of ballistic conduction [27, 28] and that the spin polarized ground state undergoes a transition to semi-metallic conduction properties when the ZGNR is doped with N atoms [29] or when a transverse electric field is applied [30]. Then we have chosen the unpolarized metallic phase of the hydrogenated ZGNR as as a paradigmatic case of metallic or half-metallic ideal 2D graphene based electrodes. The amino acids configurations crossing the gap have been identified using a NVT classical steered molecular dynamics (SMD) simulations [31] at $T = 300$ K in water ambient. Then, conformation along the translocation pathway have been selected, water molecules have been removed and the ionic degrees of freedom of the system have been relaxed at $T = 0$ K, in the context of the density functional theory (DFT) in order to approach a local energy minimum. This stage has been performed using the Quantum Espresso package [32] in the HPC Cresco infrastructure [33].

The total energy DFT calculations scheme includes a generalized gradient approximation based on the Perdew-Burke-Ernzerhof formula[34](PBE) for the electron exchange and correlation potential and norm-conserving pseudopotentials built with the Troullier-Martins scheme [35] in the framework of a plane-wave basis set expansion. A complete description of the technical aspects can be read in the recent literature [19].

Non-equilibrium Green's function (NEGF) method, as implemented in the TRANSIESTA code[36, 37], is employed to calculate the transport properties.

The NEGF method is based on the Hamiltonian decomposition:

$$H = \begin{pmatrix} H_{\mathrm{L}} + \Sigma_{\mathrm{L}} & V_{\mathrm{L}} & 0 \\ V_{\mathrm{L}}^{\dagger} & H_{\mathrm{S}} & V_{\mathrm{R}} \\ 0 & V_{\mathrm{R}}^{\dagger} & H_{\mathrm{R}} + \Sigma_{\mathrm{R}} \end{pmatrix} \tag{1}$$

where, $H_{\mathrm{L(R)}}$ and H_{S} are, respectively, the decoupled Hamiltonians of left (right) electrode and the scattering region, $V_{\mathrm{L(R)}}$ represents the interaction of left (right) electrode with the scattering region and $\Sigma_{\mathrm{L(R)}}$ is the self-energy and describes the coupling of the left (right) lead with the scattering region.

For an external bias voltage V applied along the z direction, the current $I(V)$ is given by Landauer-Büttiker formula [38]

$$I(V) = \frac{2e}{h} \int_{-\infty}^{+\infty} d\varepsilon \, T(\varepsilon, V) \times [f(\varepsilon - \mu_{\mathrm{L}}) - f(\varepsilon - \mu_{\mathrm{R}})] \tag{2}$$

where $f(\varepsilon)$ is the Fermi-Dirac distribution function and $\mu_{\mathrm{L(R)}}$ is the electrochemical potential of the left(right) electrode. $T(\varepsilon, V)$ is the transmission coefficient that is calculated from the Hamiltonian of Eq. (1), with the external bias voltage V included in the interaction terms, and is defined as:

$$T(\varepsilon) = \mathrm{Tr}\left[G(\varepsilon)\Gamma_{\mathrm{L}}(\varepsilon)G^{\dagger}(\varepsilon)\Gamma_{\mathrm{R}}(\varepsilon)\right] \tag{3}$$

where $G(\varepsilon) = \lim_{\eta \to 0^+}(\varepsilon + i\eta - H)^{-1}$ is the Green's function of the system and $\Gamma_{\mathrm{L(R)}}(\varepsilon) = i[\Sigma_{\mathrm{L(R)}}(\varepsilon) - \Sigma_{\mathrm{L(R)}}^{\dagger}(\varepsilon)]$ is the left(right) coupling function [39].

DFT and quantum transport calculations have been carried out in dry ambient, since the conductance of ZGNR nanopore does not vary significantly when the dynamical environment of water is removed from the system[40] due to the hydrophobic character of graphene based structures. Moreover, because of the narrow size of the ZGNR nano-gap, water molecules cannot be allocated between the leads together

with the PBs but are expected to cross the nano-device near the lateral ZGNR nano-gaps where the AAs side chain move across the device.

Local transport phenomena have been inspected looking at the local currents flowing across the atomic sites [41, 42, 43]. Given a suitable complete localized basis set $\{|\phi_{n,\gamma}\rangle\}$ in a subspace of the full device region where $|\phi_{n,\gamma}\rangle$ is an atomic orbital of type γ, centered at the atomic site n, the local current flowing between atoms n and n' is [42]:

$$I_{n,n'} = e \int d\varepsilon \left[f_L(\varepsilon) - f_R(\varepsilon) \right] Tr \left[G(\varepsilon) \Gamma_L(\varepsilon) G^\dagger(\varepsilon) J_{n,n'} \right] \tag{4}$$

with

$$f_L(\varepsilon) = f(\varepsilon - \mu_L); \quad f_R(\varepsilon) = f(\varepsilon - \mu_R)$$

and

$$J_{n,n'} = \frac{1}{i\hbar} \left(P_n H P_{n'} - P_{n'} H P_n \right) \tag{5}$$

and the projection operator on the n site $P_n = \sum_\gamma |\phi_{n,\gamma}\rangle\langle\phi_{n,\gamma}|$. The bond currents are calculated with the INELASTICA[44] package.

3 Results

The current signals have been measured on a piece of peptide with two bonds between three Glycines for an applied voltage $\Delta V = 1V$ between the leads. The present bias has been employed both in the theoretical and in the experimental literature concerning tunneling currents or molecular junctions [45, 46, 47] but, of course, it should be tested for breakdown in real systems, especially for GNR electrodes [22]. In any case we have not observed any density or wave-functions anomalous behavior up to a bias of 2 V. Gly side chain is a single hydrogen atom that, together with the neutral and the non-polar nature of Gly, makes the present a sort of reference case of the PBs signal.
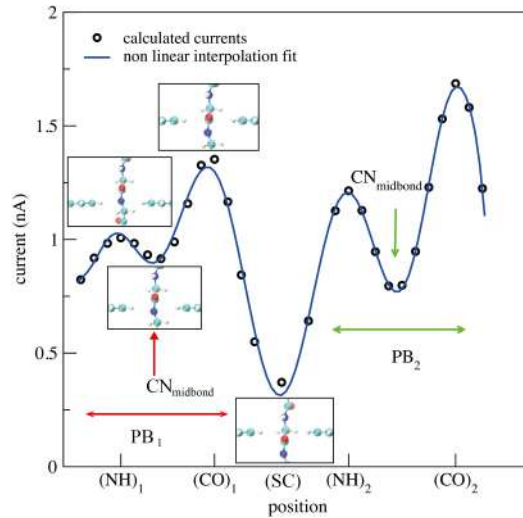

Figure 2: Electron current measured in the ZGNR based nano-gap device while a Gly peptide with three AAs translocates across the nano-gap.

In Fig.2, the current signal across the GNR nano-gap is reported as a function of the position of the peptide inside the nano-gap. Each peptide bond appears with two, well defined, current peaks. The calculated signals have been obtained in quasi-static conditions, i.e. with an idealized quasi-stationary translocation dynamics where the atoms are allowed to relax at $T = 0\ K$ at each translocation stage, see methods. The electronic current order of magnitude is comparable with typical tunneling current signals measured in nano-gap devices [11, 17, 48, 13, 49] but with the advantage of an atomic resolution.

The two peaks correspond approximately to the two positions of, respectively, the N and the O atoms of the peptide bond in the nano-gap and they are separated by a shallow current drop associated with the presence of the C-N mid-bond in the nano-gap. These configurations will be indicated as $(CO)_i$, $(NH)_i$ and $(CN)_i$, where the subscript indicates the peptide bond, PB_1 or PB_2. The signal in between two peptide bonds, i.e. with the Gly side chain in the nano-gap, is much smaller.

For comparison, we have calculated the current for the optimized configurations of one water molecule located in the gap. The resulting current is one order of magnitude smaller than maximum current signal obtained for the peptide and well below the absolute minimum at the SC configuration [19] so that the PB signals are separable from noise due to the water molecules that might eventually cross the gap.

The observed current curve reflect the corresponding transmission coefficient functions $T(\varepsilon)$ hierarchy corresponding to (CO), (NH) and (CN) configurations. The data are reported in Fig. 3(a) where the continuous (dashed) curves refer to the PB_1 (PB_2). The transmission coefficient curves show that the
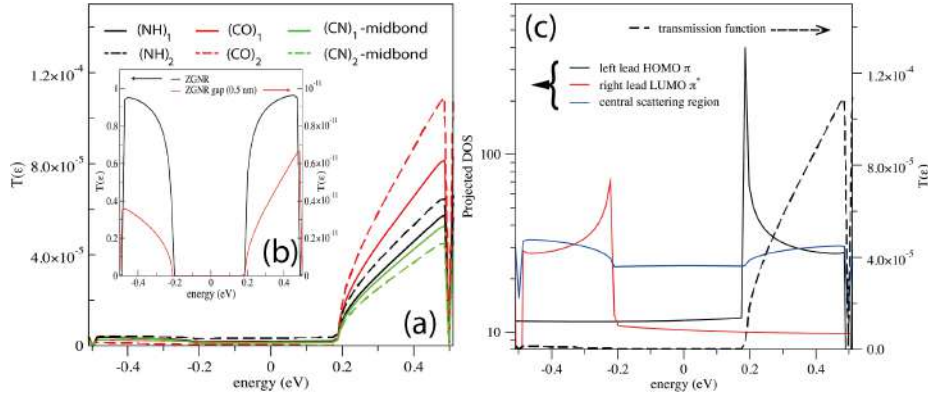
Figure 3: Transmission coefficients at different positions during the translocation of the peptide with three Gly (a); the continuous and dashed curves refer to the first and the second PB respectively. The inset (b) shows the transmission functions of the ZGNR and of the void nano-gap. In (c) are reported the transmission function calculated with the nitrogen atom of the PB in the gap and the PDOS of the left and right leads and of the central scattering region.

contribution to the current comes from the states in the energy range $[0.2\ \text{eV} \leq \varepsilon \leq 0.5\ \text{eV}]$; moreover, according to the current values of Fig. 2, for each PB the largest $T(\varepsilon)$ values are obtained for $(CO)_i$ configurations (the CO group is the ZGNR gap), the second largest occur for $(NH)_i$ configurations and the smallest ones are obtained with the CN mid-bond in the middle point of the ZGNR gap. For comparison, we reported in Fig.3(b) the transmission functions of the empty nano-gap showing that no transmission occurs in this case. Moreover, the projected density of states (PDOS), Fig. 3(c), evidences that the rising of $T(\epsilon)$ occurs in correspondence with the rising of the PDOS belonging to the scattering central region and to the left hand side ZGNR HOMO π-like states, provided that the PDOS of the right

hand side ZGNR LUMO π^*-like states are not zero. The channel decomposition of the transmission coefficient [50, 51] calculated at $V = 1\ V$ indicates the existence of just one channel contributing to the whole transmission coefficient, independently on the configuration considered with either the CO bond or the NH bond at the center of the GNR gap.

To explain the observed behavior we have analised the atomic PDOS decomposition in the localized basis set of the central scattering region have been grouped following the scheme of Fig.1(c); the main features are reported in Fig. 4 for the two PBs.
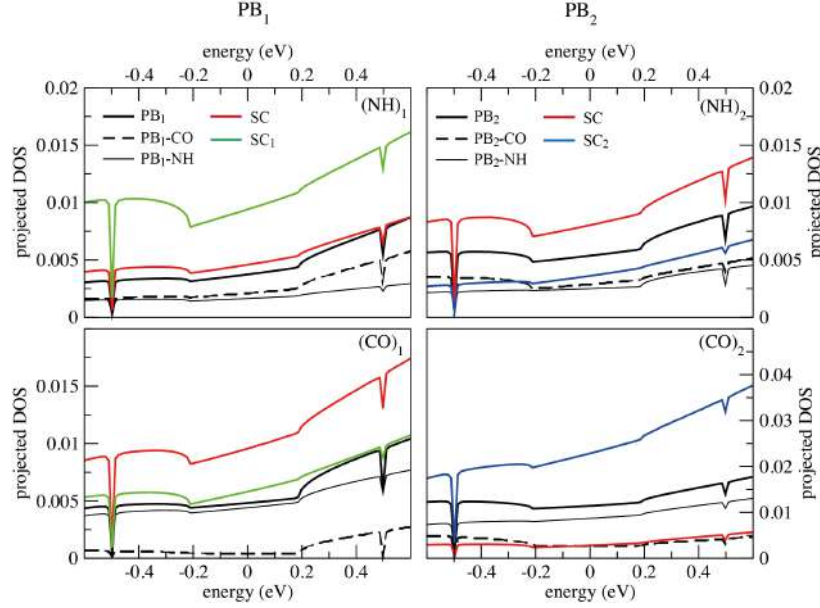
Figure 4: Atomic PDOS decomposition corresponding to the four current maxima measured in the three Gly peptide. The cases with the NH and CO groups in the middle of the nano-gap for each of the two PBs are aligned in columns (with the same legend). The atomic PDOS have been grouped together for atoms belonging to the the same unit.

For the $(NH)_i$ configurations, the largest density comes from the the Gly α-carbon and side chain that are the closest ones at the C-terminal side (SC_1 and SC for PB_1 and PB_2). We will indicate these groups as "lower" since they are just below $(NH)_i$ in the snapshot in Figure 1. Minor contributions to the PDOS of the scattering region come from the PB_i itself (with similar NH_i and CO_i PDOS values) and the closest side chain group at the N-terminal side (indicated as "upper" side chain in the following), namely SC and SC_2 for PB_1 and PB_2 (see Fig. 1(c)). At the second peak occurring with CO_i in the nano-gap, the major contribution comes from the "upper" side chain (i.e. the closest one). Concerning the PB-related PDOS, the major contribution comes from the NH_i group, while the one from the CO_i group is always lower in the entire energy range. A more detailed analysis of the DOS projected on the PBs atomic orbitals evidences the leading role played by the p_z orbitals of N and C [19].

The main atomic currents at the left lead (electrons injection) are reported in Table 1; the resulting scenario is sketched in Fig. 5 where the most relevant local atomic currents are represented by arrows for $(NH)_i$ (a) and $(CO)_i$ (b) configurations and is discussed in the following.

- **(NH)$_i$ configurations.** Consistently with the corresponding PDOS, the bond current analysis confirms that the main contributions for configurations $(NH)_i$ come from the "lower" side chain

Table 1: Main local atomic current contributions to the whole current at the left lead (electron injection from the left lead). As mentioned in the text, the subscript $i = 1, 2$ indicate the first or the second PB. In parentheses the groups and the corresponding local currents calculated for PB_2.

configuration	atomic group	electron injection into the left lead bond current (nA)
$(NH)_i$	SC_1 (SC)	0.67 (0.857)
	$(NH)_i$	0.045 (0.152)
$(CO)_i$	SC (SC_2)	0.63 (0.773)
	$(NH)_i$	0.44 (0.529)
SC	$(NH)_1$	0.114
	SC	-0.044
	$(NH)_2$	0.146

groups, i.e. the closest ones at the C-terminal side, namely SC_1 and SC for PB_1 and PB_2 respectively. Indeed, since these groups are off the ZGNR plane but close to it, the overlap of the corresponding atomic orbitals with the left lead π orbital is favored. Much minor contributions come from the upper residues and from the PBs themselves, the last ones, however, behaving in a rather complex way. Indeed a detailed analysis reveals that the CO group acts as reflectors while the NH groups may participate to the current transfer at a very small extent through the N_{p_z} orbital [19].

- **(CO)$_i$ configurations.** The same analysis of the second current peaks evidences that electrons are injected from the left lead mainly through both the "upper" α-carbon and side chain, i.e. the closest to the CO group at the N-terminal side, and, remarkably, through the NH group of the PB at almost the same extent as the "upper" residue. Then, what makes the difference between the two peaks in a given PB signal is the contribution from the NH group that is rather small in the case of the first peak (NH group in the gap) while is almost of the same magnitude as the side chain contribution in the case of the second peak. This is mainly due to the off-plane position of the NH group in this second case that favors the overlap and the hybridization between the N_{p_z} orbital and the π orbital of the left lead. As a matter of fact, the atomic current analysis reveals that the main reason why the second peak of the PB fingerprint is larger than the first one resides in the larger contribution from the NH group of the PB itself. This behavior is related to the nature of the PB resonating double bond with partial occupation of the N_{p_z} orbital that, as a consequence, can participate to the electron transfer, provided it is off the ZGNR plane. Finally, as a last comment to this part of the discussion, we emphasize that the difference between the second and the first current peaks in each PB is a clear fingerprint of the PB itself because it is due to the electrons flowing only across the NH group of the PB.

- **SC configuration.** Let's now consider the configuration with the central Gly side-chain in the gap (SC configuration- see Fig. 1) where the current signal drops. The corresponding PDOS and schematic drawing of the current fluxes are reported in Fig. 6. Here we see that PB_1 has the largest PDOS followed by PB_2 while the side chain contribution is small in the whole energy range. The main atomic current fluxes at the left lead are reported in Table 1. Electrons are injected from the left lead mainly through the closest $(NH)_2$ group, that, however, does not show the largest PDOS (see Fig.6(a)), and $(NH)_1$ of PB_1 at nearly the same extent. Contrarily to the
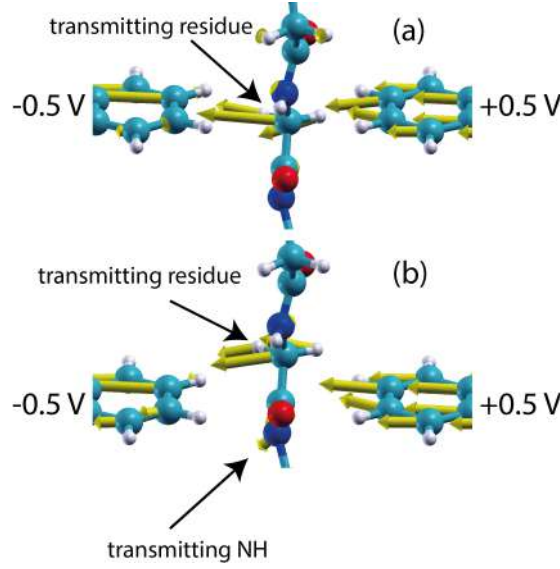
Figure 5: Schematic drawing of the atomic current flows with the NH (a) and the CO (b) groups in the middle of the nano-gap. C, O, N atoms are respectively in cyan, red and blu and atomic currents are yellow arrows. Transmission occurs via the "upper" and the "lower" side chains and, in the case of the CO group in the gap (b) also via the nitrogen atom of the PB.

configurations of two current peaks, the central side chain SC behaves as a reflecting group. A more detailed analysis shows that a meaningful charge redistribution between the two PBs occurs after injection and also that CO groups may participate to the current flow at a minor, but still meaningful, extent [19]. Therefore, because the Gly residue does not participate to the current transfer, the measured signal is a fingerprint of the two PB involved only, with a prominent role of the "upper" $(NH)_2$ group. Interestingly, we observe that the total current measured for this configuration is nearly the same as the bond current contributions through the NH group at the second PB peaks ($(CO)_i$ configurations).

We can thus conclude the discussion on the Gly homo-peptide emphasizing that for the $(CO)_i$ configurations the electron injection through the PB NH group is maximized, reflecting a large overlap between the partially occupied N_{p_z} orbital and π, it is minimized for $(NH)_i$ configurations with the NH group in the gap, while, in the SC configuration, it separates in two branches across the upper and the lower NH groups, with nearly the same total amount as the one measured in the $(CO)_i$ case, thus reflecting a partial overlap between the N_{p_z} and π orbitals.

4   Conclusions

GNR based nano-device, made of an array of nano-gaps, have been considered and studied in the context of DFT for single PB detection in a Gly based poly-peptide. The peptide translocation across the nano-gap array allows, in principle, the detection of various signals with atomic resolution. Using NEGF method and the Landauer-Büttiker formula we show that PBs from Gly poly-peptides leave a clear tunneling current fingerprint made of two, well defined current peaks of the order of magnitude of nA. We have shown that this signal, a sort of a reference PB signal (because the AAs side chain are just hydrogen atoms without any charge or dipolar source), arises from one channeled transmission
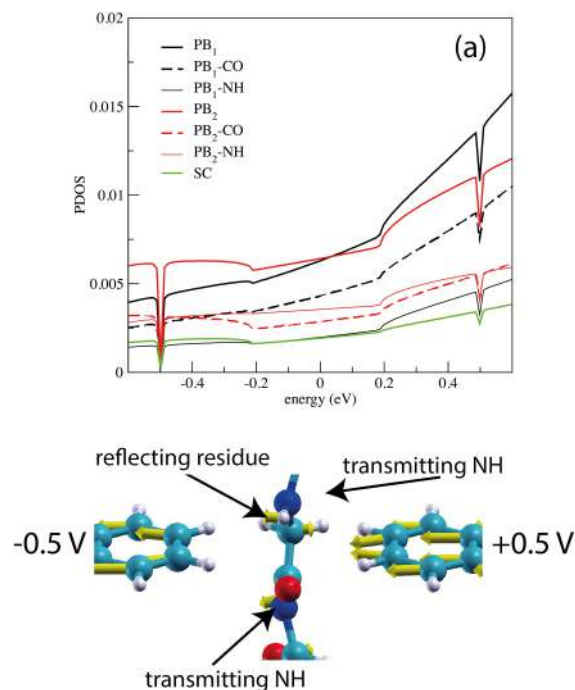
Figure 6: PDOS (a) and schematic drawing of the atomic current flows (b) with the Gly residue in the middle of the nano-gap. C, O, N atoms are respectively in cyan, red and blu nd atomic currents are yellow arrows. Transmission occurs via the nitrogen atom of the PB while the atomic current are reflected from the central Gly residue.

functions due to the superposition of the left lead pseudo-π HOMO, the right lead pseudo-π^* LUMO and the α-carbon, side chains and PB related orbitals, the last ones being the p_z orbitals directly involved in the resonant double bond of the PB. The extent of these different contributions depends on the relative positions of PBs and residues with respect to the GNR plane. The two peaks of the current signal, occurring with the NH and CO groups of the PB in the middle of the GNR nano-gap, are mainly due to the overlap of the closest off-plane residues and the π and π^* GNR states. Interestingly, the difference between the higher second peak $(CO)_i$ and the lower first peak $(NH)_i$ is due the atomic current flowing across the NH group that contributes to the total current through the off-plane overlap between N_{p_z} and the HOMO and LUMO GNR states. The PB contribution to the current is the only one that survives when the Gly residue is in the middle of the nano-gap giving the same current level as the N_{p_z} contribution at the second maximum with a prominent role played by the N_{p_z} orbital. The reported results encourages for further development of nano-devices made of graphene nano-gaps for AAs detection and protein sequencing.

However the generalization of such a procedure to generic poly-peptides, needs a long term effort because the scenario may change dramatically depending on the charge/polar state of the side chains, on the side chain size and chemistry and on the variety of the possible PBs between the different AAs.

References

[1] Miten Jain, Ian T Fiddes, Karen H Miga, Hugh E Olsen, Benedict Paten, and Mark Akeson. Improved data analysis for the minion nanopore sequencer. *Nature methods*, 2015.

[2] Grégory F Schneider and Cees Dekker. Dna sequencing with nanopores. *Nature biotechnology*, 30(4):326–328, 2012.

[3] Eamonn Kennedy, Zhuxin Dong, Clare Tennant, and Gregory Timp. Reading the primary structure of a protein with 0.07 nm3 resolution using a subnanometre-diameter pore. *Nat Nano*, 11(11):968–976, 11 2016.

[4] James Wilson, Leila Sloman, Zhiren He, and Aleksei Aksimentiev. Graphene nanopores for protein sequencing. *Advanced Functional Materials*, 26(27):4830–4838, 2016.

[5] Giovanni Di Muccio, Aldo Eugenio Rossini, Daniele Di Marino, Giuseppe Zollo, and Mauro Chinappi. Insights into protein sequencing with an ?-hemolysin nanopore by atomistic simulations. *Scientific Reports*, 9(1):6440, 2019.

[6] Abdelghani Oukhaled, Laurent Bacri, Manuela Pastoriza-Gallego, Jean-Michel Betton, and Juan Pelta. Sensing proteins through nanopores: fundamental to applications. *ACS chemical biology*, 7(12):1935–1949, 2012.

[7] Daniele Di Marino, Emma Letizia Bonome, Anna Tramontano, and Mauro Chinappi. All-atom molecular dynamics simulation of protein translocation through an α-hemolysin nanopore. *The journal of physical chemistry letters*, 6(15):2963–2968, 2015.

[8] Loredana Mereuta, Mahua Roy, Alina Asandei, Jong Kook Lee, Yoonkyung Park, Ioan Andricioaei, and Tudor Luchian. Slowing down single-molecule trafficking through a protein nanopore reveals intermediates for peptide translocation. *Scientific reports*, 4:3885, 2014.

[9] Omid Tavassoly, Sergiy Nokhrin, Oleg Y Dmitriev, and Jeremy S Lee. Cu (ii) and dopamine bind to α-synuclein and cause large conformational changes. *Febs Journal*, 281(12):2738–2753, 2014.

[10] David Rodriguez-Larrea and Hagan Bayley. Multistep protein unfolding during nanopore translocation. *Nature nanotechnology*, 8(4):288–295, 2013.

[11] Takahito Ohshiro, Makusu Tsutsui, Kazumichi Yokota, Masayuki Furuhashi, Masateru Taniguchi, and Tomoji Kawai. Detection of post-translational modifications in single peptides using electron tunnelling currents. *Nature nanotechnology*, 9(10):835–840, 2014.

[12] Christian B Rosen, David Rodriguez-Larrea, and Hagan Bayley. Single-molecule site-specific detection of protein phosphorylation with a nanopore. *Nature biotechnology*, 2014.

[13] Stephanie J. Heerema and Cees Dekker. Graphene nanodevices for dna sequencing. *Nature Nanotechnology*, 11:127 EP –, 02 2016.

[14] Massimiliano Di Ventra and Masateru Taniguchi. Decoding dna, rna and peptides with quantum tunnelling. *Nature nanotechnology*, 11(2):117–126, 2016.

[15] F Traversi, C Raillon, SM Benameur, K Liu, S Khlybov, M Tosun, D Krasnozhon, A Kis, and A Radenovic. Detecting the translocation of dna through a nanopore using graphene nanoribbons. *Nature nanotechnology*, 8(12):939–945, 2013.

[16] Eugene Paulechka, Tsjerk A Wassenaar, Kenneth Kroenlein, Andrei Kazakov, and Alex Smolyanitsky. Nucleobase-functionalized graphene nanoribbons for accurate high-speed dna sequencing. *Nanoscale*, 8(4):1861–1867, 2016.

[17] Rodrigo G. Amorim, Alexandre R. Rocha, and Ralph H. Scheicher. Boosting dna recognition sensitivity of graphene nanogaps through nitrogen edge functionalization. *The Journal-2016 of Physical Chemistry C*, 120(34):19384–19388, 2016.

[18] Jariyanee Prasongkit, Gustavo T. Feliciano, Alexandre R. Rocha, Yuhui He, Tanakorn Osotchan, Rajeev Ahuja, and Ralph H. Scheicher. Theoretical assessment of feasibility to sequence dna through interlayer electronic tunneling transport at aligned nanopores in bilayer graphene. *Scientific Reports*, 5:17560 EP –, 2015.

[19] Aldo Eugenio Rossini, Fabrizio Gala, Mauro Chinappi, and Giuseppe Zollo. Peptide bond detection via graphene nanogaps: a proof of principle study. *Nanoscale*, 10:5928–5937, 2018.

[20] Aliaksandr V. Zaretski, Brandon C. Marin, Herad Moetazedi, Tyler J. Dill, Liban Jibril, Casey Kong, Andrea R. Tao, and Darren J. Lipomi. Using the thickness of graphene to template lateral subnanometer gaps between gold nanostructures. *Nano Letters*, 15(1):635–640.

[21] S Lumetti, L Martini, and A Candini. Fabrication and characterization of nanometer-sized gaps in suspended few-layer graphene devices. *Semiconductor Science and Technology*, 32(2):024002, 2017.

[22] Syed Ghazi Sarwat, Pascal Gehring, Gerardo Rodriguez Hernandez, Jamie H. Warner, G. Andrew D. Briggs, Jan A. Mol, and Harish Bhaskaran. Scaling limits of graphene nanoelectrodes. *Nano Letters*, 17(6):3688–3693, 2017.

[23] Jinming Cai, Pascal Ruffieux, Rached Jaafar, Marco Bieri, Thomas Braun, Stephan Blankenburg, Matthias Muoth, Ari P. Seitsonen, Moussa Saleh, Xinliang Feng, Klaus Müllen, and Roman Fasel. Atomically precise bottom-up fabrication of graphene nanoribbons. *Nature*, 466:470 EP –, 07 2010.

[24] Matthias Koch, Francisco Ample, Christian Joachim, and Leonhard Grill. Voltage-dependent conductance of a single graphene nanoribbon. *Nature Nanotechnology*, 7:713 EP –, 10 2012.

[25] Young-Woo Son, Marvin L. Cohen, and Steven G. Louie. Energy gaps in graphene nanoribbons. *Phys. Rev. Lett.*, 97:216803, Nov 2006.

[26] Y. Y. Li, M. X. Chen, M. Weinert, and L. Li. Direct experimental determination of onset of electron–electron interactions in gap opening of zigzag graphene nanoribbons. *Nature Communications*, 5:4311 EP –, 07 2014.

[27] Daniel Gunlycke, Denis A. Areshkin, Junwen Li, John W. Mintmire, and Carter T. White. Graphene nanostrip digital memory device. *Nano Letters*, 7(12):3608–3611, 12 2007.

[28] Zuanyi Li, Haiyun Qian, Jian Wu, Bing-Lin Gu, and Wenhui Duan. Role of symmetry in the transport properties of graphene nanoribbons under bias. *Phys. Rev. Lett.*, 100:206802, May 2008.

[29] Yafei Li, Zhen Zhou, Panwen Shen, and Zhongfang Chen. Spin gapless semiconductor?metal?half-metal properties in nitrogen-doped zigzag graphene nanoribbons. *ACS Nano*, 3(7):1952–1958, 07 2009.

[30] Young-Woo Son, Marvin L. Cohen, and Steven G. Louie. Half-metallic graphene nanoribbons. *Nature*, 444(7117):347–349, 2006.

[31] J. C. Phillips, R. Braun, W. Wang, J. Gumbart, E. Tajkhorshid, E. Villa, C. Chipot, R. D. Skeel, L. Kale', and K. Schulten. Scalable molecular dynamics with namd. *Journal of Computational Chemistry*, 26(16):1781–1802, 2005.

[32] P. Giannozzi, S. Baroni, N. Bonini, M. Calandra, R. Car, C. Cavazzoni, D. Ceresoli, G. L. Chiarotti, M. Cococcioni, I. Dabo, A. Dal Corso, S. de Gironcoli, S. Fabris, G. Fratesi, R. Gebauer, U. Gerstmann, C. Gougoussis, A. Kokalj, M. Lazzeri, L. Martin-Samos, N. Marzari, F. Mauri, R. Mazzarello, S. Paolini, A. Pasquarello, L. Paulatto, C. Sbraccia, S. Scandolo, G. Sclauzero, A. P. Seitsonen, A. Smogunov, P. Umari, and R. M. Wentzcovitch. Quantum espresso: a modular and open-source software project for quantum simulations of materials. *J. Phys.: Condens. Matter*, 21(19):395502–1–19, 2009.

[33] G. Ponti, F. Palombi, D. Abate, F. Ambrosino, G. Aprea, T. Bastianelli, F. Beone, R. Bertini, G. Bracco, M. Caporicci, B. Calosso, M. Chinnici, A. Colavincenzo, A. Cucurullo, P. dAngelo, M. De Rosa, P. De Michele, A. Funel, G. Furini, D. Giammattei, S. Giusepponi, R. Guadagni, G. Guarnieri, A. Italiano, S. Magagnino, A. Mariano, G. Mencuccini, C. Mercuri, S. Migliori, P. Ornelli, S. Pecoraro, A. Perozziello, S. Pierattini, S. Podda, F. Poggi, A. Quintiliani, A. Rocchi, C. Scio, F. Simoni, and A. Vita. The role of medium size facilities in the hpc ecosystem: the case of the new cresco4 cluster integrated in the eneagrid infrastructure. *IEEE HPCS*, 6903807:1030–1033, 2014.

[34] J.P. Perdew, K. Burke, and M.Ernzerhof. Generalized gradient approximation made simple. *Phys. Rev. Lett.*, 77(4):3865–3868, 1996.

[35] N. Troullier and J.L. Martins. *Phys. Rev. B*, 43:1993, 1991.

[36] J.M. Soler, E. Artacho, J.D. Gale, A. García, J. Junquera, P. Ordejón, and D. Sánchez-Portal. The siesta method for ab initio order-n materials simulation. *Journal of Physics: Condensed Matter*, 14(11):2745–2779, 2002.

[37] K. Stokbro, J. Taylor, M. Brandbyge, and P. Ordejón. Transiesta - a spice for molecular electronics. *Annals of the New York Academy of Sciences*, 1006(1):212–226, 2003.

[38] K. Stokbro, J. Taylor, M. Brandbyge, J.-L Mozos, and P. Ordejón. Theoretical study of the nonlinear conductance of di-thiol benzene coupled to au(111) surfaces via thiol and thiolate bonds. *Computational Material Science*, 27:151–160, 2002.

[39] Supriyo Datta. *Electronic Transport in Mesoscopic Systems*. Cambridge Studies in Semiconductor Physics and Microelectronic Engineering. Cambridge University Press, 1995.

[40] G.T. Feliciano, C. Sanz-Navarro, M.D. Coutinho.Neto, P. Ordejón, R. H. Scheicher, and A. R. Rocha. Capacitive dna detection driven by electronic charge fluctuations in a graphene nanopore. *Physical Review Applied*, 3:034003, 2015.

[41] Gemma C. Solomon, Carmen Herrmann, Thorsten Hansen, Vladimiro Mujica, and Mark A. Ratner. Exploring local currents in molecular junctions. *Nat Chem*, 2(3):223–228, 03 2010.

[42] Tchavdar N Todorov. Tight-binding simulation of current-carrying nanostructures. *Journal of Physics: Condensed Matter*, 14(11):3049, 2002.

[43] Nick Papior, Nicols Lorente, Thomas Frederiksen, Alberto Garca, and Mads Brandbyge. Im-

provements on non-equilibrium and transport green function techniques: The next-generation transiesta. *Computer Physics Communications*, 212(Supplement C):8 – 24, 2017.

[44] Thomas Frederiksen, Magnus Paulsson, Mads Brandbyge, and Antti-Pekka Jauho. Inelastic transport theory from first principles: Methodology and application to nanoscale devices. *Phys. Rev. B*, 75:205413, May 2007.

[45] Yanan Zhao, Brian Ashcroft, Peiming Zhang, Hao Liu, Suman Sen, Weisi Song, JongOne Im, Brett Gyarfas, Saikat Manna, Sovan Biswas, et al. Single-molecule spectroscopy of amino acids and peptides by recognition tunnelling. *Nature nanotechnology*, 9(6):466–473, 2014.

[46] Hannah L. McFarland, Towfiq Ahmed, Jian-Xin Zhu, Alexander V. Balatsky, and Jason T. Haraldsen. First-principles investigation of nanopore sequencing using variable voltage bias on graphene-based nanoribbons. *The Journal of Physical Chemistry Letters*, 6(13):2616–2621, 2015.

[47] M. A. Reed, C. Zhou, C. J. Muller, T. P. Burgin, and J. M. Tour. Conductance of a molecular junction. *Science*, 278(5336):252–254, 1997.

[48] Henk W. Ch. Postma. Rapid sequencing of individual dna molecules in graphene nanogaps. *Nano Letters*, 10(2):420–425, 2010.

[49] Yanan Zhao, Brian Ashcroft, Peiming Zhang, Hao Liu, Suman Sen, Weisi Song, JongOne Im, Brett Gyarfas, Saikat Manna, Sovan Biswas, Chad Borges, and Stuart Lindsay. Single-molecule spectroscopy of amino acids and peptides by recognition tunnelling. *Nature Nanotechnology*, 9:466 EP –, 04 2014.

[50] Mads Brandbyge, Nobuhiko Kobayashi, and Masaru Tsukada. Conduction channels at finite bias in single-atom gold contacts. *Physical Review B*, 60(24):17064, 1999.

[51] B Ludoph, MH Devoret, D Esteve, C Urbina, and JM Van Ruitenbeek. Evidence for saturation of channel transmission from conductance fluctuations in atomic-size point contacts. *Physical Review Letters*, 82(7):1530, 1999.

CODE PARALLELIZATION OF THE OPTIMISATION FOR THE LOCAL TRANSPORT'S ELECTRIFICATION USING JOB ARRAY

Giuseppe Chiapparo[1*] and Massimo Celino[2†]

[1]*University of Rome Tor Vergata, Computer Science, Rome, Italy*

[2]*ENEA, C. R. Casaccia, via Anguillarese 301, 00123 Rome, Italy*

ABSTRACT. To promote the use of electric buses in public transport networks, a careful analysis of the costs is needed to find the best implementation of the electrified sub-networks. Unfortunately this task has a very high computational cost, that has till now prevented its application in real cases on large cities and forced the use of heuristic and approximate algorithms. The availability of supercomputers like CRESCO, opens the possibility to face this class of problems. In order to fully exploit its huge computing power, we developed an optimisation algorithm to model a general public transport network. Then we have parallelized it to explore the entire set of possible solutions and find out the more convenient among the many feasible sub-networks. This goal has required the implementation of branch-and-bound techniques and a careful analysis of the performance. This implementation of the parallel code has been used to address the public transport network of Rome. We used the technique of job array, in order to analyse big networks, considering all the ways to recharge a bus.

1 Introduction

The goal of this project is to find the optimal solutions for the electrification of the public transport networks to check the reliability of heuristic and approximated approaches already used in this context. We developed several methods of optimisation through the analysis of the public transport sub-networks in the different recharge configurations of the vehicles. With the realisation of these models we verified the technical and economical feasibility for the autonomous power supply, using appropriate technologies for the recharge of the electric buses. This analysis is performed for the buses of a city with significant size. Now, our work is focused on the design and engineering of algorithms that explore the space of the possible recharge configurations on appropriate subset of the bus lines for the considered public transport network, using the technique of job array.

In fact, we realised a code architecture that exploits the job array's potentiality and we designed algorithms to ease the analysis for the buses with the recharge to the stops (Architecture C).

The new code architecture has the following advantages:

- Write only a script for the shell;

- If we submit a job array and we notice that there is a mistake, we can cancel all the submission, because the job array has one Job Id;

---

*Corresponding author. E-mail: `giuseppe.chiapparo@uniroma2.it`.

†Corresponding author. E-mail: `massimo.celino@enea.it`.

- The balance of the workload isn't a critical element. In fact, the job array uses the resources that are free.

The goal of this software application is to compute the exact solution for the optimal problem, in which we consider the three architectures for the electrification: arch. A (with the recharge to the depots), arch. B (with the recharge to the depots and to the end of lines) and arch. C (with the recharge to the depots, end of lines and stops). In order to provide the best solution, we used an approach of exhaustive search, that consider all the possible eligible solutions.

However, the space of the solutions is such that, if we want to examine a network with L lines and three architectures of recharge, we should analyse a number of solutions equal to:

$$f(L) = \sum_{k=1}^{L} \binom{L}{k} \cdot 3^k = 4^L - 1 \tag{1}$$

For this reason we implemented an algorithm that:

- Explores the space of the solutions in parallel mode [1];

- Explores each possible solution once and only once by only one processor;

- Exploits the computational resources of CRESCO using the job array;

- Uses branch and bound techniques, avoiding the analysis of the unfeasible sub-networks;

- Analyze in advance the characteristics of the electrifiable lines with the type architecture C.

2   Algorithms and methods

The first result of this project was the implementation of three distinct programs, that represent the different steps that has to be executed in order to obtain the optimal solution of the problem. In detail we implemented a first step that generates many files that represent the input for each processor. In the second step we use the job array technique, in which each job analyse the input contained in a subset of file produced in the step one. Finally, the third step is used to know if all the possible cases are already analysed or it needs other computation before to understand what is the best solution of the electrification problem.

In order to simplify the computation we did different preliminary analysis:

- Maximum number of recharging station to the same stop;

- Maximum number of recharging station to the end of line;

- Minimum number of recharging station for each single line;

- Minimum number of recharging station for a subnetwork.

Each preliminary analysis is usefull to gain time during the three steps execution. In fact the preliminary analysis contain code that is executed only one time.

For further details we can refer to the Report RdS/PAR2017 [2].
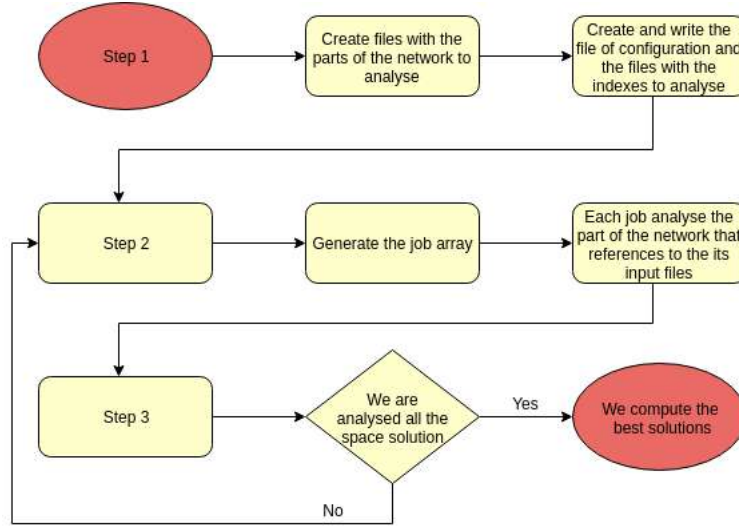
Figure 1: The workflow of the three steps that represents the flow of the program execution

3   Computational details

We used CRESCO4 for the execution of our tests. The programming language that we chose to use is C++. The reason to use C++ rather than other languages is performance. The reason for that is that C++ offers a means of abstraction that has no performance overhead at run-time. This allows the writing of very efficient code that still has a very high abstraction level. In this way we can write efficient code with an high level of abstraction.

The program is designed to be executed on numerous nodes of the cluster and requires a communication protocol between the computers. We chose to use the technique of job array for the following advantages:

- We don't manage the communication between the nodes in the cluster;

- We don't need to write algorithms for the balancing of the workload;

- We can write in C++ all the code, without using the MPI code;

- It's a statefull technique. We need to store the state of the program, in order to re-start the job during the next step.

4   Results and discussions

In order to verify our program we did many tests and we realised that the success of a test depends on many factors: the size of the analysed network, the budget for the initial investment, the number of the repeated stops in the network and the granularity of the input files.

During this work we are focused on the Rome network (283 bus lines) and we did two types of tests:

1. **Preliminary test on small networks.**

    (a) *We tested the Termini subnetwork.* In this case we analysed the bus lines that can be electri-

fied with the C architecture and pass through the main node of Termini. This is a network with 6 lines. We analysed this network when the budget for the investments increases. From this test we noticed that a good solution (when the objective function is high) corresponds to the bus lines electrified with the A architecture. See the table 1.

(b) *We tested the Corso subnetwork.* In this case we analysed the bus lines that can be electrified with the C architecture and pass through the main node of *Via del Corso*. This is a network of 13 lines. We did tests in order to compare Corso with Termini. Considering a infinite budget and a tolerance equal to 0 we obtain interesting results, for example we discovered that the architecture C isn't a best choice for both the networks. Furthermore, it's interesting to see that there is an architecture that prevails in each network. Termini seems to be better electrified with the A architecture, instead for the network Corso seems to be better the B architecture. In fact, Corso has many lines and can obtain benefits from the network effect. See table 2.

Table 1: Test on the network of Termini

Analysis of Termini Network with tolerance 0.9					
Budget (€)	Num lines	lines A	lines B	lines C	O.F. (€)
3000000	1	1	0	0	37843
5000000	2	1	1	0	170519
10000000	4	3	1	0	323266
20000000	6	5	1	0	435625
30000000	6	1	1	4	-9729261

Table 2: Test on the network of Corso

Analysis of Corso Network with tolerance 0.9					
Budget (€)	Num lines	lines A	lines B	lines C	O.F. (€)
10000000	3	0	3	0	1499108
20000000	4	0	4	0	2894050
30000000	7	0	7	0	3731795
40000000	9	0	9	0	4136561
50000000	11	3	8	0	3955103
60000000	11	0	10	1	-1330665
70000000	13	0	10	3	-7339004

obj_function_value	number_of_lines	line_id	arch_id	line_id	arch_id	line_id	arch_id	line_id	arch_id	line_id	arch_id
7228821.82600000	4	33	B	167	B	257	B	296	B		
6959461.66410000	4	33	B	236	B	257	B	296	B		
6956764.99267143	3	236	B	283	B	296	B				
6949221.57800000	4	33	B	47	B	254	B	296	B		
6941796.52000000	2	257	B	283	B						
6937298.51800000	4	33	B	164	B	254	B	296	B		
6911374.56360000	4	33	B	50	B	254	B	296	B		
6886442.79200000	4	33	B	187	B	290	B	296	B		
6885681.86010000	5	33	B	187	B	236	B	254	B	296	B
6884905.97200000	5	20	B	33	B	167	B	254	B	296	B
6858253.53200000	4	33	B	237	B	290	B	296	B		
6857492.60010000	5	33	B	236	B	237	B	254	B	296	B
6816314.49200000	4	33	B	83	B	187	B	296	B		
6810800.72600000	4	167	B	257	B	290	B	296	B		
6808172.43010000	4	16	B	33	B	257	B	296	B		

Figure 2: The result of the test over the network Rome_AB-C_big.

2. **Test for the comparison with the heuristic algorithms and the analysis of big subnetworks of Rome.**

   (a) *We tested the Rome network.* In this case we analysed three subnetworks: Roma_ABC, Roma_AB-C_big and Roma_AB-C_small. Roma_ABC includes all the bus lines that are electrified with all the three architectures. Roma_AB-C_big is a network with 99 bus lines electrified with A and B architectures. Roma_AB-C_small is a subnetwork of the previous network used to make comparisons with the Roma_ABC. These tests show how the C architecture increase the running time in a exponential way. See the figure 2.

5 Conclusion

With this work we created a new code architecture able to execute the test with more time and with the store of the state of the execution.

In fact, the use of the job array gave us significant improvements, like the automatic handle of the workload (through LFS) and the simplified writing of the code to manage the communication between several nodes.

Furthermore, we obtained a significant advantage with the preliminary analysis of the lines electrified with the C architecture.

However, there are several future developments:

- Analysis of bigger networks;

- The introduction of other preliminary analysis, in order to reduce the total time of the program.

References

[1] Introduction to parallel computing, lawrence livermore national laboratory. https://computing.llnl.gov/tutorials/parallel_comp/.

[2] Giuseppe Francesco Italiano. Sviluppo di algoritmi per l'ottimizzazione del processo di elettrificazione di reti di trasporto pubblico urbano attraverso l'analisi delle possibili configurazioni di ricarica su sottoinsiemi della rete di trasporto. *Accordo di Programma Ministero dello Sviluppo Economico - ENEA, Piano Annuale di Realizzazione 2017*, September 2018.

Alpha Spectrometry with inexpensive prototyping board: simulation, design, and experimental tests

Luigi Lepore[1][*], Giuseppe A. Marzo[1], Luca Gugliermetti[2]

[1]*ENEA Casaccia Research Center, Nuclear Material Characterization Laboratory and Nuclear Waste Management, Via Anguillarese, 301 - 00123, Roma - Italy*

[2]*Sapienza - University of Rome, Department of Astronautics Engineering, Electrical and Energy, Via Eudossiana, 18 - 00184, Rome - Italy*

ABSTRACT. A photodiode-based inexpensive detector working as counter and spectrometer for alpha particles, named *Alphaino* has been designed, constructed, and tested. Prior to detector assembly, Monte Carlo simulations by means of MC-NPX ver. 2.7.0 code have been carried out to select the most suitable sensitive element for the intended applications. The detector has been tested for low-rate alpha-particle counting and spectroscopy, demonstrating a maximum achievable count rate of $4.0 \cdot 10^3$ s^{-1}, with an energy resolution corresponding to a Full Width Half Maximum of 160 keV over the entire energy range of measured alpha, namely 4.0-6.5 MeV, the intrinsic efficiency being 100%. *Alphaino* can be used for fast and qualitative analyses to radionuclides identification, and quantitative analyses when radionuclides monitored are characterized by well distinguished energy lines in spectra.

1 Introduction

In alpha detection, charge collection can be achieved even with standard commercial silicon photodiodes. Interacting with silicon, the alpha generates electric charges proportional to the energy deposited by the particle. Alphas in silicon have a significant Linear Energy Transfer (LET), which allows the deposition of almost all the energy in just the photodiode's depletion region. As a consequence, the amount of charge collected at photodiode's pins is strongly correlated to the energy with which the alpha particle entered into the silicon layer that acts as the sensitive volume. The current signal is then converted into a voltage pulse whose maximum amplitude is proportional to the energy deposited by the alpha particle. *Alphaino* is an alpha-particle detector intended for applications where low cost and small dimension are key factors. The low-cost *Alphaino* detector here presented uses a photodiode as the sensitive part, without the need of any scintillation element coupled. Alpha particles impinge the photodiode directly releasing their energy in the active volume. The energy resolution achieved, Full Width Half Maximum of 160 keV over the entire energy range of measured alpha spectra, allows for a mathematical deconvolution and reconstruction of each nuclide activity. Excellent performance is obtained in intrinsic efficiency. *Alphaino* can also be connected both to traditional nuclear spectroscopy electronics, and to cheap prototyping boards. The detector is open-source: everyone can download the schematics, build the sensor and contribute to further development through the GITHUB repository for the project, *https://github.com/bemxgm/Radon-Monitor*.

---

[*]Corresponding author. E-mail: `luigi.lepore@enea.it`.

2 Detector Design

The detector is made by Surface Mount Device (SMD) components easily available on the market. The whole cost of the detector is about 35 $ [1]. All details about electronics and connections are available through the GITHUB repository. The sensitive element is a reverse-biased wide-area photodiode (93.6 mm^2) by Silonex [2]. Such photodiode has been found particularly suitable for the application due to its specific features: *i)* wide area, intended to be coupled with alpha-sources having an electrodeposited circular surface within 7 mm-in-diameter, when the source is lying on the detector and the air gap is minimized; *ii)* high reliability, allowing to consider the sensor to be heavy duty and stable, ensuring the measurement repeatability; *iii)* thin oxide passivation layer of the front surface, reducing the energy losses in alpha tracks toward the sensitive volume as much as possible (the coating layer was assumed to be 0.09 μm); *iv)* low capacitance and high speed, allowing for a quick collection of charges, fast generation of the voltage pulse, and detector recovery.

Prior to the detector construction and verification, the photodiode response has been studied by means of Monte Carlo simulations in the Monte Carlo N-Particles eXtended, MCNPX, code *ver. 2.7.0* [3] [4]. The transport equation for radiation is solved in Monte Carlo methods by a random sampling of the probability distribution functions ruling physical phenomena. The reproduction of such physical phenomena happening in real experiment within the simulation can be achieved by the definition of a simulation model the more accurate as possible in terms of geometry and materials (dimensions, isotopic composition and density). Regarding alpha particles transport, the code's default physics is here used.

Radionuclides in calibrated alpha sources here used are deposited onto stainless steel disc, 25 mm-in-diameter, 0.5 mm thick, and the deposition diameter is 7 mm. According to the manufacturer [5], reagents used are ultra-pure, resulting in an essentially mass-less deposit. This process minimizes line broadening and produces sources exhibiting line widths of less than 20 keV Full-Width-Half-Maximum, FWHM. So, the deposition can be considered so thin to produce only a little broadening on alpha energy lines due to self-absoption; tracks emerging can be assumed as the half of the total activity deposited, while the other half is emitted toward the stainless steel disc.

The source model in MCNPX simulations was calibrated to reproduce real sources emission spectra in order to get a first evaluation of the photodiode response, and select a suitable photodiode. Into the MCNPX code the source has been interpreted as an extended isotropic source (a thin cylinder) emitting monoenergetic alpha-particles at 4.7, 6.0 and 7.5 MeV: energies selected are theoretical values distributed over a wide range, in order to observe differences in detected peaks. The source model in MCNPX (the source definition card, the *sdef*) is modeled as a non-attenuating cylinder, as to preserve the 50% of the tracks emerging from the front side, and the other half emitted toward the source casing. Each alpha line is broadened by means of a gaussian function centered at the alpha line energy with a FWHM=20 keV. The source spectrum is reported in Figure 1. The photodiode sensitive volume has been modeled into MCNPX as a 10 mm x 10 mm x 0.4 mm silicon wafer, covered with a 0.09 μm SiO$_2$ layer, both materials at standard densities. The energy deposition in the detector sensitive volume is scored by means of a *tally f8* vs. alpha [4]. The energy deposition spectrum detected by the Silonex SLCD-61N5 photodiode is shown in Figure 1. For each alpha line, in the geometrical configuration considered i.e. the photodiode in front of the source with an air gap < 0.1 mm, an efficiency value of 49% is found for each peak. Such a result is found to be reasonable due to the fact that about the half of the total alpha emission is loss in the stainless steel disc while the other is emitted toward the photodiode. Low-energy tails in the spectrum were expected due to the continuous energy loss of alphas in their paths, because a variable amount of energy is deposited in the oxide layer according to each spe-
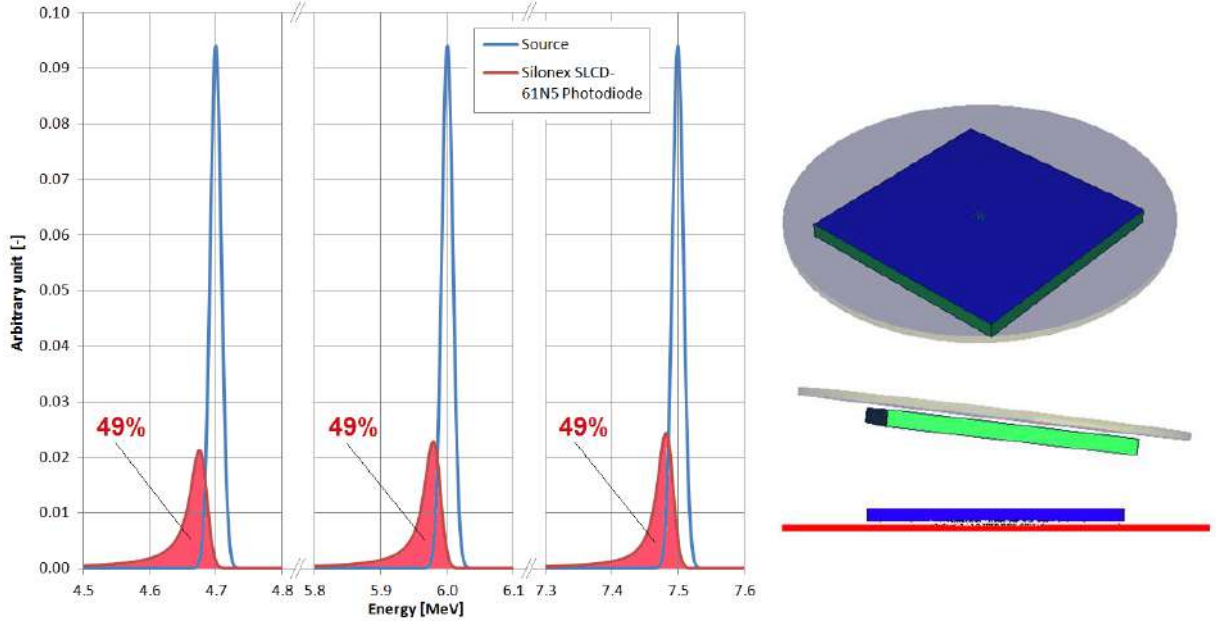
Figure 1: Left: simulated spectra by MCNPX; gaussian peaks represent alpha particles emerging from the source; asymmetric peaks represent alpha tracks detected by the Silonex SLCD-61N5 photodiode when the air gap is < 0.1 mm; percentages report the total efficiency of the photodiode in the geometrical configuration considered. Right: MCNPX 3D view of the simulation.

cific track. Having found in simulation the Silonex SLCD-61N5 photodiode [2] particularly suitable for the intended application, the *Alphaino* detector has been developed around such component. Outputs from the detector's board can be distinguished in *i)* a voltage pulse signal whose maximum amplitude is proportional to the energy deposited by the alpha particle; *ii)* a Transistor-Transistor Logic (TTL) signal for each alpha detected, for counting purposes only. A closed environment is also necessary to avoid noise due to the visible light that can reach the photodiode surface, and producing undesired signals. Such precaution can be combined in an electromagnetic-shielded (EMS) dark chamber, able to reduce to light and electronic noise during operations of Alphaino. The computing resources and the related technical support used for this work, and all future uses, are provided by CRESCO/ENEAGRID High Performance Computing infrastructure. MCNPX has been compiled for MPI multi-processing up to 500 CPU; the cluster utilized for this work is "CRESCO4".

3   Detector Characterization

Alphaino has been tested for preliminary validation with calibrated alpha sources. The spectrum of the *'Pu-Am-Cm'* source has been acquired for a live-time corresponding to 2.7 h. When measuring the *'Pu-Am-Cm'* source, Alphaino recorded a dead-time of 24.1%, the overall count-rate for the spectrum is $\sim 1.7 \cdot 10^3$ s^{-1}. With the energy calibration of the multi-channel analyzer achieved, a proper deconvolution method has been applied being the acquired spectrum the sum of contribution of many alpha peaks overlapping among themselves. The least-square fit among theoretical and measured data provided the parameters describing the observed alpha-peak shape, and the counts to assigned to each alpha peak. Results of deconvolution method applied to measured spectra are reported in Figure 2. Colored continuous lines show theoretical alpha-energy emissions from each nuclide, and the black is the sum of all such theoretical contributes. The dotted line represents the measured spectrum. The graph on the top
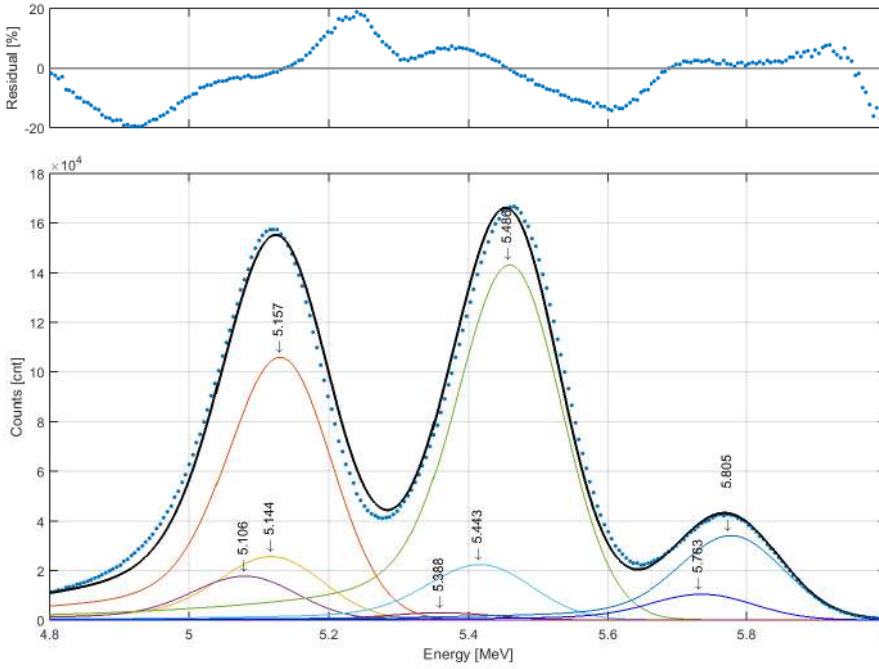
Figure 2: Left: *'Pu-Am-Cm'* calibration alpha source measured by Alphaino; continuous lines are the peaks fitting from the mathematical deconvolution while dotted line is the measured spectrum; energy tags report each single α-energy line contributing to the measured spectrum; residuals are not negligible but a very simple fitting procedure was utilized due to the economicity of the system.

of the spectrum shows residuals i.e. the difference between measured counts and theoretical counts, channel by channel. An energy resolution (FWHM) of 160 keV -constant over the entire energy range of detected alpha particles, namely 4.0-6.5 MeV has been calculated. With the deconvolution achieved, the efficiency evaluation has been carried out accordingly. In this geometrical configuration where the source is lying in front of the detector with an air-gap < 0.1 μm, alpha particles impinging the detector are about the half of the total emission from the source, the intrinsic efficiency of Alphaino vs. alpha particles can be considered about 100%.

References

[1] Luca Gugliermetti, Luigi Lepore, Romolo Remetti, and Massimiliano Colarieti Tosti. Alpha spectrometry with the inexpensive open-source detector alphaino. *Nuclear Instruments and Methods in Physics Research Section A: Accelerators, Spectrometers, Detectors and Associated Equipment*, 928:13 – 19, 2019.

[2] Silonex INC. Slcd-61n5 photodiode datasheet, 2018.

[3] J. F. Briesmeister. *MCNP - A general purpose Monte Carlo code for neutron and photon transport.* Los Alamos National Laboratory, Report LA - 12625, New Mexico, United States, 1993.

[4] D.B. Pelowitz. *MCNPX User's Manual. Version 2.7.0.* Los Alamos National Laboratory, Report LA-CP-11-00438, New Mexico, United States, 2011.

[5] Eckert & Ziegler. Alpha Spectroscopy sources, 2018.

Run-length performance estimation of the functional regression control chart

Fabio Centofanti[1], Antonio Lepore[1]*, Alessandra Menafoglio[2], Biagio Palumbo[1] and Simone Vantini[2]

[1] *Università di Napoli Federico II, Department of Industrial Engineering, P.le V. Tecchio 80, 80125 Naples, Italy*

[2] *Politecnico di Milano, MOX – Department of Mathematics, Piazza Leonardo da Vinci 32, 20133 Milan, Italy*

Abstract. In many applications, statistical process monitoring methods have to be applied to a quality characteristics that can be modelled as a functions. Moreover, sometimes measures of other functional covariates that are somehow related to the functional quality characteristic are also available. To combine the information coming from all the measures attainable, we propose a new functional control chart that relies on the residual coming from a functional linear regression of the quality characteristic on the other covariates. To illustrate the potential of the proposed monitoring scheme, it is applied to a real-case study in the shipping industry. Moreover, a computationally expensive simulation study is performed to quantify the FRCC performance, in terms of average run length (ARL), in identifying mean shifts in the functional response. Results show that the proposed control chart outperforms the competitor in terms of average run length. Thus, on average the FRCC identifies the mean shift in the response before the competitor control charts.

1 Objectives

The advent of modern high-frequency sensor technologies naturally calls for new statistical process control (SPC) methods to handle massive and complex data. In particular, in many practical situations, the quality characteristic of a process can be regarded as a smooth function defined on a compact domain. Data of such kind are the foundation of a rapidly expanding area of statistics that is referred to as functional data analysis (FDA) and is naturally prone to cross-fertilize SPC methods that allow monitoring such processes, also known as profile monitoring techniques [6]. In this context, our objective is to enhance the profile monitoring of the quality characteristic(s) by using also the information coming from other functional variables concurrently acquired and related to the latter, referred to as covariates [2].

To this end, we propose a new control chart to continuously monitor the quality characteristic, which is adjusted by the effect of functional covariates via the multivariate function-on-function linear regression model (MFLR), borrowed from FDA. This will be shown to improve the accuracy and the effectiveness of the chart in identifying assignable sources of variations acting on the process.

This chart is named functional regression control chart (FRCC) because of the similarity with

---

the regression control chart that has appeared in the multivariate (non-functional) SPC context
[5].

2   Methods

Assume that functional covariates, $X_1, \ldots, X_p$, related to the functional quality characteristic
(or response) Y, have smooth realizations in $L^2(\mathcal{S})$ and $L^2(\mathcal{T})$, i.e., the Hilbert spaces of
square integrable functions defined on the compact sets $\mathcal{S}$ and $\mathcal{T}$, respectively. Then, $X = (X_1, \ldots, X_p)$ is a random vector of functions whose realizations are in $(L^2(\mathcal{S}))^p$. Let X^{std} be
the vector of standardized covariates and Y^{std} the standardized response variable. For the
MFLR model we assume that the covariate vector X^{std} linearly influence the response Y^{std} as
follows

$$Y^Z(t) = \int_0^1 (\boldsymbol{\beta}(s,t))^T \boldsymbol{X}^Z(s)\, ds + \varepsilon(t), \tag{1}$$

where the regression coefficient vector $\beta = (\beta_1, \cdots, \beta_p)^T$ is in $(L^2(\mathcal{S} \times \mathcal{T}))^p$, whose elements
are vectors of bivariate functions in $L^2(\mathcal{S} \times \mathcal{T})$. An estimator of Y^{std} is

$$\hat{Y}^{std}(t) = \sum_{i,j=1}^{\infty} b_{i,j} \xi_i^X \psi_j^Y(t) \qquad t \in \mathcal{T} \tag{2}$$

where ξ_i^X and ψ_j^Y are the principal component scores and the principal component functions
obtained, respectively, from the multivariate and univariate Karhunen-Loève's theorem. The
rationale behind the FRCC is to monitor the residual e, i.e., the estimator of ϵ, by means of the
the Hotelling's T^2 and the squared prediction error (SPE) control charts. The standardized
residual e^{std} is defined as follows $e^{std} = Y^{std} - \hat{Y}^{std}$; whereas, the Hotelling's T^2 and the SPE
statistics are, respectively, defined as

$$T_{e^{std}}^2 = \xi^e \Sigma_{\xi^e}^{-1} \xi^e \qquad\qquad SPE_{e^{std}} = \int_{\mathcal{T}} \left(e^{std}(t) - e_K^{std}(t)\right)^2 dt, \tag{3}$$

with $e_K^{std} = \sum_{i=1}^{K} \xi_i^e \psi_j^e$, where ξ^e and ψ^e are the scores and the principal component obtained
from the the univariate FPC decomposition of e^{std}. The control limits of the Hotelling's T^2
and the SPE control charts are calculated using percentiles of the empirical distributions of
the two statistics, estimated by considering n, i.i.d. observations $(Y_i(t), X_i(t))$ acquired under
in-control conditions and an overall Type I error α.

3   Real-case Study: CO$_2$ Emission Monitoring of a Ro-Pax cruise ship

Nowadays, the issue of monitoring CO$_2$ emissions, also in view of the dramatic climate change,
is of paramount importance in the maritime field. Indeed, the new Regulation (EU 2015/757)
of the European Union (EU) Council of 25 April 2015, coherently with the previous guidelines
of the International Maritime Organization (IMO), compels maritime operators that have ships
sailing in the Mediterranean Sea to monitor, report and verify (MRV) CO$_2$ emissions. In this
setting, three year's worth of real data from a Ro-Pax cruise ship, owned by the Italian company
Grimaldi Group, are analyzed. The cumulative CO$_2$ emissions per each voyage is considered
as the response variable, whereas, the sailing time, the speed over ground and the longitudinal

Table 1. $\widehat{ARL}$s and $(1-0.05)$-bootstrap confidence intervals (CI) for the FRCC, RESP control chart and INBA control chart

	$\widehat{ARL}$	CI
FRCC	18.60	$[10.87, 50.75]$
RESP	34.09	$[14.73, 101.73]$
INBA	50	$[34.50, 370.37]$

and transverse wind components are assumed as the covariates (further information on the variables can be found in [4]). In this real-case study, a specific energy efficiency operation was performed and guaranteed CO_2 emission reduction, which shall be revealed as a shift in the response mean [4]. In the light of this, observations before the energy efficiency operation are used to build the chart (Phase I) and the control limits, whereas the remaining observations are used for the perspective monitoring (Phase II). A simulation study is performed to quantify the FRCC performance, in terms of average run length (ARL), in identifying mean shifts in the functional response. Simulated data are generated using pre-specified covariance structure and means reference model for the response and predictors, similar to simulation studies in [7]. Two different scenarios are considered: Scenario 1, where shifts affect only the conditional mean of the response given the predictors by means of changes in the response mean; Scenario 2, where both shifts in response and predictor means occurred. FRCC performance are compared with those of other two charts widely used to monitor profiles in the industrial context [7, 3]. The *cumulative fuel consumption* per each voyage is considered as the response variable, whereas, the *sailing time*, the *speed over ground* and the *longitudinal* and *transverse wind components* are assumed as the predictors (further information on the variables can be found in [1, 4]). During February 2016 energy efficiency operations were performed that produced a shift in the response mean [4]. In light of this, observations before energy efficiency operations are used in Phase I, whereas the remaining observations are used to perform Phase II. The overall Type I error α is set equal to 0.0027. To evaluate the FRCC performance, two competitor profile monitoring schemes are considered as well. They consist of monitoring scores coming from a principal decomposition of the response by means of Hotelling's T^2 and the squared prediction error (SPE) control charts (hereafter denoted as RESP control chart) [3], and of monitoring the area under the response curve (hereafter denoted as INBA control chart) [7]. Estimation $\widehat{ARL}$s of the ARLs and $(1-0.05)$-bootstrap confidence intervals are showed in Table 1. We can assert that the proposed control chart outperforms the competitor ones because both the point estimation of the ARL and bootstrap confidence interval of the $\widehat{ARL}$ for the FRCC are lower than those of the RESP and INBA control charts. Thus, on average the FRCC identifies the mean shift in the response before the competitor control charts.

4 Conclusion

In this paper, we propose a new method to monitor a functional quality characteristic when observations of other functional covariates related to it are available. It consists of monitoring the functional residual coming from a functional linear regression of the response on the predictors, instead of using the response only. An application of the FRCC to a real-case study in the shipping industry demonstrates that the proposed control chart performs better than two other well-known control charts in two different scenarios.

5 Acknowledgement

References

[1] Dario Bocchetti, Antonio Lepore, Biagio Palumbo, and Luigi Vitiello. A statistical approach to ship fuel consumption monitoring. *Journal of Ship Research*, 59(3):162–171, 2015.

[2] Fabio Centofanti, Antonio Lepore, Alessandra Menafoglio, Biagio Palumbo, and Simone Vantini. A new statistical process control method for monitoring profiles. In *49th Scientific meeting of the Italian Statistical Society. University of Palermo, Italy*, 2018.

[3] Bianca Maria Colosimo and Massimo Pacella. On the use of principal component analysis to identify systematic patterns in roundness profiles. *Quality and reliability engineering international*, 23(6):707–725, 2007.

[4] Pasquale Erto, Antonio Lepore, Biagio Palumbo, and Luigi Vitiello. A procedure for predicting and controlling the ship fuel consumption: Its implementation and test. *Quality and Reliability Engineering International*, 31(7):1177–1184, 2015.

[5] BJ Mandel. The regression control chart. *Journal of Quality Technology*, 1(1):1–9, 1969.

[6] Rassoul Noorossana, Abbas Saghaei, and Amirhossein Amiri. *Statistical analysis of profile monitoring*, volume 865. John Wiley & Sons, 2012.

[7] Alessia Pini, Simone Vantini, Bianca Maria Colosimo, and Marco Grasso. Domain-selective functional analysis of variance for supervised statistical profile monitoring of signal data. *Journal of the Royal Statistical Society: Series C (Applied Statistics)*, 2017.

[8] Giovanni Ponti et al. The role of medium size facilities in the hpc ecosystem: the case of the new cresco4 cluster integrated in the eneagrid infrastructure. In *High Performance Computing & Simulation (HPCS), 2014 International Conference on*, pages 1030–1033. IEEE, 2014.

MULTISCALE MODELING OF CARBON BLACK NANOPARTICLES IN POLYETHYLENE MELTS

Stefano Caputo[1*], Antonio De Nicola[2], Greta Donati[1] and Gianmarco Munaò[1]

[1]*University of Salerno, Chemistry and Biology Department, 84084, Fisciano, Italy*

[2]*Yamagata University, Department of Organic Material Science, 992-8510, Yonezawa, Japan*

ABSTRACT. Carbon black (CB) is a filler widely used in polymer composite materials, known to improve several properties of the medium in which it is dispersed, such as mechanical, electrical and optical ones [1]. To obtain materials with tailored properties, it is necessary to control the dispersion of the CB aggregates into the polymer matrix.
In this work we address this task by performing MD simulations, and studying the structural properties at the NP/polymer interface.

1 INTRODUTCION

At the nanoscale level, CB is made essentially by aggregates ranging from tens to few hundreds of nanometers, and these aggregates are made of coalesced nanoparticles, called primary nanoparticles [2]. The nanoparticles are composed by many graphitic like stacks, arranged in a sphere. To obtain materials with tailored properties, it is necessary to control the dispersion of the CB aggregates into the polymer matrix, and this becomes more and more challenging when increasing the filler content. In this work we address this task by performing MD simulations in a multiscale fashion, going from the atomistic scale to the coarse-grained (CG) one, in order to gain insights on the structuring of the polymer phase around the CB nanoparticle, especially in bimodal polymer melts, where we interestingly find an enrichment of the low M_w fraction at the CB/polymer interface. This finding could be relevant because it directly impacts the choice of viscosities values used in larger scale simulations (e.g. CFD-DEM) of CB aggregates in polymer melts, where shear conditions are also applied.
The only detailed molecular model of CB primary particles found in literature until now is the one proposed by Ban et al.[3]. This model, however, being an all-atom model, cannot be used to access the long time and length scales required for our study. Considering this, we have developed a CG model of the CB primary nanoparticle that correctly reproduces the experimental density and morphology of the nanoparticles. With the CB model being validated, we then performed CG simulation of the nanoparticle in several polyethylene melts with realistic M_w of the polymer chains, ranging from 30 kg/mol to 300 kg/mol, by means of a well validated hybrid particle-field molecular dynamics technique [4], [5], [6] which allows us to simulate very large systems (up to $2*10^6$ particles), with high computational efficiency. We have chosen the CRESCO HPC facilities to perform simulations in fast and accessible times.

2 RESULTS AND DISCUSSION

The results of our simulations, suggest that, in bidisperse polymer melts, short polyethylene chains (up to a certain M_w) are the most abundant fraction at the polymer/nanoparticle interface, while for higher M_w this difference becomes less evident, as shown in the polymer density profiles reported in figures 1 and 2. The origin of this structuring at the interface, is mainly entropical in nature, and we are performing conformational analysis on polymer chains at the interface (statistics on trains, tails and loops [7]) to corroborate this assumption.
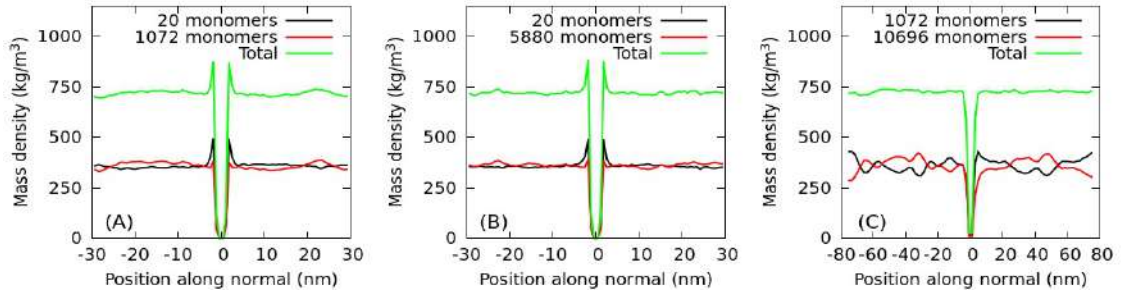

Fig.**1**: Polymer density profiles, in systems with polymer and graphite substrate. Bidisperse PE with 20 and 1072 monomers (A), 20 and 5880 monomers (B), 1072 and 10696 monomers (C).
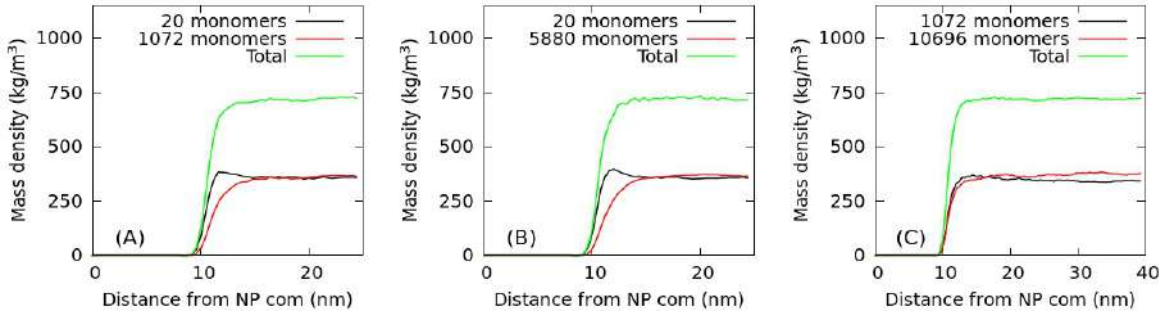

Fig.**2**: Polymer density profiles, in systems with polymer and carbon black nanoparticle. Bidisperse PE with 20 and 1072 monomers (A), 20 and 5880 monomers (B), 1072 and 10696 monomers (C).

3 CONCLUSIONS

We report here the first CG, detailed model of a carbon black nanoparticle, and perform simulations of polyethylene melts embedding it, obtaining useful structural informations. The model proposed in our simulations, can be further extended to simulations of multiparticle systems, rensembling the structure of carbon black aggregates. This work has the potential to provide predictive power and could allow the production of special CB composite materials, where control of the dispersion during the processing is crucial.

References

[1] J. B. Donnet, Carbon Black: Science and Technology, CRC press, (1993).

[2] Encyclopedia of polymer science and technology, John Wiley & Sons, (2002).

[3] S. Ban, K. Malek, C. Huang and Z. Liu, A molecular model for carbon black primary particles with internal nanoporosity, *Carbon*, **49**, pp. 3362 (2011).

[4] G.Milano and T.Kawakatsu, Hybrid particle-field molecular dynamics simulations for dense polymer systems, *J.Chem.Phys.*, **130**, pp. 214106 (2009).

[5] Y. Zhao, A. De Nicola, T. Kawakatsu, and G. Milano, Hybrid particle-field molecular dynamics simulations: Parallelization and benchmarks, *Journal of Computational Chemistry*, **33**, 868, (2012).

[6] A. De Nicola, T. Kawakatsu and G. Milano, Generation of Well-Relaxed All-Atom Models of Large Molecular Weight Polymer Melts: A Hybrid Particle-Continuum Approach Based on Particle-Field Molecular Dynamics Simulations, *J. Chem. Theory Comput.*, **10 (12)**, pp. 5651, (2014).

[7] K. Ch. Daoulas, V. A. Harmandaris and V. G. Mavrantzas, Detailed Atomistic Simulation of a Polymer Melt/Solid Interface: Structure, Density, and Conformation of a Thin Film of Polyethylene Melt Adsorbed on Graphite, *Macromolecules*, **38**, pp. 5780, (2005).

Swap dynamics in kinetically constrained models of the glass transition and in blockaded systems of cold atoms

Ricardo Gutiérrez[*]

Complex Systems Group & GISC, Universidad Rey Juan Carlos, 28933 Móstoles, Madrid, Spain

ABSTRACT. Particle swaps in atomistic simulations of liquids close to the glass transition lead to dramatic reductions in equilibration time scales, which have been used to gain insight into the physics of the glass transition at unprecentedly low temperatures. We show that the macroscopic consequences of swap moves can be easily accommodated within the dynamic facilitation theory of the glass transition by explicitly constructing a kinetically constrained model with swaps. Moreover, we also show that swaps (which are artificially introduced in the dynamics of classical systems) are physical in quantum many-body systems. We illustrate this with a study of gases of highly-excited (Rydberg) atoms, which are a versatile platform for the experimental study of strongly-interacting quantum spin systems.

1 Motivation

The nature of the glass transition (the process whereby a liquid loses its fluidity and becomes a rigid glass as the temperature is lowered) is a persistent riddle in condensed-matter physics. Close to the transition, relaxation times shoot up as the temperature decreases until they exceed all experimental time scales. The same properties that make the phenomenon interesting render its numerical exploration challenging, as the computational equilibration times in Monte Carlo or molecular dynamics simulations also increase dramatically. That is why, in numerical simulations of glassy liquids swap moves (in which distant particles of different sizes swap their locations) have attracted so much attention, as their inclusion in the dynamics leads to a remarkable reduction of equilibration times. By the use of Swap Monte Carlo (SMC), Grigera and Parisi could study the thermodynamics of glassy systems at very low temperatures [6]. Their method has enabled the numerical equilibration of strongly arrested systems [10], allowing for the study of length scales characterizing glassiness at low temperatures [3, 9], the jamming transition at high densities [2] or the configurational entropy of deeply supercooled states [1].

Theoretical explanations have been proposed to explain the observed dramatic growth of relaxation times, some of which rely on assuming the existence of an unobserved phase transition or unusual thermodynamic behavior resembling that of spin-glass models. The underlying idea is that different amorphous states of the glass are separated by large free energy barriers, which must be crossed, in order for structural relaxation to take place, irrespective of the specific dynamics. While some explanations have been proposed for the accelerating effect of swaps, such a strong dependence of relaxation times on dynamics is in principle unexpected within those theories. It can be easily accommodated within the dynamic facilitation theory of the glass transition [5], however, which is based on the idea that model systems with identical thermodynamic properties can (in general) have dramatically differ-

---

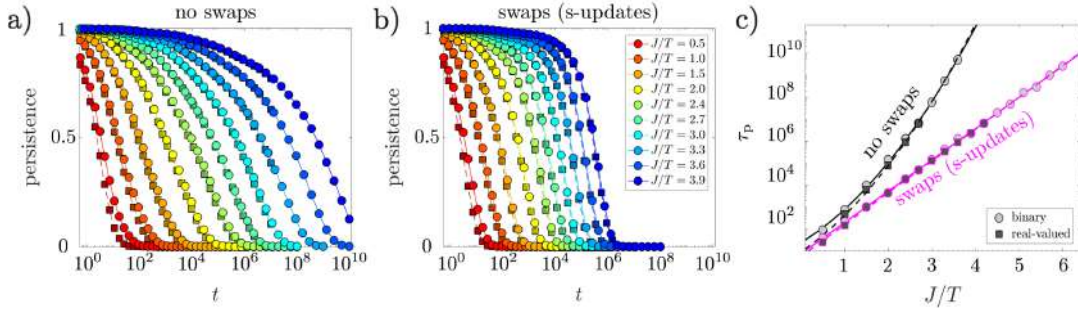[*]Corresponding author. E-mail: `rcd.gutierrez@gmail.com`.

Figure 1: Persistence function of the soft KCM for various values of the inverse temperature J/T (see legend) in a system of $N = 512$ spins. (a) Dynamics without swaps (b) Dynamics including swaps (c) Dependence of the persistence time τ_p on temperature, with second-order polynomial fits.

ent relaxation times. However, it is a priori not clear why swapping particle sizes would have such a dramatic effect. In Section 2 we propose a coarse-grained kinetically constrained model (KCM) [12] with a softness parameter that can be swapped between distant sites, and show that the accelerating effect of swaps can be naturally accounted for in such dynamic facilitation models. The role of swaps on the collective nature of the dynamics is also explored in this work, which was done in collaboration with Juan P. Garrahan (University of Nottingham) and Rob L. Jack (University of Cambridge) [7].

While particle swaps in classical glassy systems are a just numerical trick (notwithstanding their practical usefulness, and their theoretical interest as explained above), in quantum many-body systems of atoms swaps are part of the physical dynamics, as resonant dipole-dipole interactions effectuate state exchanges over long distances. In this domain, systems of interacting Rydberg atoms have emerged as a versatile platform for studying collective dynamical behaviors. Their physics is governed by block-ade effects analogous to the excluded volume interactions underlying the dynamics of glass-forming liquids and jammed systems of hard objects. Moreover, in both Rydberg gases and glassy soft-matter models dynamical phase transitions are at the heart of the observed dynamic arrest [11]. In Section 3 we report on recent results clarifying the impact of excitation swaps on the relaxation time scales, which are reduced by several orders of magnitude in their presence, and on the structure and dynamics of the stationary state of Rydberg gases. This is strongly reminiscent of the above-mentioned SMC approaches in which particle swaps accelerate the approach of highly arrested glassy systems to equilibrium. Moreover, swaps drive the system further away from equilibrium conditions, in particular in conjunction with radiative decay processes. This work has been done in collaboration with Juan P. Garrahan and Igor Lesanovsky (University of Nottingham, UK), and has been recently published [8].

A combination of analytical approaches and continuous-time Monte Carlo (CTMC) [4] simulations performed on the CRESCO/ENEAGRID HPC infrastructure was required in this research work.

2   Swap dynamics in a glassy kinetically constrained model

The predictions of dynamic facilitation theory [5] are based on KCMs. Many of these are spin models on a lattice, where a spin can only change its state if its neighbors satisfy a constraint [12]. We consider softened KCMs, where the local structure of the liquid is accounted for by an additional variable on each site of the lattice, which we call the softness. If this quantity is large, there is a substantial probability that the system can relax locally, by violating the constraint. We show that even if the softness has
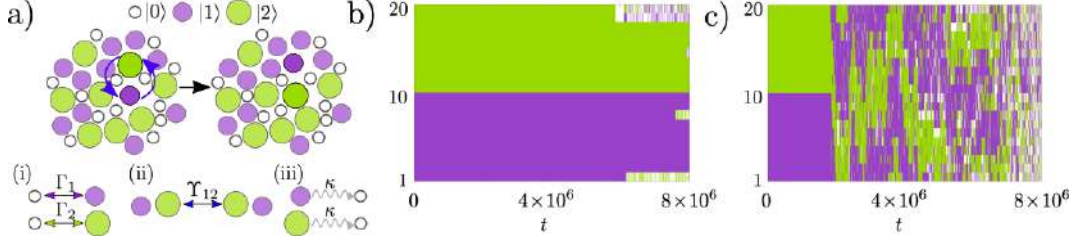
Figure 2: (a) Illustration of a swap in a Rydberg gas, and list of relevant processes: (i) excitations, (ii) swaps, and (iii) decay. Trajectories without (b) and with swaps (c) in a chain of $N = 20$ atoms.

a minimal effect on the natural dynamics of the model, introducing softness swaps can dramatically accelerate relaxation. We argue that the mechanism may be general and apply to deeply supercooled liquids, where a region temporarily swaps its particles for smaller ones, and then relax.

In our CTMC simulations, we use the persistence function $P(t)$ to explore the relaxation dynamics of the model, which gives the fraction of spins that have not flipped from time 0 to time t. In Fig. 1 we show $P(t)$ without (a) and with swaps (b). One sees a dramatic acceleration of relaxation by the swap dynamics, in agreement with theoretical arguments [7]. In panel (c) we show the persistence time τ_{p}, defined by $P(\tau_{\mathrm{p}}) = 0.01$, as a function of the inverse temperature J/T (J gives the energy units). Fits to the data are compatible with a super-Arrhenius parabolic dependence for the dynamics without swaps and an Arrhenius dependence in the presence of swaps, yielding a difference of up to three or four orders of magnitude in the temperature range that has been explored which is expected to increase at even lower temperatures. Additionally, we explore the diminished dynamic heterogeneity that results from swap moves, and discuss its relation to recent results based on atomistic simulations [7].

3   Swap dynamics in blockaded systems of cold atoms

In Ref. [8] we consider a gas of strongly interacting Rydberg atoms, whose transition from the ground state $|0\rangle$ to two highly-excited levels $|1\rangle$ and $|2\rangle$ is driven by an external field (in our theory we consider any finite number of excited levels, but here we focus on two for simplicity). We use projection operator techniques to derive the effective dynamics of such Rydberg gas, whose evolution includes dephasing and spontaneous decay as incoherent processes. The resulting dynamics proceeds along classical (diagonal) states, e.g. $|012100\cdots\rangle$, and includes the following processes [see Fig. 2 (a)]: (i) driven (de-)excitations ($|0\rangle \leftrightarrow |1\rangle$, $|0\rangle \leftrightarrow |2\rangle$) with configuration-dependent rates Γ_1 and Γ_2, (ii) excitation swaps $|12\rangle \leftrightarrow |21\rangle$ with configuration-dependent rates Υ_{12} and (iii) spontaneous decay from $|1\rangle$ or $|2\rangle$ to $|0\rangle$, with (constant) rate κ. Transitions between the ground state and each excited state – type (i) processes – slow down in the vicinity of previously excited atoms. This blockade is analogous to kinetic constraints in glassy systems. Following the rationale behind SMC, type (ii) processes are expected to unblock highly constrained configurations, as illustrated in Fig. 2 (a).

To gain insight into the effect of swaps, we study a chain of N atoms with periodic boundary conditions via CTMC. Atoms $1 \leq k \leq N/2$ start in state $|1\rangle$ and atoms $N/2 < k \leq N$ start in state $|2\rangle$. For the parameters of choice, such an initial configuration is highly arrested: in the absence of swaps, it takes a long time for the system to 'forget' its initial configuration, see Fig. 2 (b). When swaps are included, the relaxation time is drastically reduced, see Fig. 2 (c). Persistence times (defined in Section 2) are reduced by up to 4 orders of magnitude (not shown), and larger reductions could be in principle

achieved at a high computational cost. We also consider the role swaps have in the irreversibility of the dynamics. Dynamics with swaps are further away from equilibrum, as shown by entropy production results. We propose ways to quantify this in experiments [8].

4 Conclusions

We have shed light on the swaps used in simulations of glassy liquids in two different ways: on the one hand, we have shown that their dynamical effects can be naturally understood within dynamic facilitation theory and have illustrated this with a new soft KCM; on the other hand, we have pointed out that swaps, which are artificial in classical systems, are in fact physical in quantum systems, and can be studied in Rydberg gases, where they lead to shortened relaxation times and increased irreversibility.

References

[1] L. Berthier, P. Charbonneau, D. Coslovich, A. Ninarello, M. Ozawa, and S. Yaida. Configurational entropy measurements in extremely supercooled liquids that break the glass ceiling. *Proc. Natl. Acad. Sci. U.S.A*, 114:11356, 2017.

[2] L. Berthier, D. Coslovich, A. Ninarello, and M. Ozawa. Equilibrium sampling of hard spheres up to the jamming density and beyond. *Phys. Rev. Lett.*, 116(23):238002, 2016.

[3] G. Biroli, J.-P. Bouchaud, A. Cavagna, T. S. Grigera, and P. Verrocchio. Thermodynamic signature of growing amorphous order in glass-forming liquids. *Nat. Phys.*, 4(10):771–775, 2008.

[4] A. B. Bortz, M. H. Kalos, and J. L. Lebowitz. A new algorithm for Monte Carlo simulation of ising spin systems. *J. Comput. Phys.*, 17(1):10–18, 1975.

[5] D. Chandler and J. P. Garrahan. Dynamics on the way to forming glass: Bubbles in space-time. *Annu. Rev. Phys. Chem.*, 61:191–217, 2010.

[6] T. S. Grigera and G. Parisi. Fast Monte Carlo algorithm for supercooled soft spheres. *Phys. Rev. E*, 63(4):045102, 2001.

[7] R. Gutierrez, J. P. Garrahan, and R. L. Jack. Accelerated relaxation and suppressed dynamic heterogeneity in a kinetically constrained (East) model with swaps. *arXiv:1901.07797*, 2019.

[8] R. Gutiérrez, J. P. Garrahan, and I.. Lesanovsky. Physical swap dynamics, shortcuts to relaxation, and entropy production in dissipative Rydberg gases. *Phys. Rev. E*, 100(1):012110, 2019.

[9] R. Gutiérrez, S. Karmakar, Y. G. Pollack, and I. Procaccia. The static lengthscale characterizing the glass transition at lower temperatures. *EPL (Europhysics Letters)*, 111(5):56009, 2015.

[10] A. Ninarello, L. Berthier, and D. Coslovich. Models and algorithms for the next generation of glass transition studies. *Phys. Rev. X*, 7(2):021039, 2017.

[11] C. Pérez-Espigares, I. Lesanovsky, J. P. Garrahan, and R. Gutiérrez. Glassy dynamics due to a trajectory phase transition in dissipative Rydberg gases. *Phys. Rev. A*, 98(2):021804, 2018.

[12] F. Ritort and P. Sollich. Glassy dynamics of kinetically constrained models. *Adv. Phys.*, 52(4):219–342, 2003.

Mesoporous organosilica, gas sorption investigation by atomistic simulations

Antonio De Nicola[1,2*], Gianmarco Munaò[2], Antonio Pizzirusso[2], Greta Donati[2], Stefano Caputo[2] and Jose Manuel Vicent Luna[3]

[1]*Department of Organic Material Science, Yamagata University, Yonezawa 992-8510, Japan*
[2]*Dipartimento di Chimica e Biologia "A. Zambelli", Università di Salerno, Fisciano 84084, Italy*
[3]*Department of Physical, Chemical and Natural Systems, Universidad Pablo de Olavide, Ctra. Utrera Km. Seville ES-41013, Spain*

ABSTRACT. We report a computational investigation, by using Molecular Dynamics (MD) and Monte Carlo (MC) techniques, of gas sorption in a mesoporous organosilica material (PMO). In particular, we developed an atomistic model of PMO periodic structure which show good agreement with experimental evidences about periodicity of inorganic/organic layer and nanochannels. We used CRESCO HPC clusters for the execution of our tests.

1 Introduction

The Periodic mesoporous organosilica (PMOs) materials are a very interesting material due to its unique features such as high surface area, hydrophobicity, ordered organic/inorganic layer structure. Inagaki[1,2] and Asefa[3] reported synthesis of bridge-bonded species (RO)3Si-R-Si(OR)3 in 1999. Nowadays, PMOs materials are produced by sol-gel process. [4] Using hydrolytic and polycondensation reactions of (RO)3Si-R-Si(OR)3 precursor. A variety of key features such as hydrophobicity or accessible free volume can be controlled through chemical modification of R groups. [5–11] Periodic crystalline PMOs exhibit mesoscale periodicity together with the presence of regular nanochannels. [2] Due to the high surface area [2,3] PMOs materials can be used in several application areas such as: gas adsorption, [12–14], gas storage, [4,15–18] and confined polymerization,[19] molecular rotors, [15, 19–22] catalysis, [8] water adsorption and desalination[23–25]. In particular, the presence of organic/inorganic layers at nanochannel interface make interactions of PMOs with guest molecules suitable for selective adsorption/desorption properties. As an example, PMOs have been used for the selective adsorption of VOCs (benzene, toluene and hexane). [9] The adsorption of gases like as: sulfur dioxide, ammonia, octane and cyanogen chloride were studied with ethane-bridged PMO, [14] while hydrogen (using biphenylene-bridged PMO) [10] and water adsorption (using phenylene-bridge PMO) [23] were investigated too. The aim of the project is to study, by combining MD and Monte Carlo (MC) simulations, gas adsorption in the realistic PMO material including nanochannel at atomic level.

2 PMO Model

The bonding and non-bonding interaction parameters of the PMO atomistic model and guest molecules are based on OPLS-AA force field [26]. For PMO model, the torsional energy barrier involving O-Si-C-C was optimized by DFT calculation, as reported in a previous paper [27]. The energetic terms of both bond stretching and angle bending are represented as:

$$E_{bond} = \sum_{bond} K_B \left(r - r_{eq} \right)^2 \tag{1}$$

$$E_{angle} = \sum_{angles} K_\theta \left(\theta - \theta_{eq} \right)^2 \tag{2}$$

Where K_{bond} is bond harmonic constant and r_{eq} is the equilibrium distance between two connected atoms. Instead, K_θ is the harmonic angle bending constant while θ is equilibrium angle between three consecutive connected atoms. The torsional intramolecular energy is evaluated by summing the first three terms of Fourier series as:

$$E(\phi) = \frac{V_1}{2}[1 + \cos(\phi + f1)] + \frac{V_2}{2}[1 + \cos(2\phi + f2)] + \frac{V_3}{2}[1 + \cos(3\phi + f3)] \tag{3}$$

Where ϕ is the dihedral angle between for consecutive connected atoms while the Fourier coefficients are V_1, V_2, V_3, while $f1$, $f2$ and $f3$ represents the phase angles. The non-bonded interactions represented by the sum of Coulomb and Lennard-Jones terms. The functional form for two generic molecules A and B is reported in the eq. 4:

$$E_{AB} = \sum_i^A \sum_j^B \left[\frac{q_i q_j e^2}{r_{ij}} + 4\epsilon_{ij} \left(\frac{\sigma_{ij}^{12}}{r_{ij}^{12}} - \frac{\sigma_{ij}^6}{r_{ij}^6} \right) \right] f_{ij} \tag{4}$$

Where f_{ij} is equal to 0.5 for i,j =1,4, and equal to 1 for i,j greater than 4.

3 Results

Due to the presence nanochannels and high surface area, the gas adsorption capability (such as carbon dioxide, methane, benzene, nitrogen) has been experimentally proved to be relevant for PMO materials. In particular, PMO has high capability to adsorb carbon dioxide molecules up to 88% by weight at 195 K. Due to this peculiar capability of PMO materials, we performed MD simulation to relax the entire crystalline structure, and then we used such structure to calculate isothermal adsorption of CO_2 by using MC technique. In particular, we computed the loading curve for methane and carbon dioxide (points in the right panel of Figure 1) and compared with experimental behavior. As can be seen from the figure, our model is able to reproduce qualitatively and quantitatively the experimental data. Based on these results, we are confident our model can be successful used to study such kind of gas sorption in PMO material.
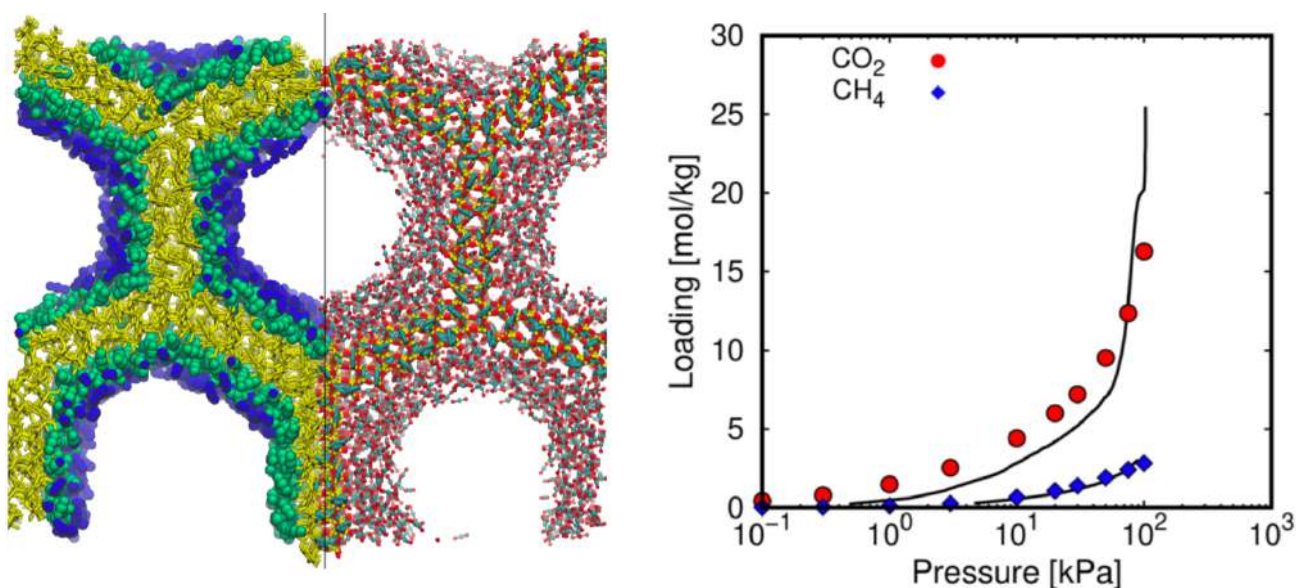
Figure 1. (Left panel) Snapshot of PMO configuration at 22.5%w/w of CO_2. the snapshot shows PMO structure in yellow and two different CO_2 molecule types, in green belonging the first shell and in blue belonging to second shell type. Hydrogen atoms have been not included for clarity. (Right panel) Loading curve calculated for CH_4 and CO_2 molecules at 195 K. Black lines represents experimental behavior.

References

[1]   S. Inagaki, S. Guan, Y. Fukushima, T. Ohsuna, O. Terasaki, Novel mesoporous materials with a uniform distribution of organic groups and inorganic oxide in their frameworks, J. Am. Chem. Soc. 121 (1999) 9611–9614. doi:10.1021/ja9916658.

[2]   S. Inagaki, S. Guan, T. Ohsuna, O. Terasaki, An ordered mesoporous organosilica hybrid material with a crystal-like wall structure, Nature. 416 (2002) 304–307. doi:10.1038/416304a.

[3]   T. Asefa, M.J. MacLachlan, N. Coombs, G.A. Ozin, Periodic mesoporous organosilicas with organic groups inside the channel walls, Nature. 402 (1999) 867–871. doi:10.1038/47229.

[4]   W.J. Hunks, G.A. Ozin, Periodic mesoporous organosilicas with phenylene bridging groups, 1,4-(CH2)nC6H4 (n = 0-2), Chem. Mater. 16 (2004) 5465–5472. doi:10.1021/cm048986p.

[5]   Y. Xia, R. Mokaya, High surface area ethylene-bridged mesoporous and supermicroporous organosilica spheres, Microporous Mesoporous Mater. (2005). doi:10.1016/j.micromeso.2005.06.040.

[6]   J. Croissant, X. Cattoën, M.W.C. Man, A. Gallud, L. Raehm, P. Trens, M. Maynadier, J.O. Durand, Biodegradable ethylene-bis(propyl)disulfide-based periodic mesoporous organosilica nanorods and nanospheres for efficient in-vitro drug delivery, Adv. Mater. (2014). doi:10.1002/adma.201401931.

[7]   F. Tang, L. Li, D. Chen, Mesoporous silica nanoparticles: Synthesis, biocompatibility and drug delivery, Adv. Mater. 24 (2012) 1504–1534. doi:10.1002/adma.201104763.

[8]   F. Hoffmann, M. Cornelius, J. Morell, M. Fröba, Silica-based mesoporous organic-inorganic hybrid materials, Angew. Chemie - Int. Ed. (2006). doi:10.1002/anie.200503075.

[9]   B.J. Johnson, N.E. Anderson, P.T. Charles, A.P. Malanoski, B.J. Melde, M. Nasir, J.R. Deschamps, Porphyrin-embedded silicate materials for detection of hydrocarbon solvents, Sensors. 11 (2011) 886–904. doi:10.3390/s110100886.

[10]   M. Kubo, K. Ishiyama, A. Shimojima, T. Okubo, Effect of organic groups on hydrogen adsorption properties of periodic mesoporous organosilicas, Microporous Mesoporous Mater. 147 (2012) 194–199. doi:https://doi.org/10.1016/j.micromeso.2011.06.014.

[11]   W. Wang, J.E. Lofgreen, G.A. Ozin, Why PMO? Towards functionality and utility of periodic mesoporous organosilicas, Small. (2010). doi:10.1002/smll.201000617.

[12]   M.A.O. Lourenço, J.R.B. Gomes, P. Ferreira, Gas-Organic and Gas-Inorganic Interfacial Effects in Gas/Adsorbent Interactions: The Case of CO 2 /CH 4 Separation , Hybrid Org. Interfaces. (2017) 413–458.

doi:10.1002/9783527807130.ch9.

[13]   M.A.O. Lourenço, R.M. Silva, R.F. Silva, N. Pinna, S. Pronier, J. Pires, J.R.B. Gomes, M.L. Pinto, P. Ferreira, Turning periodic mesoporous organosilicas selective to CO2/CH4 separation: Deposition of aluminium oxide by atomic layer deposition, J. Mater. Chem. A. (2015). doi:10.1039/c5ta05964j.

[14]   M.E. Boot-Handford, J.C. Abanades, E.J. Anthony, M.J. Blunt, S. Brandani, N. Mac Dowell, J.R. Fernández, M.-C. Ferrari, R. Gross, J.P. Hallett, R.S. Haszeldine, P. Heptonstall, A. Lyngfelt, Z. Makuch, E. Mangano, R.T.J. Porter, M. Pourkashanian, G.T. Rochelle, N. Shah, J.G. Yao, P.S. Fennell, Carbon capture and storage update, Energy Environ. Sci. 7 (2014) 130–189. doi:10.1039/C3EE42350F.

[15]   A. Comotti, S. Bracco, P. Valsesia, L. Ferretti, P. Sozzani, 2D multinuclear NMR, hyperpolarized xenon and gas storage in organosilica nanochannels with crystalline order in the walls, J. Am. Chem. Soc. 129 (2007) 8566–8576. doi:10.1021/ja071348y.

[16]   U. Martinez, G. Pacchioni, Interaction of CO, CO2 and CH4 with mesoporous organosilica: Periodic DFT calculations with dispersion corrections, Microporous Mesoporous Mater. 129 (2010) 62–67. doi:10.1016/j.micromeso.2009.08.033.

[17]   M.A.O. Lourenço, P. Ferreira, C. Siquet, J. Santos, M. Jorge, J.R.B. Gomes, Insights into CO2 and CH4 Adsorption by Pristine and Aromatic Amine-Modified Periodic Mesoporous Phenylene-Silicas, J. Phys. Chem. C. 120 (2016) 14236–14245. doi:10.1021/acs.jpcc.6b04605.

[18]   Y. Wei, X. Li, R. Zhang, Y. Liu, W. Wang, Y. Ling, A.M. El-Toni, D. Zhao, Periodic Mesoporous Organosilica Nanocubes with Ultrahigh Surface Areas for Efficient CO2Adsorption, Sci. Rep. 6 (2016) 1–11. doi:10.1038/srep20769.

[19]   A. Comotti, S. Bracco, M. Beretta, J. Perego, M. Gemmi, P. Sozzani, Confined Polymerization in Highly Ordered Mesoporous Organosilicas, Chem. – A Eur. J. 21 (2015) 18209–18217. doi:10.1002/chem.201503553.

[20]   A. Comotti, S. Bracco, P. Valsesia, M. Beretta, P. Sozzani, Fast molecular rotor dynamics modulated by guest inclusion in a highly organized nanoporous organosilica, Angew. Chemie - Int. Ed. 49 (2010) 1760–1764. doi:10.1002/anie.200906255.

[21]   S. Bracco, A. Comotti, P. Valsesia, B.F. Chmelka, P. Sozzani, Molecular rotors in hierarchically ordered mesoporous organosilica frameworks, Chem. Commun. (2008). doi:10.1039/b809559k.

[22]   S. Bracco, M. Beretta, A. Cattaneo, A. Comotti, A. Falqui, K. Zhao, C. Rogers, P. Sozzani, Dipolar rotors orderly aligned in mesoporous fluorinated organosilica architectures, Angew. Chemie - Int. Ed. (2015). doi:10.1002/anie.201412412.

[23]   B.J. Mietner, M. Fröba, R. Valiullin, Water Transport in Periodic Mesoporous Organosilica Materials, J. Phys. Chem. C. 122 (2018) 12673–12680. doi:10.1021/acs.jpcc.8b00046.

[24]   Y.T. Chua, G. Ji, G. Birkett, C.X.C. Lin, F. Kleitz, S. Smart, Nanoporous organosilica membrane for water desalination: Theoretical study on the water transport, J. Memb. Sci. (2015). doi:10.1016/j.memsci.2015.01.060.

[25]   Y.T. Chua, C.X.C. Lin, F. Kleitz, X.S. Zhao, S. Smart, Nanoporous organosilica membrane for water desalination, Chem. Commun. 49 (2013) 4534–4536. doi:10.1039/c3cc40434j.

[26]   W.L. Jorgensen, D.S. Maxwell, J. Tirado-Rives, Development and testing of the OPLS all-atom force field on conformational energetics and properties of organic liquids, J. Am. Chem. Soc. 118 (1996) 11225–11236. doi:10.1021/ja9621760.

[27]   A. De Nicola, A. Correa, A. Comotti, P. Sozzani, G. Milano, Atomistic Model of Realistic Crystalline Mesoporous Organosilica Materials Including Nanochannels, J. Phys. Chem. C. 122 (n.d.) 17825–17835. doi:10.1021/acs.jpcc.8b04645.

Modeling electrical and thermal properties of carbon nanotubes enforced composite materials

Y. Zhao[1*], G. Donati[2], A. De Nicola[3] , A. Pizzirusso[2], G. Munao[2], S. Caputo[2] , G. Milano[2,3]

[1] *Dalian Minzu University, Institute of Nano-Photonics, School of Physics and Materials Engineering, 116600, Dalian, China.*

[2] *Salerno University, Department of Chemistry and Biology "Adolfo Zambelli", 84084, Via Giovanni Paolo II, 132, Fisciano (SA), Italy.*

[3] *Department of Organic Materials Science, Yamagata University 4-3-16 Jonan Yonezawa, Yamagata-ken 992 8510, Japan*

ABSTRACT. A huge scientific and technological interest is continuously growing for the so-called *smart materials.* This classification includes composite materials made of a polymer matrix (such as a resin) and a filler whose electrical and thermal properties are of key importance, and carbon nanotubes (CNTs) are among the possible fillers (beside graphite, carbon fibers etc.). When such filler is added to polymer matrices, it makes them conductive once they overcome a specific (so-called percolative) concentration. When this percolative threshold is reached, a CNT electric circuit is formed and the composite materials become conductors. We simulate the self-assembly processes of carbon nanotubes dispersed in different polymer phases using a hybrid particle-field molecular dynamics technique (MD-SCF). This efficient computational approach allows to simulate large- scale systems (up to ∼1 500 000 particles) of flexible rod-like particles in different matrices on the millisecond time scale. It is indeed very important to catch the impact of different morphologies on the electrical properties and how these affect the performances of the system. The equilibrium morphologies are in good agreement with those proposed by several experimental studies that hypothesized a two level "multiscale" organization of CNT assemblies. Once these materials become conductive, these are characterized by specific features such as the Joule heating, that is important for their employment in self-deicing or self-curing, i.e the material is able to detect and react to its own condition, and for these reasons they are called *smart.* We are currently working on modeling Joule effect on the nanoscale, simulating the heat generation due to the conductive filler and the diffusion of the produced heat. Our studies are focused on the understanding of the effect of the applied voltage, the morphology and the filler concentration, with the final aim to help understanding which are the limits of these materials and how to improve their performances.

1 Introduction

Theoretical-computational modeling represents nowadays an established crucial approach to help in understanding experimental results, giving the molecular picture necessary to interpret the phenomena under study in chemical field. Moreover, in-silico experiments are very important to make previsions on processes under study thanks to the capability to model a system and/or a process before actually perform it in practice. Limits of materials performances can be detected and strategies to improve them can be defined.
This approach becomes extremely crucial for the study of composite materials, to investigate electrical and thermal properties that can be employed in many different technological and industrial fields

from automotive to aeronautics to civil engineering. In particular, carbon nanotube/polymer nanocomposites have received attention from the scientific and technological point of view since CNTs were first observed by Iijima[1] in 1991. Once the CNT concentration overcomes a specific threshold (*percolation threshold*), a continuous conductive network of CNTs is formed and the material becomes conductive. This critical concentration depends on several aspects, among which the nature of the filler itself, the CNTs length, the aspect ratio, the polymer nature, the alignment of the CNTs, the composite processing methods. These are all crucial elements whose control and understanding is important to define which are the best working conditions, and in this context the computational modeling is very important, since a systematic study can be performed and each of the aspects can be investigated in detail.

In this project an efficient Molecular Dynamics (MD) simulation scheme, based on hybrid particle-field representation called Molecular Dynamics-Self Consistent Field (MD-SCF)[2] is employed. We investigate the percolation threshold and electrical conductivity of nanocomposites in homopolymer matrices using parallel hybrid particle-field MD-SCF simulations[3]. Self-assembly processes of flexible rod-like particles (mimicking CNTs) dispersed in polymer phases have been examined at different concentrations near percolation. The obtained CNT morphologies have then been used to calculate the conductivity behavior using a resistor network approach.[4]

From the electrical properties knowledge, we can move further and investigate the Joule heating pow of such systems, i.e. the heat generation and diffusion due to the electrical current flow. The Joule effect produced by these systems can be employed for self-deicing applications such as for on-the-fly de-icing of air planes wings, for automotive industry or civil engineering. The optimization of the Joule heating power performances is very important since it has to be a compromise between the optimal working conditions and the limits imposed by the practical applications such as maximum applicable voltage or maximum amount of CNTs in the polymer matrix without altering the mechanical properties.

We performed several MD simulations to investigate the importance of assembled vs. random CNT conformations, showing that an optimized morphology can increase the Joule heat produced.

All the calculations are performed by using the CRESCO HPC resources because of the high computer performances, allowing us to run massive calculations in short amounts of time. Moreover, the capability to perform calculations in parallel, thanks to the CRESCO parallel architecture, has even more improved our calculation efficiency.

2 Methods and Results

The simulation of CNTs enforced polymer matrices at the nanoscale is computationally expensive for both the sizescale (> 100 nm) and the timescale necessary to simulate the assembly process of the CNTs. For this reason we employed the hybrid MD-SCF approach, based on the evaluation of the non-bonded force and its potential between atoms of different molecules by the evaluation of an external potential dependent on the local density at position **r.** According to the SCF theory, a many-body problem such as molecular motion can be reduced to a problem of deriving the partition function of a single molecule with an external potential V(**r**). Then, the nonbonded force between atoms of different molecules can be obtained from a suitable expression of V(**r**) and its derivatives. In the framework of SCF theory, a molecule is regarded to be interacting with the surrounding molecules through a mean field, rather than direct interactions among the molecules. Assuming that the density dependent interaction potential **W**, where each species is specified by the index K, takes the following form:

$$W[\{\phi_K(\mathbf{r})\}] = \int d\mathbf{r} \left(\frac{k_B T}{2} \sum_{KK'} \chi_{KK'} \phi_K(\mathbf{r}) \phi_{K'}(\mathbf{r}) + \frac{1}{2\kappa} \left(\sum_K \phi_K(\mathbf{r}) - \phi_0 \right) \right)$$

where $\varphi_K(\mathbf{r})$ is the coarse-grained density of species K at position r and $\chi_{KK'}$ are the mean field parameters for the interaction of a particle of type K with the density fields due to particles of type K′, it can be shown using the so-called saddle point approximation that the external potential is given by:

$$V_K(\mathbf{r}) = \frac{\delta W[(\phi_K(\mathbf{r}))]}{\delta \phi_K(\mathbf{r})} = k_B T \sum_{K'} \chi_{KK'} \phi_{K'}(\mathbf{r}) + \frac{1}{\kappa}\left(\sum_K \phi_K(\mathbf{r}) - \phi_0\right)$$

All simulations (MD-SCF) reported in the present work have been performed using the parallelized version of the OCCAM MD code. [5] The system is composed by an insulator part (polymer matrix) and conductive part (CNTs).
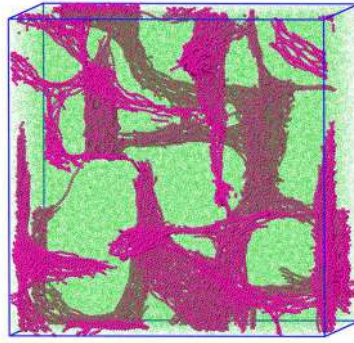

Figure 1 – schematic picture of a configuration of assembled CNTs (purple) in a polymer matrix (green).

The calculation of the CNT resistor network conductivity has been performed by explicitly calculating the resistance contributions coming from both the direct contacts among CNTs (intrinsic resistance) and the one coming from the electrons tunneling (contact resistance) among CNTs closer than a threshold distance under which the electron hopping is possible.
When all the contributions are known, the electrical conductivity of the circuit is calculated and the conductivities at different CNT concentrations can be fitted by using the percolation law:

$$\sigma/\sigma_{CNT} = \eta\left(f - f_c\right)^\tau$$

In **Figure 2** we show how the percolation law fits the conductivities at different CNT contents.
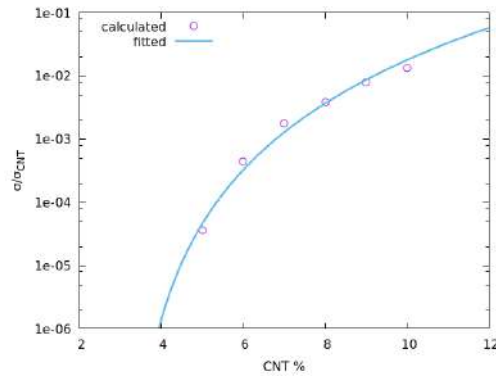
We propose a modeling strategy to simulate the Joule effect and its heat diffusion at the nanoscale for the first time for these systems.[6]

To calculate the Joule heat, we evaluate the local resistance contributions, to take into account the local CNT content and, on the basis of the applied voltage, the Joule heating power can be evaluated:

$$P = I^2 R$$

where R is the local resistance and I is the current intensity. From the heating power, the heat and local temperature, depending on the local regions more or less rich in CNTs, can be calculated and added to the resolution of the heat diffusion equation solved numerically by using the finite difference method approximation:

$$T_{new(i)} = T_{old(i)} + \Delta t D \left(\sum_{\alpha} \frac{T_{i+1}^{\alpha} - 2T_i^{\alpha} + T_{i-1}^{\alpha}}{\Delta r_{\alpha}^2} \right) + T_{Joule}(i)$$

this equation is solved on a grid (in which the explicit system is translated), where the information on the CNT local concentration is kept. In the equation, D is the thermal diffusivity, the subscript is referred to the grid elements, Δ_{ra} is the grid spacing in *a* direction. The temperature due to the local Joule heating power is added in the equation.

We can follow the temporal evolution of the temperature of the system during the time and from it we calculate the heating rate (Celsius/s) to evaluate the performance of the system, the dependence on the applied voltage, concentration and morphology.

In **Figure 3** the heating rate is shown as function of the voltage at different concentrations: the discrepancy due to the CNT content increases with the applied voltage. Moreover, more heat is generated with a larger CNT content.
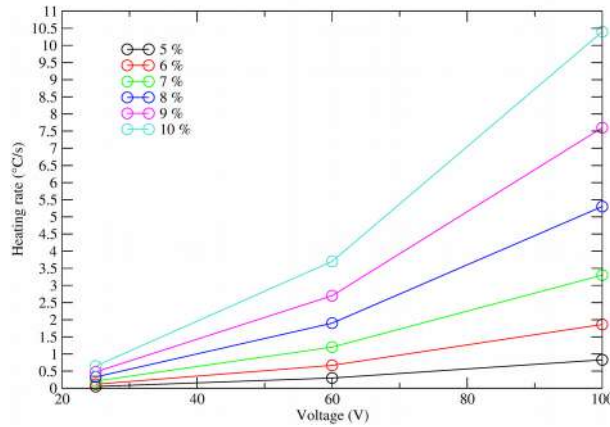
In **Table 1** we show the comparison with experimental results: a good agreement is found, moreover the effect of the morphology is also shown: higher heating rates are found with assembled morphologies compared to randomly dispersed CNTs.

	Random (10 % CNT)	Assembled (5 % CNT)	experimental
67 V	0.071	0.099	0.082
83 V	0.11	0.15	0.13
108 V	0.18	0.26	0.21

References

1 - S. Iijima, Nature, 1991, 354, 56-58.

2 - G. Milano and T. Kawakatsu, J. Chem. Phys., 2009, 130, 214106.

3 - Y. Zhao, M. Byshkin, Y. Cong, T. Kawakatsu, L. Guadagno, A. De Nicola, N. Yu, G. Milano, B. Dong,Nanoscale, 2016, 8, 15538-15552.

4 - M. S. Byshkin and A. A. Turkin, J. Phys. A: Math. Gen., 2005, 38, 5057.

5 - Y. Zhao, A. DeNicola, T. Kawakatsu and G. Milano, J. Comput. Chem., 2012, 33, 868–880.

6 – G. Donati et al. Manuscript in preparation.

DNS of a $CH_4/CO_2/O_2$ Non-Premixed Flame at 300 bar

D. Cecere[1]*, E. Giacomazzi[1], N. Arcidiacono[1] and F.R. Picchia[1]

[1]*Process and Energy Systems Engineering Laboratory, ENEA, Rome, Italy*

ABSTRACT. The next-generation supercritical carbon dioxide (sCO_2) combustors need deeper understanding of flame dynamics and its morphology. The aim of this work is to investigate turbulent non-premixed methane oxy-combustion in an atmosphere rich in CO_2 at supercritical conditions by means of 2D Direct Numerical Simulation. A simple shear-layer configuration typical of slot burners is considered: the fuel is CH_4 and flows through the central slot, the oxidant O_2/CO_2 (90% O_2 by mass) mixture flows on both sides of the slot, and a pilot flame is imposed at the inlet between the two streams of reactants to force ignition. Fully compressible Navier-Stokes equations coupled to the Peng-Robinson cubic equation of state (PR-EoS) for real gases in its improved translated volume formulation (VTPR) are solved with a revised simplified nine species kinetic scheme including radicals. Among the diffusive mechanisms only the Dufour effect is neglected; transport properties are accurately calculated. Numerical results are examined to highlight different physical aspects of the flow: the effect of oxygen stream dilution on the flame anchoring and topology; diffusive mechanisms, to identify the fastest processes through the comparison of characteristic times.

1   Introduction

High-pressure combustion of reactants exhibiting real gas behaviour is becoming an important research topic not only for the growing interest in supercritical CO_2 next generation gas turbine cycles (to efficiently operate and exhibit extremely low polluttant emission to address environmental limitations) [8], but also in other industrial applications, such as organic supercritical CO_2-based Rankine [18], diesel engines with higher and higher pressures, liquid oxygen rocket engines, cooling systems. When sCO_2 is adopted in direct contact with combustion gases, the capture of CO_2 is facilitated and higher thermal efficiency and simpler design can be achivied [35]. Injection pressures are usually above the critical values of common propellants, like oxygen, hydrogen and hydrocarbons; for example, oxy-combustors of s-CO_2 gas turbines are being designed to operate at $300\,\mathrm{bar}$. Furthermore, in some applications, e.g., rocket engines, O_2 may be injected at cryogenic temperatures: these conditions are far away from ideal thermodynamics, and the different fluid behaviour has to be accounted for by means of real gas equations of state and specific models for molecular transport properties. Experimental work at such high-pressure conditions may be prohibitive: the use of advanced laser diagnostics is not an easy task to achieve, and very few examples exist in literature; besides, facilities themselves may be very expensive. Hence, most of research and design in this area is based on numerical simulation. However, also

---

*Corresponding author. E-mail: `donato.cecere@enea.it`.

the numerical approach is not an easy task, suffering problems of both modelling accuracy (e.g., the ability to capture huge variations of fluid properties when crossing the pseudo-boiling line) and computational efficiency (too complex and accurate equations of state cannot be used in time-consuming simulations, like LES and DNS). Furthermore, numerical schemes are stressed hardly: the high-density gradients typical of some applications (as those involving liquid injection) and the multi-species transport enhance wiggle formation in fully compressible solvers. This work is devoted to numerical simulation of methane oxy-combustion in supercritical carbon dioxide at 300 bar. Although adopting a simple chemical scheme and a two-dimensional computational domain, some interesting observations are highlighted, and needs for future work identified.

2 The Numerical Experiment and Its Set-Up

The numerical experiment here simulated has a nominal pressure around 300 bar and consists in a simple shear-layer configuration that can be encountered in slot burners; the flow is confined by means of two no-slip adiabatic walls (at left and right of the domain). At the bottom of the computational domain there is the inlet, while the outlet is located at the top. In this work, simulations are perfomed in a two-dimensional framework to reduce computational time. The domain y × z is 8×10 mm and is discretised by means of 4000×5000 nodes. The computational nodes are not uniformly distributed along the streamwise direction z, with a minimum $\Delta z \sim 5. \cdot 10^{-7}$ m, and stretched from the center towards the sides along the transversal direction y, with $\Delta y_{min} \sim 3. \cdot 10^{-7}$ m and $\Delta y_{max} \sim 5.74 \cdot 10^{-5}$ m; the aspect ratio $\Delta z/\Delta y$ is in the range $[0.25, 1.7]$. The fuel is CH_4 and is injected centrally at 50 m/s and 388 K; its width is $4 \cdot 10^{-4}$ m. The oxidant O_2/CO_2 mixture flows on both sides of the methane, and a pilot flame is imposed at the inlet between the two streams of reactants to force ignition. Each oxidant jet flows at 100 m/s and 450 K; their width is $1.95 \cdot 10^{-4}$ m. The pilot flames imposed at the inlet exhibit a temperature distribution ranging from 900 to 2049 K and a coherent distribution of chemical species; such data come from separate calculations previously performed; these hot gases flow at 5 m/s and are 10^{-4} m widen. Adjacent to each of the oxidant streams, there is a coflowing stream of CO_2 at 50 m/s and 973 K. The (isotropic) turbulence characteristics of the jets are specified in terms of velocity fluctuations and auto-correlation length-scales: $u' = 5$ m/s and $l_y = 3 \cdot 10^{-5}$ m for the methane jet; $u' = 1$ m/s and $l_y = 5 \cdot 10^{-5}$ m for the pilot flames; $u' = 10$ m/s and $l_y = 5 \cdot 10^{-5}$ m for the oxidant jets; $u' = 5$ m/s and l_y ranging from 2 to $6 \cdot 10^{-5}$ m for the CO_2 coflowing streams. The methane jet Reynolds number (based on its bulk velocity and diameter) is nearly 142500 while its turbulent counterpart (based on the imposed velocity fluctuation and length-scale) is around 1070. The oxidant jet Reynolds number is nearly 141500, while its turbulent counterpart is around 3600; inceasing dilution with CO_2 results in higher values. The smallest dissipative scale expected comes from the Re_{Ox}^t and is nearly $3 \cdot 10^{-7}$ m. It is observed that the present simulations are aimed at better understanding the physics of methane oxy-combustion in a s-CO_2 environment: no particular strategies are adopted to enhance injection of reactants from the point of view of mixing. With the simple shear-layer configuration chosen, a 30% O_2 case with a small pilot flame, results in no ignition of the mixture apart from some small flame pockets released downstream from the forced anchoring regions, rapidly quenched by the high aerodynamic stretching. These results higlight that future studies should be focused on injection strategies to ensure efficient combustion with diluted oxygen streams, at least 30% by volume as imposed primarily by safety reasons in power plants. Hence, since stable and efficient combustion has been achieved only in the 90% O_2 by mass case (corresponding to nearly 92% by volume), in the following the attention will be focused on the analysis of this case.

3 Physical and Numerical Models Adopted

3.1 Termodynamic relations

In this work the compressible Navier-Stokes equations are solved for a reacting real gas flow at supercritical conditions for which the Peng-Robinson cubic equation of state in its improved volume translated formulation is assumed:

$$p = \frac{R_u T}{v - b_m + c} - \frac{a_m}{(v + c)(v + c + b_m) + b_m(v + c - b_m)} \, , \tag{1}$$

where R is the gas constant, ν the specific volume, and the $a_m (\mathrm{J\,m^3\,mol^{-2}})$ and $b_m (\mathrm{m^3\,mol^{-1}})$ coefficients are function of composition and temperature, accounting for intermolecular forces, and c is the translation parameter and effectively shifts or translates each v term in the EOS. For a N_s species mixture the coefficients a_m and b_m are calculated as [16, 25]:

$$a_m = \sum_{i=1}^{N_s} \sum_{j=1}^{N_s} x_i x_j a_{ij} \, , \tag{2}$$

$$b_m = \sum_{i=1}^{N_s} x_i b_{ij} \, , \tag{3}$$

where x_i is the mole fraction of species i. The binary coefficients a_{ij} are estimated as

$$a_{ij} = (1 - k_{ij})(a_i a_j)^{1/2} \, , \tag{4}$$

k_{ij} are binary interaction parameters (to take into account non linear intermolecular effects) tabulated [17] or calculated empirically [26], i.e.:

$$1 - k_{ij} = \left(\frac{2 V_{c_i}^{1/6} V_{c_j}^{1/6}}{V_{c_i}^{1/3} + V_{c_j}^{1/3}} \right)^3 \, , \tag{5}$$

with A_i and B_i given by :

$$b_i = 0.0077796 \frac{R_u T_{ci}}{p_{ci}} \, , \tag{6}$$

$$a_i = 0.457236 \frac{(R_u T_{ci})^2}{p_{ci}} \alpha(T_{ri}) \, , \tag{7}$$

$$\alpha(T_{ri}) = [1 + f(\omega_i)(1 - ((T_{ri})^{1/2}))] \, , \tag{8}$$

$$f(\omega_i) = \begin{cases} 0.374640 + 1.54226\omega_i \\ -0.26992\omega_i^2 & \omega_i \leq 0.49 \\ 0.379642 + 1.48503\omega_i - 0.164423\omega_i^2 \\ +0.016666\omega_i^3 & \omega_i > 0.49 \end{cases} \tag{9}$$

Species	T_c [K]	P_c [bar]	$V_c\ 10^{-5}[m^3/mol]$	ω [-]	Source
CH_4	190.60	46.1000	9.860	0.1100	[2]
CO	134.45	34.9875	9.009	0.0510	[2]
CO_2	304.18	73.8000	9.434	0.2250	[2]
H_2	33.180	13.0000	6.640	-0.2140	[2]
H	182.60	251.900	1.630	0.3290	[22]
H_2O	647.00	220.640	5.586	0.3443	[2]
N_2	126.19	33.9780	8.944	0.0390	[2]
O	100.70	57.6000	3.930	0.3290	[22] as OH
O_2	154.58	50.4300	7.353	0.0222	[2]
OH	100.70	57.6000	3.930	0.3290	[21]

Table 1: Species critical properties of $CH_4/O2$ combustion, with T_c p_c, ν_c and ω are, respectevely, the critical temperature, critical pressure, critical molar volume and acentric factor of the chemical species.

p_{ci}, T_{ci}, $T_{ri} = T/T_{ci}$ being the species i critical pressure, critical and reduced temperature.

Critical data for some tipical species are reported in table 1. The PR-EoS requires only the acentric factor ω_i on top of the critical properties and is thus easy to implement for a wide range of species. It provides slightly better accuracy than the Redlich-Kwong EoS because of a more complex temperature dependence. As a consequence, energies and specific heats predictions are more accurate, an important feature for reacting flows. The mathematical models adopted are derived for a fluid of N_s chemical species. The constitutive laws assumed to describe the behaviour of the fluid are here reported. They simply model the microscopic molecular diffusion of momentum, energy and mass, i.e., they model the momentum flux S, the heat flux Q and the species mass flux J_i. A Newtonian fluid is considered and the Stokes' assumption is made: it is characterized by the following constitutive relation between the stress, S, and the strain rate, E,

$$S = -(p + 2/3\,\mu\nabla \cdot u)\,I + 2\mu E = -pI + \mathcal{T}\,, \tag{10}$$

μ being the viscosity; $\mathcal{T}$ is the viscous part of the stress tensor.

The mass diffusion flux has three contributions [6]. The first one is due to concentration gradients (here modelled through the Hirschfelder and Curtiss' law for multi-component mixtures) [15], the second due to pressure gradients (the baro-diffusion mechanism), and the third one due to temperature gradients (the thermo-diffusion or Soret effect) [27]:

$$
\begin{aligned}
J_i &= \rho Y_i V_i = J_i^{HC} + J_i^{BD} + J_i^{S} \\
&= -\rho Y_i D_i \left[\frac{\nabla X_i}{X_i} + \frac{X_i - Y_i}{X_i}\frac{\nabla p}{p} \right] - \mathcal{D}_i^T \frac{\nabla T}{T}.
\end{aligned}
\tag{11}
$$

The diffusion coefficient D_i is an *effective* diffusion coefficient of the i-th species into the mixture (mixture-average assumption). The thermo-diffusion, or Soret effect, is the mass diffusion due to temperature gradients, driving light species towards hot regions of the flow [32]. This effect, often neglected, is nevertheless known to be important, in particular for hydrogen combustion, and in general when very light species play an important role [5].

Keeping apart the radiative heat transfer of energy, the heat flux has three contributions too. The first due to temperature gradients (the Fourier diffusion), the second due to mass diffusion fluxes, and the

third one is the Dufour effect (reciprocal of the Soret effect):

$$\boldsymbol{Q} = \boldsymbol{q}_F + \boldsymbol{q}_{V_i} + \boldsymbol{q}_D = -K\nabla T + \rho \sum_{i=1}^{N_s} h_{s_i} Y_i \boldsymbol{V_i} + \boldsymbol{q}_D. \tag{12}$$

Note that this is the heat flux expression entering into the energy transport equation where formation energies are isolated in a source term, i.e., not included in the energy definition. Usually the Dufour effect (the third term) is negligible even when thermo-diffusion is not [27, p. 768] and hence it is neglected in the present work. Molecular transport properties for individual species are accurately modelled through NIST models [2] for viscosity and thermal conductivity. The diffusion coefficient D_i of the i-th species into the rest of mixture is modelled according to the Hirschfelder and Curtiss expression [15], where the required binary diffusion coefficient is calculated by means of kinetic theory. The thermo-diffusion coefficient $\mathcal{D}_i^T$ is estimated by means of the EGLIB routines [1].

At temperature higher than $2500\,\mathrm{K}$, not only $CO - CO_2$ equilibrium is in favor of CO and $H_2 - H_2O$ equilibrium foreses a significant amount of H_2, but also the radical pool has significant impact in limiting the heat release. Simplified mechanisms do not always account for the dissociation reactions [4] and none of them include radicals [11]. Therefore it is necessary to adopt mechanisms available in literature specifically conceived for their application in numerical simulation of oxy-fuel combustion. For the present study, a finite-rate methane-oxygen kinetics is employed using 9 species $(O_2, CH_4, CO_2, H_2O, CO, H_2, O, H, OH)$ and 6 step mechanism developed for oxy-combustion in [9]. To account for the inherently smaller and wider range of scales efficiently (and feasibly), the transport equations are solved in the framework of a quasi-2d Direct Numerical Simulation.

3.2 Numerical Schemes and Boundary Conditions

The numerical simulations are performed by means of the in-house parallel code HeaRT and ENEA's supercomputing facility CRESCO [7]. The HeaRT code solves the compressible Navier-Stokes equations discretised through staggered finite-difference schemes. A second-order accurate centered scheme is adopted for diffusive fluxes; Convective terms are discretized through an $AUSM^+\text{-}up$ method [19] coupled with a third/fifth-order accurate $WENO$ interpolation to reduce spurious oscillations (strongly experienced using centered schemes in high-pressure tests); a density/pressure based sensor is adopted in this study to switch between the two schemes and apply $WENO$ schemes in regions of strong gradients. The low-storage third-order accurate Runge-Kutta method of Shu-Osher is used for time integration. The total energy is defined as sum of internal (thermal) and kinetic energy only. Non-reflecting boundary conditions [28, 30, 31] are implemented at open boundaries in their extended form to take into account the effect of variable transport properties [3], local heat release [14] and real gas effects [24]. It is observed that in previous and present real gas simulations the authors had to impose a higher value of the relaxation constant in the partially non-reflecting treatment of the outlet with respect to the ideal gas theoretical value (1.5 against 0.27) [28, 33] to avoid unphysical pressure drift in the whole computational domain. A synthetic turbulence generator is adopted at flow inlets [20].

4 Results and discussion

The 2D-DNS results are presented in terms of a general flow field overview; a flame structure analysis based on the flame index, statistics of the curvature mixture fraction isosurfaces and transport properties; characterization of the diffusion time scales and effective Lewis and Prandtl numbers.
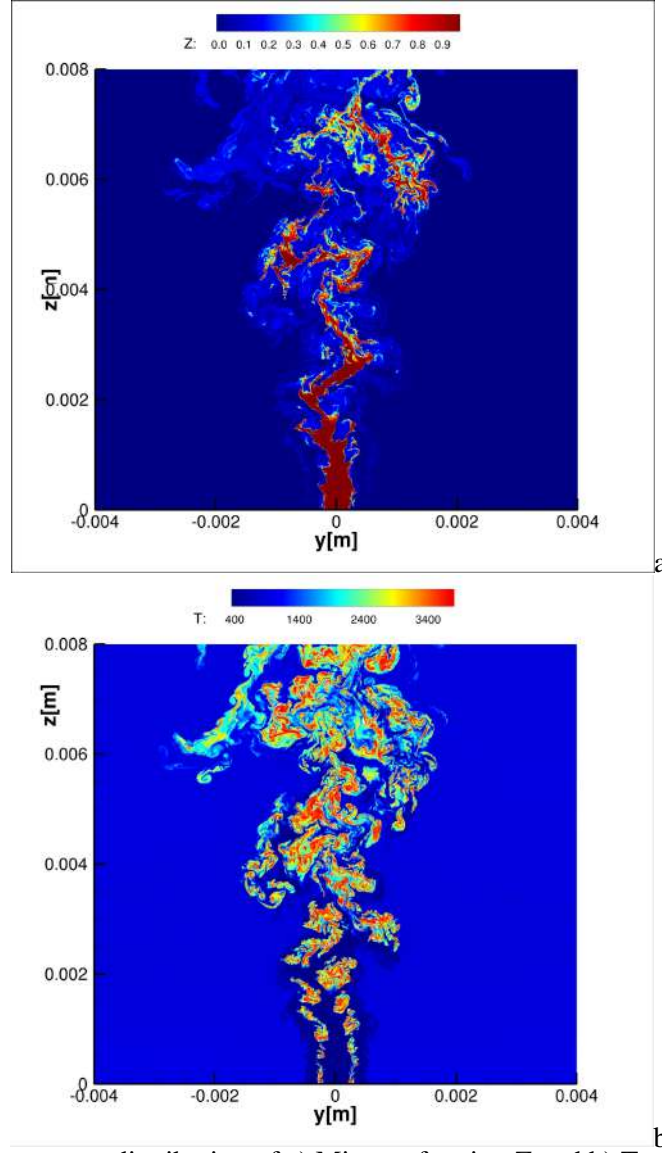
Figure 1: Instantaneous distribution of a) Mixture fraction Z and b) Temperature T [K].

4.1 Flame structure analysis

Fig.1a shows instantaneous profile of mixture fraction Z. The mixture fraction is generally adopted, together with a progress of reaction variable, to describe the local thermochemical state of a diffusion flame. These CH_4/O_2 flame is diluted with CO_2. The dilution process has a direct effect on the flame structure.

The dilution parameter α is defined as the mass ratio between fresh reactants and diluents: $\alpha = 0$ in absence of diluent and $\alpha = 1$ when diluents saturate the mixture:

$$\alpha = \frac{Y_k^F - Y_k^{F,0}}{Y_k^{Dil} - Y_k^{F,0}} = \frac{Y_k^{Ox} - Y_k^{Ox,0}}{Y_k^{Dil} - Y_k^{Ox,0}}. \tag{13}$$
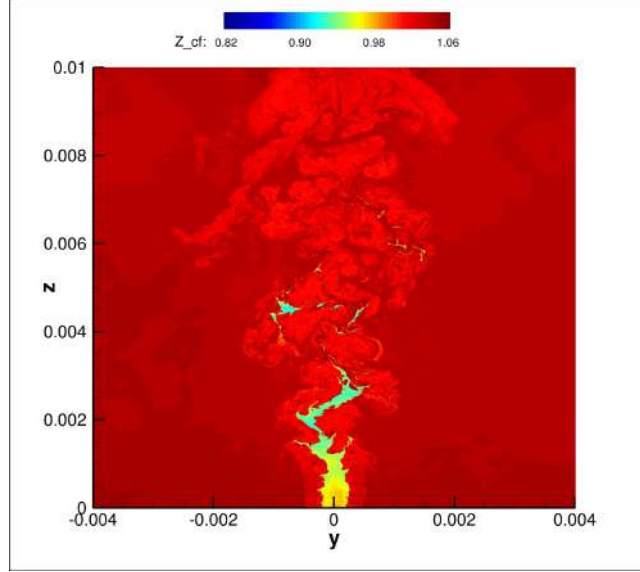
Figure 2: Compressibility Factor.

where Y_k^F and Y_k^{Ox} are the mass fractions of species k in the fuel and oxidizer streams respectively, and the superscript , 0 is the undiluted mixture. Defining Z from a set of element mass fraction Y_e as $(Y_e - Y_e^{Ox}(\alpha))/(Y_e^F(\alpha) - Y_e^{Ox}(\alpha))$ [29], it would be dependent by the local dilution ratio.

If, following Fiorina et al.[13], we define the $\mathcal{Z} = (Y_e - Y^{Ox}(\alpha = 0))/(Y_e^F(\alpha = 0) - Y_e^{Ox}(\alpha = 0))$ this is related to the local mixture fraction by $Z = (\mathcal{Z} - \alpha \mathcal{Z}_G)/(1 - \alpha)$, with $\mathcal{Z}_G$ being the mixture fraction evaluated under global equivalence ratio conditions ($\mathcal{Z}_G = 0.0706$ in our case). In this way the local mixture fraction is related to the classical definition by means of dilution factor $\alpha = Y_{CO_2}/Y_{CO_2}^{Dil}$, where $Y_{CO_2}^{Dil} = 1$ in this case.

Fig.3 shows instantaneous temperature points versus mixture fraction colored with diluent mass fraction Y_{CO_2}. At the nominal stoichiometric line ($Z = 0.184$) the maximum temperature, decreases as the dilution increases. The same trend is observed for the chemical species. If we solve the adiabatic/flamelet real gas equations [23] at different level of dilution (α) and scalar dissipation rate we obtain the results of Fig.4. Temperature, and some species mass fractions are shown versus mixture fraction and parameterized with dilution factor α and scalar dissipation rate χ near equilibrium and at the quenching points.

The temperature peak decreases as flame strain increases, while increasing dilution α also the peak position shifts towards smaller levels of the mixture fraction. The quenching dissipation rate decreases as the dilution factor increases and so the strength of the flame. Increasing the dilution factor decreases the formation of CO as the temperature decreases (see Fig.4b).

Fig.5 shows the results of a real gas laminar counterflow diffusion flame at $\alpha = 0.1$ and strain rate a $= 1 * 10^3$. The maximum temperature is around $3800K$ and the flame thickness is of the order of $\sim 10\mu m$, confirming the correlation of flame thickness with pressure-weighted strain rate $\delta = 1/\sqrt{pa}$, a is the strain rate defined as the maximum absolute velocity gradient in the counterflow field and p the pressure [34]. This demonstrating the necessity of a very small grid and time step to capture, at this pressure, the characteristics of the flame, due to different levels of oxidant and fuel dilution and local strain rate.

As shown in Fig.1a the fuel core ($Z = 1$) penetrates the computational domain maintaining its radial
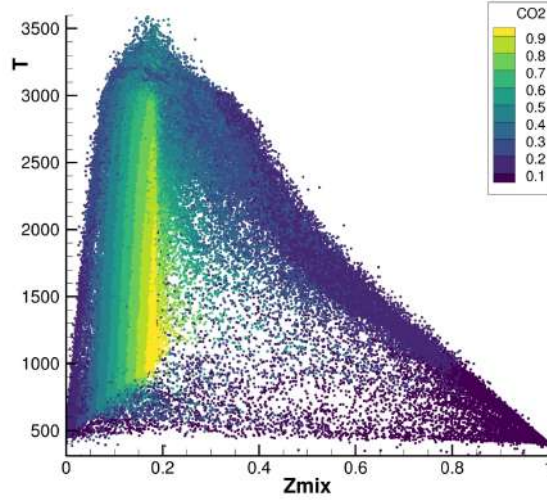
Figure 3: Temperature versus Mixture fraction Z coloured with CO_2 mass fraction.
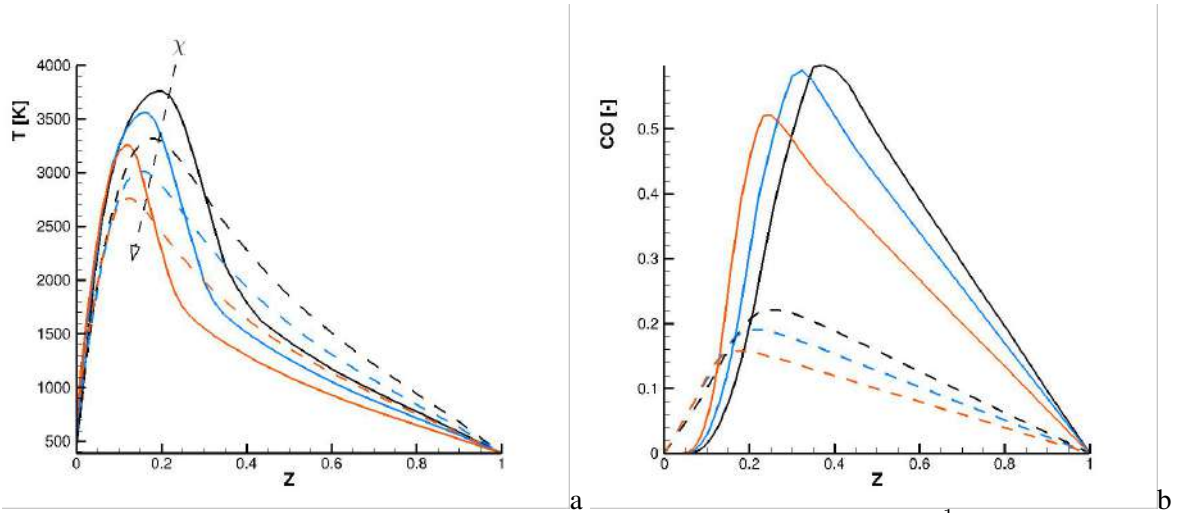

Figure 4: a) Temperature versus Mixture fraction. Black solid line ($\chi = 0.01 s^{-1}$ and $\alpha = 0.1$), Blu solid line ($\chi = 0.01 s^{-1}$ and $\alpha = 0.3$), Orange solid line ($\chi = 0.01 s^{-1}$ and $\alpha = 0.5$), Black dashed line ($\chi = 1.85 * 10^6 s^{-1}$ and $\alpha = 0.1$), Blu dashed line ($\chi = 7. * 10^5 s^{-1}$ and $\alpha = 0.3$), Orange dashed line ($\chi = 1.4 * 10^5 s^{-1}$ and $\alpha = 0.5$); b) CO mass fraction.

dimension for ~ 1mm, then the fresh reactant, close to the inlet, mixes with the oxidant and forms in the shear layer typical finger-like structures associated with the high-density difference between inner and outer stream.

The high velocity gradient of the shear layer promotes the formation of the classical Kelvin-Helmotz instability with vortices that force the internal, fast and light ($\sim 140\,\mathrm{Kg\,m^{-3}}$) gas towards the external, slow and very dense stream ($\sim 250\,\mathrm{Kg\,m^{-3}}$). The extruded structures are elongated by the velocity difference to form the ligaments since the diffusion processes have not time to smear out the momentum and species gradients between the jet core and the surroundings. These very thin structures $\sim 50\,\mu$m, protruding from the inner core, contribute to speed up the external stream and consequently to form new vortices.
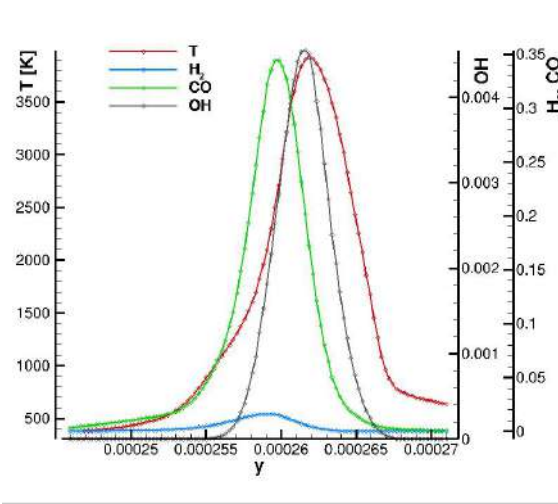
Figure 5: Temperature and species mass fractions of non premixed counterflow flame at $\alpha = 0.1$ and strain rate a $= 1 * 10^3$.

Fig. 1b shows instantaneous temperature profile. The flame is stably anchored and at stoichiometric isolines the temperature reaches very soon a maximum value of 3700K. At the jet exit, the flame structures are rapidly stretched by the velocity gradients until they divide into small pockets successively rotated, convected downstream and corrugated by micro vorticity. The maximum temperature level is also controlled by CO_2 diluent (see the effect on temperature in Fig. 4), in fact the maximum level of temperature are reached at stoichiometric lines but in the center of these flame pockets, where CO_2 dilution effects are not present. Regarding the CO formation inside the flame, we observe that, until turbulence is not able to mix efficiently the coflowing CO_2 with oxygen z < 0.005 m, the CO mass fraction reaches its maximum value ~ 0.5 at the two stoichiometric isolines surrounding the fuel core and the CO_2 reaches maximum value around ~ 0.3. When the central fuel jet core is broken by turbulence, the surrounding CO_2 coflow is able to penetrate the central jets and mixing with oxidizer. In these zones, where $Y_{CO_2} > 0.5$, although T > 2000 K, the maximum value of carbon monoxide mass fraction never exceeds approximately the value of 0.05. This is in agreement with what seen in the study on the effect of dilution parameter α in counter diffusion flames. Displayed in Fig. 6 is the CO mass fraction conditioned on CO_2 mass fraction and different mixture fraction iso-lines. The plotted mass fraction is restricted to values of temperature larger than 1200K and represents averages over all points in A $= L_1 x L_2$ for each of the CO_2 mass fraction values. The effect of CO_2 dilution, at different values of mixture fraction, is to reduce the CO formation. This is more evident in the rich part of the flame ($Z > Z_{st}$).

Fig. 2 shows the compressibility factor (it corrects for deviation from the ideal gas law). Within the flame the compressibility factor varies in a range of $0.8 - 1.2$. The minimum values are reached inside the CH_4 jet core (at lower temperature) while the highest inside the CO_2 coflow and at flame location where high pressure flactuations are present.

4.1.1 Flame index

The Takeno index [10], tipically defined as $G_{FO} = \Delta Y_{CH_4} \cdot \Delta Y_{O_2}$, is used to discriminate the reaction burning mode between diffusion flames ($G_{FO} < 0$) and premixed flames ($G_{FO} > 0$). Its value increases as the supplying rate of fuel and oxidant by molecular diffusion increases. Including in the
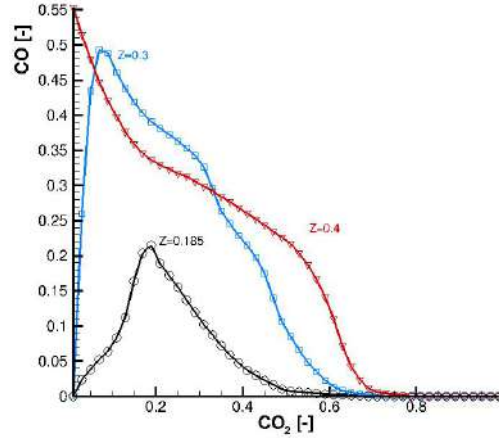
Figure 6: CO species mass fractions as a function of CO_2 conditioned with mixture fraction and temperature.

species transport equation also the Baro-diffusion and Soret effect, the flame index definition is revised [12] as $G_{FO} = \boldsymbol{J}_{CH_4} \cdot \boldsymbol{J}_{O_2}$, with $\boldsymbol{J_i}$ being the complete diffusion flux of species i. The instantaneous distribution of G_{FO} is shown i Fig. 7. The maximum G_{FO} absolute value is reached in the diffusion flame mode. The fresh fuel flows downstream the jet exit and due to high velocities, species and temperature gradients, mixes with oxygen forming an ensemble of instantaneous local premixed and diffusion flames. A comparison between Fig.7 and Fig.1a shows that, near the fuel jet exit, the highest temperatures are reached in the diffusion flames localized towards the fuel jet core. These flames are bordered by thinner reactive premixed regions. Fig.8 shows the distribution of the heat release reaction rate in the diffusion and premixed flames. In this figure, the $\dot{\omega} = \sum_{i=1}^{N_s} h_0 Y_i$ as a function of the normalized $G_{FO,nz} = G_{FO}/\max|G_{FO}|_z$ conditioned on the level of the progress variable in the computational domain A $=$ L$_1$xL$_2$.
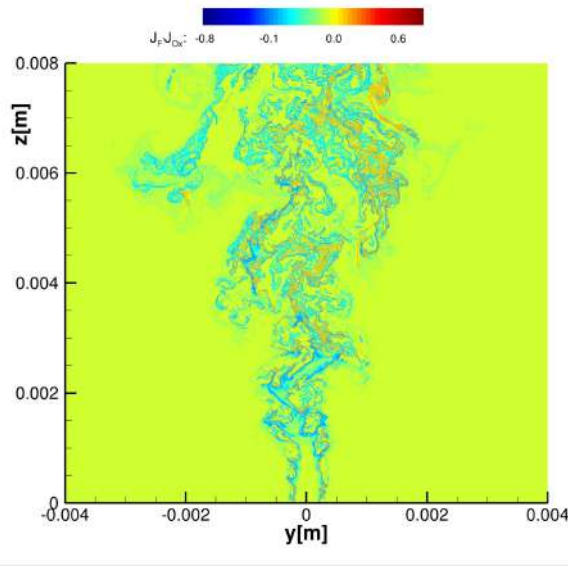
Figure 7: a) Instantaneous distribution of Flame Index G$_{FO}$.

To ensure that we analyze the reaction zone, we shows the $\dot{\omega}$ at high values of the Progress variable.
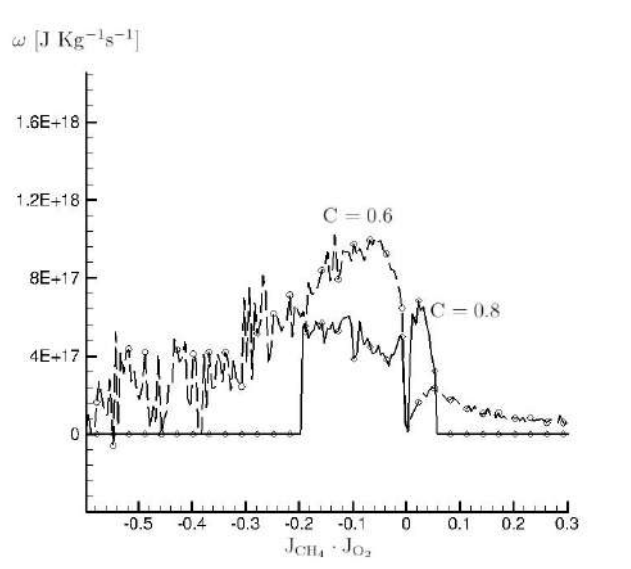
84

Figure 8: Heat release reaction rate as a function of Flame index and Progress Variable $C = (Y_{CO} + Y_{H_2O} + Y_{H_2})/(Y_{CO} + Y_{H_2O} + Y_{H_2})_{MAX}$.

At the value of $C \sim 0.6$, the heat release is maximum at ~ -0.2 and its module, in the diffusion-controlled combustion mode, is quantitatively less sensitive to the G_{FO} than the premixed-controlled. The extension of the last one is smaller than the first $0 - 0.3$ and it decrease as the flame index value increases. At higher values of the progress variable the contribution of the diffusion-controlled mode decreases and the heat release rate reaches its maximum in the premixed-controlled mode despite its smaller range $FI \in [0 - 0.06]$.

5   Conclusions

We perform 2D Direct Numerical Simulation on a $CH_4/CO_2/O_2$ diffusion flame. We found that, although the flame has a general diffusion character, a non-negligible part of the combustion takes place in a pre-mixed regime. This is due to the mixing effect carried out by the turbulence vortices at the exit of the main jets. The CO_2, acting as a diluent, reduces temperature peaks and consequently the formation of COThe CO_2 acting as a diluent, decreases the temperature peaks and CO polluttant formation especially at the hish strain rate regions.

References

[1] Ern A. and Giovangigli V. EGlib: A general-purpose fortran library for multicomponent transport property evaluation. *Manual of EGlib version 3.4*, 12 July 2004.

[2] NIST (Agency of the US Department of Commerce). NIST Reference Fluid Thermodynamic and Transport Properties Database, http://webbook.nist.gov/chemistry/.

[3] M. Baum, T. Poinsot, and D. Thévenin. Accurate Boundary Conditions for Multicomponent Reactive Flows. *Journal of Computational Physics*, 116(2):247–261, feb 1995.

[4] Westbrook C.K. and Dryer F.L. Simplified reaction mechanisms for the oxidation of hydrocarbon fuels in flames. *Combustion Science and Technology*, 27:31–43, 1981.

[5] de Charentenay J. and Ern A. Multicomponent transport impact on premixed turbulent H2/O2 flames. *Combustion Theory and Modelling*, 3(6):463–478, 2002.

[6] Giacomazzi E., Picchia F.R., and Arcidiacono N. A review on chemical diffusion, criticism and limits of simplified methods for diffusion coefficients calculation. *Combustion Theory and Modeling*, 12(1):135–158, 2008.

[7] Ponti G. et al. The role of medium size facilities in the HPC ecosystem: the case of the new CRESCO4 cluster integrated in the ENEAGRID infrastructure. In *Proceedings of the 2014 International Conference on High Performance Computing and Simulation*, volume HPCS 2014, pages 1030–1033, 2014.

[8] Crespi F., Gavagnin G., Sánchez D., and Martínez G.S. Supercritical carbon dioxide cycles for power generation: A review. *Appl. Energy*, 195:152–183, 2017.

[9] A. Frassoldati, A. Cuoci, T. Faravelli, E. Ranzi, C. Candusso, and D. Tolazzi. Simplified Kinetic Schemes for Oxy-Fuel Combustion. In *1st International Conference on Sustainable Fossil Fuels for Future Energy - S4FE*, Rome, Italy, 6-10 July 2009.

[10] Yamashita H., Shimada M., and Takeno T. A numerical study on flame stability at the transition point of jet diffusion flames. *International Symposium on Combustion*, 26(1):27–34, 1996.

[11] Andersen J., Rasmussen C.L., Giselsson T., and Glarborg P. Global combustion mechanisms for use in CFD modelling under oxy-fuel conditions. *Energy & Fuels*, 23:1379–1389, 2009.

[12] Bellan J. Direct numerical simulation of a high-pressure turbulent reacting temporal mixing layer. *Combustion and Flame*, 176:245–262, 2017.

[13] Lamouroux J., Ihme M., Fiorina B., and Gicquel O. Tabulated chemistry approach for diluted combustion regimes with internal recirculation and heat losses. *Combustion and Flame*, 161(8):2102–2136, 2014.

[14] Sutherland J.C. and Kennedy C.A. Improved boundary conditions for viscous, reacting, compressible flows. *Journal of Computational Physics*, 191:502–524, 2003.

[15] Hirschfelder J.O., Curtiss C.F., Bird R.B., and Spotz E.L. *The Molecular Theory of Gases and Liquids*. John Wiley & Sons, New York, 1954.

[16] Harstad K.G., Miller R.S., and Bellan J. Efficient high-pressure state equations. *American Institute of Chemical Engineers Journal*, 43(6):1605–1610, 1997.

[17] Pedersen K.S., Christensen P.L., and Shaikh J.A. *Phase Behavior of Petroleum Reservoir Fluids*. 6000 Broken Sound Parkway NW, 2014.

[18] Santini L., Accornero C., and Cioncolini A. On the adoption of carbon dioxide thermodynamic cycles for nuclear power conversion: A case study applied to mochovce 3 nuclear power plant. *Appl. Energy*, 181:446–463, 2016.

[19] M.S. Liou. A sequel to AUSM, part II: AUSM$^+$-up for All Speeds. *J. of Computational Physics*, 214:137–170, 2006.

[20] Klein M., Sadiki A., and Janicka J. A digital filter based generation of inflow data for spatially

developing direct numerical or large eddy simulations. *J. of Computational Physics*, 186:652–665, 2003.

[21] M.M. Masquelet. *Appendix B in: Large-Eddy Simulations of High-Pressure Shear Coaxial Flows Relevant for H2/O2 Rocket Engines*. Ph.d., School of Aerospace Engineering, Georgia Institute of Technology, May 2013. Adviser: Prof. Suresh Menon.

[22] Masquelet M.M. *Large-Eddy Simulations of High-Pressure Shear Coaxial Flows Relevant for H_2 /O_2 Rocket Engines*. PhD thesis, School of Aerospace Engineering, Georgia Institute of Technology, May 2013.

[23] Peters N. *Turbulent Combustion*. Cambridge, 2000.

[24] Nora Okong'o and Josette Bellan. Consistent Boundary Conditions for Multicomponent Real Gas Mixtures Based on Characteristic Waves. *Journal of Computational Physics*, 176(2):330–344, mar 2002.

[25] Gülder Ö.L., Smallwood G.J., Wong R., Snelling D.R., and Smith R. Flame front surface characteristics in turbulent premixed propane/air combustion. *Combustion and Flame*, 120:407–416, 2000.

[26] Chueh P.L. and Prausnitz J.M. Vapor-liquid equilibria at high pressures, calculation of partial molar volumes in nonpolar liquid mixtures. *AIChE Journal*, 13(6):1099–1107, 1967.

[27] Bird R.B., Stewart W.E., and Lightfoot E.N. *Transport Phenomena*. John Wiley and Sons, New York, 2nd edition, 2002.

[28] David H. Rudy and John C. Strikwerda. Boundary conditions for subsonic compressible Navier-Stokes calculations. *Computers & Fluids*, 9(3):327–338, sep 1981.

[29] Bilger R.W., Starner S.H., and Kee R.J. On reduced mechanisms for methane-air combustion in nonpremixed flames. *Combustion and Flame*, 80(2):135–149, 1990.

[30] Kevin W Thompson. Time-dependent boundary conditions for hyperbolic systems, II. *Journal of Computational Physics*, 89(2):439–461, aug 1990.

[31] Poinsot T.J. and Lele S.K. Boundary conditions for direct simulations of compressible viscous flows. *Journal of Computational Physics*, 101:104–129, 1992.

[32] Giovangigli V. *Multi-Component Flow Modeling*. Birkhauser, Boston, 1999.

[33] Polifke W. and Wall C. Non-reflecting boundary conditions for acoustic transfer matrix estimation with LES. In *Center for Turbulence Research Proceedings of Summer Program*, Summer 2002. Stanford.

[34] Wang X. and Yang V. *Comb. Sci. Technol*, 187:60–82, 2015.

[35] Ahn Y. and Bae S.J. Kim M. Cho S.K. Baik S. Lee J.I. Cha J.E. Review of supercritical co2 power cycle technology and current status of research and development. *Nuclear Engineering and Technology*, 47:647–661, 2015.

OZONE RISK ASSESSMENT TO FOREST IN ASIA: COMPARISON BETWEEN DIFFERENT APPROACHES

Alessandro Anav[1*], Alessandra De Marco[2]

[1] *ENEA SSPT-MET-CLIM, Italian National Agency for New Technologies, Energy and Sustainable Economic Development, CR Casaccia, Rome, Italy*

[2] *ENEA SSPT-PVS, Italian National Agency for New Technologies, Energy and Sustainable Economic Development, CR Casaccia, Rome, Italy*

ABSTRACT. Surface ozone concentration is rising over Asia, while it is declining or stagnating in Europe and North America. Ozone is the most widespread air pollutant negatively affecting vegetation, and its increase poses a major threat to forests in Asia. To estimate the risk for forests related to ozone pollution, the regional model WRF-Chem was applied over the Asian domain. Meteorological data and ozone concentration were then used to derive the most relevant standards for forests protection against negative impacts of ozone, AOT40 (European standard), W126 (US standard) and POD1 (new European standard).

1 Introduction

Asia is the world's largest emitter of the two precursors: China emits 30% of NOx and 19% of NMVOCs, followed by India's emissions of 13% (NOx) and 11% (NMVOCs) of the global emissions. Ozone is the most widespread air pollutant negatively affecting agricultural crops and ecosystems. At European level, a few indicators have been developed and used to protect vegetation from ozone. A concentration-based metric (i.e. AOT40), defined as a weighted sum or mean of hourly ozone concentration exceeding 40 ppb across a daily and seasonal time windows, is currently used in Europe for risk assessment. Besides, the PODy, developed more recently in Europe, is based on phytotoxic ozone dose entering the leaves and is a function of stomatal aperture. The two metrics show inconsistent spatial and temporal patterns on local to regional scales. In addition, the standard actually used in US for forests protection is W126, defined as sum of the hourly concentrations during growing season, where each concentration is weighted by a sigmoidal function to assign greater emphasis to the higher concentrations. Here we performed a high spatial resolution simulation with the WRF-Chem model to compute risk assessment metrics over South-East Asia.

2 Setup

The Weather Research and Forecasting (WRF) model is a limited-area, non-hydrostatic, terrain-following eta-coordinate mesoscale model widely used worldwide for climate studies. This model has been further developed to include various gas-phase chemistry and aerosol mechanisms creating a coupled climate-chemistry model (i.e. WRF-Chem).

In this study we applied the WRF-Chem (v3.9) over a large region covering the South-East Asia: the model domain is projected on a Lambert conformal grid with an horizontal spatial resolution of 8 km and with 30 vertical levels extending from land surface up to 50 hPa. We performed 1-year simulation for the whole 2015, with a spin up of 1 month (1st-31st December 2014).

The initial and boundary meteorological conditions required to run the model are provided by the European Centre for Medium-range Weather Forecast ERA5 dataset with a horizontal resolution of about 31km every 3 hours.

The WRF model system offers different gas phase chemistry and aerosol parameterizations to simulate the atmospheric chemistry. We employed the MOZART (Model for OZone And Related chemical Tracers) scheme to simulate the gas-phase chemistry (Emmons et al. 2010) whereas for the aerosols we used the GOCART (Global Ozone Chemistry Aerosol Radiation and Transport) bulk aerosol approach.

Anthropogenic emissions are based on the EDGAR-HTAP (*Emission Database for Global* Atmospheric Research for Hemispheric Transport of Air Pollution) global emission inventory which includes emissions of gaseous pollutants such as SO_2, NO_x, CO, non-methane volatile organic compounds (NMVOCs) and NH_3 as well as of particulate matter. Fire emissions are provided using the FINN (Fire INventory from NCAR) inventory, while biogenic emissions are calculated online using the MEGAN (Model of Emissions of Gases and Aerosols from Nature) model. Finally, MOZART-4 data have been used to provide to WRF-Chem time-variant chemical boundary conditions with a horizontal resolution of 1.9°×2.5° every 6 h.

The WRF-Chem modes has been compiled with the intel compiler (mpiifort) and ran over CRESCO6 using 384 CPUs; the domain decomposition has been achieved with MPI.

3 Main results

Three different metrics were used to estimate the potential risk for Asian forests; figure 1 shows the spatial distribution of these metrics. Considering the AOT40, the limit for forest protection (i.e. 5000 ppb h), is exceeded almost over all the selected domain, except for northern part, dominated by boreal forests. Similarly, low AOT40 levels were found in the southern part of the domain (Vietnam, Laos, Thailand) dominated by moist and dry broadleaf forest types. Conversely, we found high risk in the central part of China and the northern part of India, characterized mainly by temperate broadleaf and mixed forest or temperate coniferous forest, respectively.

Distribution of W126 (secondary standard for assessing risk to ecosystems from ozone exposure in the US, with a critical level of 7000 - 21000 ppb h over 3 months), is very similar to AOT40, but for the nature of the metric the higher and lower O3 values were amplified. This metric generally exceeded critical levels all over the Asian domain, with the exception of the northern and southern areas. The spatial pattern of the PO1 appears to eliminate the hot spots highlighted for concentration-based metrics, showing higher POD values in all the southern part of the domain, characterized by tropical climate, thus higher permissive conditions for ozone uptake into the plants (i.e. lower limiting factors due to less dry conditions). A clear example of the inconsistency from spatial distribution of POD1 and concentration-based metrics is the Sri Lanka and the area of Thailand and Philippines where AOT40 and W126 provide a completely different risk to forest compared to POD1 results.
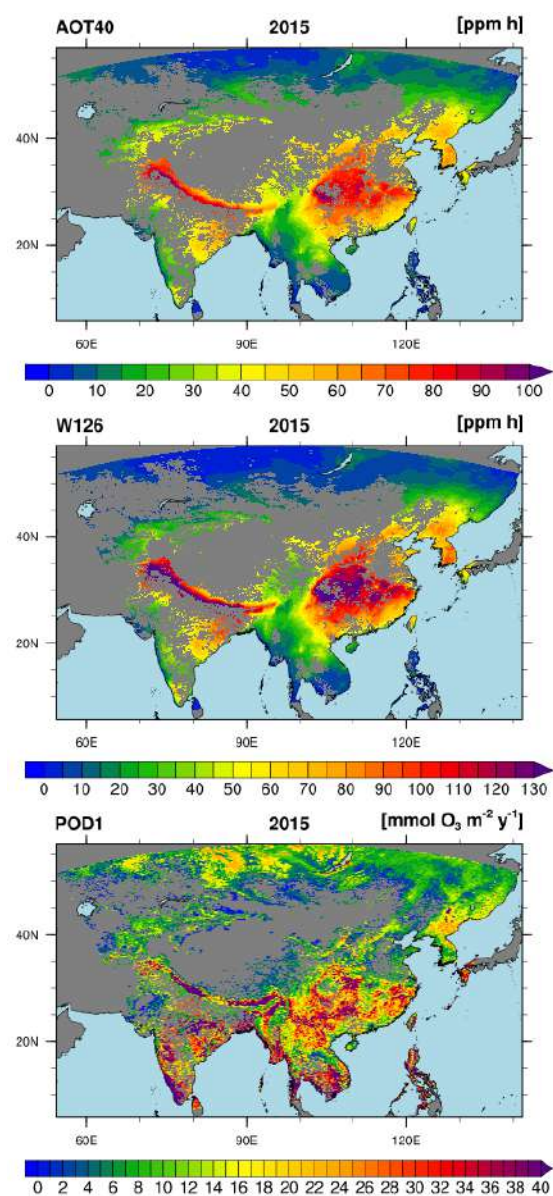
Fig.1: Ozone risk assessment for Asian forest computed using three different metrics (AOT40, W126 and POD1).

Ab Initio Simulations Of Amorphous GeO$_2$ Under Pressure: A First Search For Phase Transitions

Giorgio Mancini[1]*, Massimo Celino[2], Andea Di Cicco[1] and Emanuela Covino[1]

[1] *Università Di Camerino, Sezione di Fisica della Scuola di Scienze e Tecnologie, Via Madonna delle Carceri 9B, 62002 Camerino (MC), Italia*

[2] *ENEA, Ente per le Nuove Tecnologie, l'Energia e lo Sviluppo Economico Sostenibile, C. R. Casaccia, Via Anguillarese 301, 00123 Roma, Italia*

ABSTRACT. A series of *Ab-initio* molecular simulations oriented to get a first qualitative picture have been performed on amorphous GeO$_2$ at room temperature, submitted to increasing hydrostatic pressure up to 20GPa and released back to 0GPa. Unlike for pure Ge, simulations for GeO$_2$ show no pressure–induced low-density to high–density phase transition (LDA-HDA) in this pressures range: a result in line with preliminary experimental measurements that encourages for further investigations.

1 Introduction

During the last years –due to higher charges mobility and lower operating voltage– germanium gained increasing consideration for use in new energy-saving solid state devices, stimulating the interest of many scientists for further investigations of its properties. Amorphous Germanium and Germania (a-Ge, a-GeO$_2$) are among the disordered substances showing glass polymorphism or polyamorphism, a natural phenomenon yielding numerous interesting implications in various scientific fields (chemistry, material science, geology, etc) [1–9]. Glass polymorphism can manifest itself in different substances both in their liquid and glassy states, inducing changes in local structures, density and conduction properties, among others. In particular, evidence of glass polymorphism was recently found and studied in fourfold coordinated systems like amorphous Si (a-Si) ([10, 11] and Ge (a-Ge) [9, 12]. In such substances, pressure can induce low-density (LDA) to high-density (HDA) amorphous states transitions, resulting in new properties of these materials, possibly useful for technological applications. Such transformations and properties are usually studied by high-pressure experiments and Molecular Dynamics (MD) simulations. Careful investigations have been carried out including x-ray absorption spectroscopy (XAS) and Raman scattering experiments; nevertheless –since important aspects of the structural changes associated with LDA-HDA transitions are still to be assessed– advanced MD simulations are performed to clarify this transformation [9, 12–23]. A complete series of *ab-initio* Car-Parrinello MD simulations (CPMD) [24–26] for a system consisting in 125 Ge atoms was presented and illustrated, showing how high pressure induced an irreversible LDA-HDA transition around 10GPa, in close adherence to experimental results [17, 18, 23]. The results of CPMD simulations for GeO$_2$ (80 Ge and 160 O atoms) in the range 0-4000K were subsequently presented, showing how GeO$_2$ simulations resulted more challenging than Ge ones under various aspects [19–21, 27]. In particular, we found Goedecker's potentials (GOE) [28], requiring larger computing resources and power than

---

*Corresponding author. E-mail: `giorgio.mancini@unicam.it`.

Martin-Trueller's (M-T) ones [29], led to closer agreement with experimental data (M-T gave shorter distances), the differences attributed to the sole potential for oxygen (all potentials were downloaded from CPMD official distribution site): a discrepancy we intend to investigate on. Nevertheless, both GOE and M-T were in good qualitative agreement in the whole range 0-4000K. This encouraged us to continue and complete a first simulations cycle using Martin-Trueller's potentials to study the behavior of amorphous solid-state GeO_2 under pressure, while slower Goedecker simulations were in progress.

2 Computational resources

The calculations were performed using the facilities and services available at the ENEA GRID infrastructure (Italy). Molecular Dynamics simulations have been carried out using CPMD v3.15.3 running on CRESCO4 cluster. 800GB of disk storage has been granted on the PFS file system.

3 Simulations details

Our starting point was constituted by liquid GeO_2 at 4000K consisting in 240 atoms contained in a cubic simulation box of edge 15.602Å to give a density ρ= 3.66 gr/cm^3. The simulations were performed using CPMD software, describing the self consistent evolution of the electronic structure within the frame of density functional theory. A generalized gradient approximation (BLYP-GGA) was adopted for the exchange and correlation part of the total energy [30,31] together with norm conserving pseudo-potentials using the Troullier-Martins parametrization in the Kleinman-Bylander separable form for the core-valence interactions [29]. The electronic wave functions were expanded in plane waves up to a kinetic energy cutoff of 90 Ry. A value of 400a.u. was used for the fictitious electronic mass, 1000 cm^{-1} and 10000 cm^{-1} for the characteristic frequencies of ions and electrons, respectively, and 3a.u. (0.072 fs) for the time-step. The initial system was quenched down to 300K and relaxed at an initial pressure of 0Pa; it subsequently was submitted to increasing pressures up to 20GPa and directly relaxed back to 0Pa. Pressures were applied via the Parrinello-Rahman method [32], by steps of 2GPa. At each stage the atomic system was equilibrated according to the criterion that all the physical quantities converged. Thermostatting was obtained by Nosé-Hoover chain thermostats [26,33,34] set on ions and electronic degrees of freedom.

4 Results

A comparison of the volumes evolutions with pressure is reported in Fig. 1 for Ge [18] and GeO_2: it clearly shows that, unlike Ge, GeO_2 undergoes no LDA-HDA transformation (its volume decreases linearly with pressure, whilst Ge shows a deep volume drop). Furthermore while the density change induced by pressure on Ge have a permanent nature, it results reversible for GeO_2. The same behavior is observed in pair distribution, nearest neighbors distribution and structure functions, as depicted in Fig. 2,3.
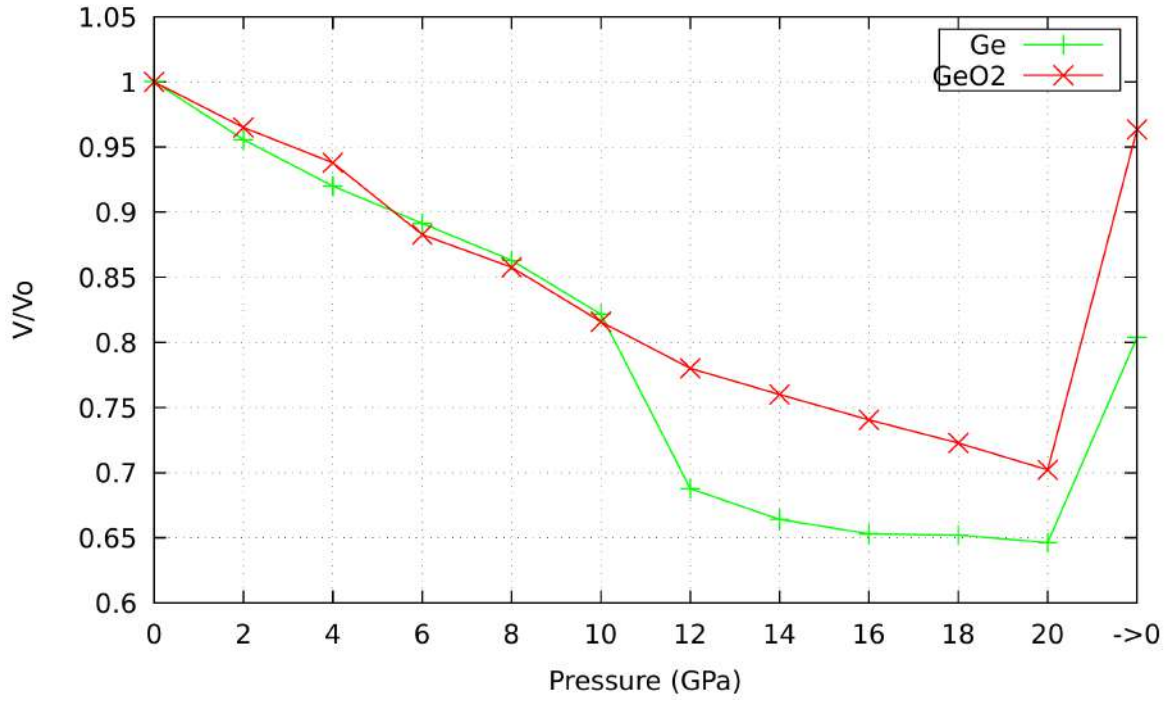
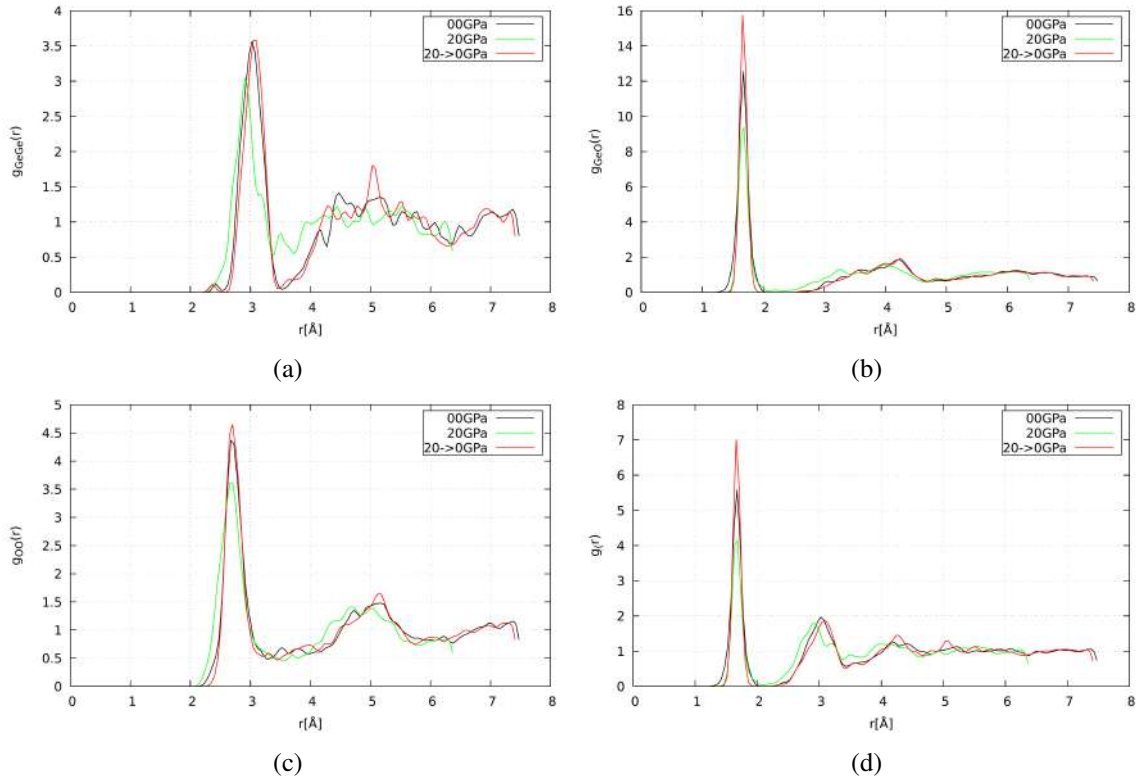Figure 1: Evolution of Ge and GeO$_2$ volumes with pressure. $\rightarrow$0 indicates the final 0Pa pressure.

(a)

(b)

(c)

(d)

Figure 2: Pair (a-c) and total (d) distribution functions at 0, 20 and $20 \rightarrow 0$ GPa for GeO$_2$
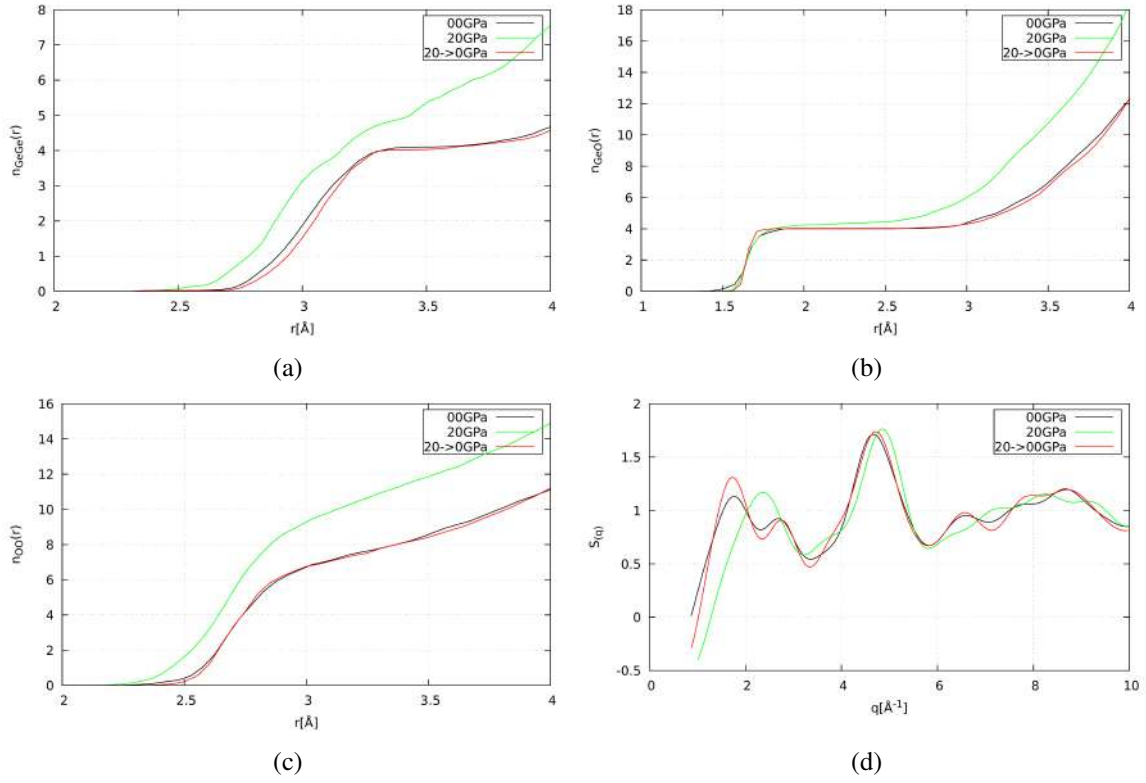
(a)

(b)

(c)

(d)

Figure 3: Nearest neighbors (a-c) and structure (d) functions at 0, 20 and 20→0 GPa for GeO_2

5   Conclusions

A preliminary study on amorphous GeO_2 under pressure in the range 0-20GPa was performed by a series of *ab-initio* Car-Parrinello molecular dynamics simulations using CPMD software. For a first qualitative exploration, faster norm conserving Troullier-Martins pseudo-potentials in the Kleinman-Bylander form were used. In contrast with both experimental and simulations results obtained for Ge, GeO_2 shows no LDA-HDA transition in the 0-20GPa range. This result is in line with experimental measurements carried out up to 10GPa by our group. Finally, while the structural changes induced by pressure in Ge are permanent, pressure effects GeO_2 are not retained when the system is released back to 0GPa.

References

[1] P.H. Poole, T. Grande, C.A. Angell, and P.F. McMillan. Polymorphic phase transitions in liquids and glasses. *Science*, 257(5298):322–323, 1997.

[2] O. Mishima and H.E. Stanley. The relationship between liquid, supercooled and glassy water. *Science*, 257(6709):329–335, 1998.

[3] Y. Katayama, T. Mizutani, W. Utsumi, O. Shimomura, M. Yamakata, and K. Funakoshi. A first-order liquidliquid phase transition in phosphorus. *Nature*, 403(6766):170–173, 2000.

[4] G. Franzese, G. Malescio, A. Kibinsky, S.V. Buldyrev, and H.E Stanley. Generic mechanism for generating a liquidliquid phase transition. *Nature*, 409(6821):692–695, 2001.

[5] W.A. Crichton, M. Mezouar, T. Grande, S. Stølen, and A. Grzechnik. Breakdown of intermediate-range order in liquid gese2 at high pressure. *Nature*, 414(6864):622–625, 2001.

[6] O. Mishima and Y. Suzuki. Propagation of the polyamorphic transition of ice and the liquidliquid critical point. *Nature*, 419(6907):599–603, 2002.

[7] R. Kurita and H. Tanaka. Critical-like phenomena associated with liquid-liquid transition in a molecular liquid. *Science*, 306(5697):845–848, 2004.

[8] Y Katayama. Macroscopic separation of dense fluid phase and liquid phase of phosphorus. *Science*, 306(5697):848–851, 2004.

[9] A. Di Cicco, A. Congeduti, F. F. Coppari, J.C. Chervin, F. Baudelet, and A. Polian. Interplay between morphology and metallization in amorphous-amorphous transitions. *Physical Review B.*, 78(3), 2008.

[10] A. Hedler, S.L. Klaumnzer, and W. Wesch. Amorphous silicon exhibits a glass transition. *Nature Materials*, 3(11):804–809, 2004.

[11] P. F. McMillan, M. Wilson, D. Daisenberger, and D. Machon. A density-driven phase transition between semiconducting and metallic polyamorphs of silicon. *Nature Materials*, 4(9):680–684, 2005.

[12] F. Coppari, J.C. Chervin, A. Congeduti, M. Lazzeri, A. Polian, E. Principi, and A. Di Cicco. Pressure-induced phase transitions in amorphous and metastable crystalline germanium by raman scattering, x-ray spectroscopy, and ab initio calculations. *Physical Review B.*, 80(115213), 2009.

[13] T. Tamura, G-H. Lu, R. Yamamoto, and M. Kohyama. First-principles study of neutral oxygen vacancies in amorphous silica and germania. *Physical Review B*, 69:195204–195213, 2004.

[14] P.S. Salmon. The structure of tetrahedral network glass forming systems at intermediate and extended length scales. *Journal of Physics: Condensed Matter*, 19:455208–455224, 2007.

[15] P.S. Salmon, A.C. Barnes, R.A. Martin, and G.J. Cuello. Structure of glassy GeO_2. *Journal of Physics: Condensed Matter*, 19:415110–415132, 2007.

[16] M. Hawlitzky, J. Horbach, S. Ispas, M. Krack, and K. Binder. Comparative classical and ab-initio molecular dynamics study of molten and glassy germanium dioxide. *Journal of Physics: Condensed Matter*, 20:285106–285121, 2008.

[17] G. Mancini, M. Celino, and A. Di Cicco. Ab-initio study of amorphous germanium. *High Performance Computing on CRESCO infrastructure: research activities and results 2012*, pages 87–92, March 2014. ISBN: 978-88-8286-302-9.

[18] G. Mancini, M. Celino, and A. Di Cicco. First-principles study of amorphous germanium under pressure. *High Performance Computing on CRESCO infrastructure: research activities and results 2013*, pages 97–105, December 2013. ISBN: 978-88-8286-312-8.

[19] G. Mancini and M. Celino. *Ab-Initio* molecular dynamics simulation of high temperature GeO_2. *High Performance Computing on CRESCO infrastructure: research activities and results 2014*, pages 6–9, December 2015. ISBN: 978-88-8286-342-5.

[20] G. Mancini and M. Celino. *Ab-Initio* Carr-Parrinello simulations of high temperature GeO_2: a comparison of the effects of plane waves cut-off and time step choice. *High Performance Computing on CRESCO infrastructure: research activities and results 2015*, pages 6–9, November 2016. ISBN: 978-88-8286-342-5.

[21] G. Mancini, M. Celino, and A. Di Cicco. Molecular dynamics of GeO_2: Car-Parrinello simulations in the range 10-4000k. *High Performance Computing on CRESCO infrastructure: research activities and results 2016*, pages 117–121, November 2017. ISBN: 978- 88-8286-362 2-3.

[22] E. Principi, A. Di Cicco, F. Decremps, A. Polian, S. De Panfilis, and A. Filipponi. Polyamorphic transition of germanium under pressure. *Phys. Rev. B*, 69:201201, May 2004.

[23] G. Mancini, M. Celino, F. Iesari, and A. Di Cicco. Glass polymorphism in amorphous germanium probed by first-principles computer simulations. *Journal of Physics: Condensed Matter*, 28:15401–15406, 2016.

[24] R. Car and M. Parrinello. Unified approach for molecular dynamics and density-functional theory. *Physical Review Letters*, 55(22):2471–2474, 1985.

[25] CPMD v3.13.2 copyright ibm corp 1990-2008, copyright mpi fr festkrperforschung stuttgart 1997–2001.

[26] The CPMD Consortium. Car-Parrinello Molecular Dynamics: An ab-initio Electronic Structure and Molecular Dynamics Program. Manual for CPMD version 3.15.1.

[27] G. Mancini, M. Celino, A. Di Cicco, and E Covino. Dependence on pseudopotentials of *Ab-Initio* molecular dynamics simulations of high temperature geo$_2$. *High Performance Computing on CRESCO infrastructure: research activities and results 2018*, pages 89–93, November 2017. ISBN: 978-88-8286-373-9.

[28] S. Goedecker, M. Teter, and J. Hutter. Separable dual-space gaussian pseudopotentials. *Physical Review B*, 54:1703–1710, 1996.

[29] N. Troullier and J. L. Martins. Efficient pseudopotentials for plane-wave calculations. *Physical Review B*, 43:1993–2006, 1991.

[30] A. D. Becke. Density-functional exchange-energy approximation with correct asymptotic behavior. *Phys. Rev. A*, 38:3098–3100, Sep 1988.

[31] Chengteh Lee, Weitao Yang, and Robert G. Parr. Development of the colle-salvetti correlation-energy formula into a functional of the electron density. *Phys. Rev. B*, 37:785–789, Jan 1988.

[32] M. Parrinello and A. Rahman. Crystal structure and pair potentials: A molecular-dynamics study. *Phys. Rev. Lett.*, 45:1196–1199, Oct 1980.

[33] S Nosé. A molecular dynamics method for simulations in the canonical ensemble. *Molecular Physics*, 52:255–268, 1984.

[34] S.A Nosé. A unified formulation of the constant temperature molecular dynamics methods. *The Journal Of Chemical Physics*, 81:511–519, 1984.

Percolation paths through simulated granular superconductors

Giorgio Mancini[1*]

[1]*Università Di Camerino, Sezione di Fisica della Scuola di Scienze e Tecnologie, Via Madonna delle Carceri 9B, 62002 Camerino (MC), Italia*

ABSTRACT. A method is presented to determine the superconducting percolation paths through granular superconductors showing re-entrant resistivity peaks. It introduces an original approach capable of an effective reduction of intermediate data handling and, although originated from such a specific problem, it can be used as an effective method to determine percolation paths through more general networks.

1 Introduction

Based on Josephson junctions array and Coulomb blockage, a model capable to explain re-entrant resistivity peaks in diamond-like carbon-silicon films containing tungsten was presented by Chudinov et al. [1, 2]. Such granular superconductors present one or two re-entrant (or quasi-re-entrant) resistivity peaks at lower temperatures than the critical ones T_c. The hypothesis was investigated that the phenomenon was due to a competition between the Coulombian blockage arising from the inter-granular capacitance of nearest neighboring grains and the unblocking process related to tunneling junctions coupling, this competition determining the presence or the absence of percolation paths on superconducting grains crossing the entire system. Computer simulations confirmed with clear evidence the experimental data. The method devised to determine the presence of superconducting percolation paths in simulated granular systems was a direct derivation from the one developed and implemented for the ring perception problem (a method to gain detailed information on rings and chains of atoms in the analysis of medium-range order in computer-simulated solids) [3–5]. Its key features are the *path messages* propagation and reduction of information handling. Although it was developed fairly long ago, it remained unpublished up to now; anyway, at the best of the author's knowledge, it still constitutes an original approach for the determination of percolation paths.

2 The physical background

A metallic granular systems is a superconductor if it is entirely crossed by Cooper pairs moving from grain to grain. In order to obtain a superconducting shunt in a percolative system, there must be a path consisting of superconducting connected grains. The absence of such a path at temperatures lower than T_c characterizes the appearance of re-entrant resistivity peaks. According to theoretical analyses [6–8], superconducting metallic granular systems are governed -at low temperatures- by the competition between two energies E_c and E_J, being E_c the energy of the Coulombian blockage acting

---

on grains i and j:

$$E_c^{i,j} = \frac{1}{2}\frac{Q_i Q_j}{C_{ij}}, \tag{1}$$

(with C_{ij} the inter-granular capacitance, Q_i and Q_j the charges excess in the grains i and j due to Cooper pairs (charge 2e)) and E_J the characteristic energy of Josephson junction coupling for nearest neighboring grains ($i = j \pm 1$):

$$E_J^{i,j}(T) = \frac{\pi\hbar}{4e^2}\frac{1}{R_N^{i,j}}\Delta(T)\tanh(\frac{\Delta(T)}{2k_B T}) \tag{2}$$

where $\Delta(T) = \Delta(0)(1 - \frac{T}{T_c})^{\frac{1}{2}}$ is the superconducting gap at temperatures $T < T_c$, Δ_0 the super-conducting gap at $T = 0K$ [9], $R_N^{i,j}$ the resistance for single electron tunneling between neighboring grains and k_B the Boltzman constant. Finally, taking into account all energies involved at each temperature $T < T_c$, (namely E_c, E_J and $k_B T$), two granules are connected -or activated- when one of the conditions

$$(a)\quad k_B T \geq E_c^{i,j} \quad (b)\quad k_B T < E_c^{i,j} \text{ and } zE_J^{i,j} > E_c^{i,j} + k_B T \tag{3}$$

holds with z -the nearest neighbors average number- accounting for shielding effect. For each couple of connected grains (i,j) a critical super-current $I_c^{i,j}$ and its associate density $J_c^{i,j}$ are defined which depend on the grains distance and radii R_i, R_j according to the relations:

$$I_c^{i,j} = \frac{\pi}{2eR_N^{i,j}}\Delta(T)tanh(\frac{\Delta(T)}{2k_B T}) \quad \text{and} \quad J_c^{i,j} = \frac{I_c^{i,j}}{\pi\,(R_{min}^{i,j})^2} \tag{4}$$

where $R_{min}^{i,j}$ is the smallest radius of the two grains.

3   The model

A numerical representation of a disordered granular system was generated positioning spherical grains in a simulation box, their radii and mutual distances distributed gaussianly around known experimental values. Two opposite sides of the box were chosen to be the injection (source) and ejection (drain) electrodes, constituted by their closest grains. In correspondence of a given temperature $T < T_c$ a graph was then built associating a node to each grain and an edge to each couple of activated grains (conditions 3). As a first data-reduction task, subsequent searches and removals of nodes linked by a single edge were performed.

4   The method

The search for paths in a graph is a problem that rises from a great variety of problems from many different fields, stimulating continuous interest since many years (see [10–12] and references therein). Here we present the method we devised to achieve our goal. It represents an exact, original - and hopefully interesting- approach to the problem. As anticipated, it was derived from the method we proposed for the determination of a smallest set of smallest rings in a graph, based on an analogy to a communication network letting *path-messages*, conveying information on their walk through the network, propagate by means of *transceivers* and communication channels during alternate, synchronous *send* and *receive* states of the network ([3,4]).

5 Basic definitions

- An *edge sequence* of length (size) $k - 1$ in a graph is a finite sequence of edges (n_1, n_2), (n_2, n_3), (n_3, n_4), ..., (n_{k-1}, n_k), where each edge is denoted by the pair of nodes it connects. If $n_1 = n_k$ or $n_1 \neq n_k$ the edge sequence is *closed* or *open*, respectively.

- An edge sequence of distinct edges constitutes an *edge train*.

- An open edge train in which all nodes are distinct is called a *path*.

- An edge train containing a closed edge sequence will be indicated as a *collapsed path*.

Together with the common standard definitions given above, the following ones will prove useful to ease future descriptions:

- A physical record of a path, stored as the sequence of the nodes it traversed $(n_1, n_2, ..., n_k)$, will be indicated as a *path-message*.

- A path-message that can be propagated will be indicated as an *active path-message*.

- A path-message containing a closed edge sequence will be indicated as a *collapsed path-message*.

- A node traversed by a path-message will be indicated as a *visited node*

- An edge traversed at most once will be indicated as an *active edge* .

- An edge traversed in both directions will be indicated as an *exhausted edge*.

- A node whose edges are all exhausted will be indicated as an *exhausted node*.

6 Process overview

The initial graph is abstracted to a synchronous communication network by the association of each node to a *transceiver* and considering each edge a *communication channel*. Each transceiver consists of a receive and a send buffer. A node and its transceiver constitute a $Tnode$. Tnodes receive and send *path-messages* containing the sequence of nodes they crossed. $Tnodes$ belonging to the electrodes are reserved a different approach: the source ones act as pure transmitters, the drain ones as pure receivers. A Tnode is said *active* when it contains at least a path-message. The process of determining the percolation paths is based on a "post office" similitude: the underlining idea is that all active Tnodes, during alternating, synchronous send/receive cycles propagate their path-messages through the communications channels linking adjacent nodes. The key feature of our method is constituted by **deferred path-messages**: the path-messages contained in the send buffers of visited Tnodes. They will be indicated by a trailing hyphenation, e.g. (1,7,12,-). It is important to note that a Tnode becomes a visited one as soon as its first path-message is sent.

6.1 Sending

During the send cycles, Tnodes forward path-messages in such a way that:

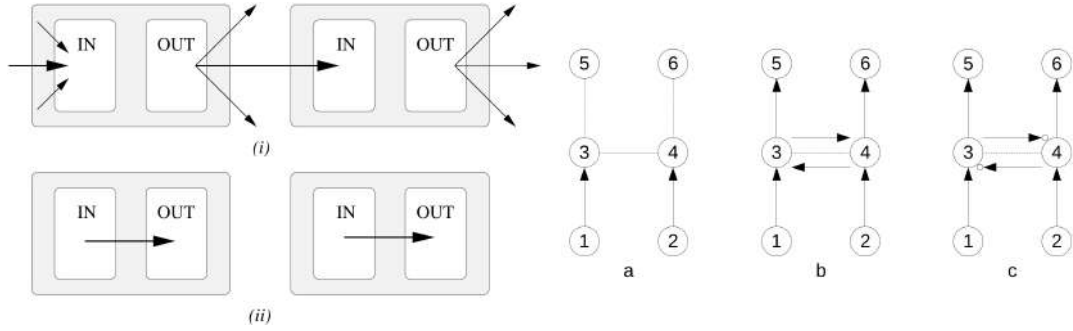1. (a) edges can be traversed no more than once in both direction;

Figure 1: Transceivers sending (*i*) and receiving (*ii*) path-messages. Path-messages propagation (*a*),(*b*),(*c*).

    (b) any path-message sent from node m and received by node n is forwarded by n to all the other connected nodes (so that there are no collapsed path- messages);

    (c) path-messages are cleared as soon as they are sent;

    (d) deferred path-messages are removed from the send process and stored.

6.2   Receiving

During the receiving cycles each transceiver updates -adding itself- the path-messages in its incoming buffer and move them to the outgoing one.

6.3   Initialization

The communication network initialization is done putting in the send buffer of each source Tnode a path-message consisting in the sole indication of the source itself. A scheme of the send and receive phases is given in Fig. 1 (*i*),(*ii*).

6.4   Execution

The entire process is such that, at any stage, all active path-messages are the same length, this length being increased each time messages are re-transmitted; path-messages reaching the drain receivers are then collected and processed in increasing length. Basically, the whole process consists of four phases:

1. initialize the communication network;

2. as long as there are active Tnodes:

    (a) send path-messages;

    (b) receive path-messages;

    (c) identify complete paths;

3. build complete paths from intersecting complete and deferred path-messages.

100

Fig.1 (*a*),(*b*),(*c*) illustrates the entire process of path-messages propagation in a simple communication network in which electrodes are constituted by the Tnodes 1,2,5,6 and Tnodes 3 and 4 are standard ones (Tnodes are processed in ascending order). In Fig.1.a, at the end of the first send cycle, we have two paths: (1,3) and (2,4); in Fig.1.b we have two active nodes: 3 and 4. After the first transmission from node 3, we have the path (1,3,4) and the node 3 as a visited one. At the end of the transmission from the node 3, we have the paths (1,3,4), (1,3,5); at the end of the transmission from the node 4 we have two active paths:(1,3,4),(2,4,3), two complete ones: (1,3,5),(2,4,6), two visited nodes: 3,4 and an exhausted edge: (3,4). In Fig.1.c, the send cycle individuates the two deferred paths (1,3,4-),(2,4,3,-) and no active path remains. Now we have two complete paths c_1=(1,3,5),c_2=(2,4,6) and two deferred ones d_1=(1,3,4-),d_2=(2,4,3,-). Combining the intersecting complete and deferred paths we have the two additional complete paths (2,4,3,5) from c_1,d_2 and (1,3,4,6) from c_2,d_1. We have then individuated all the percolation paths: (1,3,5),(2,4,6),(2,4,3,5),(1,3,4,6). In large networks, the impact of deferred paths on the number of propagate messages is dramatically effective, in particular when deferred paths are nested.

7 Results and conclusions
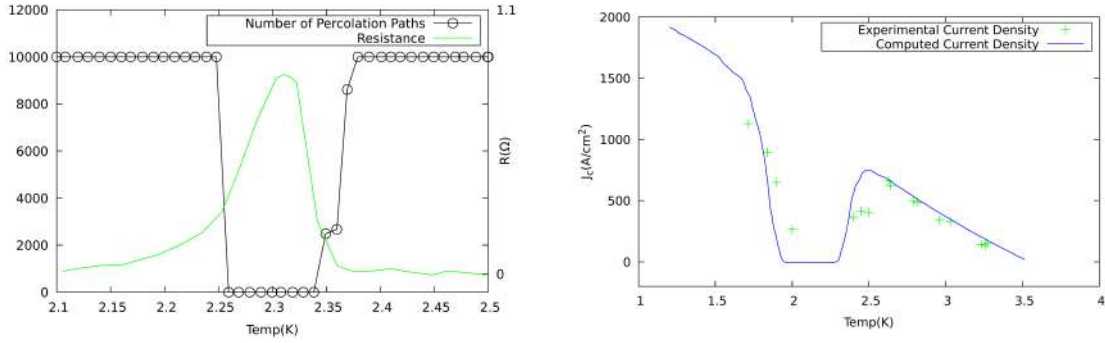
Figure 2: Left: re-entrant resistivity and percolation paths. Right: experimental and computed current densities.

A comparison of experimental and computer simulations results for a sample of diamond-like carbon-silicon film containing tungsten are shown in Fig.2. On the left, the number of percolation paths in the re-entrant resistivity peak region is shown. On the right, the measured value for the maximum current density allowed for the film while retaining its superconducting state, and its value obtained from the simulation network. Notice how the mechanism of paths propagation and rebuilding from deferred paths allow to manage the number of the processed paths avoiding growth beyond reasonable time and hardware resources (Fig.2, left, a limit of 10000 is used as the maximum number of reconstructed complete paths). Even though the simulation sample was constituted by only 1000 grains, the agreement of experimental and computed results is particularly strict and clear.

8 Computational resources

The calculations were performed using the facilities and services available at the ENEA GRID infrastructure (Italy). The simulation software was written in Fortran90 and compiled using the GNU and

Intelcompilers available on CRESCO4 cluster. 800GB of disk storage has been granted on the PFS file system.

References

[1] S M Chudinov, R Ferretti, S Fusari, G Mancini, and S Stizza. Reentrant superconductivity mechanisms in amorphous carbon-silicon films containing tungsten. *Physical Review B*, 62:12516–12521, 10 2000.

[2] S M Chudinov, G Mancini, M Minestrini, R Natali, S Stizza, and A Bozhko. Critical current in granular superconductor c-si-w with peak-type re-entrant superconductivity. *Journal of Physics: Condensed Matter*, 14(2):193–209, dec 2001.

[3] Mancini G. A redundancy eliminating approach to linearly independent rings selection in the ring perception problem. *Computer Physics Communications*, 143(2):187–197, 2002.

[4] R. Balducci and R.S. Pearlman. Efficient exact solution of the ring perception problem. *Journal of Chemical Information and Computer Sciences*, 34(4):822–831, 1994.

[5] Rybicki J., Bergmaski G., and Mancini G. A new program package for investigation of medium-range order in computer-simulated solids. *Journal of Non-Crystalline Solids*, 293-295:758–763, 2001. 8th Int. Conf. on Non-Crystalline Materials.

[6] B. Abeles. Effect of charging energy on superconductivity in granular metal films. *Phys. Rev. B*, 15:2828–2829, Mar 1977.

[7] E. E. imnek. Effect of charging energy on transition temperature of granular superconductors. *Solid State Communications*, 31(6):419–421, 1979.

[8] K.B. Efetov. Phase transition in granulated superconductors. *Zh. ksp. Teor. Fiz. [Journal of Experimental and Theoretical Physics]*, 78:2017–2032, May 1980.

[9] V. Ambegaokar and A. Baratoff. Tunneling between superconductors. *Phys. Rev. Lett.*, 10:486–489, Jun 1963.

[10] N.J.A. Sloane. On finding the paths through a network. *The Bell System Technical Journal*, 51:371–390, 02 1972.

[11] R. Potdar, G.and Thool. Comparison of various heuristic search techniques for finding shortest path. *International Journal of Artificial Intelligence & Applications*, 5:63–74, 07 2014.

[12] A. T. Rahem, M. Ismail, N. F. Abdullah, and I. A. Najm. New mathematical model to find the shortest path based on boolean algebra operations for networks. In *2016 IEEE 3rd International Symposium on Telecommunication Technologies (ISTT)*, pages 112–114, Nov 2016.

Dynamical complexity as a proxy for the network degree distribution

A. Tlaie[1,2], I. Leyva[1,2] [*], I. Sendiña-Nadal[1,2]

[1] *Complex Systems Group & GISC, Universidad Rey Juan Carlos, 28933 Móstoles, Madrid, Spain*

[2] *Center for Biomedical Technology, U. Politécnica de Madrid, 28223 Pozuelo de Alarcón, Madrid, Spain*

Abstract.

We explore the relation between the topological relevance of a node in a complex network and the individual dynamics. When the system is weakly coupled, the effect of the coupling strength against the dynamical complexity of the nodes is found to be a function of their topological role, with nodes of higher degree displaying lower levels of complexity. Our results imply that it is possible to infer the degree distribution of a network only from individual dynamical measurements.

1   Introduction

Since the beginning of the research on the dynamics of complex networks, the deep relationship between topology and dynamics has been thoroughly explored with regard to its effect in the collective state, particularly in the synchronization between the nodes' dynamics [4, 2]. The knowledge gathered so far has driven the advances in crucial applications where synchronization is relevant, as brain dynamics or power grids.

The role of the nodes in the synchronization differs as a result of their topological positions [6, 11] as well as of their own dynamics [15]. It is known the role of the hubs as coordinators of the dynamics [12, 5], while the rest of the nodes follow them hierarchically. But correspondingly, the units dynamics changes due to the ensemble, encoding the information coming from the rest of the network. We explore how this last feature could be used to extract information about the network even in the cases where the structure is unknown.

2   Model

Let us consider a network of N dynamical units whose state vector evolves according to $\dot{\mathbf{x}}_i = \mathbf{f}(\mathbf{x}_i, \tau_i) - d \sum_j \mathcal{L}_{ij} \mathbf{h}(\mathbf{x}_j)$ where $\mathbf{f}(\mathbf{x}_i, \tau_i)$ is the function governing the node dynamics with τ_i accounting for some parameter heterogeneity, d is the coupling strength and $\mathcal{L}_{ij}$ is the Laplacian matrix describing the coupling structure.

In order to address our hypothesis about the relationship between the changes in the dynamical properties of each single unit and the number of neighbors it has, we measure the statistical complexity

---

[*]Corresponding author. E-mail: `inmaculada.leyva@urjc.es`.
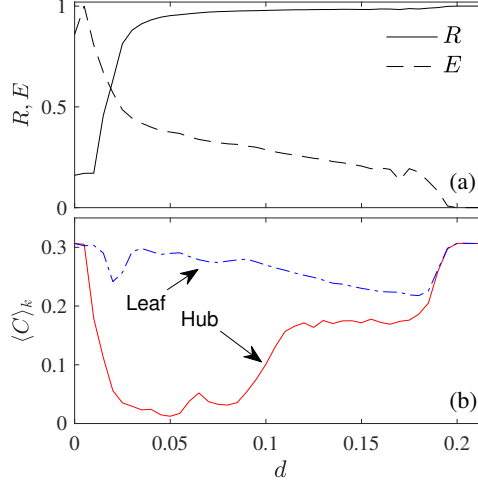
Figure 1: (a) Phase order parameter R and synchronization error E vs. d for a star of $N = 30$ Rössler oscillators. (b) Complexity C for the hub and the leaves vs. d, using $D = 4$, averaged over 10 initial conditions, storing sequences of 10^4 maxima per node.

[8, 9] of ordinal patterns extracted from the signal produced by each dynamical unit, as a function of the node degree k_i and the coupling strength d. The ordinal patterns formalism [3, 13] transforms the actual values of a series into a set of natural numbers. For doing that, the series is divided in bins of size D, where the data values are ordered in terms of its relative amplitudes, which provides a symbolic sequence. Then, we count how many times a certain symbolic sequence appears (N_π), which allows to define a probability of occurrence for each pattern: $P_\pi = \frac{N_\pi}{N_T}$, where N_T is the total number of bins $N_T = N/D$. Finally, we construct an *empirical probability distribution*, $P = \{P_\pi\}$. Once P is obtained, we can now define the statistical complexity $C = HQ$ where H is the permutation entropy and Q the disequilibrium. C is minimal both for pure noise and absolute regularity, and bounded value for other regimes.

H is defined as $H = S/S_{max}$, where $S[P] = -\sum_{j=1}^{D!} p_j \cdot \log(p_j)$ is the Shannon entropy, that gives an idea of the *disorder* of the series, and $S_{max} = S[P_e]$ corresponds to the entropy of the probability distribution in the equilibrium, $P_e \equiv \{1/D!\}_{1,\ldots,D!} \implies 0 \leq H \leq 1$.

The disequilibrium Q measures the statistical distance of P with P_e, given by the Kullback-Leibler [7] relative entropy $K[P|P_e] = S[P|P_e] - S[P]$ where $S[P|P_e]$ is the Shannon cross entropy. The symmetric version is the Jensen-Shannon divergence $J[P|P_e] = (K[P|P_e] + K[P_e|P])/2 = S[(P + P_e)/2] - S[P]/2 - S[P_e]/2$. Finally, we can write the disequilibrium Q as the normalized version of J as $Q = Q_0 J[P|P_e]$ with $Q_0 = \frac{N+1}{N} \log(N+1) - 2\log(2N) + \log(N)^{-1}$, implying again $0 \leq Q \leq 1$.

3 Numerical results

3.1 Numerical methods and use of computational resources

For the numerical integration ande the analysis of the results we used homemade C codes implementing fix-step fourth-order Runge-Kutta integration algorithms. The standard GCC compiler was used. Extensive serial simulations have been performed for large parameters ranges, with statistical validation of the results. The calculations were performed in CRESCO5 and CRESCO6, using the *h144* queues for full evolution simulations. Homemade MatLab scripts were used for visualizing the results.
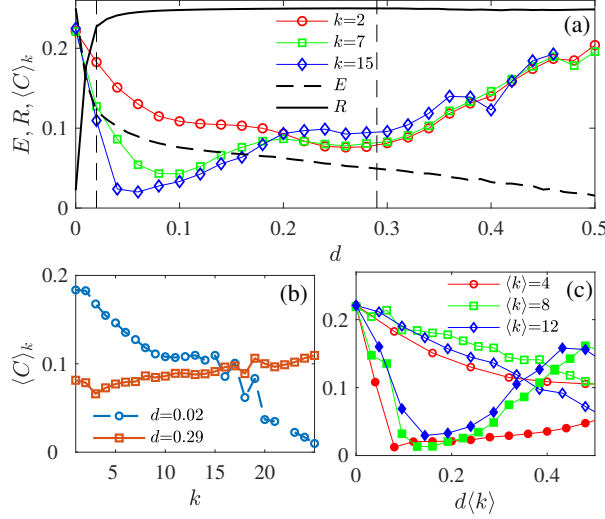
Figure 2: Dependence of C in a SF network of $N = 150$ Rössler oscillators. (a) C_i vs. d for different k_i in a network with $\langle k \rangle = 4$. The rescaled E, (black dashed line) and R, (black continuous line) are shown. (b) $\langle C \rangle_k$ vs. k for the two values of d marked in (a) with vertical lines. (c) $\langle C \rangle_k$ vs. $d\langle k \rangle$ for the highest (filled markers) and lowest (void markers) node degree classes for different mean degrees $\langle k \rangle$ of the networks. Each point is the average of 10 network realizations.

3.2 Networks of chaotic oscillators

We first check our conjecture by investigating a network of N bidirectionally coupled identical Rössler oscillators [14] with $\mathbf{x} = (x, y, z)$ as the state vector and $\mathbf{f}(\mathbf{x}) = (-y - z, x + ay, b + z(x - c))$ and $\mathbf{h}(\mathbf{x}) = (0, y, 0)$ as the vector field and output functions respectively. The chosen parameters $a = b = 0.2$ and $c = 9.0$ are such that each unit is chaotic when isolated. From the time series of x_i we extract 10^4 maxima, that we use to measure the *complexity* C_i of each node as defined above, with $D = 4$. As we expect that nodes having the same degree k will play equivalent roles, we compute the evolution of C_k by averaging over nodes that have same degree k. In addition, we monitor the collective state vs. d by calculating the phase order parameter R and the synchronization error E. Throughout the paper, the results are averaged over 10 different realizations.

We begin our study with a star of $N = 30$ nodes, to grasp the evolution of the complexity and the role of hubs in heterogeneous networks. In Fig. 1(a) we report the degree of R (solid line) and normalized E (dashed line) vs. d, observing first a phase synchronization (PS) transition when $R \sim 1$ and for larger d, a complete synchronization (CS) transition with $E = 0$. In Fig. 1(b) we plot C_i of the hub (red solid line) and the leaves (blue dashed-dotted line) as a function of d, whose values at $d = 0$ coincide as the nodes are identical. For small values of d, still far from PS, the hub suffers a strong depletion of C reflecting that the hub's trajectory is driven out of the original chaotic attractor to a much simpler dynamics, whereas the leaves remains almost unchanged. As d increases, leaves and hub converge to the original chaotic state and the initial value of C is recovered.

We check whether this correlation is still observable in more complex topologies. We choose to couple ensembles of $N = 150$ Rössler oscillators on top of Barabasi-Albert scale-free (SF) networks [1], with $\langle k \rangle = 4$. In Fig. 2(a) we plot E (dashed line) and R (solid line) along with the $\langle C \rangle_k$ for several values of k. There is a clear decrease of $\langle C \rangle_k$ for weak coupling with also a strong hierarchical dependence on k that is lost when the network is phase synchronized. This dependence is evident in Fig. 2(b) where

the $\langle C \rangle_k$ trends for two different coupling regimes are plotted as a function of k, showing an anti-correlation (blue circles) between k and C for small d. This behaviour is suggesting that potentially we can use this anti-correlation as a proxy for the degree sequence.

To explore the scaling properties of this correlation, we varied $\langle k \rangle$ of the $P(k)$ while preserving the rest of the properties. We found that it scales with $\langle k \rangle$ as shown in Fig. 2(c) for ensembles of SF networks ($N = 150$) with three different mean degrees, where the $\langle C \rangle_k$ is plotted vs. the rescaled coupling $d\langle k \rangle$. It can be seen that the three curves of $\langle C \rangle_k$ for the nodes with the respective highest degree (filled markers) collapse up to exhibiting the same behaviour with $d\langle k \rangle$, as well as those for the nodes with the lowest degree (void markers), whose decreasing trends are much less pronounced.

4   Conclusions

In this work, we have inspected the relationship between the topological role of a node in a complex network and its dynamical behaviour, represented by its complexity. We show that in a simple star of identical chaotic oscillators, the hub exhibits a minimum of complexity in the route to synchronization while the leaves almost keep unperturbed their initial complex behaviour. When considering more heterogeneous degree distributions, the same behaviour is observed in the route to synchronization, with higher degree nodes exhibiting lower values of complexity. Importantly, when comparing the complexity of each node and its degree, we found a distinctive linear correlation with higher degree nodes exhibiting less complexity and that is generally observed in networks of other types of chaotic oscillators or pulse-coupled neurons. The reported results could explain recent observations about the low complexity of the hubs in functional brain networks [10] but, beyond than that, they suggest that the role played by the topology of a network could be unveiled by just computing the dynamical complexity associated with the time series sampled at each node. The fact that structural information of a network can be inferred without computing pairwise correlations like those commonly performed in functional networks could be exploited in diverse fields as neuroscience, econophysics or power grids.

References

[1] R. Albert and A.L. Barabási. Statistical mechanics of complex networks. *Rev. Mod. Phys.*, 74(1):47, 2002.

[2] A. Arenas, A. Díaz-Guilera, J. Kurths, Y. Moreno, and C. Zhou. Synchronization in complex networks. *Phys. Rep.*, 469(3):93 – 153, 2008.

[3] C. Bandt and B. Pompe. Permutation entropy: A natural complexity measure for time series. *Phys. Rev. Lett.*, 88:174102, 2002.

[4] S. Boccaletti, V. Latora, Y. Moreno, M. Chavez, and D.-U. Hwang. Complex networks: Structure and dynamics. *Phys. Rep.*, 424(4–5):175–308, 2006.

[5] G. Deco, T. J. Van Hartevelt, H. M. Fernandes, A. Stevner, and M. L. Kringelbach. The most relevant human brain regions for functional connectivity: Evidence for a dynamical workspace of binding nodes from whole-brain computational modelling. *NeuroImage*, 146:197–210, 2017.

[6] J. Gómez-Gardeñes, Y. Moreno, and A. Arenas. Paths to synchronization on complex networks. *Phys. Rev. Lett.*, 98(3):034101, 2007.

[7] S. Kullback and R. A. Leibler. On Information and Sufficiency. *The Annals of Mathematical Statistics*, 22:79–86, 1951.

[8] R. López-Ruiz, H.L. Mancini, and X. Calbet. A statistical measure of complexity. *Phys. Lett. A*, 209(5):321 – 326, 1995.

[9] M.T Martin, A Plastino, and O.A Rosso. Statistical complexity and disequilibrium. *Phys. Lett. A*, 311(2):126 – 132, 2003.

[10] J. H. Martínez, M. López, P. Ariza, M. Chavez, J. Pineda-Pardo, D. López-Sanz, P. Gil, F. Maestú, and J. M. Buldú. Functional brain networks reveal the existence of cognitive reserve and the interplay between network topology and dynamics. *Sci. Rep.*, 8(1):10525, 2018.

[11] A. Navas, J. A. Villacorta-Atienza, I. Leyva, J. A. Almendral, I. Sendiña-Nadal, and S. Boccaletti. Effective centrality and explosive synchronization in complex networks. *Phys. Rev. E*, 92:062820, 2015.

[12] D. Papo, M. Zanin, J. Pineda-Pardo, S. Boccaletti, , and J. M Buldú. Functional brain networks: great expectations, hard times and the big leap forward. *Phil. Trans. R. Soc. B*, 369(1653):20130525–20130525, 2014.

[13] A. Rad, I. Sendiña-Nadal, D. Papo, M. Zanin, J. M. Buldú, F. del Pozo, and S. Boccaletti. Topological measure locating the effective crossover between segregation and integration in a modular network. *Phys. Rev. Lett.*, 108:228701, 2012.

[14] O.E. Rössler. An equation for continuous chaos. *Phys. Lett. A*, 57(5):397–398, 1976.

[15] P. S. Skardal, D. Taylor, and J. Sun. Optimal synchronization of complex networks. *Phys. Rev. Lett.*, 113(14):144101, 2014.

DIFFRACTION LINE PROFILES OF SPHERICAL HOLLOW NANOCRYSTALS

Emiliano Burresi[1] and Leander Tapfer[1]

[1]*ENEA - Italian National Agency for New Technologies, Energy and Sustainable Economic Development, Brindisi Research Centre, Strada Statale 7 "Appia" km.7+300, 72100 Brindisi, Italy*

ABSTRACT. An analytical expression of diffraction line profiles of spherical hollow nanocrystals is derived in [1]. In this brief report we reported a summarized of the results about the calculation of the profile lines as a function of the nanocrystal size parameters. A more complete and exhaustive discussion about profile lines and other parameters such as integral breadth, the Fourier particle size and the Scherrer constants are given in [1]. The diffraction line profiles of hollow CdS nanocrystals of zincblende and wurtzite crystallographic structure are calculated and compared with Debye scattering profiles which were computed on the CRESCO Platform for High Performance Computing.

1 Introduction

Recently, hollow nanocrystals are attracting an increased scientific and technological interest due to their intriguing optical, electronic, electro- and photochemical and catalytic properties that may find use in potential applications in diverse fields such as nanoscale encapsulation and drug delivery, photocatalysis and plasmon photonics, energy storage (anode material in Li-ion batteries) and nanoreactors. Different synthesis approaches for the fabrication of nanoscale hollow structures are reported in literature: as examples Kirkendall cavitation process [2], template-free hydrothermal method [3], solvothermal method[4]. A more complete bibliography about synthesis methods is reported in [1].

X-ray scattering methods are experimental tools frequently used to investigate the structural properties and to determine morphological and structural parameters. In particular, for nanocrystalline materials X-ray diffraction is a very powerful and nondestructive evaluation tool that provides useful information for a better comprehension and understanding of the functional properties of nanocrystalline materials and that allows to optimize fabrication processes and synthesis procedures. In most cases the interpretation of the experimental data is achieved only by modeling of the diffraction profiles. Here it is fundamental to use the correct model for the data analysis. Indeed, the diffraction line profile and breadth are related to the size and shape of the nanocrystallites and analytical formulae for some particle shapes (spheres, cubes, cylinders, octahedral, tetrahedra) were found and are frequently used.

2 Diffraction on hollow spherical nanocrystals

The intensity diffraction line profile of a crystallite of dimension D can be expressed as [5]

$$I(k_s, D) = \frac{1}{V_0} \int_{-\tau}^{+\tau} V(t, D) \cdot e^{-2\pi i k_s t} dt \qquad (1)$$

with $k_s = k - k_0 = \frac{2}{\lambda} \cdot (\sin \theta - \sin \theta_0)$, where θ_0 is the Bragg angle and θ is the scattering angle. $V(t,D)$ is the common-volume-function of the crystallite and the "ghost" crystallite shifted by distance t parallel to the diffraction vector; τ is the value for which $V(t,D)=0$. $V(t,D)$ is an even function and the common-volume-function has the boundary conditions:

$$\lim_{t \to 0} V(t, D) = V_0 \quad \text{and} \quad \lim_{n \to \pm\tau} V(t, D) = 0 \ ,$$

where V_0 is the volume of the crystallite. In order to solve Eq.(1) the volume-function $V(t,D)$ must be known. For spherical shell structures, with internal radius r and outer radius R, first the solution of the volume function $V(t,r,R)$, i.e. the common-volume-function of the shell crystallite and the "ghost" crystallite shifted by distance t parallel to the diffraction vector, has to be found. As a consequence of diffraction in the far-field-approximation, the diffraction intensity profile corresponds to the Fourier transform of the crystallite. It follows that the Fourier transform of a crystallite, $V(t,D)$, represents the crystallite-size broadened and shape dependent line profile.

Of course, this is not the case of hollow structures that are geometrically defined by an inner surface too. In the case of spherical crystals the geometrical shape is defined simply by their inner and outer radius (or diameter). Hence, solving eq.(1) for spherical shell structures, with inner radius r and outer radius R, we obtain the normalized peak profile function

$$I(k_s, r, R) = \frac{1}{(R^3 - r^3) \cdot (2\pi \cdot k_s)^4} \cdot \sum_{j=1}^{5} T_j(k_s, r, R) \tag{2}$$

where the terms $T_j(k_s, r, R)$ are given in [1]. The diffraction profile patterns of hollow nanospheres calculated with Eq.(2) exhibit peculiar features. In Figure 1 are shown the diffraction line profiles for a hollow nanosphere of outer radius R=15nm and different inner radius values r=3, 8 and 15nm. No appreciable difference is observed between the diffraction profiles of the full sphere and the hollow sphere with r=3nm. However, with increasing inner radius the maximum peak intensity decreases as expected (decrease of the scattering volume) while the intensity of the tails increases with increasing hole radius. In particular for hollow spheres of thin shells a pronounced broadening and tail intensity enhancement is observed. The central peak width remains essentially the same for full and hollow spheres indicating that the main parameter that determines the peak width (FWHM) is the outer radius value R, while the intensity decay of the diffraction peak tails is determined by the inner radius r. The high frequency intensity oscillations (labeled as "h") close to the peak maximum are due to the whole dimension of the sphere, i.e. the periodicity is related to the outer radius R. In contrast, the low frequency oscillations (labeled as "s") and their periodicity is related also to the inner radius r of the hollow sphere, more precisely the periodicity is related to the shell thickness (R-r). From the experimental point of view, in most cases it will be difficult to observe the intensity oscillations in the diffraction profile curves. But the low frequency oscillations could be observed experimentally similarly to the oscillations of spherical crystallites.
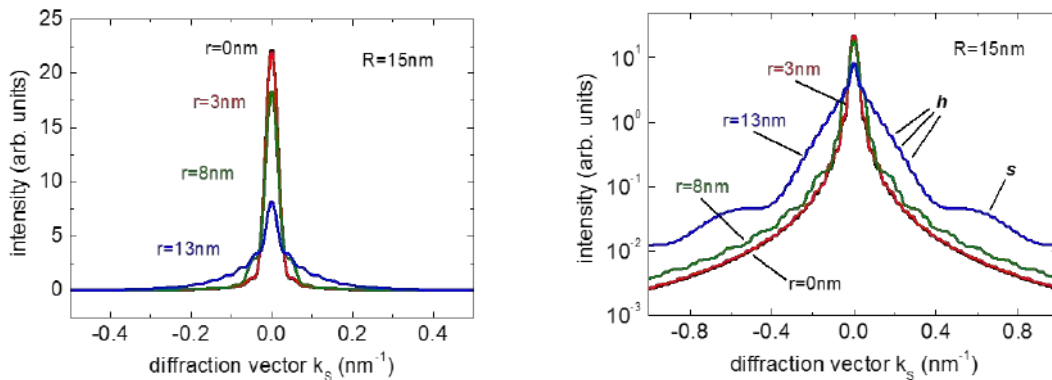
Fig.1: Calculated diffraction profiles of hollow spheres of outer radius R=15nm and inner radius r= 3nm, 8nm and 13nm,respectively (linear (left) and logarithmic scale (right)). The profiles for r=0nm correspond to the full sphere diffraction pattern.

3 Diffraction intensity profiles: a comparison with Debye diffraction

For a comparison of diffraction intensity profiles and powder patterns we consider a CdS spherical shell nanocrystals of both, zincblende (zb) and wurtzite (w), crystallographic structure. Figure 2 shows a schematic representation of the hollow zincblende and wurtzite CdS nanocrystals.
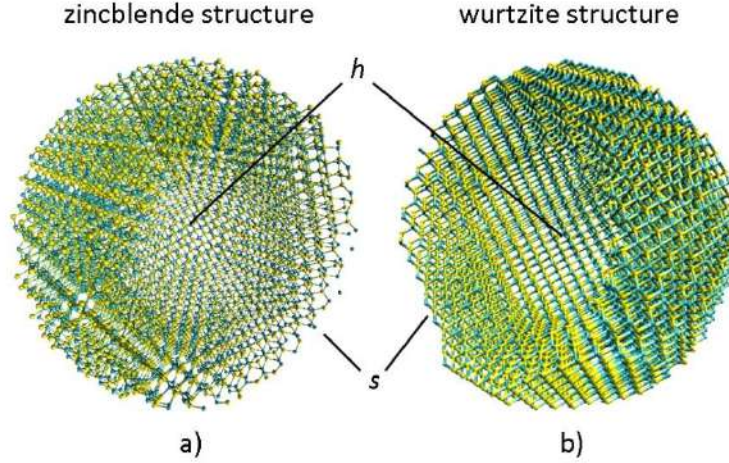

Fig.2: Constructed CdS hollow nanocrystal of zincblende (a) and wurtzite structure (b) used for the Debye diffraction calculation; Cd and S atoms are in blue and yellow color, respectively. Here, for a better visualization of the hollow structure (labelled h) of the CdS nanocrystals, part of the shells are removed (labelled s).

For small crystal structures the calculation of the intensity $I(s)$, with the scattering vector $s = 2\pi \cdot k$, can be also performed considering direct crystalline space, using the Debye scattering equation :

$$I(s) = \sum_{i,j=1}^{N} f_i(s)f_j(s)\frac{\sin(s \cdot r_{ij})}{s \cdot r_{ij}} \qquad . \tag{3}$$

where r_{jk} is the distance between the i-th and j-th atoms. In order to obtain the intensity for given values of momentum transfer, the atomic scattering factors $f_i(s)$ are calculated by using the known relation

$$f(s) = \sum_{i=1}^{4} a_i e^{\left(\frac{-b_i s^2}{16\pi^2}\right)} + c \tag{4}$$

with the corresponding coefficients a_i, b_i and c for Cd and S atoms, respectively. First, in order to calculate the Debye diffraction pattern (Eq. 3) unrelaxed spherical CdS clusters with zincblende and wurtzite phase were built (Fig.2); a first cutoff radius R from the center of the crystal defines the external size whereas a second cutoff radius r corresponds to the internal radius of the hollow cluster. For the spherical nanocrystals of both the crystallographic structures an outer radius R=3.60nm has been considered, while an inner radius of r=2.00nm and r=1.95nm for the zb and w crystallographic structure, respectively, is considered in order to fulfill the requirements to have a hollow nanocrystal constituted by an integer number of atoms. The whole diffraction patterns of a hollow zincblende CdS NC calculated by the Debye scattering (curve A) and the Eq.(2) (curve B) are shown in fig 3_1 and 3_2. In the same way, in [1] we reported the profile curves and relative discussion for wurtzite CdS NC. The diffraction peak positions and relative intensity ratios in curve B are in accordance with the data of ICCD n.80-0019 of bulk zincblende CdS. For some diffraction peaks, the Debye scattering pattern shows a noticeable discrepancy in the relative intensity ratios.
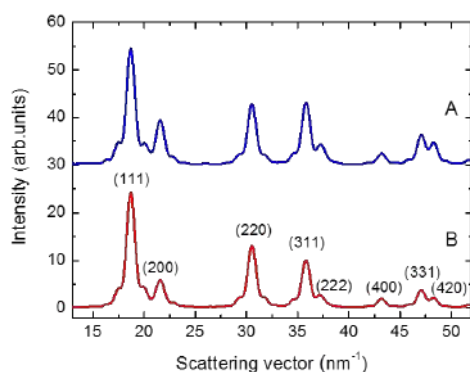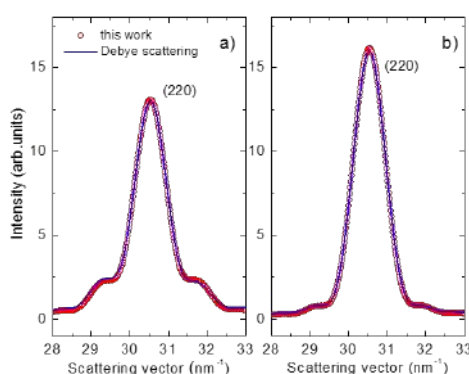
Fig.3: Whole diffraction patterns of hollow CdS nanocrystal of zincblende structure calculated with the Debye scattering formula (A) and Eq.(2) of this work (B) (Fig 3_1). In figure 3_2 diffraction line patterns of the (220) peak for the hollow CdS NC (a) calculated with the Debye scattering formula (blue line) and Eq.(2) of this work (red circles) were shown. For comparison the (220) diffraction line profile of the full CdS NC (r=0nm) is also shown (b).

The tail intensity enhancement, as discussed above and shown in Fig.1, is a fingerprint of line diffraction profiles of hollow nanocrystals. Figure 3_2 shows the diffraction line profiles of the (220) for the Debye scattering (blue solid line) and the model of this work, Eq.(2), (red circles). A perfect correspondence of the line profiles is observed. The code for Debye calculation has been written in FORTRAN programming language; It was compiled and executed in serial mode on CRESCO platform.

4 Conclusion

Summarizing, an analytical expression of the diffraction line profile of spherical hollow nanocrystals, with outer and inner radius R and r, respectively, has been derived by using Wilson's approach. The diffraction line profiles of spherical hollow nanocrystals exhibit an enhanced intensity at the tails of the diffraction peaks that can be considered as a fingerprint of the hollow nanostructure. For comparison, the diffraction profiles of spherical hollow CdS NCs of zincblende and wurtzite crystallographic structure were compared with the diffraction curves calculated by using the Debye scattering equation.

5 References

[1] E. Burresi, L Tapfer, Nanomaterials and Nanotechnologies 2019; 9:1 https://doi.org/10.1177/1847980419832386

[2] Yin Y, Rioux RM, Erdonmez CK, Hughes S, Somojai GA and Alvisatos AP, Science 2004; 304(5671): 711-714. DOI: 10.1126/science.1096566.

[3] Jiao S, Lian G, Jing L, Xu Z, Wang Q, Cui D, Wong C-P. ACS Omega 2018; 3: 1329-1337. DOI: 10.1021/acsomega.7b01340.

[4] Kobayashi M, Kato H and Kakihana M, Nanomater Nanotechnol 2013; 3: 23:2013. DOI: 10.5772/57533.

[5] Langford IJ and Wilson AJC J Appl Cryst (1978); 11: 102-113 DOI: 10.1107/S0021889878012844

Validation and Analysis of the MITO circulation forecast model for the Mediterranean Sea-Black Sea

G. Sannino, A. Bargagli, A. Carillo, R. Iacono, E. Lombardi, E. Napolitano, M. Palma, G. Pisacane, and M.V. Struglia

ENEA, SSPT-MET-CLIM Laboratory

ABSTRACT. MITO, a new 3D, tide including oceanic model of the Mediterranean and the Black Sea circulation has been developed and tested using the CRESCO4 cluster in 2017. After the test phase, the model has been implemented operationally and provides daily forecasts of the circulation. During 2018, the outputs of MITO have been analysed to assess the skill of the forecasts, and the local effects of the dynamics.

1 The MITO model

Tidal amplitudes in the Mediterranean Sea are generally small, but they are locally amplified by bathymetric features in several regions, such as the Strait of Gibraltar, which is the entrance door for the Atlantic water (AW) and for the tides propagating from the Atlantic, and the Sicily Channel, which separates the western Mediterranean from the eastern sub-basin. Tidal effects are also relevant in the northern part of the Adriatic Sea, and in the Strait of Messina, where rich dynamics have been observed, including propagating solitary waves (see, e.g., the recent work by Droghei *et al*. [1] and references therein) and very intense tidal currents. A recent assessment [2] indicates that these currents are strong enough to be harvested by actual tidal turbines.

When modelling ocean circulation in these areas, the effect of tides cannot be neglected, particularly in high-resolution models of coastal dynamics, which therefore need to be nested with coarser resolution models that fully account for tidal effects. To resolve the short-time, local effects that are relevant to the applications, we have developed and implemented a high-resolution, operational model of the Mediterranean Sea-Black Sea system.

The main features of the model have been described in [3]. Here we only recall that the model domain covers a wide domain, extending from the Gulf of Cadiz to the Black Sea, with a constant horizontal resolution of 1/48° in most of it, which is further increased in the Strait of Gibraltar and in the Turkish Strait System. The model is discretized vertically using 100 unevenly distributed Z-levels; with a minimum thickness of 2 m in the upper layer.

2 Model validation

Besides looking at the operational forecasts, we have also analyzed a longer, dedicated simulation, spanning the period 19 March-30 April 2018. This simulation, which does not include any kind of data assimilation or relaxation, has been performed to assess the capability of the model to correctly describe the variability of the circulation and hydrology in the period in consideration.

Figure 1 shows the time evolution of the average sea surface temperature (SST) for the whole Mediterranean Sea (Med), the western Mediterranean (Wmed), the eastern Mediterranean (Emed), and the Black Sea (Black). The black curves correspond to the values from the simulation, whereas the red curves are obtained from satellite data. The model and data SST values are quite close all along the simulation, with differences smaller than 0.5 °C everywhere, except in the Black Sea, in

the last ten days of the simulation. This is a good result, also considering that the simulation period is characterized by a relevant warming of the Mediterranean basin.
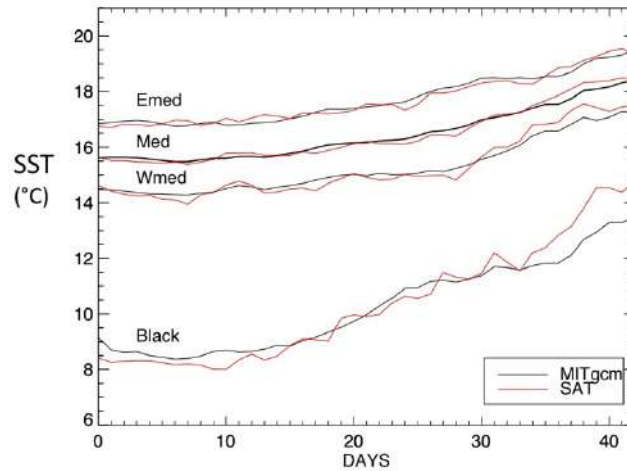

Fig. 1. Evolution of the average SST for four basins: the whole Mediterranean Sea (Med), the western Mediterranean (Wmed), the eastern Mediterranean (Emed), and the Black Sea (Black). The black curves correspond to the values from the simulation, whereas the red curves are obtained from satellite data.

Good agreement with data is also found when looking at the spatial distribution of the SST. After one month of simulation, the bias between the model and the satellite SST fields is smaller than 1 °C in most of the Mediterranean Sea, and is comparable to the bias in the initial condition (not shown). Likewise, the circulation patterns are found to remain in very good agreement with satellite observations (altimeter data) over the whole span of the simulation.

Local time series of the model surface elevation, covering the period of the run, have been compared with corresponding surface height time series extracted from the tide gauges available through the Copernicus portal, whose positions (54 stations) are shown in panel a of Figure 2.
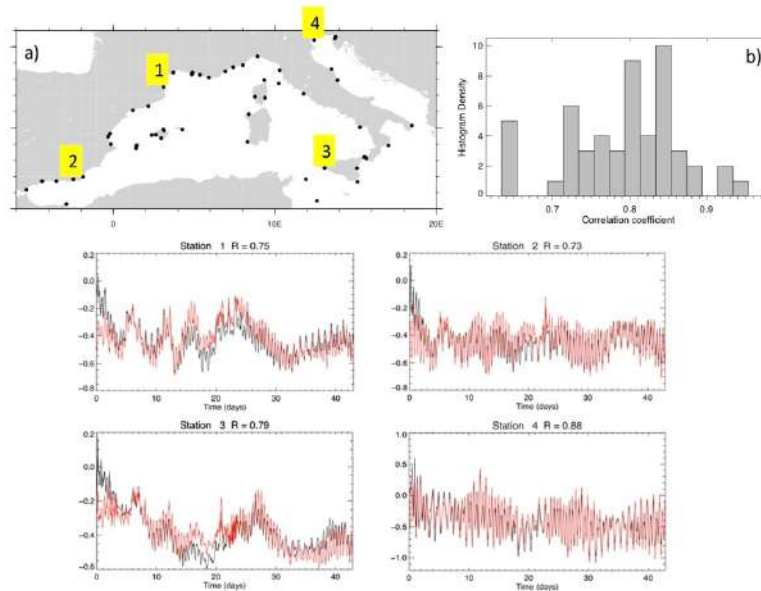
Fig. 2. Example of validation of the tidal dynamics through comparison with tide gauge data, taken at the stations indicated in the left upper panel. The lower panels show time series (hourly data) of the model (black) and tide gauge (red) elevation at stations 1-4, with the corresponding correlation coefficients (R) indicated in the titles. The right upper panel is a histogram of R over the whole dataset.

Panel b of the figure provides a histogram plot of the correlation coefficient (R) between the two time series, computed at each site. Values of the coefficient are high in almost all stations (R > 0.8 for 31 of the 54 tide gauges). In the lower panels, we plot the experimental (red) and model (black) time series in four stations, representative of different regions of the computational domain. The experimental and numerical time series agree quite well; maximum discrepancies are usually concentrated in the first days of the simulation, in which adjustment to the initial conditions takes place.

3. Tidal effects

We have also explored the effects of tides on the circulation, in specific regions of our model domain. Among these, the Sicily Channel, which plays a crucial role in the Mediterranean Sea dynamics, and is one of the places where tides are known to have a strong effect on the dynamics [4]. Figure 3 focuses on the portion of the Channel that hosts a wide, shallow area named Adventure Bank (red box in the upper panel, where the bathymetry of the area is displayed).
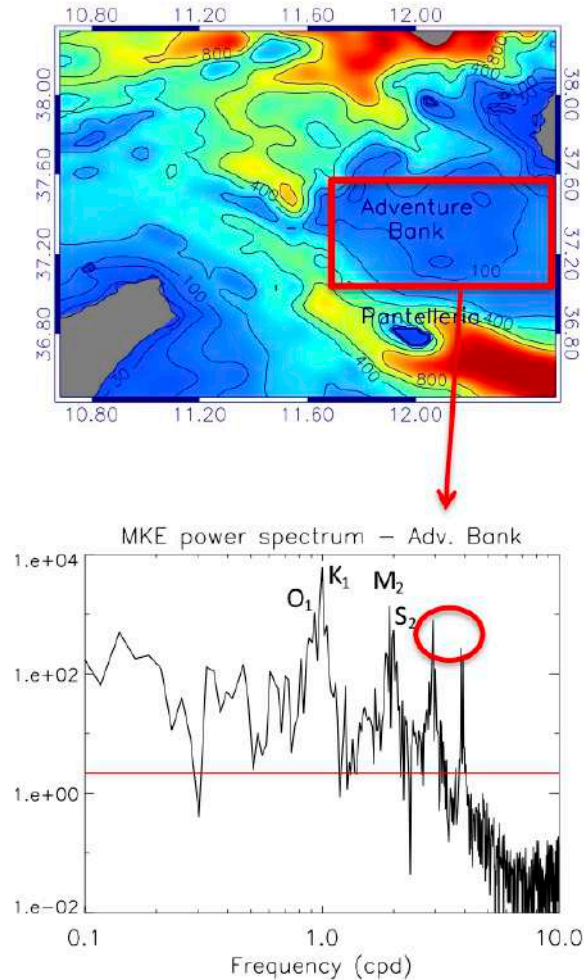
Fig. 3. Upper panel: bathymetry of the Sicily Channel. Lower panel: power spectrum of the time series of MKE (averaged over the red box over the Adventure Bank, and over the first 100 m), with the red line indicating a 95% confidence level. Besides the peaks corresponding to the four main tidal components, there are two significant peaks (red oval), at 8 and 6 hours, produced by nonlinear interactions.

In the lower panel of the figure is shown the power spectrum computed from the the time series of mean kinetic energy (MKE), averaged over the red box, and over the first 100 m of the water column (the red line indicates the standard significance level, corresponding to a 95% confidence level). We have highlighted the peaks corresponding to the four tidal components that are included in the model; the main diurnal component (K1) is found to be the dominant one, in agreement with the observations [4]. It should be noted, however, that two other significant spectral peaks are also present, corresponding to shorter periods (8 and 6 hours). Since no other physical forcing acts on these time scales, they must represent harmonics of the diurnal and semidiurnal components. The nonlinear interactions that produce these components have been studied in the English Channel and in the North Sea (see the review [5]), but these effects have not been observed before inside the Mediterranean Sea. This is an important result, because it shows that in the Sicily Channel the effect of the tides cannot be correctly recovered by just adding the appropriate tidal signal to the results of a not tide-including simulation.

References

[1] Droghei R., Falcini F., Casalbore D., Martorelli E., Mosetti R., Sannino G., Santoleri R., Chiocci F.L., "*The role of Internal Solitary Waves on deep-water sedimentary processes: the case of up-slope migrating sediment waves off the Messina Strait.*" Scientific Reports **6** (2016), pp. 36376.

[2] Coiro D., Troise G., Nadia B., "*Experiences in Developing Tidal Current and Wave Energy Devices for Mediterranean Sea*", Frontiers in Energy Research **6** (2018) pp. 136.

[3] M. Palma, R. Iacono, A. Bargagli, A. Carillo, E. Lombardi, E. Napolitano, G. Pisacane, G. Sannino, M. V. Struglia, and B. M. Fekete, "Mediterranean and Black Sea pre-operational tidally forced ocean model," submitted to Ocean Modelling.

[4] Gasparini G.P., Smeed D.A., Alderson S., Sparnocchia S., Vetrano A., Mazzola S.," *Tidal and subtidal currents in the Strait of Sicily*," J. Geophys. Res. **109** (2004), C02011.

[5] Anderson O.B., Egbert G.D., Erofeeva S.Y., Ray R.D, "*Mapping nonlinear shallow-water tides: a look at the past and the future*," Ocean Dynam. **56** (2006) pp. 416-429.

AIR QUALITY FORECAST SYSTEM OVER ITALY: FORAIR-IT

Adani Mario[1*], Guarnieri Guido[2], Vitali Lina[1], Mircea Mihaela[1], D'Isidoro Massimo[1], Cappelletti Andrea[1], and Ciancarella Luisella[1]

[1]*ENEA, SSPT-MET-INAT, via Martiri di Monte Sole 4, 40129, Bologna, Italy[1]*

[2]*ENEA, DTE-ICT-HPC, Piazzale E. Fermi, 1 (Porto del Granatello), 80055, Portici (NA), Italy*

ABSTRACT. A new high resolution air quality forecasting system has been developed by the SSPT-MET-INAT group in ENEA consisting of a modelling chain implemented on CRESCO4 HPC. The system is operating on daily basis and deliver forecasts of pollutant concentrations up to 3 days in advance over Europe and Italy. This paper presents briefly the modeling system, the input data used and some results as an example.

Introduction

Since 2002 ENEA has been developed the Italian Integrated Assessment Modelling System (MINNI) for supporting the International Negotiation Process on Air Pollution and assessing Air Quality Policies at national/local level [1,2], supported by Italian Ministry of the Enviroment, Land and Sea. Based on such experience, ENEA developed a prototype for a national air quality forecasting system [3]. Starting from this, it was developed FORAIR-IT system by increasing horizontal spatial resolution up to 4 km over the Italian territory, including the islands: Sicily and Sardinia. FORAIR is operational since 2017 and delivers pollutant concentrations up to 3 days in advance.

2 Description of the forecasting system

FORAIR modeling system runs on European domain (12.35°W-27.59°E and 30.54°N-56.17°N) at 20 km grid resolution and on Italian domain (6.39°E-18.67°E and 36.26°N-46.77°N) at 4 km grid resolution using two-way nesting approach. The modeling chain downloads GFS meteorological forecast from NCEP (U.S. meteorological system); NCEP fields are used to feed RAMS [4] prognostic meteorological model. SURFPRO pre-processor [5] prepares the RAMS model output as input for the chemical transport model FARM [6] which also requires chemical boundaries conditions and emissions as input. Chemical boundary conditions for EU domain are retrieved from Copernicus Atmospheric Service (CAMS, http://atmosphere.copernicus.eu). Emission inventory for Italian domain has been provided by ISPRA (http://www.sinanet.isprambiente.it/it/sia-ispra/inventaria) and for European domain has been provided by TNO (www.tno.nl), same inventory with the one used by European air quality forecast system Copernicus (https://www.regional.atmosphere.copernicus.eu/). The anthropogenic emissions for all the pollutants were disaggregate in space and time by the EMMA [7] software considering the gas phase SAPRC99 [8] photochemical mechanism and AERO3 aerosol model [9] included in air quality model FARM. Natural aerosol emissions such as dust erosion, sea-salt and biogenic emissions of volatile organic carbon (BVOC) are computed using SURFPRO software. The BVOC emissions are computed using MEGAN model [10]. The thermodynamic equilibrium between gas and aerosol phases of condensable inorganic and organic species are based on ISOROPIA model [11,12] and SORGAM model [13], respectively. The main characteristics of the air quality forecasting system are

---

[1] Corresponding author. E-mail: mario.adani@enea.it.

summarized in Table 1 and Error: Reference source not found for European and Italian domains, respectively.

Table 1: Summary of main characteristics for European forecasting system set up.

Modeling system: Current Forecast System.	EU domain	IT domain
Horizontal resolution	20 km	4 km
Vertical resolution	16 vertical levels	16 vertical levels
Chemical Transport model FARM		
Gas phase chemistry	SAPRC99	SAPRC99
Heterogeneous chemistry	Not in operational version yet	Not in operational version yet
Aerosol size distribution	AERO3	AERO3
Inorganic aerosols	ISORROPIA	ISORROPIA
Secondary organic aerosols	SORGAM	SORGAM
Aqueous phase chemistry	Sulphate	Sulphate
Dry deposition/sedimentation	Yes	Yes
Mineral dust	Yes	Yes
Sea Salt	Yes	Yes
Pollens (which species)	No	No
Boundary values	CAMS Global Service Provider (aerosol, reactive gases)	EU domain
Initial values	D-1 form EU domain	D-1 form IT domain
Anthropogenic emissions	TNO 2005	ISPRA 2010
Biogenic emissions	Yes (MEGAN model)	Yes (MEGAN model)
Meteorological forecast system		
Meteorological driver	RAMS (boundary and initial values from GFS NCEP)	RAMS (boundary from EU domain and initial values from GFS NCEP)
Assimilation system in development		
Assimilation method	Successive Correction Method Optimal Interpolation	Successive Correction Method

		Optimal Interpolation
Observations (in-situ and satellite if relevant) assimilated	In-situ	In-situ
Frequency of assimilation	Hourly	Hourly

3 Discussion and future work

The forecasting system is composed by serial and parallel processes that use up to 384 cores. The entire procedure takes about 7 hours. Results for the major pollutants are usually available before 3:00 local time for the present day (D0) and the two following day (D1 and D2).
An example of the results is shown in Figure 1 for the European and Italian domain.
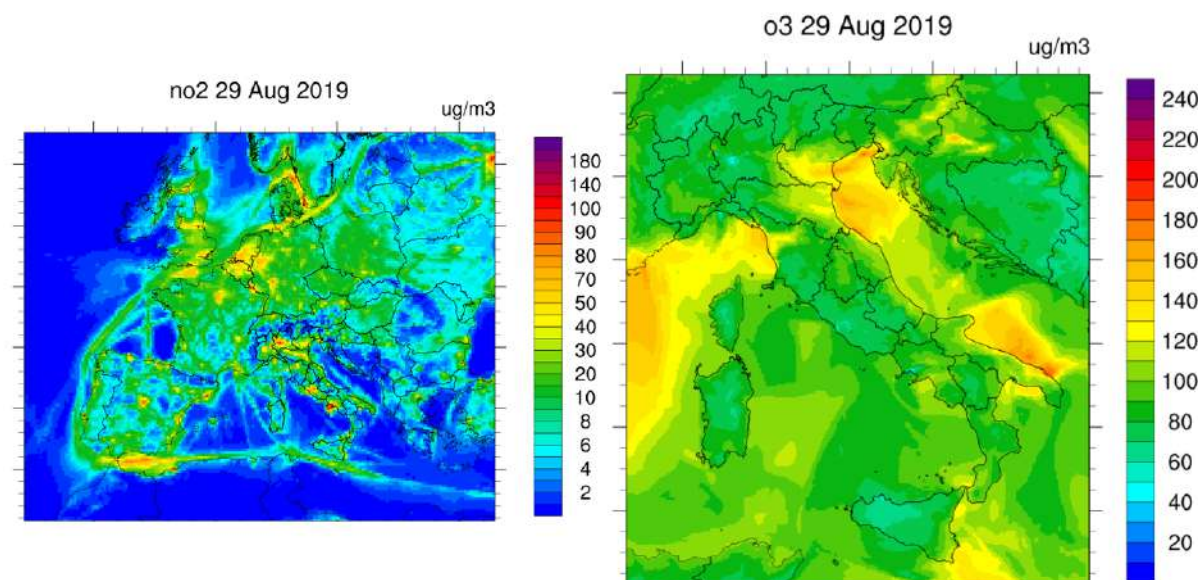
Fig.**1**: Hourly daily max for nitrogen nioxide (panel a) and maximum 8h average for ozone (panel b). A detailed analysis of the model skills is available at the following link: http://www.afs.enea.it/project/ha_forecast/verification_report_FORAIR_2017.pdf
Next upgrades to FORAIR systems will be the substitution of the meteorological model RAMS with WRF, the implement fire emissions, the update the antropogenic emission inventories both for European and Italian domains, the assimilation of available observations and provide tailored products for the end users.

References

[1] M. Mircea, L. Ciancarella, G. Briganti, G. Calori, A. Capelletti, I. Cionni, M. Costa, G. Cremona, M. D'Isidoro, S. Finardi, G. Pace, A. Piersanti, G. Righini, C. Silibello, L. Vitali, G. Zanini. Assessment of the AMS-MINNI system capabilities to simulate air quality over Italy for the calendar year 2005. *Atmospheric Environment*, **84**, pp. 178-188, (2014).

[2] I. D'elia, , M. Bencardino, L. Ciancarella, M. Contaldi, G. Vialetto. Technical and non-technical measures for air pollution emission reduction: the integrated assessment of the regional air quality management plans through the italian national model. *Atmospheric Environment*, **43**, pp. 6182-6189, (2009).

[3] M. Adani , M. D'isidoro, G. Briganti, A. Cappelletti. Implementation of an air quality forecast system over italy. H*igh Performance Computing on CRESCO infrastructure:research activity and results 2015*, enea, (2016).

[4] W.R. Cotton, R. A, Pielke, R.L. Walko, G. E. Liston, C. J. Tremback, H. Jiang, R. L., Mc anelly, J.Y. Harrington, M. Nicholls, G. G, Carrio and J. P. Mcfadden. RAMS 2001: Current status and future directions. *Meteorology and Atmospheric Physics*, **82**, pp 5-29, (2003).

[5] Arianet. SURFPRO3 user's guide (surface-atmosphere interface processor, version 3). *arianet report R2011.31* (2011).

[6] C. Silibello, G. Calori, G. Brusasca, A. Giudici, E. Angelino, G. Fossati, E. Peroni, E. Buganza. Modelling of pm10 concentrations over milano urban area using two aerosol modules. environmental *modelling and software*, **23**, pp. 333-343, (2008).

[7] Arianet. *EMission MAnager – processing system for model-ready emission input.user's guide. arianet report R2013.19.* (2013)

[8] W. P. L. Carter. Documentation of the saprc-99 chemical mechanism for voc reactivity assessment. *Final report to california air resources board,* Contract no. 92-329, and (in part) 95-308, (2000)

[9] F.S. Binkowski, S. J. Roselle. Models-3 community multiscale air quality (cmaq) model aerosol component 1. model description. *Journal of geophysical research*, **108**, 4183. (2003)

[10] A Guenther, T. Karl, P. Harley, C. Wiedinmyer, I. Palmer. Estimates of global terrestrial isoprene emissions using megan (model of emissions of gases and aerosols from nature). *Atmos. chem. Phys.*, **6 (11)**, pp. 3181-3210. (2006)

[11] C. Fountoukis. and A. Nenes. ISOROPIA II: A new aerosol equilibrium model, *Atmos. chem. Phys.*, **7**, pp. 4639–4659. (2007)

[12] nenes a., pandis s.n. , pilinis c. ISORROPIA: A new thermodynamic equilibrium model for multiphase multicomponent inorganic aerosols, *Aquatic Geochemistry*, 4: 123. (1998)

[13] B. Schell, I. J. Ackermann, H. Hass, F. S. Binkowski, A. Abel. Modeling the formation of secondary organic aerosol within a comprehensive air quality modeling system. *j geophys. res.*, **106**, d22, pp. 28275-28293 (2001)

WAVE DIFFRACTION AND TRANSMISSION BY A SUBMERGED BREAKWATER

Pasquale Filianoti[1]*, Luana Gurnari[1],

[1] *University Mediterranea of Reggio Calabria, DICEAM, Salita Melissari,89122, Reggio Calabria, Italy*

ABSTRACT. The main challenge in building submerged breakwaters consists in guaranteeing the effectiveness of the breakwater, in terms of coast protection, achieving the maximum submergence. In this work, we carried out a numerical experiment on a submerged breakwater that incorporates an Oscillating Water column device (named REWEC1), able to work 2-3 meters below the sea water level, comparing results with the 'passive' configuration of a REWEC1. The numerical simulation was carried out through CRESCO platform, using the CRESCO3 cluster. In this work, we used the word or cresco3_16h24 code with 48cores (16x3).

1 Introduction

Breakwaters are commonly used to protect coasts, reducing the impact of waves on the beach. The main challenge in building submerged breakwaters is to guarantee the effectiveness in attenuating wave energy maintaining a moderate submergence. To this aim, the possibility of improving the breakwater effectiveness is here investigated analysing in depth various phenomena involved in the wave-structure interaction (i.e. reflection, dissipation, absorption and transmission). The investigation is carried out by a numerical experiment on a particular kind of submerged breakwater in protecting coasts. It consists in a reinforced concrete breakwater that incorporates a Wave Energy Converter, belonging to the family of Oscillating Water Column devices, named REsonant Wave Energy Converter, realization no. 1 ([1]). The REWEC1 is a submerged caisson breakwater for protecting coasts which remains on the seabed typically 2 or 3 m below the sea surface. The breakwater performs an "active" defence, in that it is able to absorb a share of the incident wave energy ([2]), with a very small environmental impact. The performance of this plant was investigated by [3], that proposed an original methodology for linearizing the differential equations to describe the flow motion inside the plant. To quantify the share of the energy transmitted in the lee of the plant, in respect to an impermeable submerged breakwater, the results of the numerical experiment were compared with the result obtained with 'passive' configuration of REWEC1 breakwater, in that the plant plenum is filled by water.

2 The numerical experiment

The REWEC1 is a caisson breakwater embodying an Oscillating Water Column device, with an U-shaped conduit, able to absorb wave energy. For this reason, REWEC1 is also named the U-OWC. The branch of the U-conduit is a vertical duct which extends along the wave-beaten wall of the caisson, and it is connected with the sea through an outer opening. The other branch is a plenum which extends along the whole caisson with an air pocket. Under the wave action, the pressure on the outer opening of the

---

*Corresponding author. E-mail: `filianoti@unirc.it`.

vertical duct fluctuates and, as a consequence, water goes up and down in the vertical duct and in the box, and the air mass in the plenum behaves as a spring. The plant has two configuration:"active" (able to absorb wave energy) during summer seasons, "passive", in the rest of the year, with the absorption box flooded. The dimensions of the plant are the same described in [2].

In order to analyse the wave field around the 'active' and the 'passive' submerged breakwater, we carried out an experiment in a numerical wave flume. This is equipped by a piston type wavemaker on the left side of the domain and a vertical wall on the right. The dimensions of the computational domain and the characteristics of the spatial discretization are shown in Fig. 1. The wave flume is 1 km long and the submerged breakwater is placed at the middle of the domain, the water depth is 10 m and the structure is 22.5 m long and 7 m high. The length of the numerical flume has been chosen in order to have many wavelengths, L, in front of and behind the absorber, where stationary condition are well established.
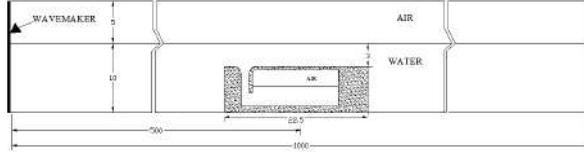
Figure 1: Sketch of the computational domain [measures are in meters].

The numerical approach is based on a two-dimensional CFD simulation using the Euler-Euler approach, implemented in the commercial code Ansys Fluent 17.0. To represent the air-water interface we used the volume of fluid (VOF) model in which two or more fluids (or phases) are not interpenetrating between each other. In order to obtain the spatial discretization of the convection terms in the governing equations, we used the Green-Gauss Cell-Based method to gradient evaluation and the PRESTO! (PREssure STaggering Option) scheme for pressure equation. In this work, we use the all 'triangles mesh' in the domain far from the structure and rectangular mesh in the nearby of the structure and near the air-water interface (see Fig. 2). The latter choice is made to achieve a better resolution of the instantaneous free surface displacement. The size of mesh is variable according to geometrical needs. In particular, we adopted a ticker mesh near the structure edges than elsewhere in the domain.

The wave-flume has a piston-type wavemaker placed on the left extremity of the computational domain. Starting from rest, the wave generation process has been simulated assigning a sinusoidal velocity to the left wall of the wave flume, by means of a User Defined Function (UDF). The Fluent dynamic mesh feature has been used for both the wall motion and the deformation of the neighbouring cells. The wave field generated is characterized by 4.8 s of wave period T, and 1.5m of wave height H.
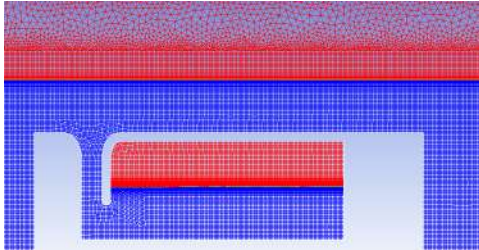
Figure 2: Spatial discretization of the computational domain; water and air are represented in blue and red, respectively.

3 The wave field around the 'active' configuration of the U-OWC

In order to verify the share of the incident wave energy absorbed, reflected and transmitted by the U-OWC device, we have calculated the energy flux in different cross sections along the wave flume. To

this aim, we have evaluated the pressure fluctuation Δp and the velocity, v_n, in 24 points along several vertical cross section of the flume and in 5 points along the horizontal cross section on the outer opening of the U- duct. The mean energy flux per unit length is evaluated as:

$$\bar{\Phi}(y) = \frac{1}{T} \int_0^T \int_l \Delta p(y, z, t) v_n(y, z, t) \mathrm{d}l \mathrm{d}t, \tag{1}$$

being v_n the velocity, normal to the cross section considered and l is the line section. In particular, we have evaluated the energy flux in 4 cross sections:

(i) at 3 L far from the wavemaker (energy flux of the incoming wave train, Φ_{in});

(ii) at 2 L in front of the U-OWC (energy flux of the reflected waves, Φ_0);

(iii) at 1 L far from the structure (energy flux of the transmitted waves, Φ_{tr});

(iv) at the outer opening od the plant, in the middle of the U-duct (energy flux absorbed by the U-OWC of the plant, Φ_{abs}).

The instantaneous energy flux of the incident waves, representing the energy of the waves generated by the wavemaker, was evaluated during the time interval in which a stationary progressive wave is established. Applying Eq.(1) at the vertical cross section near the piston type wavemaker, we have obtained a mean energy flux of the incident wave equal to 9.4 kW/m.

The wave field in front of the submerged absorber is not a pure reflective wave field. It is a superimposition of the incoming waves, the reflective waves and the pulsating discharge through the plant. The mean energy flux of this quasi standing wave field is equal to 5.6 kW/m. The reflection coefficient was estimated by means of the Healy's (1952) formula:

$$\mathcal{R} = (H_v - H_n)/(H_v + H_n); \tag{2}$$

where H_v and H_n are the quasi-antinode and the quasi-node height, respectively. They are equal to 2.1 m and to 1 m, respectively and then $\mathcal{R}$ is equal to 0.35.

The instantaneous energy flux absorbed by the plant, Φ_{abs}, was evaluated multiplying the pulsating discharge through the outer opening of the U-duct by the pressure fluctuation. The mean value evaluated by means of Eq. (1) is equal to 2.2 kW/m. The ratio between time averaged values of Φ_{abs} and energy flux Φ_{in} of incident waves, represents the absorption coefficient, $\mathcal{A}$. It is the 24% of the mean energy flux of the incident waves. On the other hand, the performance of the plant depends on several aspect (i.e. the ratio between the widths of the chamber and the U-duct, the air mass in the plenum, the submergence, the resonance conditions). In this simulation, the pressure fluctuation and the pulsating discharge are not in phase between them, and the time difference is about a quarter of wave period, highlighting that the plant is working not in resonance conditions.

Finally, the instantaneous energy flux transmitted in the lee of the submerged absorber is equal to 3.3 kW/m. The ratio between the height of the wave transmitted behind the breakwater and the height of the incident waves represents the transmission coefficient, $\mathcal{T}$. Being the the average height of the wave transmitted equal to 0.96 m, $\mathcal{T}$ is equal to 0.64.

4 Comparison between 'active' and 'passive' breakwater

Summarizing, starting from 9.4 kW/m generated by the wavemaker, the absorption coefficient $\mathcal{A}$ is equal to 0.24, the reflection coefficient $\mathcal{R}$= 0.35 and finally the transmission coefficient $\mathcal{T}$=0.64. Applying the energy balance to a control volume around the submerged absorber breakwater in a dissipative medium:

$$\mathcal{T}^2 + \mathcal{R}^2 + \mathcal{L}^2 + \mathcal{A} = 1, \tag{3}$$

the energy loss $\mathcal{L}^2$, on the roof of the breakwater is equal to 0.23. The quasi standing wave field before the breakwater is strongly affected by the presence of the pulsating discharge through the U-OWC for

what regards both the amplitude and the shape of the waves. Indeed the mean value of the energy flux in front of the 'passive' submerged breakwater is 8.7 kW/m, that is about 36 % greater than in front of the 'active' submerged breakwater. The reflected wave height can be calculated by means of Haely's formula [4]:

$$H_r = \frac{H_v - H_n}{2}. \tag{4}$$

In front of the U-OWC, H_r is about 40 % greater than in front of the passive breakwater. It follows that the reflection coefficient is

$$\mathcal{R} = \begin{cases} 0.38 & \text{'Active' submerged breakwater,} \\ 0.20 & \text{'Passive' submerged breakwater.} \end{cases}$$ Comparing the transmitted wave energy we have 3.9

kW/m behind the 'passive' submerged breakwater that is 15 % greater than behind the 'active' breakwater. In term of transmission coefficient, we have:

$$\mathcal{T} = \begin{cases} 0.64 & \text{'Active' submerged breakwater,} \\ 0.7 & \text{'Passive' submerged breakwater.} \end{cases}$$

being the wave height transmitted in the lee of the 'active' submerged breakwater 10 % less than the wave height transmitted in the lee of the' passive' one. Finally, the loss coefficient is

$$\mathcal{L}^2 = \begin{cases} 0.23 & \text{'Active' submerged breakwater,} \\ 0.47 & \text{'Passive' submerged breakwater.} \end{cases}$$

Concluding, in front of the 'active' configuration of REWEC1 we have a higher wave height than in front of the 'passive' configuration and, a lower dissipation over the roof. In the energy balance of Eq. (3), this difference is covered by the presence of the absorption coefficient $\mathcal{A}$. However, the latter is too small to modify, sensitively, the transmission of energy in the lee of the submerged breakwater, that remains, practically, unchanged in both REWEC configurations.

5   Conclusions

In order to improve the effectiveness of submerged breakwaters in attenuating the transmitted energy, maintaining a moderate submergence, we investigated a submerged breakwater incorporates a REsonant Wave Energy Converter, able to protect coast, although remains 2 or 3 m below the sea surface. The breakwater performs an "active" defence, in that it is able to absorb a share of the incident wave energy. The "passive" configuration is that the REWEC1 plenum is filled by water. Results show the capability of the plant to modify, strongly, the wave field around of itself. The reflected wave height increases about 40% in front of the absorber breakwater. The U-OWC absorbs only the 24% of the incident wave energy and the presence of the pulsating discharge, probably, modify only the wave field close to the outer opening of the plant. Indeed, the energy losses are the same in both cases, but they are dissipated in a different way: in the 'passive' configuration, the energy losses on the roof was dissipated by breaking waves and frictions; in the 'active' configuration the energy losses on the roof were absorbed by the plant and dissipated by minor hydrodynamic losses inside the absorber.

The energy reflected is reduced only about 10 % in respect to the "passive" configuration. It means that to reduce the waves transmitted at the lee of the breakwater it is necessary to improve the absorption by the plant. Under this point of view, this active submerged breakwater, if suitably optimized, should be used to protect coasts and, simultaneously, to produce energy, installing a power take off system. Clearly, to achieve the high performance of this U-OWC submerged breakwater largely described in literature, it is necessary a frequency analysis of the plant, in order to better tune it with the incoming waves.

References

[1] P. Boccotti, "On a new wave energy absorber," *Ocean Engineering*, no. 30, pp. 1191–1200, 2003.

[2] P. Filianoti and R. Piscopo, "Sea wave energy transmission behind submerged absorber caissons," *Ocean Engineering*, no. 93, pp. 107–117, 2015.

[3] P. Filianoti and S. M. Camporeale, "A linearized model for estimating the performance of submerged resonant wave energy converters," *Renewable energy*, no. 33, pp. 631–641, 2008.

[4] J.-J. Healy, "Wave damping effect of beaches," *Proc. Int. Hydraulics Convention*, pp. 2013–220, 1952.

ENEA-INMRI Monte Carlo calculations for the update of the IAEA TRS 398 dosimetry protocol

Maria Pimpinella[*] and Massimo Pinto

ENEA, National Institute of Ionizing Radiation Metrology, ENEA-FSN-INMRI, 00123 Rome, Italy

Abstract. The Monte Carlo system EGSnrc is used to calculate beam quality correction factors and related parameters required for absorbed dose to water determination in megavoltage and medium-energy (100-250 kV) x-ray beams using ionization chambers calibrated in a reference beam. Calculation results are submitted to the IAEA to contribute to the revision of the International Code of Practice IAEA TRS 398.

1 Introduction

The IAEA TRS 398 [1] is a code of practice for dosimetry in external beam radiotherapy based on absorbed-dose-to-water (D_w) standards, covering all types of clinical radiation sources (low and medium energy x-rays, megavoltage photon and electron beams, protons and heavy ions). Since its first publication in 2000, the TRS 398 has been applied worldwide allowing harmonization of measurement procedures and improvement of accuracy in radiotherapy dosimetry. Recent technological and scientific advances have posed the need for a major revision of the TRS 398 that includes update of recommended values of the beam quality correction factors, k_{Q,Q_0}, required to convert the ionization chamber calibration factor from the calibration beam (Q_0, i.e. reference quality) to the user beam (Q). Accordingly, in 2016 the IAEA issued two calls for organizations, or consortia, to determine and provide up-to-date measured or Monte Carlo calculated k_{Q,Q_0} factors and related parameters. Aiming at participating in the TRS 398 revision process, nine European laboratories including the Italian National Institute of Ionizing Radiation Metrology (ENEA-INMRI) set up a consortium and promoted the European-Funded Joint Research Project "RTNORM" (www.rtnorm.eu) finalized to calculate and measure sets of k_{Q,Q_0} factors.

In the following, we report on Monte Carlo simulations carried out at ENEA-INMRI, in the framework of the RTNORM project, to contribute to the revision of the TRS 398 recommendations for dosimetry of high energy (megavoltage) photon beams and medium-energy x-ray beams.

2 Materials and methods

2.1 Monte Carlo simulations

The EGSnrc system (https://nrc-cnrc.github.io/EGSnrc/) [2] installed on the cluster CRESCO4 in shared mode was used to simulate irradiation of ionization chambers in the reference conditions recommended in the TRS 398 (see Table 1). The geometry package egs++, with the C++ class library, was used to model in detail different types of ionization chambers (see Table 2) according to the drawings provided by the chamber manufacturers. Radiation transport parameters were set to the values that would provide the most accurate simulation of electron and photon interactions with materials. Recent recommendations on key dosimetric data [3] were adopted, including the renormalized photoelectric cross-sections.

Table 1: Reference conditions for the determination of absorbed dose to water.

Influence quantity	Reference value	
	Medium-energy x-ray beams	*High energy photon beams*
Water phantom	20 cm x 20 cm x 20 cm	30 cm x 30 cm x 30 cm
Ionization chamber type	cylindrical	cylindrical
Measurement depth	2 g cm^{-2}	10 g cm^{-2} (5 g cm^{-2} for ^{60}Co)
Field size	10 cm x 10 cm	10 cm x 10 cm
Source to surface distance	100 cm	100 cm

Table 2: Main characteristics of ionization chambers considered for Monte Carlo simulations.

Ionization chamber type	Cavity volume (cm^3)	Cavity length (mm)	Cavity radius (mm)	Wall material	Wall thickness (mm)	Central electrode material
NE 2571	0.69	24.0	3.1	graphite*	0.36	Al
IBA FC65-G	0.67	23.6	3.1	graphite	0.40	Al
PTW 30013	0.61	22.9	3.1	PMMA, graphite	0.30 0.10	Al
IBA FC65-P	0.67	23.6	3.1	Delrin	0.40	Al
IBA CC13	0.13	6.05	3.0	C552	0.40	C552

* A PMMA waterproofing envelope, 1 mm thick, was included in the chamber model.

2.2 Calculation of beam quality correction factors

Under assumption that the energy required to produce a couple of ions in air is independent of photon energy, an assumption that can be considered valid in the photon energy range of this study, k_{Q,Q_0} factors were calculated as

$$k_{Q,Q_0} = \frac{D_{w,Q}/D_{ch,w,Q}}{D_{w,Q_0}/D_{ch,w,Q_0}} \tag{1}$$

where $D_{ch,w}$ is the absorbed dose to air in the cavity of the ionization chamber placed in water and D_w is the absorbed dose to water at the measurement point in absence of the ionization chamber, evaluated for the beam quality Q or Q_0.

High energy photon beams in the range 6-25 MV and medium-energy x-ray beams in the range 100-250 kV were considered for k_{Q,Q_0} calculation. The radiation source in the Monte Carlo simulations was modelled as a collimated point source with specific energy distributions (spectra). As an example, some of the spectra used are shown in Figure 1. In the medium-energy range the spectra pertaining to beam qualities available at ENEA-INMRI laboratories were used and the 250 kV beam was chosen as reference quality. For megavoltage photons spectra relevant to beams produced by clinical accelerators were used. For dosimetry in clinical accelerators, ionization chambers are currently calibrated in terms of D_w in a ^{60}Co gamma beam, then the Q_0 quality in Eq. (1) refers to the ^{60}Co gamma radiation.

Several preliminary tests were performed to assess the reliability of models developed for chambers and beams and to evaluate the impact of simulation modalities, including the implementation of variance reduction techniques, on the calculated quantities.
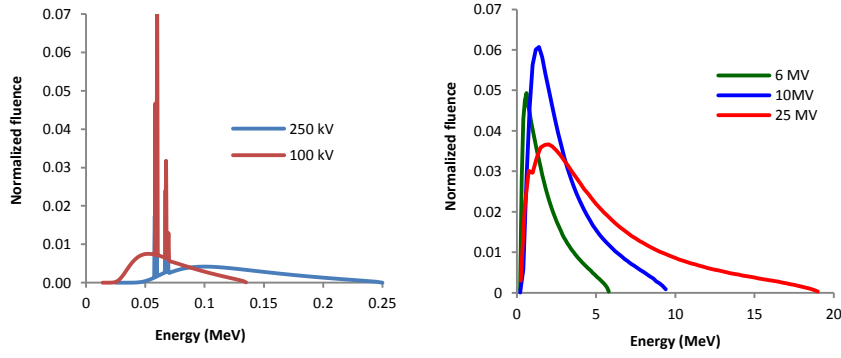
Fig.1: Typical shapes of spectra referring to kilovoltage (left) and megavoltage (right) beams.

2.3 Perturbation factors in medium-energy x-ray beams

To date, only a few Metrological Institutes have developed D_w primary standards in the medium energy range, so that there is still interest in measuring D_w using ionization chambers calibrated against an air kerma (K_{air}) standard. This requires chamber-dependent perturbation factors (p_Q) accounting for the different response of ionization chamber in air and in water, and values of the ratio of mass energy absorption coefficients, water to air, averaged over the photon spectrum at the measurement point in water ($\left[\overline{(\mu_{en}/\rho)}_{w,air}\right]_Q$) [1]. Monte Carlo simulations were run to determine both $\left[\overline{(\mu_{en}/\rho)}_{w,air}\right]_Q$ and p_Q through calculated: i) photon spectra at the measurement point in water; ii) K_{air} at the reference point in air; iii) absorbed dose to air in the chamber cavity when the ionization chamber is irradiated at the reference point in air ($D_{ch,air}$).

3 Results

For megavoltage beams, k_{Q,Q_0} factors were calculated for all the chambers listed in Table 2 with statistical uncertainties of about 0.1%. General aspects referring to the impact of beam model, simulation modalities and transport parameters, have been reported and discussed in [4]. For all the chambers, the Monte Carlo k_{Q,Q_0} values are in agreement with the TRS 398 values within the 1% uncertainty stated in the protocol. Nevertheless, the Monte Carlo values are systematically lower with differences up to about 0.7% at the highest energies, as can be seen in Figure 2, where data for two types of ionization chambers are shown.
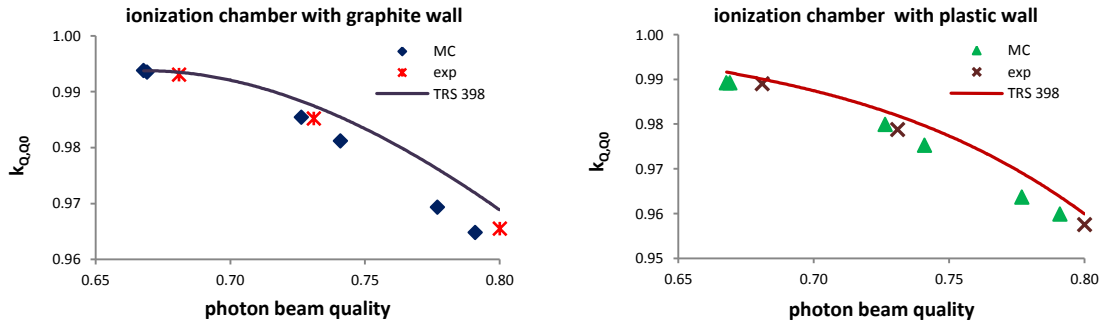
Fig.2: Monte Carlo beam quality correction factors for two types of ionization chambers compared to the TRS 398 values [1] and the experimental values from [5].

Figure 2 also shows a very good agreement (within 0.3%) between Monte Carlo and measured values of k_{Q,Q_0} available from literature [5]. The same level of agreement with the experimental data in [5] applies to all the chambers listed in Table 2.

For medium-energy x-rays, Monte Carlo simulations were run for the first three types of ionization chambers listed in Table 2. The calculated k_{Q,Q_0} values decrease with beam energy, indicating an increase of the chamber response (i.e. ratio of the chamber signal to D_w) when the energy decreases. Of note, this is opposite to the behaviour observed in the megavoltage range where the chamber response increases with energy from the ^{60}Co gamma beam (mean energy ≈ 1.25 MeV) to the 25 MV photon beam (mean energy ≈ 6 MeV). Taking the 250 kV beam (mean energy ≈ 123 keV) as reference (i.e. $k_{Q,250kV} = 1$), at the lowest energy considered in this work (i.e. 100 kV beam, mean energy ≈ 51 keV) corrections from 1.5% to 5% have been obtained for the three chambers.

Values of $\overline{[(\mu_{en}/\rho)_{w,air}]}_Q$ calculated in this work are in agreement with the existing values within a few tenths of a percent. Perturbation factors p_Q obtained in this work vary from 1.01 to 1.03 and show similar trends with beam energy for the three chamber models.

Validation of the ENEA-INMRI Monte Carlo results within the RTNORM project is ongoing. Final set of data will be submitted to the IAEA working group for the revision of the TRS 398 code of practice by the end of October 2019.

Acknowledgments

References

[1] P. Andreo, D.T. Burns, K. Hohlfeld, M. Huq, T. Kanai, R. F. Laitano, V. Smyth, S. Vynckier. Absorbed dose determination in external beam cancer therapy; An International Code of Practice for Dosimetry Based on Standards of Absorbed Dose to Water. IAEA-TRS 398 (2000) (Vienna: IAEA).

[2] I. Kawrakow, E. Mainegra-Hing, D.W.O. Rogers, F. Tessier, B.R.B. Walters. The EGSnrc Code System: Monte Carlo simulation of electron and photon transport. NRCC Report PIRS-701 (2018).

[3] ICRU. Report 90. Key Data for Ionizing-Radiation Dosimetry: Measurement Standards and Applications. Journal of the International Commission on Radiation Units and Measurements 2016;Vol 14, Issue 1.

[4] M. Pimpinella, L. Silvi, M. Pinto. Calculation of k_Q factors for Farmer-type ionization chambers following the recent recommendations on new key dosimetry data. *Phys. Med. EJMP* **57**, pp. 221-230, (2019).

[5] M.R. McEwen. Measurement of ionization chamber absorbed dose k_Q factors in megavoltage photon beams. Med Phys. **37**, pp 2179-2193, (2010).

RESENT DEVELOPMENTS AND APPLICATIONS OF HYBRID MHD-GYROKINETIC CODES TO REALISTIC PLASMA SCENARIOS

Sergio Briguglio[1], Giuliana Fogaccia[1*],Gregorio Vlad[1] and Tao Wang[2]

[1]*ENEA, Dipartimento FSN, C. R. Frascati, via E. Fermi 45, 00044 Frascati (Roma), Italy*

[2]*Institute for Fusion Theory and Simulation and Department of Physics, Zhejiang University, Hangzhou, People's Republic of China*

ABSTRACT. In this paper the main activities carried on in 2018 will be reported, regarding numerical simulations of the interaction between Alfvén modes and energetic particles in nuclear fusion devices. In Sec.1 results related to the code HYMAGYC, for a realistic shaped cross section model scenario are shown, retaining the effects of the radial orbit extent (FOW), finite Larmor radius (FLR) and magnetic compression both in the energetic particles equations of motion and in the computation of energetic particles pressure tensor; in Sec.2 the trapped energetic particle transport in DTT plasmas is analyzed by HMGC simulation, showing that the transport mechanism is convective in the core. In this paper the main activities carried on in 2018 will be reported, regarding numerical simulations of the interaction between Alfvén modes and energetic particles in nuclear fusion devices. In Sec.1 results related to the code HYMAGYC, for a realistic shaped cross section model scenario are shown, retaining the effects of the radial orbit extent (FOW), finite Larmor radius (FLR) and magnetic compression both in the energetic particles equations of motion and in the computation of energetic particles pressure tensor; in Sec.2 the trapped energetic particle transport in DTT plasmas is analyzed by HMGC simulation, showing that the transport mechanism is convective in the core.

1 Full exploitation of the HYMAGYC code for a shaped cross section scenario

The HYMAGYC code [1] is an HYbrid MAgnetohydrodynamics Gyrokinetic Code that describes the nonlinear dynamics of one or more energetic particle populations by the nonlinear gyrokinetic Vlasov equation expanded up to order $O(\varepsilon^2)$ and $O(\varepsilon\varepsilon_B)$, ε being the gyrokinetic ordering parameter $\varepsilon \simeq \rho_H/L_n$ and $\varepsilon_B \simeq \rho_H/L_B$, with ρ_H the energetic particle Larmor radius, and L_n and L_B the characteristic equilibrium plasma density and magnetic-field nonuniformity length scales, respectively. The following space-time ordering for the fluctuating electromagnetic fields holds: $k_\perp\rho_H = O(1)$, $k_\parallel\rho_H = O(\varepsilon)$, $\omega/\Omega_H = O(\varepsilon)$, being $k_\perp$ the perpendicular (to the equilibrium magnetic field) wave vector of perturbed fields, $k_\parallel$ the parallel one, ω the characteristic fluctuation frequency and Ω_H the energetic particle gyrofrequency. Thermal plasma is described for general axisymmetric magnetic equilibria by linear full resistive MHD equations (then, the perturbed electromagnetic fields include the electrostatic potential φ, and both parallel and perpendicular components of the vector potential **A**, and also high-β plasmas can be studied, β being the ratio of the plasma pressure to the magnetic pressure).

With the aim exploiting the full capabilities of HYMAGYC, recent activities studied the effects of the energetic particle (EP) Finite Larmor Radius (FLR) and the effect of the magnetic compression, for a realistic shaped cross section AUG model scenario [2]. The AUG reference case has been identified and analyzed, in collaboration with the NLED Enabling Research group, both characterizing the Alfvén continua for different toroidal mode numbers (n=1,2,3) and studying the global, ideal MHD TAEs present in such equilibrium. A Maxwellian energetic particle population of deuterium was assumed, characterized by dimensionless thermal velocity $v_{th,H0}/v_{A0} \approx 0.257$, and $\rho_{H0}/a \approx 0.04$, being v_{A0} and ρ_{H0} the on-axis Alfvén velocity and Larmor radius corresponding to a temperature value $T_H = 0.093$ MeV; the energetic particle temperature is considered as constant along the flux-like radial coordinate. Moreover, a monotonic EP radial density profile has been considered, with a on-axis value $n_{H0} = 2 \times 3.552 \times 10^{18}$ [m^{-3}]$= 7.104 \times 10^{18}$ [m^{-3}] (the EP on-axis density has been doubled w.r.t. the reference case in order to increase the growth-rate of the unstable modes); on-axis bulk deuterium plasma density is $n_{D0} = 1.71587 \times 10^{19}$ [m^{-3}].

In the HYMAGYC code it is possible to selectively switch on or off the terms related to the FLR effects, both in the equation of motion of the energetic particles and in the computation of the pressure tensor. When retaining the FLR terms, several scalar quantities, proportional to perturbed fields, must be computed, at the particle position **x** along the Larmor orbit, and then averaged on the gyroangle, being $\mathbf{x} = \mathbf{X_{gc}} + \boldsymbol{\rho_H}$ with $\mathbf{X_{gc}}$ the guiding center position and $\boldsymbol{\rho_H}$ the energetic particle gyroradius vector which depends by the gyroangle.

In 2017 the activity related to the code HYMAGYC concerned the verification of the magnetic compression and FLR terms contained into the equations of particle motion. In the year 2018, the verification of HYMAGYC has been completed: the FLR terms in the computation of the energetic particle pressure tensor have been verified. In the following we will present results both considering only Finite Orbit Width (FOW) effects retained and cases retaining FLR and magnetic compression effects. For the latter cases we will use a number of points along the Larmor orbit equal to NORBIT=32 to perform the gyro-average, if not specified elsewhere.

For n=1, the most unstable mode is a Reversed Shear Alfvén Eigenmode (RSAE) driven by the energetic particles; for the case retaining only FOW effects the mode is localized in frequency at $\omega/\omega_{A0} = 0.081$, just below the lower Alfvén continuum, and radially at s=0.39 close to the location of the minimum of the q-profile. Results related to the same simulation but retaining all the FLR and magnetic compression effects are characterized by radial corrugations of the the poloidal Fourier components of the eigenfunction, which are typical of kinetic effects.

As a second example, the results for n=3 have been considered. The most unstable mode is located, in frequency, within the toroidal gap, and, radially, close to the position of the maximum of the energetic particle density gradient.

In Fig. 1 the growth rate and frequency for n=1 and n=3 are shown vs. T_H, both retaining and not retaining all the FLR and δA effects. From Fig. 1, Left, it is possible to observe how the FLR effects contribute to decreasing the growth rate, as expected from theory. Note that the effect is stronger the higher the toroidal mode number is (higher toroidal mode number implying larger $k \rho_H$).
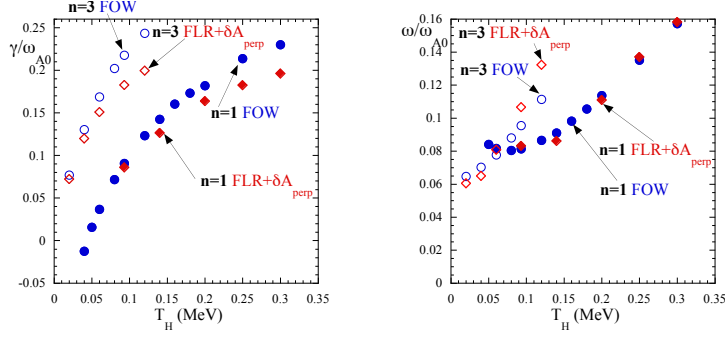
Fig.1: Growth-rate (left) and frequency (right) vs. T_H, for the toroidal mode numbers n=1 (full symbols) and n=3 (open symbols). Results considering only FOW effects are shown in blue circles while results retaining full FLR and $\delta A_\perp$ effects are shown using red diamonds.

In Fig.2 the dependence of the growth rate on the number of points NORBIT used to perform the gyro-average is shown, for the reference case of the AUG equilibrium and n=1: an adequate number of points to compute the gyro average is required (NORBIT$\gtrsim$32) in order to correfctly retain the FLR effects.
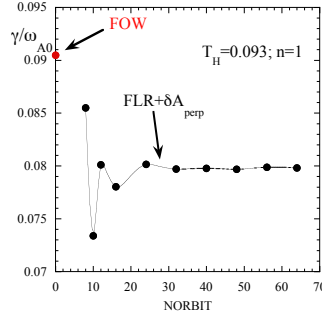
Fig.2: Growth-rate, for T_H=0.093 and n=1 vs. the number of points(NORBIT) used to compute the gyro average. Also the growth-rate for the case in which only FOW effects are retained is shown (in red, at NORBIT=0)

The present activity completes the full exploitation of the HYMAGYC basic capabilities, namely, retaining all the EP FLR effects, the finite magnetic compression, and considering realistic shaped plasma equilibria. In the meanwhile, more improvements have been implemented in the hybrid MHD-gyrokinetic simulation code HYMAGYC, and tested on the CRESCO6 cluster. In particular, the possibility of simulating the evolution of many different particle species, with various equilibrium distribution functions, while chosing, for each of them, between a delta-F and a full-F approach, has been introduced. Moreover, the code is now able to retain electromagnetic perturbations characterized by many toroidal mode numbers, instead of just single-mode perturbations. Finally, in order to perform large-size simulations, while complying the job-duration limits imposed by the cluster management, a stop-and-restart facility has been developed, allowing for subdividing a single simulation into several subsequent jobs.

2 Phase space transport of energetic particles in DTT plasmas

Energetic particles (EP), such as fusion born alphas, play crucial role for future tokamaks including the Divertor Test Tokamak facility (DTT) [3] as they are responsible for plasma heating and eventual fusion burning. Thus, it is crucial to understand their transport and confinement properties in collisionless fusion plasmas. In this work, a DTT reference scenario is investigated by HMGC[4] simulation, and the EP transport are analysed by Hamiltonian mapping techniques.

We adopt a DTT reference equilibrium with weakly reversed magnetic shear, EPs are assumed to be ITER-relevant via dimensionless parameters [5]. This is consistent with DTT's parameter choice and project objective. We focus on a reference case with toroidal mode number n=4, it is shown that reversed shear Alfvén eigenmode (RSAE) can be readily driven unstable by magnetically trapped EPs. In order to gain more insights in the wave-EP resonant interaction, the resonance radial structure is analysed and is shown in Fig.1 [6]. Here, the green curve is the toroidal precession resonance frequency, the red and blue ones correspond to mode structure and wave-EP power transfer profiles, respectively. It is clear that the effective resonant power transfer is more limited by finite mode width, rather than resonance frequency matching condition. Consistent with Fig.3, Fig.4 shows the evolution of EP phase space structure during mode growth and saturation, where red and blue markers indicate particles born from different side of resonance location. Indeed, the response of resonant particles is comparable with mode width, which plays a significant role in describing the nonlinear wave-EP interactions. As a result, the EP transport is convective and may lead to avalanche. The transport in longer time scale is subject to future investigation.

In summary, we show that the RSAE-induced transport of trapped EPs in DTT plasmas is convective, with a radial scale comparable with mode width. This is due to the peculiar wave-EP resonance structure and may have impact on future burning plasmas.
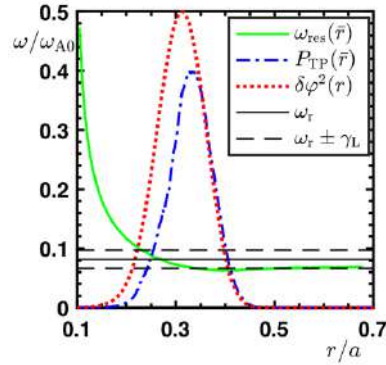
Fig.3: Radial resonance structure RSAE and trapped EPs.
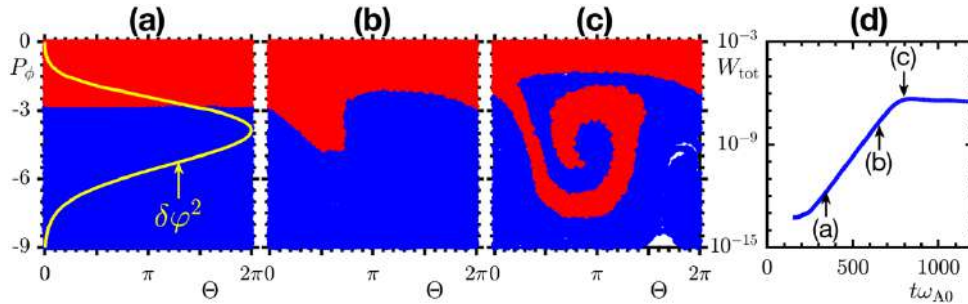
Fig.4: Phase space structure of resonant EPs illustrated by Hamiltonian mapping techniques.

References

[1] G. Fogaccia, G. Vlad, S. Briguglio, Nucl. Fusion 56 (2016) 112004

[2] Ph. Lauber et al., NLED- AUG reference case, http://www2.ipp.mpg.de/~pwl/NLED_AUG/data.html

[3] R. Albanese, A. Pizzuto, WPDTT2 Team, and DTT project proposal contributors. The DTT proposal. a tokamak facility to address exhaust challenges for DEMO: Introduction and executive summary. Fusion Engineering and Design, 122:274–284, 2017.

[4] S. Briguglio, G. Vlad, F. Zonca, and C. Kar,Phys. Plasmas2, 3711(1995).

[5] T. Wang, Z. Qiu, F. Zonca, S. Briguglio, G. Fogaccia, G. Vlad and X. Wang. Shear Alfvén fluctuation spectrum in Divertor Tokamak Test facility plasmas. *Phys*. *Plasmas* **25**, 062509 (2018).
[6] T. Wang, X. Wang, S. Briguglio, Z. Qiu, G. Vlad and F. Zonca. Nonlinear dynamics of shear Alfvén fluctuations in Divertor Tokamak Test facility plasmas. *Phys*. *Plasmas* **26**, 012504 (2019).

Silicene on an Insulating Substrate

Olivia Pulci[1*], Paola Gori[2]

[1]*Roma Tor Vergata University, Physics Department, via della Ricerca Scientifica 1, I-00133, Rome, Italy[1]*

[2]*Roma TRE University, Engineering Department, via della Vasca Navale 79, I-00146, Rome, Italy*

Abstract. The adsorption of a silicene layer on top of the insulating surface $Al_2O_3(0001)$ was studied by means of first principles calculations, within Density Functional Theory (DFT). The structural, electronic and optical properties were calculated with the Quantum Espresso code, with the objective of interpreting the results of the experimental characterization of epitaxially grown samples of silicene/$Al_2O_3(0001)$.

1 Introduction

The enormous interest raised by the ever-expanding number of peculiar properties of graphene has stimulated the birth of many parallel research paths devoted to the exploration of other two-dimensional materials and, among them, to group-IV based nanomaterials and to silicene, in particular [1].

Up to now, preserving the properties of silicene when it is deposited on a substrate has proven to be a hard task, given the larger reactivity of silicon compared to carbon. A much studied substrate is Ag(111) [2], with which, however, silicon significantly interacts [3]. Recently, $Al_2O_3(0001)$ has been proposed as a viable substrate to grow silicene, in view of its insulating behaviour [4].

In this project, we therefore investigated the system silicene/$Al_2O_3(0001)$ by means of DFT calculations of its structural, electronic and optical properties, with the aim of interpreting the measured optical conductivity of silicon nanosheets synthesized by molecular beam epitaxy (MBE) [5].

2 Methods

The silicene/$Al_2O_3(0001)$ system was studied by means of DFT. Norm-conserving pseudopotentials and Perdew-Burke-Ernzerhof exchange and correlation potentials were used, with a kinetic energy cutoff of 65 Ry. Van der Waals interactions were evaluated by means of the vdW-DF method [6]. The structural, electronic and optical properties were calculated with the Quantum Espresso code [7]. Quantum Espresso largely exploits parallelization, achieved using both MPI and OpenMP. Several MPI parallelization levels are implemented, in which both calculations and data structures are distributed across processors. In our case, in particular, calculations were parallelized both on k-points and as 'PW parallelization', which distributes wavefunctions across processors both in real

---

[1] Corresponding author. E-mail: olivia.pulci@roma2.infn.it

and reciprocal space. HPC CRESCO resources (CRESCO4 cluster) have been used to simulate the system as composed by a symmetric 3×3 Al$_2$O$_3$(0001) slab made of 18 layers and, on top of this, a single silicene layer with a periodicity of √13×√13R13.9° with respect to ideal freestanding silicene. A vacuum layer of 14 Å has been used to decouple periodic images of the slab along the direction perpendicular to it.

The relaxation of the system was performed by means of the BFGS algorithm with a mesh of 3×3×1 k-points for several starting configurations.

Optical spectra were calculated within the single particle approximation (Fermi golden rule) using 18×18×1 k-points for the √13×√13R13.9° silicene on substrate and 400×400×1 k-points for 1×1 freestanding silicene.

3 Results

Several stable configurations have been found for the system after relaxation. Two resulting groups of configurations were obtained that we classified as Weakly Interacting Silicene (WIS) system and Strongly Interacting Silicene (SIS) system. The most stable configurations belong to the SIS class, while the most stable geometries in each of the two groups are shown in Fig. 1.

In all cases, the silicene overlayer is subjected to a strain of about 3.3% because of the lattice mismatch with the substrate. The average distance between the substrate and the overlayer is about 2.8 Å for SIS system and about 3.3 Å for WIS system.

The energy differences among the two classes of geometries are not large (of the order of 70 meV/Si atom) and therefore their coexistence is possible even at room temperature.

However, a non-negligible deformation of the silicene overlayer is observed in the SIS geometry, and a gap as large as 0.44 eV opens at K point of BZ, with the Dirac cone that is hardly identifiable (as shown in the left panel of Fig. 2). On the contrary, in the WIS geometry, the Dirac cone still survives, but a small gap of about 0.05 eV opens at K point (see right part of Fig. 2).
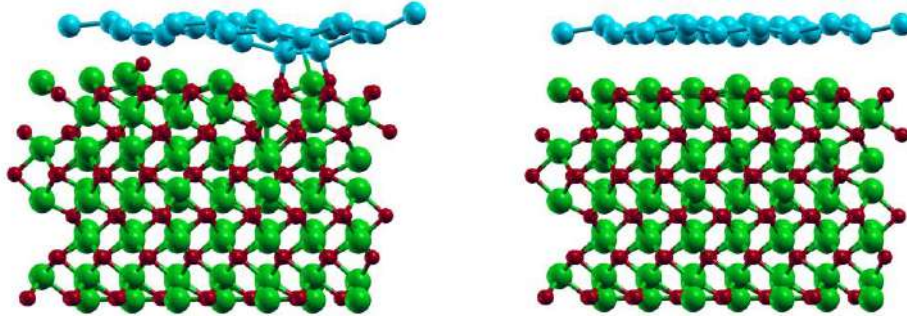
Fig.1: Side-view geometry of the most stable SIS system (left) and of the most stable WIS system (right). Aluminium atoms are represented in green, oxygen atoms in red and silicon atoms in cyan.

The highlighted differences in the electronic properties of the two alternative models reflect in the low-energy behaviour of their calculated optical spectra. The normalized optical conductance, derived as discussed in detail in [5], has been calculated for SIS and WIS geometries and compared to that of the ideal silicene system. In the SIS geometry, the low-energy optical conductance (dashed green line in Fig. 3) strongly differs from that of freestanding silicene (dash-dotted blue line), due to the opening of a significant gap in the mid-IR (about 0.5 eV). Such gap is not observed in the experimental data, whereas the first experimentally detected peak is not discernible in calculations.
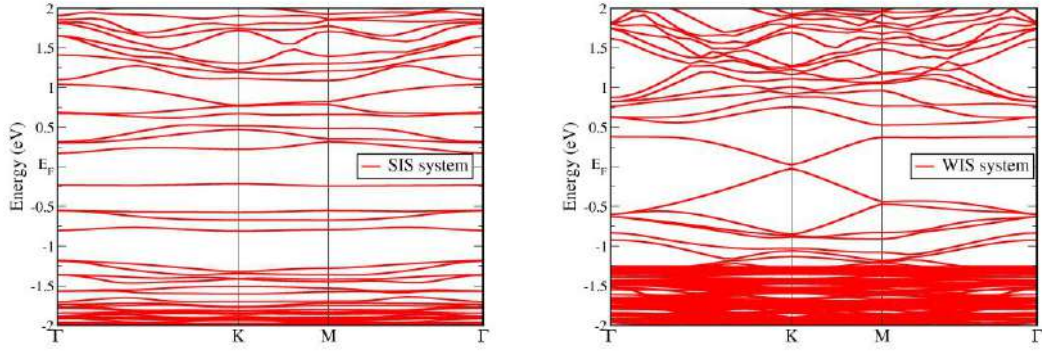
Fig.2: Electronic band structure of the most stable SIS system (left) and of the most stable WIS system (right). E_F denotes the Fermi level, where zero energy is set.

Instead, in the WIS geometry (full black line in Fig. 3) optical properties are remarkably similar to those of ideal silicene and qualitatively comparable to experimental data reported in [5]: a discernible first peak appears and a nearly flat conductance before this peak is observed.
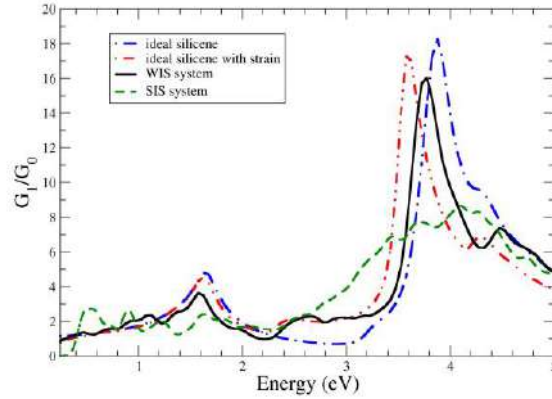
Fig.3: Normalized conductance calculated for the most stable SIS system (dashed green line), for the most stable WIS system (full black line), for ideal freestanding silicene (dash-dotted blue line) and for strained freestanding silicene (dash-dotted red line).

4 Conclusions

In conclusion, DFT calculations have proven useful to understand measured optical spectra of the system obtained by epitaxially growing silicon on $Al_2O_3(0001)$. The resulting picture is consistent with the interpretation of silicon behaving very closely to ideal silicene, even on top of a substrate. The weak interaction between the overlayer and the optically transparent substrate allows to

substantially preserve both the electronic band structure and the low-energy optical conductance of silicene.

References

[1] J. Zhao et al.. Rise of silicene: a competitive 2D material. Progress in Materials Science **83**, pp. 24-151, (2016).

[2] P. Vogt, P. De Padova, C. Quaresima, J. Avila, E. Frantzeskakis, M. C. Asensio, A. Resta, B. Ealet and G. Le Lay. Silicene: Compelling Experimental Evidence for Graphenelike Two-Dimensional Silicon. *Phys. Rev. Lett.* **108**, 155501, (2012).

[3] M. Satta, S. Colonna, R. Flammini, A. Cricenti, and F. Ronci. Silicon Reactivity at the Ag(111) Surface. *Phys. Rev. Lett.* **115**, 026102, (2015).

[4] M. X. Chen, Z. Zhong, and M. Weinert. Designing substrates for silicene and germanene: First-principles calculations. *Phys. Rev. B* **94**, 075409, (2016).

[5] C. Grazianetti, S. De Rosa, C. Martella, P. Targa, D. Codegoni, P. Gori, O. Pulci, A. Molle, and S. Lupi, Optical Conductivity of Two-Dimensional Silicon: Evidence of Dirac Electrodynamics. *Nano Lett.* **18**, 7124-7132, (2018).

[6] K. Berland, V. R. Cooper, K. Lee, E. Schröder, T. Thonhauser, P. Hyldgaard, and B. I. Lundqvist. Van der Waals forces in density functional theory: a review of the vdW-DF method. *Reports on Progress in Physics*. **78**, 066501 (2015).

[7] P. Giannozzi et al.. Advanced capabilities for materials modelling with Quantum ESPRESSO. *J. Phys.: Condens. Matter* **29**, 465901 (2017).

ADVANCED D1S DYNAMIC CODE VALIDATION THROUGH A SHUTDOWN DOSE RATE BENCHMARK EXPERIMENT AT JET

Rosaria Villari[*1], Davide Flammini[1], Nicola Fonnesu[1], Stefano Loreti[1] and Giovanni Mariano[1,2]

[1]*ENEA, Department of Fusion and Nuclear Safety Technology, I-00044 Frascati (Rome), Italy[1]*

[2] *University LA Sapienza of Rome, DIAEE department, I-00186 Rome, Italy*

ABSTRACT. The present report describes the validation of Advanced D1S dynamic code through a shutdown dose rate benchmark performed at the end of the JET 2016 Deuterium campaign. The shutdown dose rate values calculated with Advanced D1S dynamic have been compared with the results of other European R2S and D1S codes and with measurements. The results of the benchmark are presented.

1 Introduction

The scope of this benchmark experiment carried-out within EUROfusion WPJET3 NEXP program is the validation of Rigorous Two-Step (R2S) and Direct One-Step (D1S) tools for ITER shutdown dose rate predictions. The present activity has been performed by ENEA in collaboration with other European research institutes: CCFE (United Kingdom), KIT (Germany), UNED (Spain) and NCSRD (Greek). The last Shutdown dose rate (SDR) benchmark experiment was performed in 2015-2016 during and at the end of the high performance Deuterium-Deuterium campaign [1]. On-line continuous gamma dose rate measurements were performed for four months at two ITER relevant ex-vessel positions close to Radial Neutron Camera and on the top of ITER-like Antenna (ILA) using high-sensitive ionization chambers by ENEA and KIT [2]. Decay gamma spectra at the shutdown were also collected by CCFE using High Purity Germanium spectrometer to identify dominant radionuclides contributing to the dose. Neutron fluence measurements during operations were performed as well by NCRSD using activation foils assembly installed close to ionization chambers. ENEA, CCFE, KIT and UNED performed the neutron/decay gamma transport simulations of the SDR experiment [3] with the same geometry, materials, neutron and decay photon tallies, source, irradiation histories and cooling times using different MCNP-based D1S and R2S tools. The neutronic MCNP models of Octant 1 and Octant 2 with the detector assemblies (ionization chambers and activation foil holder) and ILA are shown in Figure 1. Figure 2 shows the shutdown dose rate map in Octant 2 at 6 hours and 12 days after shutdown calculated with Advanced D1S dynamic (ENEA) on CRESCO cluster. The results from ENEA, CCFE, KIT and UNED in terms of Air-kerma rate and the comparison with ionization chamber measurements in Octant 1 and Octant 2 from 2 hours to 2 months after shutdown are shown in Figure 3 and 4, respectively.

---

[1]   Corresponding author. E-mail: rosaria.villari@enea.it
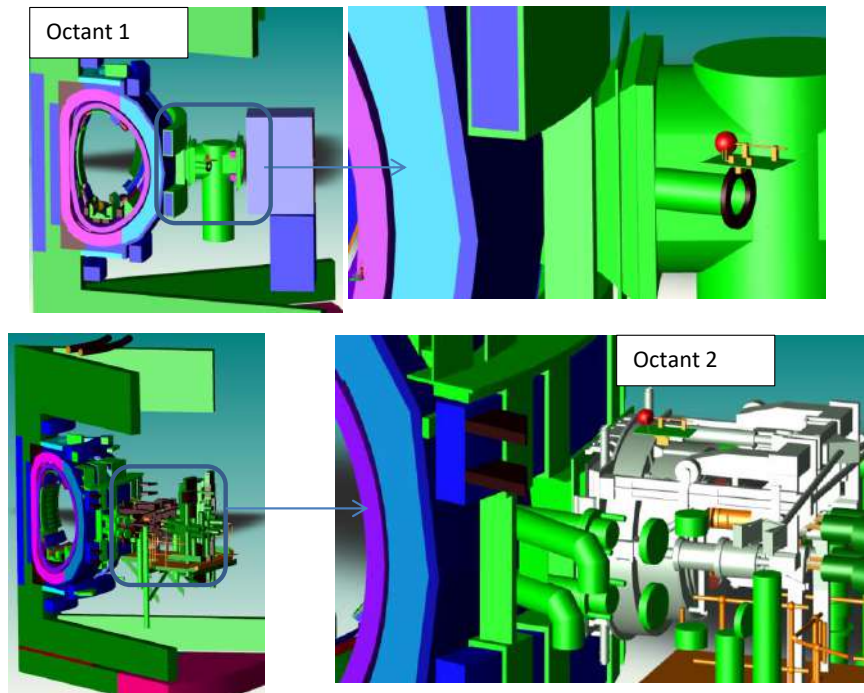
Fig. 1. 3D plots of JET MCNP models of Octant 1 (top) and Octant 2 (bottom): overall model view (left) and detail of the experimental assembly (right)
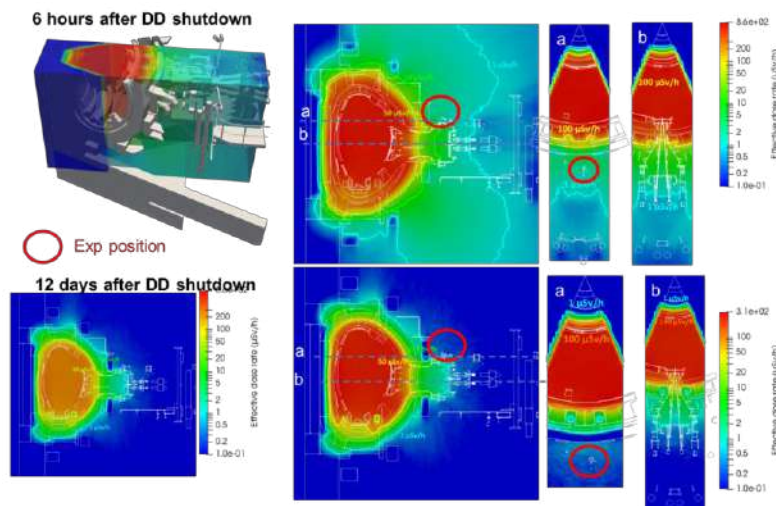
Fig. 2. Shutdown dose rate maps in Octant 2 calculated with Advanced D1S dynamic (ENEA) on CRESCO HPC at 6 hours (top) and 12 days (bottom) after shutdown

Concerning the shutdown dose rate results in Octant 1, Advanced D1S has a general good agreement with measurements and with the other codes. The ratio between the calculation and the measurement (C/E) varies between 0.78±0.08 after 2 hours and 1.52±0.17 after 2 months. The overestimation of the calculation increases with time after shutdown, in agreement with the other codes, maybe because

139

of modelling uncertainties and due to the assumption that all JET components are assumed as permanent. Regarding the Octant 2, the C/E of Advanced D1S varies between 0.47±0.05 at 2 hours to 1.06±0.14 after 2 months. The results are in general better for R2S-based codes within the first month. The Advanced D1S as D1SUNED tend to underestimate the doses, especially at short cooling times in this Octant. The reasons for discrepancies among D1S and R2S codes and with measurements are under investigation. Preliminary studies seem to exclude that D1S missed important activation reactions compared to R2S codes but further analyses including R2S sensitivity to voxel size resolution, study of the experimental temporal behaviour and investigation of modelling uncertainties are in progress.
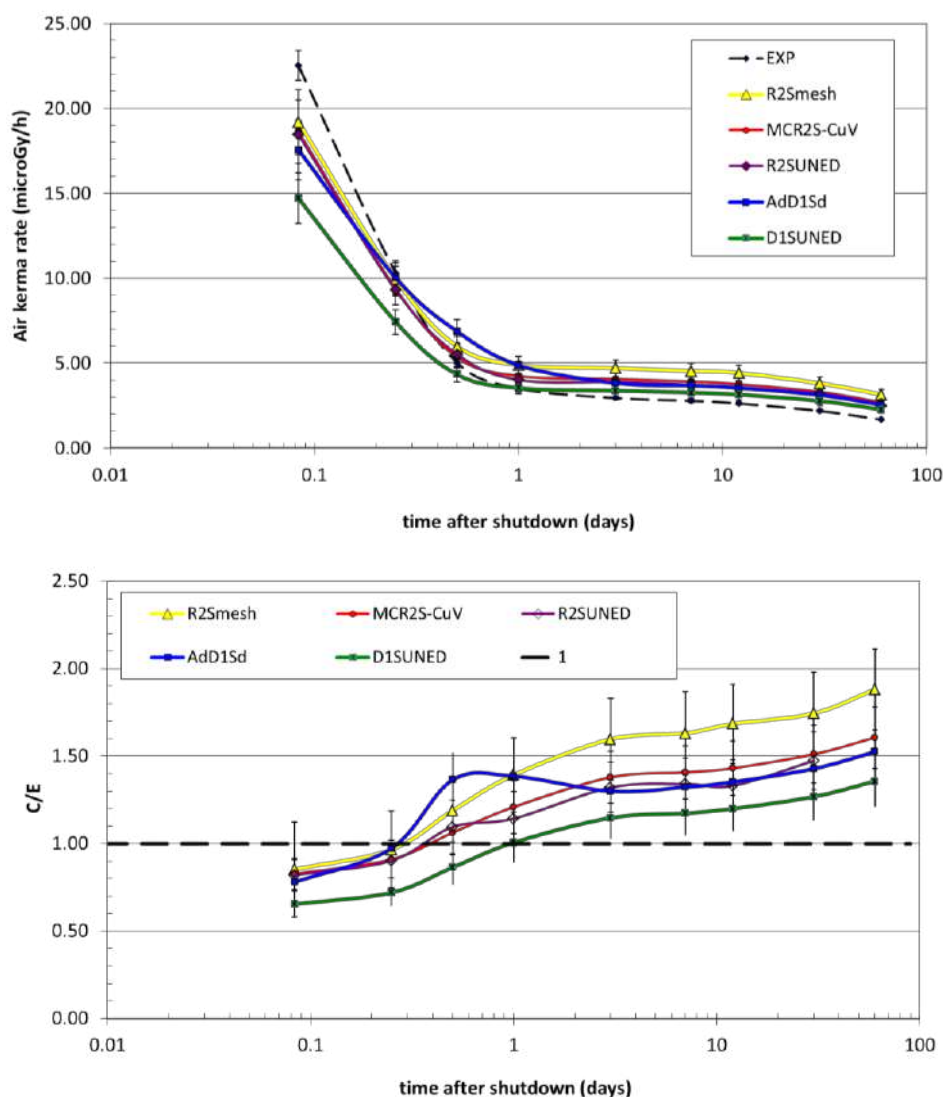
Fig. 3. Air-kerma rate and C/E in Octant 1: IC measurements (EXP) and calculations with Advanced D1S dynamic (ENEA), R2Smesh (KIT), D1SUNED and R2SUNED (UNED), MCR2S_CuV (CCFE) from 2 hours to three months after shutdown (top) and C/E (bottom).
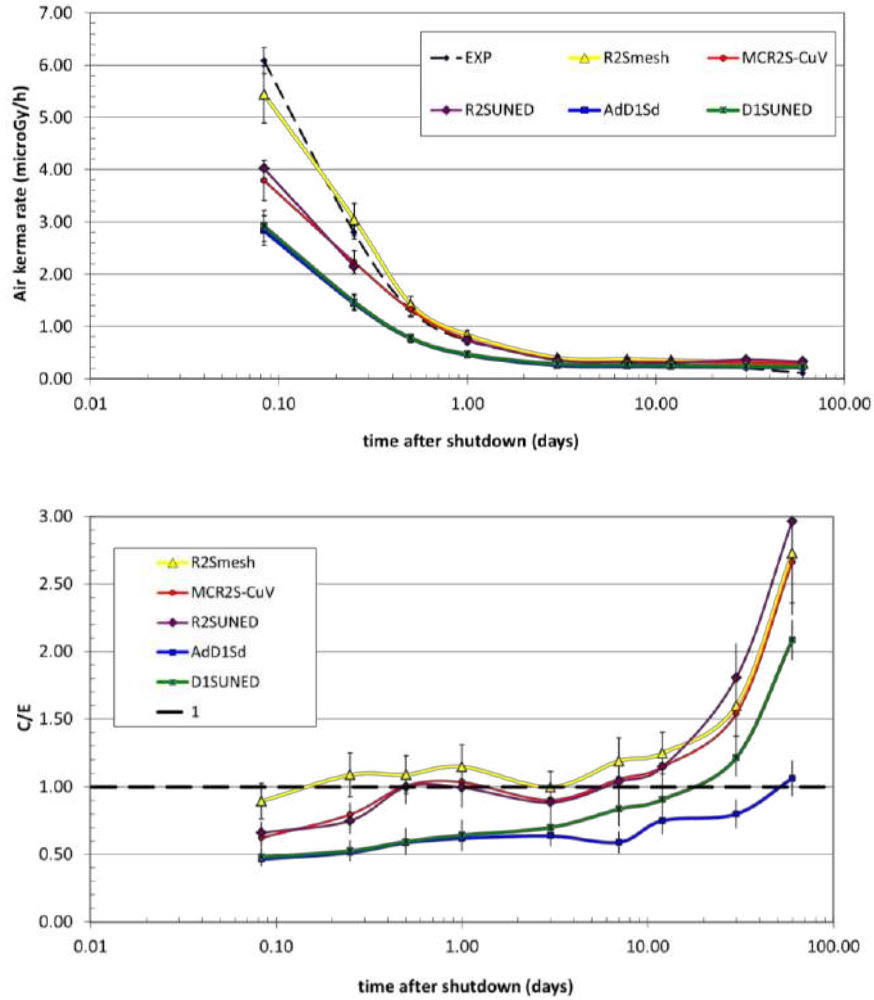
Fig. 4. Air-kerma rate and C/E in Octant 2: IC measurements (EXP) and calculations with Advanced D1S dynamic (ENEA), R2Smesh (KIT), D1SUNED and R2SUNED (UNED), MCR2S_CuV (CCFE) from 2 hours to three months after shutdown (top) and C/E (bottom).

References

[1] R.Villari, P. Batistoni, S. Bradnam, B. Colling, U. Fischer , D. Flammini, N. Fonnesu, Z. Ghani, A. Klix, S. Loreti, J. Naish, L. Packer, M. Pillon, S. Popovichev, I. E. Stamatelatos, T. Vasilopoulou and JET Contributors. Shutdown Dose Rate neutronics experiment during high performances DD operations at JET. *Fusion Engineering and Design*, **136**, pp 1545-1549 (2018)

[2] N. Fonnesu, R. Villari, S. Loreti, P. Batistoni, A. Klix and JET Contributors. Shutdown Dose Rate Measurements after the 2016 Deuterium-Deuterium Campaign at JET. *Fusion Engineering and Design*, 1**36**, pp 1348-1353 (2018)

[3] R. Villari, J. Alguacil, J.P. Catalan, D. Flammini, N. Fonnesu, G. Mariano, J. Naish, P. Pereslatstev,P. Sauvan. Shutdown dose rate calculations with different numerical approaches for the DD shutdown. WPJET3 D20 Final Report *https://idm.euro-fusion.org/?uid=2NFBMG* (2019)

COMPARISON BETWEEN DETERMINISTIC AND STOCHASTIC CODES ON DEPLETION CALCULATIONS FOR AN ER-SHB PWR FA

Roberto Pergreffi[1*], Federico Rocchi[1], Antonio Guglielmelli[1] and Patrizio Console Camprini[1]

[1]*ENEA – Italian National Agency for New Technologies, Energy and Sustainable Economic Development
Via Martiri di Monte Sole 4, 40129 Bologna - Italy[1]*

ABSTRACT. This activity takes the move from a previous work in which an erbia fully poisoned PWR fuel assembly was characterized from a neutronics point of view by means of the deterministic transport code APOLLO2. The neutronic performance of that assembly, developed according to the erbia-credit super high burnup (Er-SHB) fuel concept, was found to be, up to 120,000 MWd/MTU, at least as good as that of a conventional fuel assembly enriched to 5 wt.% in ^{235}U in terms of some fundamental properties. Since APOLLO2 is not validated at those burnup levels, the validation of the calculation scheme adopted in that work deserved to be investigated. For this reason the values of criticality and isotope concentrations at varying of burnup obtained with APOLLO2 have to be compared with those obtained with the Monte Carlo transport code MCNP6.1. In this context the four depletion scenarios developed to investigate the discrepancy between the two codes are documented.

1 Introduction

Although nuclear technology is one of the cheapest sources of electricity in terms of levelized cost of energy (LCOE) [1], the industrial demand for further cost reductions in the fuel cycle of commercial Nuclear Power Plants (NPPs) has never failed over the years. In order to reduce these costs, it is common to increase the amount of fuel loaded into the core and therefore achieve higher burnup (BU) levels. For safety reasons, this is possible through a compensation of this excess reactivity with poison materials characterized by high neutron absorption cross section. Erbia (Er_2O_2) is one of these materials. An innovative solution involving erbia was discussed in a previous study [2] in which a 17x17 PWR fuel assembly (FA) enriched to 10.27 wt.% in ^{235}U with an erbia content of 1 at.% was characterized, from a neutronics point of view, by means of the deterministic transport code APOLLO2 version 2.8-3.E [3]. The innovative aspect of that solution concerned the fact that erbium oxide was homogeneously dispersed into all fuel pins according to the erbia-credit super high burnup (Er-SHB) fuel concept developed about ten years ago to go beyond the so called "5 wt.% barrier" (corresponding to the current enrichment limit for commercial-type LWR fuel) without requiring significant modifications and relicensing of fuel cycle facilities [4,5]. In that study, the neutronic performance of an erbia fully poisoned PWR FA was found to be, up to 120,000 MWd/MTU, at least as good as that of a conventional FA enriched to 5 wt.% in ^{235}U in terms of some fundamental properties such as multiplication factor, residual reactivity penalty, neutron spectrum, spectral index, boron reactivity worth and temperature reactivity coefficients.

Among the outstanding issues of that work, the one concerning the validation of the results obtained with APOLLO2 is crucial. In fact APOLLO2, reference code for deterministic cell calculations for LWRs, is not validated at burnup levels higher than 85,000 MWd/tHM [6]. So, the validation of the calculation scheme adopted in APOLLO2 deserved to be investigated. According to the VVQ-UQ (Verification/Validation/Qualification/Uncertainties Qualification) method [7], the validation is based on the comparison of the results obtained with a deterministic code with those calculated with a stochastic code. In fact, the continuous energy Monte Carlo burnup methodology is a reliable tool

---

[1] Corresponding author. E-mail: roberto.pergreffi@enea.it.

for depletion calculations for critical nuclear systems [8]. In this case, the values of criticality and isotope concentrations at varying of burnup obtained with APOLLO2 are compared with those obtained with MCNP6.1 [9]. From this viewpoint, this activity, being still focused on the neutronic performance of the erbia fully poisoned PWR FA, can legitimately be considered as a follow-up of that activity. At the same time, in a broader and more independent perspective, this activity can also be seen as an example of comparison between deterministic and stochastic codes for depletion calculations. After a first part in which materials and methods are described, the four depletion scenarios simulated in MCNP6.1 to investigate the discrepancy between the two codes are reconstructed summarily.

2 Materials and methods

2.1 Geometry and material data

The geometry adopted in this study corresponds largely to that described in [2]. All relevant data about the erbia-doped FA are shown in Table 1.

Table 1. Geometrical and material data.

Parameters	Unit	Value
Fuel rods		
Expanded cell side	cm	1.26278
Fuel radius = expanded inner clad radius	cm	0.4190
Expanded outer clad radius	cm	0.4761
^{235}U enrichment	wt.%	10.27
Er_2O_3 content	wt.%	0.7
Boron concentration	ppm	1000
Guide tubes		
Expanded inner radius	cm	0.5738
Expanded outer radius	cm	0.6240
Density		
$(U_{0.99}Er_{0.01})O_2$ smeared density	g/cm3	9.696
M5 density	g/cm3	6.407
H_2O density (without boric acid)	g/cm3	0.702
Temperature		
Effective fuel temperature	K	800
Clad temperature	K	600
Moderator temperature	K	600
Assembly		
Pin configuration	-	17 x 17
No. fuel rods	-	265
No. guide tubes positions	-	24
Expanded side	cm	21.4672
Expanded pitch	cm	21.6024
Half water blade	cm	0.0676
Expanded active length	cm	420.992
Core		
Thermal Power	MWth	4500
Power percentage in fuel	%	0.974
No. fuel assembly	-	241

Like [2], the FA contains 265 fuel rods, each with an active length of 420 cm, and 24 guide tubes (filled with water), and is assumed to be composed of fuel, cladding and moderator material only. No gap between fuel and cladding is taken into account. The fuel is assumed to be pure UO_2, only containing [235]U and [238]U, mixed with a quantity of Er_2O_3 of 0.7 wt.% (i.e. 1 at.%). Cladding and guide tube are taken to be M5. Its chemical composition at BoL (Beginning of Life) is described in [2]. Structural materials (e.g., spacer grids) are ignored. Unlike [2], the operating temperatures have been modified. The new operating temperatures are 800 K for fuel and 600 K for cladding and moderator. This choice is due to the fact that a further possible source of uncertainty related to the nuclear data processing has been intentionally avoided. For this reason, the code-to-code comparison has been carried out only using the cross sections provided by JEFF (Joint Evaluated Fission and Fusion File) neutron data libraries. This implies that all expanded dimensions obtained using linear thermal expansion coefficients detailed in [2] are changed.

2.2 Description of transport codes

APOLLO2 is a modular cell code for 2-dimensional multigroup transport calculations. Microscopic cross sections refer to 281 groups master library with a SHEM group structure CEA2005V4.1.2.patch, based on JEFF-3.1.1 evaluations [10]. Calculations are done assuming reflective boundary conditions and taking advantage of all symmetries of the system, so that only 1/8 of assembly is considered. Elementary fuel cell is divided into four concentric zones corresponding, from centre to periphery, to 50%, 30%, 15% and 5% of the total volume respectively, one clad zone and one moderator zone. Collision Probability method is used to solve the transport equation to compute the neutron flux. Self-shielding calculations are done bearing in mind the following isotopes: [238]U, [235]U, [167]Er, [239]Pu, [240]Pu, Zr_nat. The TR (all resonances) approximation is used over the entire energy range. The FA power used for the normalization of the neutron flux is computed multiplying the total core thermal power in MeV/s by the power percentage generated in the fuel and dividing by the number of assemblies and by the expanded active length. The depletion calculation strategy is performed to attain a total average burnup of 120,000 MWd/tHM. The 75 depletion steps used are as follows (in MWd/tHM): 9.375, 18.75, 37.5, 75, 112.5, 150, 325, 500, 750, 1000, 1500, 2000, 2500, 3000, 4000, 5000, 6000, 7000, 8000 every 2000 up to 120000. Every three burnup steps, self-shielding correction is recalculated and cross sections updated. The standard depletion chain associated with the CEA2005V4.1.2.patch library which includes 162 isotopes of which 127 fission products, has been extended by adding the Erbium depletion chain and the depletion chain beyond Americium. The isotopes added to the standard depletion chain are as follows: [162]Er, [164]Er, [167]Er, [168]Er, [169]Er, [170]Er, [171]Er, [172]Er, [169]Tm, [170]Tm, [171]Tm, [170]Yb, [171]Yb, [249]Bk, [249]Cf, [250]Cf, [251]Cf, [252]Cf.

MCNP6 is a general-purpose Monte Carlo radiation-transport code also used for depletion calculations. The depletion is made possible by coupling between the steady-state flux calculations with MCNP6 and the nuclide depletion calculations with the CINDER90 depletion code. According to the modelling in APOLLO2, the fuel pin is divided into the same four concentric zones. To minimize statistical variations, 150 k-eigenvalue source iteration cycles (of which the first 30 cycles skipped) with 300,000 histories per cycle are used. This corresponds to a standard deviation (1σ) of the criticality values never exceeding 12 pcm. The neutron flux is normalized with a FA power obtained multiplying the total core thermal power in MW by the power percentage generated in the fuel and dividing by the number of assemblies. The nuclear data libraries used in this study are the JEFF-3.1.2 and the JEFF-3.2 both provided by NEA Data Bank and processed at temperatures of interest (600 and 800 K). None of these libraries match the one used in APOLLO2. This is due to the fact that the JEFF-3.1.1 cross section library cannot be used in MCNP6.1. Moreover it is worth noting that even if it was, a code-to-code comparison using the JEFF-3.1.1 library would not be possible because the cross section library implemented in APOLLO2 is not exactly the same of the JEFF-3.1.1. In particular the following isotopes, [131M]Te, [153]Gd, [165]Dy, [169]Er, [171]Er, [172]Er, [169]Tm, [170]Tm,

^{171}Tm, ^{170}Yb, and ^{171}Yb are present in the APOLLO2 library but not in the JEFF-3.1.1. The JEFF-3.1.2 release is an update of the JEFF-3.1.1 available in ACE format since the end of 2011 [11]. This library contains incident neutron data for the same number of isotopes (381) of the previous one, but unlike that version, 115 material files have been modified [12]. The JEFF-3.2 library contains incident neutron data for 472 nuclides included the isotopes present in the APOLLO2 library but not in the JEFF-3.1.1 nor in the JEFF-3.1.2 [12].

3 Results and discussion

The infinite neutron multiplication factor as a function of burnup of the FA enriched to 10.27wt.% in ^{235}U and with an erbia content of 1at.% calculated with APOLLO2 is shown in Figure 1. These values, although slightly different from those presented in [2] due to the temperature modifications, have the same trend.

Figure 1. Multiplication factor vs. burnup.
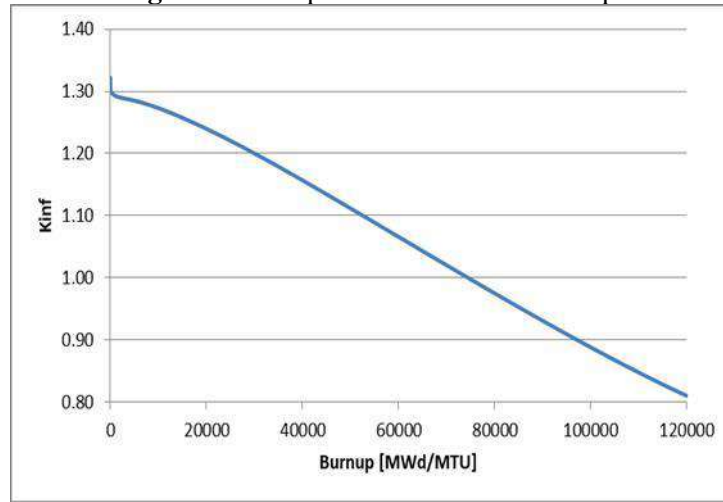
To validate these values, four subsequent depletion scenarios are performed with MCNP6. These scenarios are described below:
- ✓ Scenario 1 → the same configuration adopted in APOLLO2 in terms of initial isotopic composition and burnup steps (76) is implemented. All other isotopes contained in the JEFF-3.1.2 library are listed in the initial fuel composition with low weight fraction values (1E-36 wt.%) in order to track their build-up during the FA depletion.
- ✓ Scenario 2 → much higher number of burnup steps, 248 in place of 75, is taken into account to reduce the uncertainty in the flux calculation. The new steps are as follows (in MWd/tHM): 9.375, 18.75, 37.5, 75, 112.5, 150, 325, 500, 750, 1000 every 500 up to 120,000.
- ✓ Scenario 3 → to include in the depletion chain the isotopes present in the APOLLO2 library but not in the JEFF-3.1.2, the JEFF-3.2 library is used. All the isotopes contained in the JEFF-3.2 library and not related to the initial composition are listed in the initial fuel composition with low weight fraction values (1E-36 wt.%). Same burnup steps of the scenario 2 are taken into account.
- ✓ Scenario 4 → finally, to weight the difference of the isotopic sets between the two depletion chains in terms of criticality, the isotopes present in the JEFF-3.2 but not in the APOLLO2 library are omitted from the transport calculation making the two chains exactly the same. Same burnup steps of scenarios 2 and 3 are taken into account.

All calculations are being performed on CRESCO6, the Linux cluster composed by 434 interconnected nodes integrated in the ENEAGRID infrastructure.

Acknowledgments

References

[1] IEA, NEA, Projected costs of generating electricity, 2015 Edition.

[2] Roberto Pergreffi, Davide Mattioli, Federico Rocchi, Neutronics characterization of an erbia fully poisoned PWR assembly by means of the APOLLO2 code, *EPJ Nuclear Sci. Technol.* 3, 8, (2017).

[3] R. Sanchez *et al.*, APOLLO2 Year 2010, *Nuclear Engineering and Technology*, Vol. 42, No. 5, October 2010.

[4] M. Yamasaki, The study on erbia credit super-high-burnup fuel with isotopically modified erbia, in ANS 2010 Winter Meeting, Las Vegas, November 7-11, (2010).

[5] M. Yamasaki *et al.*, Development of erbia-credit super high burnup fuel: experiments and numerical analyses, *Nucl. Technol.* 177, 63, (2012).

[6] A. Santamarina *et al.*, APOLLO2.8: A Validated Code Package For PWR Neutronics Calculations, Advances in Nuclear Fuel Management IV, Hilton Head Island, South Carolina, USA, April 12-15, (2009).

[7] A. Santamarina *et al.*, Validation of the new Code Package APOLLO2.8 for Accurate PWR Neutronics Calculations, International Conference on Mathematics and Computational Methods Applied to Nuclear Science & Engineering (M&C 2013), Sun Valley, Idaho, USA, May 5-9, (2013).

[8] G. Kepisty *et al.*, Parametric studies of the PWR fuel assembly modelling with Monte-Carlo method, *Annals of Nuclear Energy* 94, 189-207, (2016).

[9] J.T. Goorley *et al.*, Initial MCNP6 Release Overview – MCNP6 version 1.0, LA-UR-13-22934, (2013).

[10] A. Santamarina, D. Bernard, P. Blaise, M. Coste, A. Courcelle, T. D. Huynh, C. Jouanne, P. Leconte, O. Litaize, S. Mengelle, G. Noguère, J.-M. Ruggiéri, O. Sérot, J. Tommasi, C. Vaglio, and J.-F. Vidal, The JEFF-3.1.1 Nuclear Data Library, Validation Results from JEF-2.2 to JEFF-3.1.1. JEFF Report 22, OECD NEA No. 6807, ISBN: 978-92-64-99074-6, France, (2009).

[11] O. Cabellos, Processing of the JEFF-3.1.2 Cross Section Library with the NJOY Code System into Various Formats (ACE, PENDF, GENDF, MATXSR and BOXER) for Testing Purposes & Processing the Most Recent Cross-section Libraries into JANIS Format, Report NEA-2012, France, (2012).

[12] www.oecd-nea.org/dbdata/jeff/

IMPROVEMENT OF THE ENEA NEUTRON ACTIVE INTERROGATION SYSTEM PERFORMANCES

G.Gandolfo[1*]

[1]*ENEA, Italian National Agency for New Technologies, Energy and Sustainable Economic Development, C.R. Frascati, Rome, Italy*

ABSTRACT. The Italian National Agency for New Technologies, Energy and Sustainable Economic Development (ENEA) developed a new device to improve CBRNe resilience, the Neutron Active Interrogation system (NAI). It has been conceived and optimized to identify transuranic-based Radioactive Dispersal Devices potentially hidden in packages, envisaging its utilization in field applications. The original experimental setup was tested on the field during the live demo open to the public at the EDEN Project Demonstration occurred in September 2015 at ENEA Frascati Research Centre in Rome. Since then, the setup has been modified to improve the device detection capabilities. NAI performances have been tested within different environmental conditions, e.g. open field geometry vs. bunker-like geometry, to study the effects of scattering phenomena. The optimized configuration here presented is transportable, lightweight, and able to detect 2 grams of ^{235}U contained in a salt of depleted uranium in real time, independently from the measurement environmental conditions.

1 Introduction

Since September 2013, ENEA - the Italian National Agency for New Technologies, Energy, and Sustainable Economic Development – has been involved in the EDEN (End-user DEmo for cbrNe) project in order to develop advanced and innovative tools for the detection of explosives, the prevention of threats to nuclear plants, the simulation of the dispersion of contaminants in the atmosphere, and the management of such emergency situations. In particular, the ENEA Nuclear Material Characterization and Radioactive Waste Management Laboratory has been involved in the design and realization of the Neutron Active Interrogation (NAI) system whose purpose is the non-destructive inspection of samples suspected of containing fissile or fertile material and explosives. The main goal of such an instrument is the detection of transuranic Radiological Dispersal Devices (RDDs), potentially designed for spreading radioactive contamination. This paper describes the experimental improvement of NAI device performances in comparison to the first experiment carried out on September 2015 at ENEA Frascati Research Centre described in [1].

2 Identification of possible improvements through simulation

The original experimental layout is shown in fig. 1 and it is composed by:
1. a compact d-t neutron generator;
2. a sample cavity composed by 4 polyethylene blocks;
3. ten ^{3}He proportional counters housed in two of the polyethylene blocks (detection blocks);
4. two cadmium sheets surrounding part of lateral surface of detection blocks to cut the background effects caused by thermalized interrogation neutrons;
5. the sample containing about 6 g of ^{235}U dispersed in a depleted uranium salt surrounded by a moderating structure.
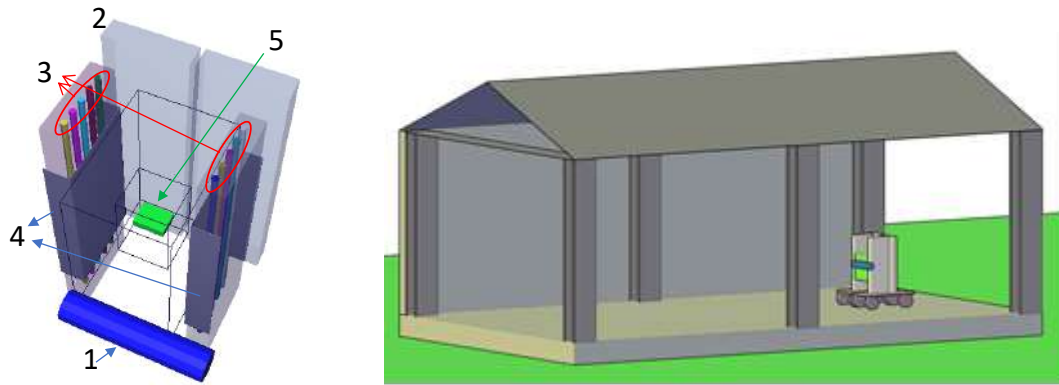
Figure 1 – On the left the NAI device original experimental layout (numbers refer to the bulleted list). On the right the measurement layout.

The experiment was carried out outdoors in the layout shown in fig. 1: NAI device was laid down inside a structure with a concrete floor, a concrete lateral wall, and a metallic roof.
The operating principle of NAI device is the Differential Die-Away time Analysis, an active neutron interrogation technique based on the difference between the die-away time of fast interrogation neutrons and prompt fission neutrons induced by thermal neutrons in the moderating system [2, 3, 4]. The logarithmic trend of registered counts in time is shown in the left panel of fig. 2: red and blue lines respectively show the signal collected by NAI device with and without the sample placed in the cavity.
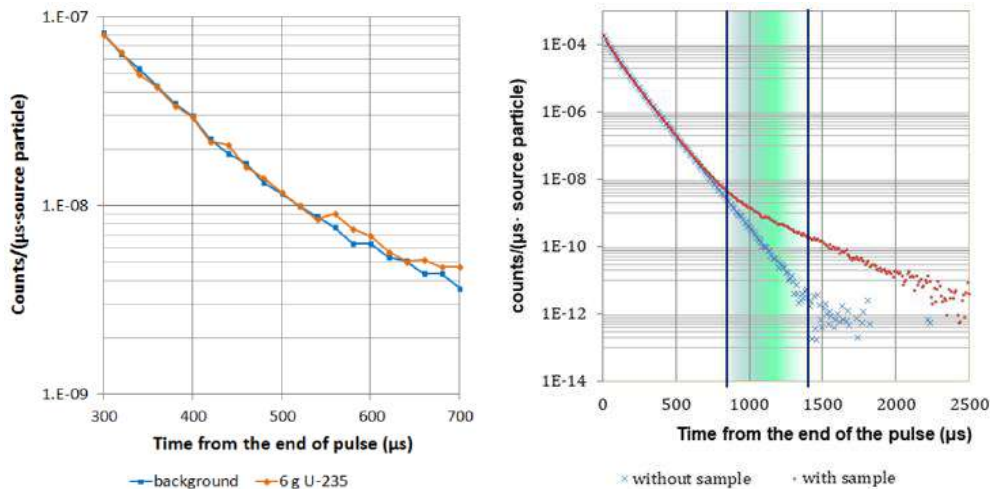
Figure 2 – Experimental results (on the left) vs. simulation results (on the right)

Quantitative considerations about the observed deflection of the measured signal from the background, when a sample containing fissile material is analyzed, are reported in [1] and led to establish a positive detection of potential dangerous material. However, there is a significant difference between experimental data and expected values from simulation results (right panel of fig. 2) referred to the ideal case in which no walls, ceiling, or floor are present while operating the NAI system. Such a difference suggested the possibility to enhance NAI detection capabilities by acting on the critical parameters of the setup.
In order to identify the potential for improving the detection performance of the NAI device a simulation study has been carried out. First, the effects of the thermal background neutrons have been considered.

148

In order to maximize the noise of the background measurement due to neutron scattering effects, the system is simulated within a 4 m x 4 m x 3 m concrete structure (bunker geometry) with 20 cm thick walls. Neutron scattering reactions with surrounding walls, floor, and ceiling cause a significant increase of the background signal that makes impossible to discriminate the fission neutrons contribution.
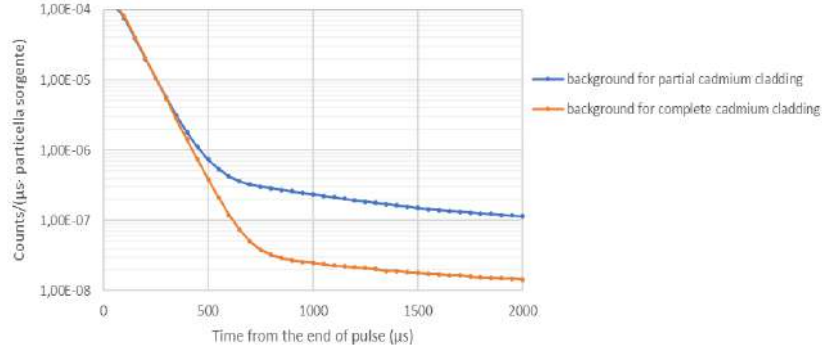
Figure 3 – Comparison between the background for partial and complete cadmium cladding

In order to minimize the effects of the measurement environmental conditions on the background signal the simulation has been repeated by modifying cadmium geometry. The background signal will decrease of more than one order of magnitude if cadmium sheets cover all sides of the polyethylene detection blocks. In fig. 3, the comparison between the background for partial or complete cadmium cladding is reported. The background reduction allows a better discrimination of the useful signal: in the time interval 600 – 1100 μs after the end of the interrogation pulse, the signal is +23% over the background, while in the partial cladding condition it was +3%.

On the basis of these results, the experimental setup has been modified and several measurements have been carried out in different conditions. [5]

3 Experimental results

The NAI performances have been tested in two opposite geometrical conditions: open field geometry vs. bunker-like geometry. The first experimental campaign (open field geometry) has been carried out in a very large space on a metallic grid 4 meters above the floor to minimize the effects of building materials, while the second campaign (bunker-like geometry) has been carried out in a 4 m x 8 m x 3 m concrete structure in order to approach expected real experimental geometries that for radiation protection reasons oblige to operate the neutron generator inside shielding structures.

The polyethylene detection blocks are covered by cadmium sheets on all their sides. Neutron generator yield is about 3 x 10^7 n/s. Experimental data have been collected for three different samples: the same of the original experiment containing 6 g of ^{235}U, a sample containing 2 g of ^{235}U and a metallic sample (to demonstrate that a non-fissile metal does not give any alarm).
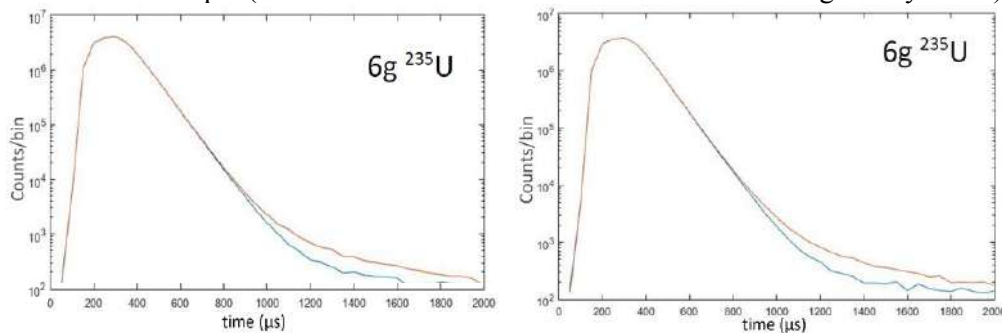
Figure 4 – Experimental DDAA curves for the sample of the original experiment in open field geometry (on the left) and in bunker-like geometry (on the right)

NAI device performances (fig.4) have been significantly improved if compared with the original results. As shown in tab. 1 the deviation between signal and background for a sample containing fissile material is more than one order of magnitude greater than the case of a sample containing no fissile material. These new conditions allowed to identify an amount as low as 2 g of ^{235}U.

Table 1 – Deviation of signal with respect to background for different samples (1000 – 1500 μs)

	(signal-background)/background	
	Open field geometry	*Bunker-like geometry*
Fe	(5±2) %	(1±2) %
2g ^{235}U	(62±3) %	(67±3) %
6g ^{235}U	(80±4) %	(81±3) %

4 Conclusions

This paper described the experimental improvement of the Neutron Active Interrogation device with respect to the preliminary experiments carried out on September 2015 at ENEA Frascati Research Centre, and presented the outcome of the simulation studies which allowed to obtain better performances. This work was articulated in two phases. The first one was a simulation study originated from the experimental results of September 2015. It led to the development of possible improvements to NAI device. The second phase of the activities was the experimental implementation of the improvements identified. The experimental campaign here described is showing that the NAI device is technically able in prompt detection (10-20 s) of gram-quantities of fissile materials, when the neutron generator is used at its maximum neutron yield (10^8 n/s).

References

[1] N. Cherubini, A. Dodaro, G. Gandolfo, L. Lepore, G.A. Marzo, E. Piccinelli, R. Remetti, Field Prototype of the ENEA Neutron Active Interrogation Device for the Detection of Dirty Bombs. Challenges 2016, 7(2), 17; http://dx.doi.org/10.3390/challe7020017

[2] R. Remetti, G. Gandolfo, L. Lepore, N. Cherubini, In field application of differential Die-Away time technique for detecting gram quantities of fissile materials, Nuclear Instruments & Methods in physics research. section A, vol 870, pages 123-130, 2017

[3] Jordan, K.A., Gozani, T., Pulsed neutron differential die away analysis for detection of nuclear materials, Nucl. Instrum. Methods Phys. Res. B, 2007, 261, 365-368

[4] Jordan, K.A.; Gozani, T.; Vujic, J. Differential die-away analysis system response modeling and detector design. Nucl. Instrum. Methods Phys. Res. A 2008, 589, 436–444

[5] N. Cherubini, A. Dodaro, G. Gandolfo, L. Lepore, G.A. Marzo, E. Piccinelli, R. Remetti, The neutron active interrogation system for in-field detection of transuranic-based radioactive dispersal devices for security applications, 26th ICONE, London, UK. Published in ASME Proceedings, Nuclear Safety, Security, and Cyber Security (Vol. 4), July 2018.

[6] G. Ponti et al., "The role of medium size facilities in the HPC ecosystem: the case of the new CRESCO4 cluster integrated in the ENEAGRID infrastructure", Proceedings of the 2014 International Conference on High Performance Computing and Simulation, HPCS 2014, art. no. 6903807, 1030-1033

Mapping renewable energy potential map over Lesotho

Massimo D'Isidoro[2], Gino Briganti[1], Lina Vitali[2], Gaia Righini[2] and Mario Adani[2]

[1] *ENEA - National Agency for New Technologies, Energy and Sustainable Economic Development, Pisa, Italy*

[2] *ENEA - National Agency for New Technologies, Energy and Sustainable Economic Development, Bologna, Italy*

ABSTRACT. Mapping wind and photovoltaic energy potential over Lesotho has been performed by means of the Weather Research and Forecasting (WRF) atmospheric numerical model. The model were applied at high resolution (1km) using the CRESCO6 ENEA HPC facility. Here some preliminary results are showed.

1 Introduction

Here we present some preliminary results of the project «Building renewable potential maps for Lesotho», conducted by ENEA and funded by IMELS (Italian Ministry for Environment, Land and Sea) under the UNFCCC Paris agreement on climate change (https://unfccc.int/process-and-meetings/the-paris-agreement/the-paris-agreement). The project started on March 2018 and will be completed at the beginning of 2020, with the aim to build solar photovoltaic (PV) and wind energy potential maps, besides an hydrological map, for Lesotho. Here we present preliminary PV and wind energy potential maps produced for the test year 2015 by means of the atmospheric numerical model WRF.

2 Methodology

Solar and wind energy potential maps were produced running WRF [1] for the year 2015 by means of three 2-way nested domains at 15km, 3km and 1km horizontal resolution, respectively, with the latter as target area. Model orography for the three domains is depicted in Figure 1.

The annual simulation consisted of 30 hours runs initialised every day at 18UTC using ERA5 reanalyses from ECMWF (European Centre Medium-range Weather Forecast) as boundary conditions for the parent domain, considering 6 hours spin-up period: model outputs from 00UTC to 23UTC were retained every day in order to cover whole 2015 at the end of the process.

ENEA CRESCO6 HPC facility was used to perform the simulation. Every 30hours simulation was performed using hybrid parallelization with 192 cores (with 2 OMP threads), requiring about 1.5 hours computing time each, with a total of about 550 hours to perform the whole year.

3 Photovoltaic power estimation over Lesotho

The PV power was calculated at hourly time step from WRF modelled solar radiation, considering the solar radiation that hits the tilted surface of a PV module as the sum of three components: direct,

151

diffuse and reflected radiation (see e.g. [2]). Also panel efficiency was taken into account, considering cSi modules and following the model described in [3]. The results were integrated over the year obtaining yearly cumulated energy production, expressed in kWh/kWp; namely energy production (kWh) has been normalized to the peak power of the PV system (kWp), i.e. the power of the system operating in Standard Test Conditions (STC). The photovoltaic power potential map derived from WRF 2015 simulation is presented in Figure 2.
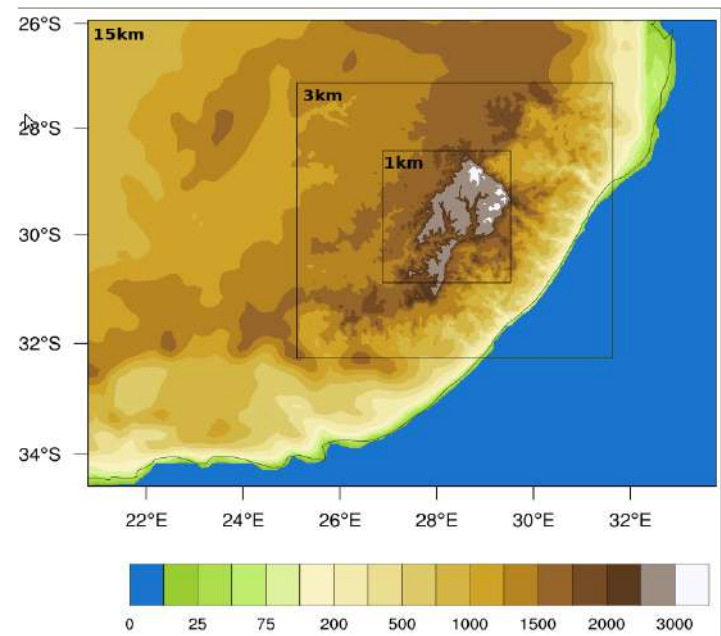
Figure 1: WRF orography for the three nested domains.
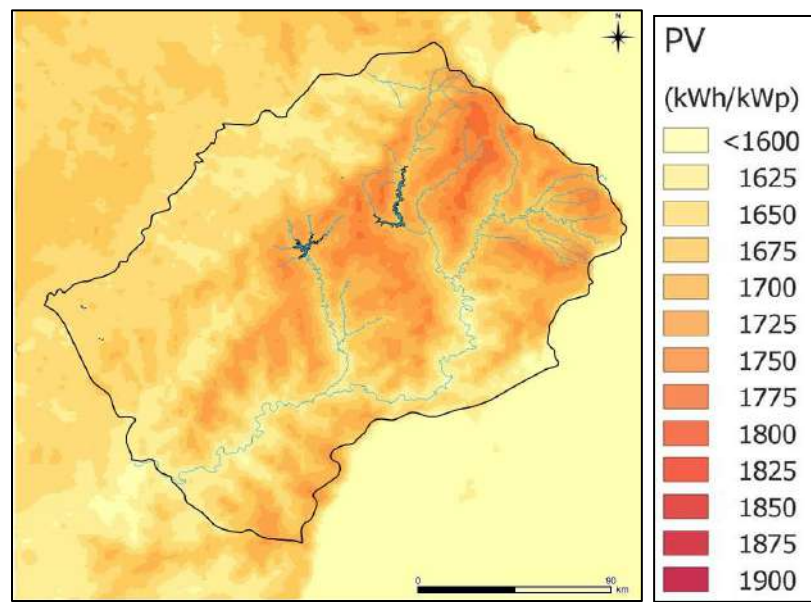
Figure2: PV energy potential over Lesotho (kWh/kWp) at 1km horizontal resolution.

4 Wind power density estimation over Lesotho

Wind Power density, which represents the maximum power obtainable by the wind is expressed in W/m^2 and can be approximated as proportional to the cube of hourly wind speed v using air density p as follows:

$$\text{WPD} = \frac{1}{2}\, pv^3$$

WRF simulated hourly outputs of wind speed and air density were used to produce WPD at every grid point at 100m height above ground. The obtained map is depicted in Figure 3.
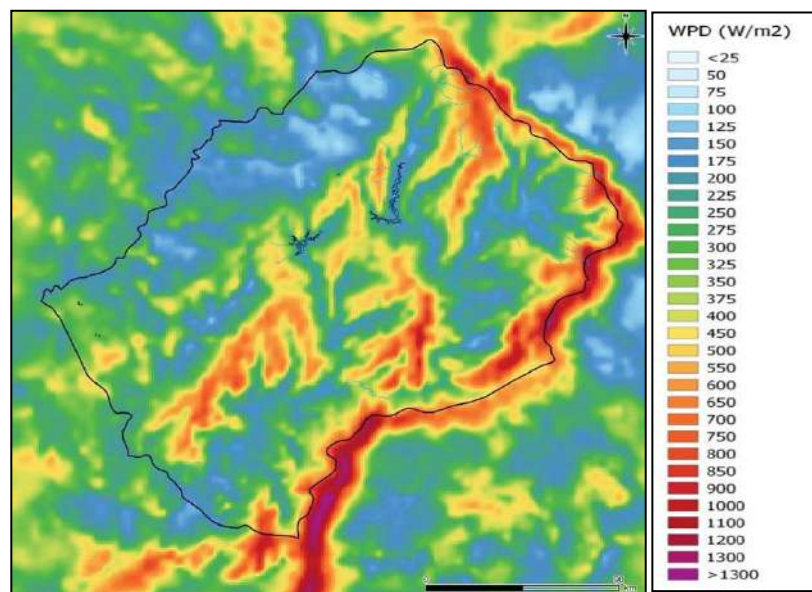
Figure 3: Wind Power Density map (W/m²) over Lesotho at 100m above ground level.

References

[1] Skamarock, W. C., and J. B. Klemp. 2008. "A time-split nonhydrostatic atmospheric model for weather research and forecasting applications." Journal of Computational Physics 227 (7):3465-3485. doi: 10.1016/j.jcp.2007.01.037.

[2] La Gennusa, M., A. Nucara, M. Pietrafesa, and G. Rizzo. 2007. "A model for managing and evaluating solar radiation for indoor thermal comfort." Solar Energy 81 (5):594-606. doi: 10.1016/j.solener.2006.09.005.

[3] Huld, T., G. Friesen, A. Skoczek, R. P. Kenny, T. Sample, M. Field, and E. D. Dunlop. 2011. "A power-rating model for crystalline silicon PV modules." Solar Energy Materials and Solar Cells 95 (12):3359-3369. doi: 10.1016/j.solmat.2011.07.026.

MOLECULAR DYNAMICS SIMULATION OF PEPTIDES FOR BRAIN THERANOSTIC NANOSYSTEMS

Caterina Arcangeli[1*], Chiara Lico[2], Selene Baschieri[2] and Mariateresa Mancuso[3*]

[1]Laboratory of Health and Environment. Department of Sustainability, Italian National Agency for New Technologies, Energy and Sustainable Economic Development (ENEA), Rome, Italy

[2]Laboratory of Biotechnology. Department of Sustainability, Italian National Agency for New Technologies, Energy and Sustainable Economic Development (ENEA), Rome, Italy

[3]Laboratory of Biomedical Technologies. Department of Sustainability,, Italian National Agency for New Technologies, Energy and Sustainable Economic Development (ENEA), Rome, Italy

ABSTRACT. In this report, part of the results published by Arcangeli et al [1] and obtained during the first year of activity of NANOCROSS project "Plant virus nanoparticles for blood-brain barrier crossing and medulloblastoma targeting" (IG 20314), granted by the Associazione Italiana per la Ricerca sul Cancro (AIRC) to M. Mancuso, will be presented. In particular, a structural and dynamical characterization, by means of molecular dynamics (MD) simulations, of specific peptides suitable for NP functionalization is here reported. All the simulations were performed on the CRESCO platform.

1 Introduction

The development of theranostic nanosystems, able to delivery diagnostic/therapeutic agents to specific targets, is the new frontier of cancer diagnosis and treatment. In the case of brain tumors, the presence of the blood brain barrier (BBB) represents the main obstacle for achieving this goal. Peptides have been revealed as excellent candidates for both BBB crossing and specific tumor homing (TH). Nanoparticles (NPs), functionalized with BBB-crossing and TH peptides, are emerging as smart theranostic nanosystems [2,3]. However, the knowledge of the molecular structure and dynamical properties of these peptides, which are essential requirements for a suitable functionalization of the delivery systems itself, is up to now still poor. Here, we report a structural and dynamical characterization of four BBB-crossing and five TH peptides. The simulations evidenced that, on the basis of their conformational dynamics, the peptides can be classified in two main groups: i) peptides adopting specific structural conformations, a feature that may limit their use as functionalizing molecules, and ii) highly flexible peptides that may represent good candidates for the functionalization of theranostic NP-based platforms.

2 Computational Methods

Peptides were solvated by water molecules and 100 mM of NaCl to neutralize the systems. All the simulations were performed with the GROMACS 2016.3 package [4], using the AMBER 99sb-ildn

force field [5] in combination with TIP3P [6] water models. Periodic boundary conditions were applied. The systems were energy minimized and equilibrated for 400 ps. Unrestrained MD were carried out in NPT ensemble. Table I summarizes some details of the simulations and lengths of the trajectories.

Table 1: Simulation details and MD simulations carried out

Simulation details	
Temperature	310K [7]
Dielectric constant	1
Integration time step	2 fs
Long-range electrostatic force	PME method [8]
Short-range electrostatic and van der Waals cutoff	1 nm
BBB-crossing peptides	**Length of simulations**
BBB-pep1	1μs
BBB-pep2	950 ns
BBB-pep3	1μs
BBB-pep4	1μs
TH peptides	**Length of simulations**
TH-pep1	1μs
TH-pep2	1μs
TH-pep3	1μs
TH-pep4	1μs
TH-pep5	950 ns

3 Results and Discussion

In order to characterize the dynamical behaviour of the selected peptide a number of structural features as a function of simulation time were monitored. Figure 1 shows the Cα RMSD to the initial equilibrated structures as a function of the simulation time and the distribution of the clusters along the trajectories. The Cα RMSD values of BBB-pep1 simulation reach a plateau within 500 ns of simulation, indicating that a conformational stability is achieved. The RMSD values of the TH-pep2 peptide seem to reach a temporary stability within the first 300 ns, then the peptides starts to explore several conformational states. A different trend is observed for the remaining peptides. Indeed, the RMSD values of all the peptides show large fluctuations around 0.6 nm for ang2, 0.5 nm for BBB-pep3, 0.8 nm for BBB-pep4, 0.4 nm for TH-pep3, 0.2 nm for TH-pep1, 0.3 nm for TH-pep4 and 0.3 nm for TH-pep5 throughout all the simulation time. The number of clusters throughout the trajectories of the peptides is also reported in Figure 1. The number of clusters provides information about the level of population of the sampled conformational space during the simulation [9]. A limited conformational sampling is observed for TH-pep1, whose total number of clusters is only about 25. The conformational sampling of BBB-pep1 reaches the stability after 500 ns of simulation, whereas TH-pep2 shows a conformational stability only during the first 300 ns of simulation. On the contrary, the distribution of clusters along the MD trajectory of BBB-pep2, BBB-pep3, BBB-pep4, TH-pep3, TH-pep4 and TH-pep5, indicates several transitions among the clusters. Generally, this behavior indicates that the peptides do not cluster into peculiar structures suggesting that the

structures of these peptides may be intrinsically flexible.
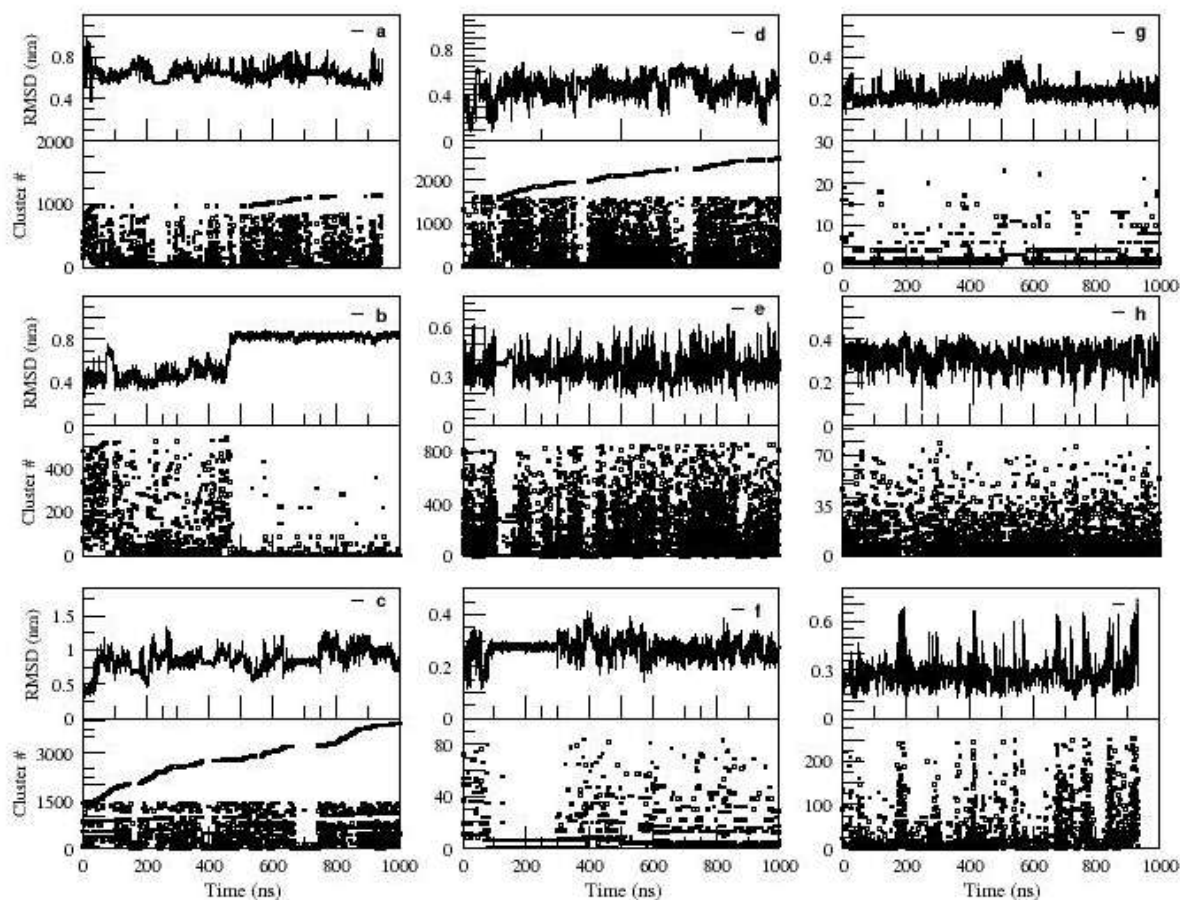
Fig.1: Cα RMSD values to the initial equilibrated structure and the cluster occupancy throughout the trajectory of the BBB-pep2 (a), BBB-pep1 (b), BBB-pep4 (c), BBB-pep3 (d), TH-pep3 (e), TH-pep2 (f), TH-pep1 (g), TH-pep4 (h), TH-pep5 (i).

A visual inspection of the structural configurations sampled by the peptides in the simulations is shown in Figures 2, 3 and 4. The initial conformation of BBB-pep1 undergoes misfolding process during the first 500 ns of simulation then the peptide adopts a stable beta hairpin conformation; the structural conformation adopted by the TH-pep1 peptide is maintained throughout the simulation with some fluctuations of the apical loop; whereas the circular conformation of TH-pep2 peptide, after 300 ns of simulation, undergoes deformations (Figure 2). The simulation snapshots of BBB-pep2, BBB-pep3, BBB-pep4 (Figure 3), TH-pep3, TH-pep4, and TH-pep5 peptides (Figure 4) capture different structural conformations indicating that they do not assume a specific and unique structure, exploring several conformational configurations.
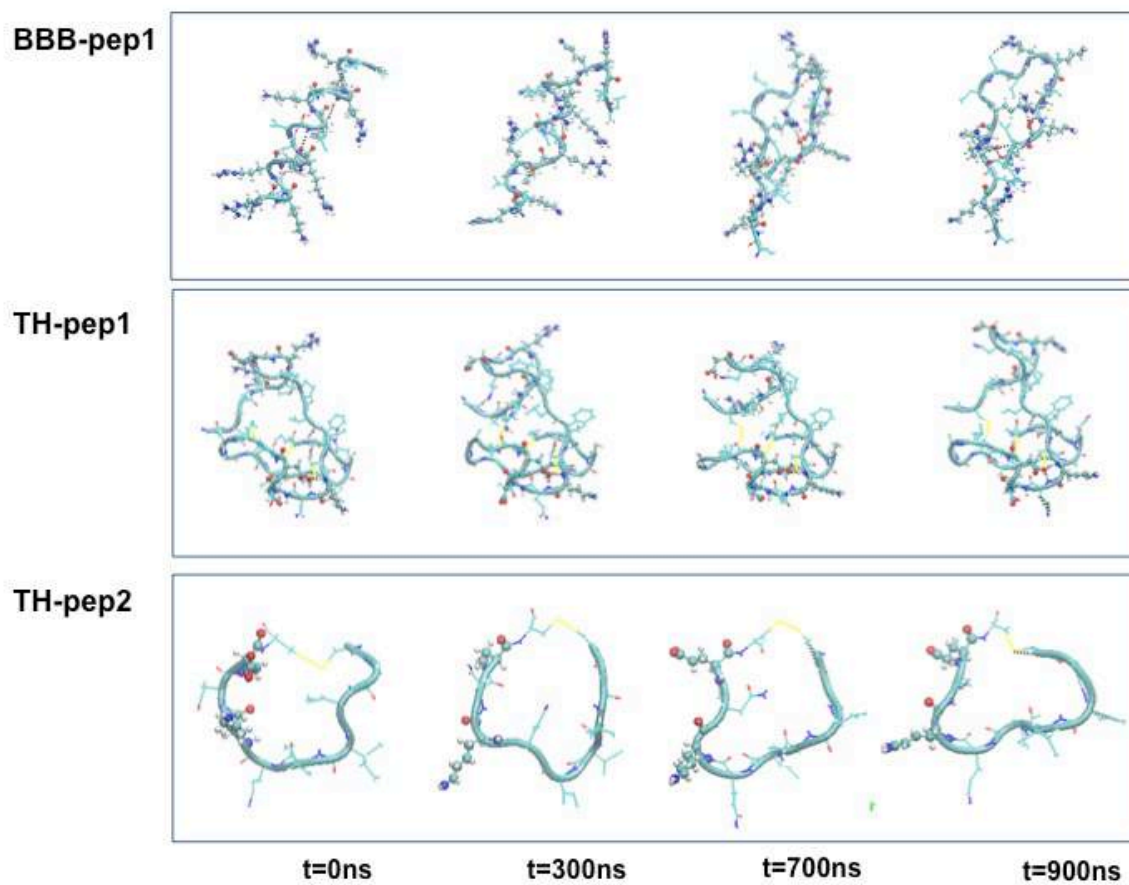
Fig.**2**: Simulation snapshots taken at selected times of MD trajectories. The peptide backbone is shown as a ribbon. Charged residues (Arg, Lys, Glu, Asp) are represented by CPK model.
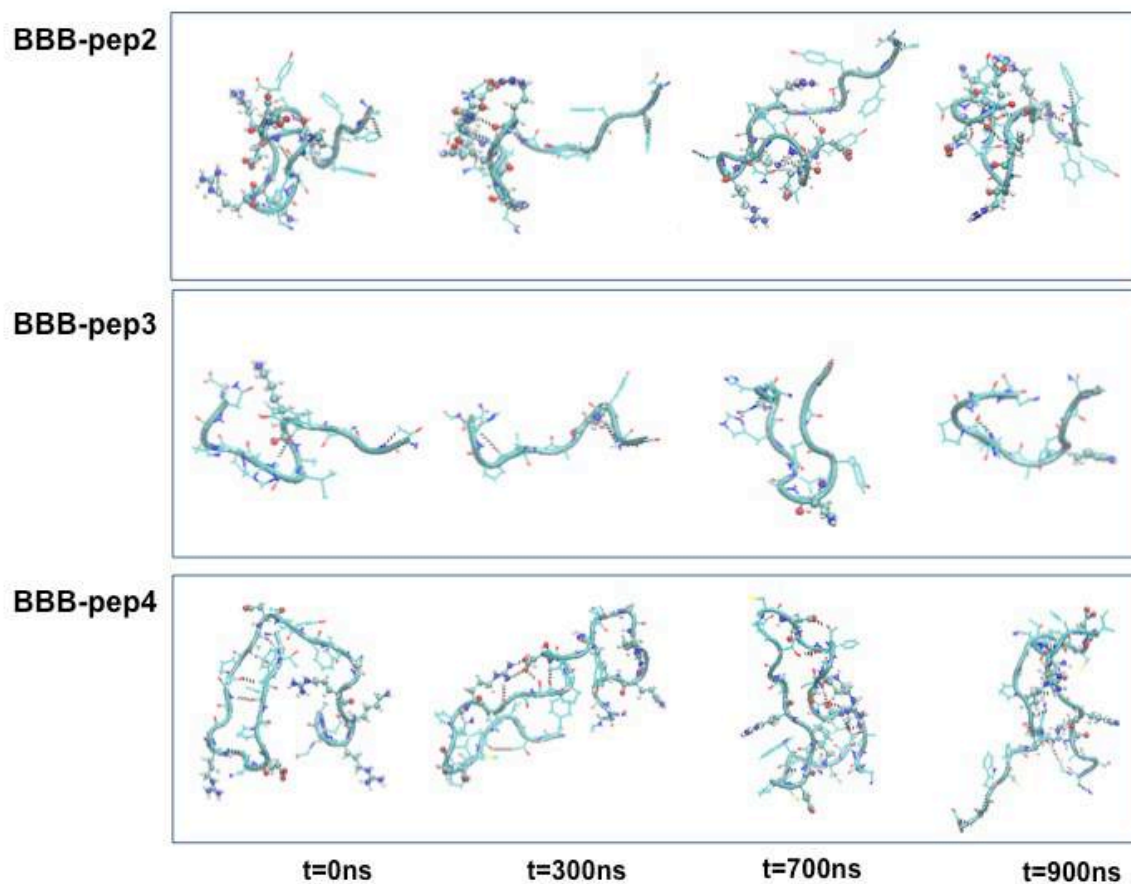
Fig.**3**: Simulation snapshots taken at selected times of MD trajectories. The peptide backbone is shown as a ribbon. Charged residues (Arg, Lys, Glu, Asp) are represented by CPK model.
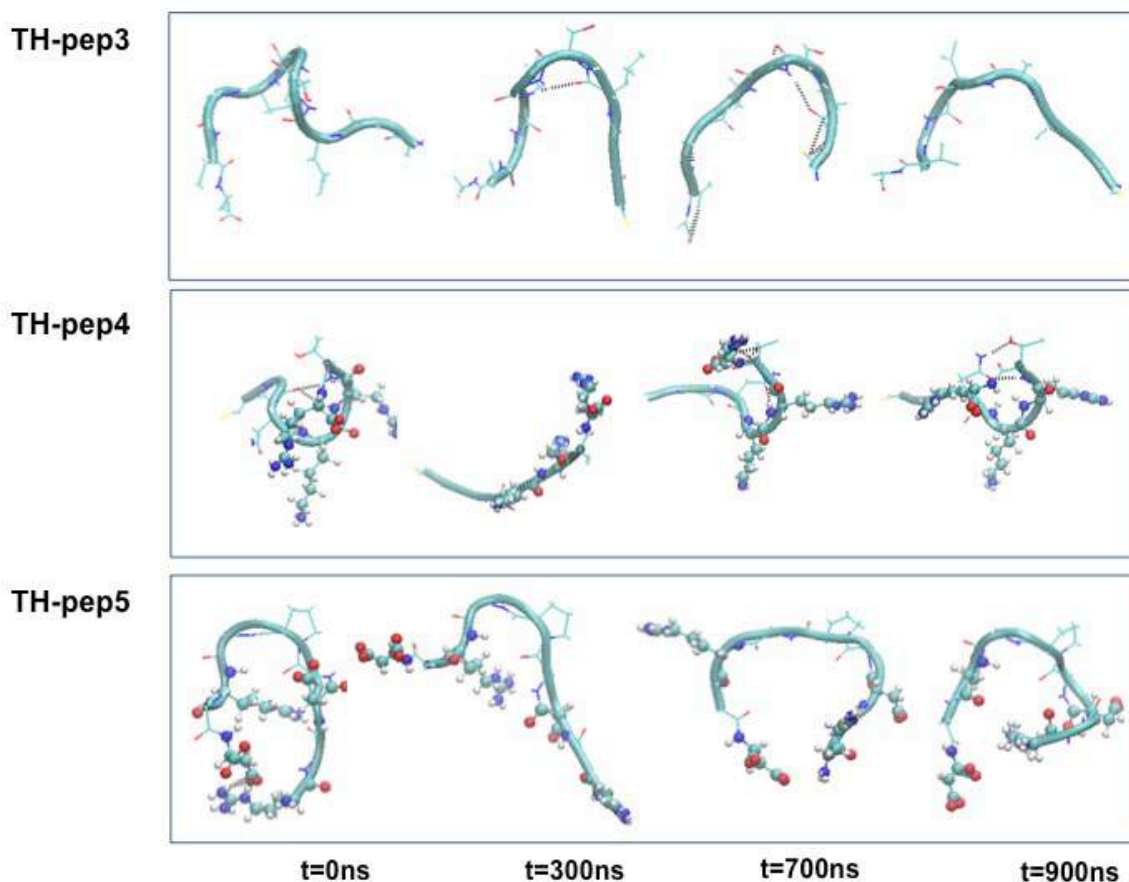
Fig.4: Simulation snapshots taken at selected times of MD trajectories. The peptide backbone is shown as a ribbon. Charged residues (Arg, Lys, Glu, Asp) are represented by CPK model.

3 Conclusions

Our preliminary simulations suggest that, on the basis of their conformational dynamics, the peptides can be classified in two main groups: i) peptides adopting a specific structural conformation, a feature that may limit their use as functionalizing molecules, and ii) highly flexible peptides that may represent good candidates for the functionalization of theranostic NP-based platforms. Further analysis and simulations are however required for a full validation of the peptide classification here hypothesized.

References

[1] Arcangeli C, Lico C, Baschieri S, Mancuso M. Characterization of blood brain barrier crossing and tumor homing peptides by molecular dynamics simulations. *Int J Nanomed.* 2019; in press.

[2] Oller-Salvia B, Sànchez-Navarro M, Teixidò M. Blood-brain barrier : an emerging paradigm for brain delivery. Shuttle. *Chem Soc Rev.* 2016; 45(17):4690-4707.

[3] Le Joncour V, Laakkonen P. Seek & destroy, use of targeting peptides for cancer detection and drug delivery. *Bioorg Med Chem.* 2018; 26(10):2797-2806.

[4] Van Der Spoel D, Lindahl, E, Hess B, Groenhof G, Mark AE, Berendsen HJC. Gromacs: fast, flexible, and free. *J Comput Chem*. 2005; 26(16):1701–1718.

[5] Lindorff-Larsen K, Piana S, Palmo K et al. Improved side-chain torsion potentials for the Amber ff99SB protein force field. *Proteins Struct Funct and Bioinform*. 2010; 78(8):1950–1958.

[6] Jorgensen WL, Chandrasekhar J, Madura JD, Impey RW, Klein ML. Comparison of simple potential functions for simulating liquid water. *J Chem Phys*. 1983; 79(2):926–935.

[7] Bussi G, Donadio D, Parrinello M. Canonical sampling through velocity rescaling. *J Chem Phys*. 2007; 126(1):014101.

[8] Essmann U, Perera L, Berkowitz ML, Darten T, Lee H, Pederson LGA. Smooth Particle Mesh Ewald method. *J Chem Phys*. 1995; 103(19):8577-8592.

[9] Daura X, Gademann K, Jaun B, Seebach D, van Gunsteren W, Mark, A. Peptide folding: when simulation meets experiments. *Angew Chem Int Ed*. 1999; 38(1-2):236−240

NUCLEAR ANALYSIS OF THE WATER COOLED LITHIUM LEAD DEMO REACTOR

Fabio Moro[1], A. Colangeli[1,2], A. Del Nevo[3], D. Flammini[1], G. Mariano[1,4], E. Martelli[1], R. Mozzillo[5], S. Noce[1,6], R. Villari[1]

[1]ENEA, Department of Fusion and Nuclear Safety Technology, I-00044 Frascati, Rome, Italy
[2]Sapienza University of Rome, Department of Basic and Applied Sciences for Engineering, Rome 00161, Italy
[3]ENEA, Department of Fusion and Nuclear Safety Technology, 40032, Camugnano (Bologna), Italy
[4]Sapienza University of Rome, Department of Astronautical, Electrical and Energy Engineering, 00186, Rome, Italy
[5]CREATE Consortium, Federico II University of Naples, Naples, 80125, Italy
[6]Tor Vergata University of Rome, Industrial Engineering Department, Rome, 00133, Italy

ABSTRACT. In the frame of the EUROfusion roadmap, the development of a conceptual design for the Demonstration Fusion Power Reactor (DEMO), beyond ITER, is a key issue. The DEMO reactor shall guarantee the tritium self-sufficiency, generate electricity and operate as a test facility for the fusion power plant relevant technologies, such as the breeding blanket (BB). The Water Cooled Lithium Lead (WCLL) concept has been chosen as a candidate for the DEMO BB: it relies on liquid Lithium Lead as breeder and neutron multiplier, Eurofer as structural material and pressurized water as coolant.

A detailed MCNP model of the latest WCLL BB layout has been generated and integrated in the DEMO MCNP generic model suitably designed for neutronic analyses. Three-dimensional neutron and gamma transport simulations have been carried out by means the MCNP Monte Carlo code and JEFF nuclear data libraries in order to assess the WCLL-DEMO performances in terms of tritium self-sufficiency and shielding effectiveness to protect the vacuum vessel and the toroidal field coils.

1 Introduction

The neutronic analyses on the WCLL breeding blanket are devoted to the assessment of the nuclear performances of the blanket concept present design, verifying its compliancy with the design targets both in terms of tritium self-sufficiency and shielding performances. The analyses have been performed on the latest design of the SMS (Single Module Segment) WCLL DEMO concept, that is presently under development: the outcomes of the present study provide guidelines for the optimization of the breeding blanket structure and its future development.

The TBR assessment is a key issue to verify the self-sufficiency of a WCLL DEMO reactor: according to the recommendations, the total TBR should be greater than 1.10 to guarantee the necessary tritium generation to sustain the reactor, considering the impact of the in-vessel components that reduce the tritium generation and the losses. The estimation of the nuclear loads provides data for the thermo-mechanical analyses and allows the evaluation of the breeding blanket and manifold/back supporting structure (BSS) shielding capabilities, verifying their compliancy with the recommended requirements on the Vacuum Vessel (VV) and Toroidal Field Coils (TFC). The blanket and manifold/BSS system should ensure that the damage on Vacuum Vessel (VV) steel, cumulated over DEMO lifetime (equivalent to 6 FPY), is below 2.75 dpa, in order to prevent the degradation of the stainless-steel properties (fracture toughness is reduced by no more than 30%).

Furthermore, the He concentration should be below 1 appm in reweldable zones. The protection of the superconductive TFC is one of the most critical issues in the design of the breeding blanket: different nuclear quantities are estimated in order to assess the effect of the radiation streaming from the plasma on the magnets. In particular, the evaluation of the fast neutron fluence on the superconductor coils ($<10^9$ n/cm^2/s) and the estimation of the nuclear heating due to neutrons and gammas deposited on the winding pack (<0.05x10^3 W/m^3), provide a reliable verification of the WCLL breeding blanket shielding efficiency. The above-mentioned nuclear responses have been assessed through three-dimensional coupled neutron and gamma transport simulations by means of the MCNP5v1.6 Monte Carlo code [1] and the Joint Evaluated Fusion File JEFF 3.3 nuclear data libraries [2].

2 The WCLL Breeding Blanket: structure and MCNP modeling

The present WCLL BB design [3] is based, as for on Single-Module-Segment (SMS) concept where a basic breeding unit (BU), is replicated in Inboard and Outboard along the poloidal direction. The single BU (Fig. 1) includes the FW and side walls, top and bottom caps, internal stiffening and baffle plates, BSS, cooling pipes, LiPb manifolds and water manifolds for FW and breeding zone cooling.
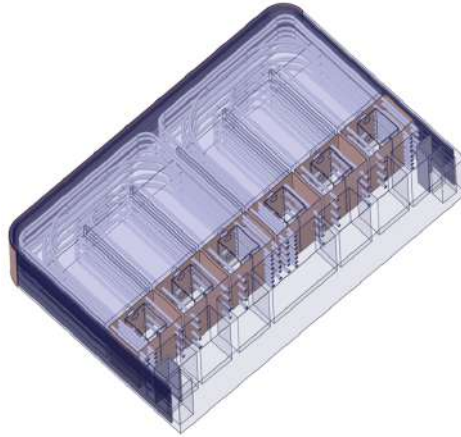
Fig. 1: WCLL BU: perspective view of the Outboard breeding unit, showing the inner cooling pipes layout.

Considering the complexity of the BU cooling pipes assembly, the WCLL BB MCNP modeling approach has been based on the segmentation of the outboard BB into radial sectors (Fig. 2) with specifically defined material mixture. The pre-processing and simplification of the layered WCLL BB CAD model has been performed by means of the 3D modeling software Ansys SpaceClaim 2019 [4] in order to generate a CAD model suitable for neutronic analyses. Successively the simplified WCLL BB model has been converted into the equivalent MCNP geometrical representation by means of the CAD-to-MCNP interface SuperMC [5] and manually integrated into the 2017 DEMO 1 generic MCNP model. The obtained WCLL DEMO MCNP model is shown in Fig. 2: the reduced radial extension of the inboard module has been handled through the decrease of the toroidal extension of the innermost sector of the breeding zone, thus, ideally, keeping the distance between the FW and the cooling channels fixed. The DEMO reactor baseline layout used in the present studies is the EU DEMO1 2017 reference configuration model representing a 11.25° toroidal sector of the tokamak [6].
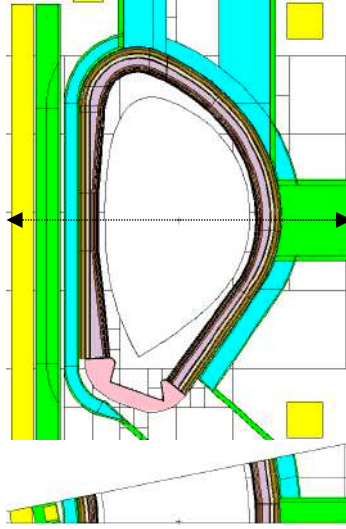
Fig. 2: WCLL DEMO MCNP model: poloidal section showing the Inboard and Outboard breeding blanket (top) and toroidal section along the equatorial plane (bottom).

3 Nuclear analyses

The assessment of the tritium breeding ratio (TBR) has been performed for each region of the BB that contributes to the Tritium generation (i.e. the BU sectors and the LiPb manifolds). The resulting total TBR for this configuration is 1.138, thus the present design target for Tritium self-sufficiency is satisfied: 94.4% of the tritium is produced in the breeding zone, while the residual portion is generated in the manifold zone.

The shielding performances of the WCLL BB have been assessed through the evaluation of the neutron flux, nuclear heating, dpa and He-production in steel components along the inboard and outboard midplane. The total and fast (E>100 keV) neutron fluxes radial profiles are shown in Fig. 3 for both the inboard and outboard. The total neutron fluxes at the inboard and outboard W armour are 5.13×10^{14} n/cm^2/s and 5.5×10^{14} n/cm^2/s, respectively. In inboard, the blanket/manifold system provides an attenuation of more than two orders of magnitudes to the VV inner shell and the neutron flux further decreases of three orders of magnitude across the VV, being 1.17×10^9 n/cm^2/s (total), and 7.93×10^8 n/cm^2/s (fast) on the TFC.
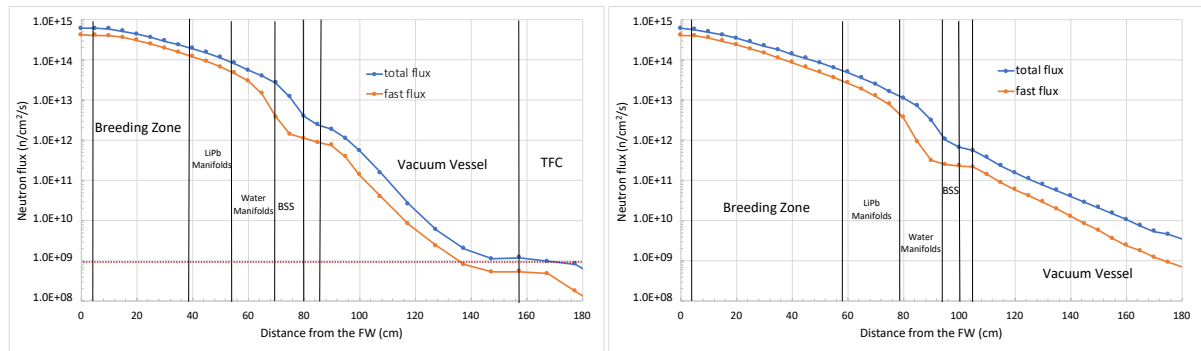
Fig. 3. Radial profile of the total (blue) and fast (red) neutron flux at the equatorial plane for the inboard (panel) and outboard (lower panel) midplane. The dotted red line indicates the design target for the fast neutron flux on the TFC (10^9 n/cm^2/s).

The radial profiles of the nuclear heating density evaluated on Eurofer and LiPb (blanket) and SS316L (Vacuum Vessel and TFC) is shown in Fig. 4 for the both the inboard and outboard sectors.

As far as the inboard is concerned, the maximum values are 25.7 W/cm^3 on W armour and 8.8 W/cm^3 on Eurofer in the FW and 0.046 W/cm^3 on the VV inner shell SS316L. In the TF coil, the maximum nuclear heating density is 1.73×10^{-5} W/cm^3: even with a consistent reduction of the BB inboard radial extension, the design limit of 5×10^{-5} W/cm^3 is satisfied. For the outboard segment, the heat load on the W armour is 28.4 W/cm^3, while the higher values assessed for the FW Eurofer and SS316L VV inner shell are 9.59 W/cm^3 and 1.66×10^{-2} W/cm^3 respectively.
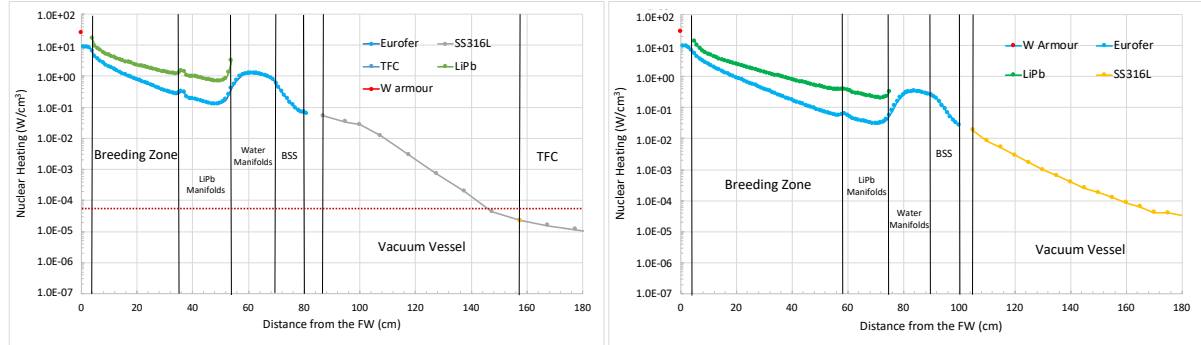
Fig. 4. Nuclear heating radial profile in W armour, Eurofer, LiPb and SS316L assessed at the equatorial plane for the inboard (left panel) and outboard (right panel). The dotted red line indicates the design target on the TFC (5×10^{-5} W/cm^3).

The radiation damage has been assessed in terms of dpa per FPY (dpa/FPY) produced in the structural steel of the blanket (Eurofer) and in the Vacuum Vessel SS316L. Considering the design limit of 2.75 dpa integrated over 6 FPY, the cumulated damages over the DEMO lifetime for the VV inner shell are 0.059 dpa and 0.015 dpa in inboard and outboard respectively: in both cases the design target limit is satisfied. The aim of the Helium production calculations is to verify that the gas generated at locations where re-welding of steel components is required, is lower than 1 appm at the end of DEMO lifetime: the most critical locations for the steel re-weldability are the vessel zones, thus the Helium production has been assessed in terms of appm per FPY (appm/FPY) produced in the structural steel of the blanket (Eurofer) and in the SS316L steel of the VV. Integrating the He-production results for the VV over the foreseen 6 FPY lifetime, the maximum cumulated He-production is 0.48 appm for the inboard and 0.24 for the outboard: in both cases the limit of 1 appm is fulfilled. The assessment of the above-mentioned nuclear responses needs statistically reliable results (statistical error below 10%), thus the usage of the MCNP MPI multiprocessor version installed on the CRESCO cluster has been required. Each MCNP run generates about 2×10^9 particles (neutrons, photons or both depending on the nuclear responses evaluated), using 800 processors for a total computing time of about 4×10^6 seconds. The typical dimension of a single output file is approximately 300 Mbyte, so the study required the analysis of some Gbyte data.

References

[1] X-5 Monte Carlo Team: MCNP - A General Monte Carlo N-ParticleTransportCode, Version 5, Los Alamos National Laboratory, Los Alamos, New Mexico, USA, April 2003.

[2] JEFF3.3 nuclear data library, http://www.oecd-nea.org/dbdata/jeff/jeff33/#neutron

[3] A. Del Nevo et al., 'Recent progress in developing a feasible and integrated conceptual design of the WCLL BB in EUROfusion project, Fus. Eng. Des. 146, (2019), 1805-1809

[4] www.spaceclaim.com.

[5] Y. Wu, FDS Team, CAD-based interface programs for fusion neutron transport simulation, Fus. Eng. Des., 84, (2009), 1987 – 1992.

[6] C. Bachmann et al., 'Overview over DEMO design integration challenges and their impact on component design concepts', Fus. Eng. Des., 136, (2018), 87-95.

AB INITIO SIMULATION OF ADVANCED MAGNETIC MATERIALS

Federico Totti[1*], Andrea Albino[1] and Francesco Buonocore[2]

[1]*LAboratory of Molecular Magnetism, Dipartimento di Chimica* "Ugo Schiff",
Università degli Studi di Firenze & INSTM RU of Firenze, via della Lastruccia 3-13,
50019 Sesto Fiorentino (FI), Italy.
[2]*ENEA, Casaccia Research Centre, 00123 Rome, Italy.*

ABSTRACT. In recent years we have witnessed a social and technological revolution due to the increased capacity of computational units and information storage/processing. Such a revolution have had major impacts on our society up to a level where virtually any task is now computationally processed. In particular, one can design a range of quantum algorithms, which scale with the complexity of the problem in a much more favorable way than their classical counterparts. The difficult technological challenge of implementing quantum devices strongly affects the coming of the quantum supremacy in information theory. Several systems are currently investigated for the practical realization of molecular devices. Addressing the fundamental questions about microscopic quantum behaviour is of paramount importance for modern material-science applications. For instance, it is crucial in quantum information processing and storage, where spin-phonon relaxation is the ultimate origin of decoherence of solid-state electron spin at room temperature. The incomplete understanding of the spin-relaxation mechanism and the need of extending the current paramagnetic metal complexes and SMMs design strategies must be fulfilled, so that molecules presenting long-living spin-states can be synthesized.

1 Introduction

Recently a new computational power revolution has been foreseen to happen in the imminent future. This revolution is related to the possibility to actually implement quantum bits as logical devices and exploit the rules of quantum mechanics, such as superposition and entanglement, to process information to an increased speed with respect to classical logic, as it implemented in current computers. Although this is a relatively old idea [1] only recent advances in material science rewived the actual realization of this technology. In the context of molecular magnetism several research groups have proposed both systems and methodologies to create a molecular based quantum computer. One of the great advantage of molecular compounds is their structural versatility. Synthetic chemistry can here play a fundamental role in modulating specific interactions between microscopic constituents as phonons and spins in order to achieve the desired molecular properties. Remarkable results have been achieved in the field in the last years placing magnetic molecules in a leading position in the "race" to the build an efficient quantum device. Among the open challenges, the possibility to retain the magnetization of molecular spins for a time long enough to apply a series of gates represents a fundamental one. The description of magnetization dynamics is developed through the theory of paramagnetic relaxation. [1], [2] The advances in quantum technology can be applied not only for volatile memory, the observation of magnetic bistability in single molecules [3] could open new frontiers in the high-density data storaging with a potential increase of orders of magnitude with respect to capabilities available in nowadays magnetic data supports. In order to reach such great technological performances, a system able to show an intrinsic magnetic hysteresis loop coming from its intramolecular properties is needed. In this context single molecule magnets

(SMMs) represent some of the best candidates to be used for magnetic data recording and in spintronic devices in general, though up to now only at cryogenic temperature. A wide variety of experimental investigations is available in this field, [4]–[10] on the other hand the theoretical description is still at an early stage. [11]–[15] In particular, modeling molecules in a more realistic environment in an ab initio computational framework has become possible only in the past few years, enabled by an extensive work of the integration of density functional theory (DFT), post-Hartree−Fock (post-HF) methods, and spin dynamics for calculation of the dynamical magnetic properties of multispin systems. The present work introduces a first principles investigation of a vanadium-(IV) molecular complex, [VO(TPP)] (2) (TPP = tetraphenylporphyrinate), a terbium-based single molecule magnet (SMMs), $TbPc_2(OC_{11}H_{21})_8$ (Pc = Phtalocianine) was chosen for a detailed analysis, too. Pushing forward the analysis, the grafting on surface of such molecules could lead to the addressability of single qubits (vanadium-based complex) or stored information (terbium-based complex) in view of molecular quantum computers. Different or enhanced effects could arise from adsorption of molecules on different substrates. In these regards, graphene, its half hydrogenated derivative graphone and its fully hydrogenated graphane are the substrates under investigation (this last aspect of the study is in collaboration with Francesco Buonocore, ENEA).
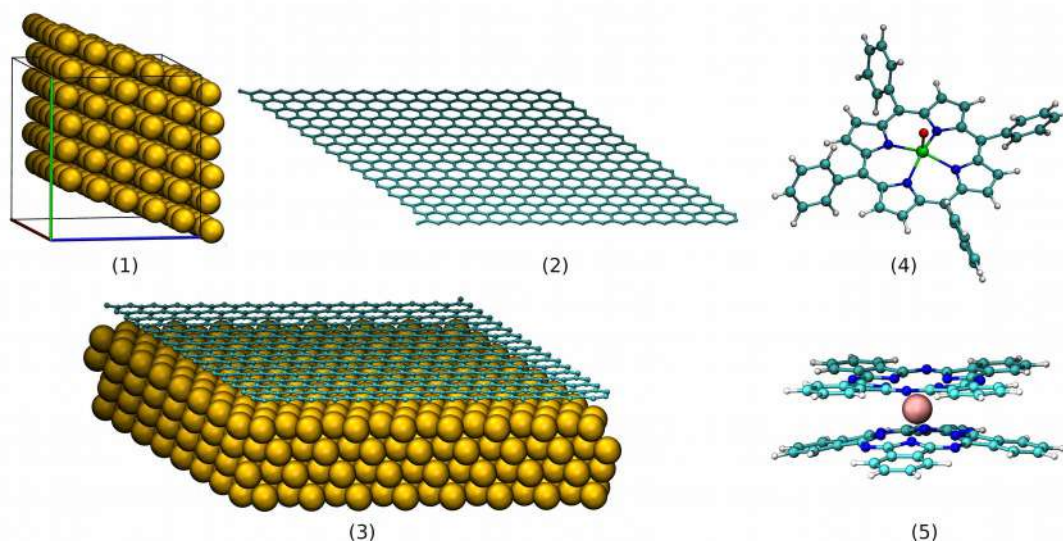
Fig.1: Crystalline structure of Au(111) (1); graphene (2); adsorbed graphene on Au(111) (3). Molecular structures of [VO(TPP)] (4); $TbPc_2$ (5).

3 Methods

Our approach aims at addressing the spin-lattice relaxation time T_1 that is the primary limiting parameter for the development of higher working temperature molecular qubits. It consists of modeling the magnetic properties by first principles, when perturbing the molecular structures along the normal modes of vibration, following a strategy adopted in previous works. [14] The exploration of the magnetic properties of TbPc2 on insulators, on the other hand, can shed some light into the type of tunnelling events occurring when the TbPc2 is in contact with strongly or weakly interacting substrates.

3.1 Cell Optimisation

In order to correctly account for the vibrational properties of the solid-state systems, where intermolecular interactions become relevant, DFT calculations are performed in the crystal phase with a Gaussian plane-wave and pseudopotentials formalism, as implemented in the Quickstep module of the CP2K package. [16] Van der Waals interactions are taken into account with the non-local rVV10 correction scheme. It is mandatory to establish a robust protocol to correctly relax the composite structure of graphene adsorbed to Au(111) (graphene@Au(111)) before grafting molecular systems on it.

The main issue when facing up the optimisation problem is the different cell parameters of Au(111) and graphene. This aspect requires the previous cell optimisation of the single constituents to ascertain the reliability of the cell parameters when superimposing graphene to Au(111). Several functionals were tested against both graphene and Au(111). The generalized gradient approximation (GGA) functional in the PBE parametrization is chosen for all the calculations as it constitutes a good tool for the further description of metal complexes (revPBE). Once demonstrated the agreement of the Au(111) structure and graphene alone against the experiments, the next step will consists in the assembling of the composite system and to relax it keeping the lowest layer in the Au slab frozen.

5 Conclusions

The continuation of this work foresees the grafting of the mentioned molecules on the prepared substrate and on other mentioned substrates and the detailed vibrational analysis of the whole system. Calculation of the spin and spin−phonon Hamiltonian parameters is the next step. Calculation of the spin−phonon coupling coefficients will be performed following a tensor differentiation procedure, as previously reported in literature on single-molecule magnets. [14] This procedure will be here applied to the Landé g tensor that describes the coupling between the spins and an external magnetic field.

Acknowledgments

References

[1]   A. Abragam and B. Bleaney, Electron Paramagnetic Resonance of Transition Ions. Clarendon Press: Oxford, U.K., 1970.

[2]   K. W. H. Stevens, "The theory of paramagnetic relaxation," *Reports Prog. Phys.*, vol. 30, no. 1, pp. 189–226, 1967.

[3]   S. Loth, K. Von Bergmann, M. Ternes, A. F. Otte, C. P. Lutz, and A. J. Heinrich, "Controlling the state of quantum spins with electric currents," *Nat. Phys.*, vol. 6, no. 5, pp. 340–344, 2010.

[4]   L. Tesi *et al.*, "Quantum coherence in a processable vanadyl complex: new tools for the search of molecular spin qubits," *Chem. Sci.*, vol. 7, no. 3, pp. 2074–2083, 2016.

[5]   M. Atzori *et al.*, "Quantum Coherence Times Enhancement in Vanadium(IV)-based Potential Molecular Qubits: the Key Role of the Vanadyl Moiety," *J. Am. Chem. Soc.*, vol. 138, no. 35, pp. 11234–11244, 2016.

[6]   M. Atzori *et al.*, "Spin Dynamics and Low Energy Vibrations: Insights from Vanadyl-Based Potential Molecular Qubits," *J. Am. Chem. Soc.*, vol. 139, no. 12, pp. 4338–4341, 2017.

[7]   M. Atzori *et al.*, "Structural Effects on the Spin Dynamics of Potential Molecular Qubits," *Inorg. Chem.*, p. acs.inorgchem.7b02616, 2017.

[8]   M. Atzori, L. Tesi, E. Morra, M. Chiesa, L. Sorace, and R. Sessoli, "Room-Temperature Quantum Coherence and Rabi Oscillations in Vanadyl Phthalocyanine: Toward Multifunctional Molecular Spin Qubits," *J. Am. Chem. Soc.*, vol. 138, no. 7, pp. 2154–2157, 2016.

[9]   S. Carretta *et al.*, "A two-qubit molecular architecture for electron-mediated nuclear quantum simulation," *Chem. Sci.*, 2018.

[10]   E. Moreno Pineda, T. Komeda, K. Katoh, M. Yamashita, and M. Ruben, "Surface confinement of TbPc2-SMMs: structural, electronic and magnetic properties," *Dalt. Trans.*, vol. 45, no. 46, pp. 18417–18433, 2016.

[11]   L. Escalera-Moreno, N. Suaud, A. Gaita-Ariño, and E. Coronado, "Determining Key Local Vibrations in the Relaxation of Molecular Spin Qubits and Single-Molecule Magnets," *J. Phys. Chem. Lett.*, vol. 8, no. 7, pp. 1695–1700, 2017.

[12]   J. Ferrando-Soria *et al.*, "Switchable Interaction in Molecular Double Qubits," *Chem*, vol. 1, no. 5, pp. 727–752, 2016.

[13]   A. Lunghi, F. Totti, R. Sessoli, and S. Sanvito, "The role of anharmonic phonons in under-barrier spin relaxation of single molecule magnets," *Nat. Commun.*, vol. 8, pp. 1–7, 2017.

[14]   A. Lunghi, F. Totti, S. Sanvito, and R. Sessoli, "Intra-molecular origin of the spin-phonon coupling in slow-relaxing molecular magnets," *Chem. Sci.*, 2017.

[15]   A. Lunghi, M. Iannuzzi, R. Sessoli, and F. Totti, "Single molecule magnets grafted on gold: magnetic properties from ab initio molecular dynamics," *J. Mater. Chem. C*, vol. 3, no. 28, pp. 7294–7304, 2015.

[16]   J. Hutter, M. Iannuzzi, F. Schiffmann, and J. Vandevondele, "Cp2k: Atomistic simulations of condensed matter systems," *Wiley Interdiscip. Rev. Comput. Mol. Sci.*, vol. 4, no. 1, pp. 15–25, 2014.

Neutronics analyses of DEMO divertor

Davide Flammini[*1], Rosaria Villari[1], Fabio Moro[1], Nicola Fonnesu[1], Giovanni Mariano[2], Andrea Colangeli[3]

[1] *ENEA, Department of Fusion and Nuclear Safety Technology, I-00044 Frascati, Rome, Italy*
[2] *DIAEE Department, Sapienza University of Rome, 00186, Roma, Italy*
[3] *DIAEE Department, Sapienza University of Rome, 00186, Roma, Italy*

ABSTRACT. This report summarises the 3-D neutronics analyses performed in 2018 with MCNP5 to evaluate the nuclear responses and optimize the design the DEMO divertor. The results in term of neutron flux, nuclear heating, dpa and He-production are presented. The impact on VV loads are evaluated as well.

1 Introduction

The assessment of nuclear loads on DEMO divertor has been carried-out within EUROfusion WP-DIV project [1]. The neutronics analyses performed in 2018 by means of the Monte Carlo code MCNP5 [2], using JEFF 3.3 [3] nuclear data library. The analyses were aimed to evaluate the nuclear responses on the divertor components, i.e. neutron flux, nuclear heating, radiation induced damage in terms of displacement per atom (d.p.a.), to provide inputs for thermo-hydraulic and thermo-mechanical analyses and to assess its shielding performances.

2 Model description

A detailed heterogeneous MCNP representation of the last design of the divertor cassette and liner has been developed (see Fig. 1). The divertor cassette and liner have been represented by explicitly modelling the structural parts (EUROFER plates) and the cooling channels (water). Plasma Facing Components instead have been modelled in a homogenized layered structure (see Fig. 2). In Table 1 the composition of each layer representing the PFC has been reported. The divertor model has then been integrated in the 11.25° Water Cooled Lithium Lead (WCLL) DEMO model (see Fig. 3).
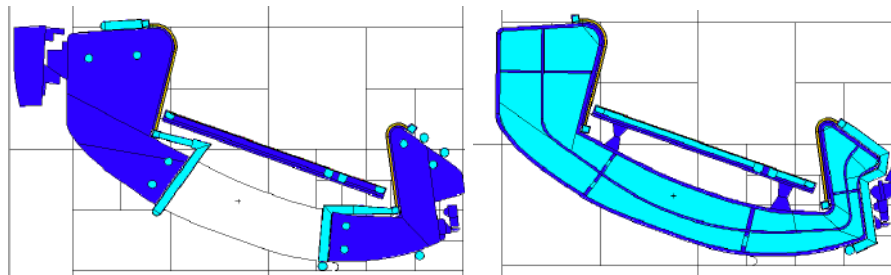
Fig.1:MCNP model of the divertor and liner. Water cooling channels (in light blue) have been modelled separately from EUROFER structure both in cassette and in liner.

Table 1: Composition of divertor PFC

PFC component	Thickness (mm)	composition (vol %)				
		W	**CuCrZr**	**H2O**	**Void**	**EUROFER**
1st layer	5	94			6	
2nd layer	17	39	16	28	16	
3rd layer	3	94			6	
4th layer	17				78	22
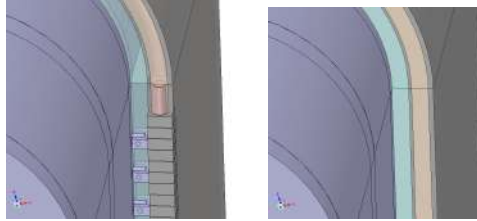
Fig.2: PFC of the divertor, original and simplified model.
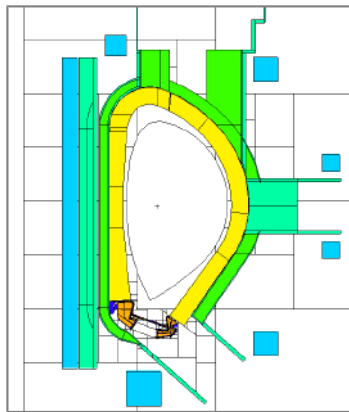
Fig.3: MCNP model of the divertor and liner.

3 Calculations and results

Three-dimensional simulations have been performed to calculate the spatial distributions of the neutron flux, nuclear heating, neutron damage and the He-production. The total nuclear power and breakdown in all divertor sub-components and the nuclear loads on Vacuum Vessel (VV) and Toroidal Field Coils (TFC) have also been calculated. The results have been normalized to 1998 MW of fusion power. The amount of nuclear power deposited on the divertor is 129 MW (P_{div}/P_{fus} is 6.5%): 52% on the cassette body (44.1 MW on Eurofer and 23.5 MW on water), 12.6% on the plasma facing components (16.3 MW), and ~31% on the liner (40.2 MW), the rest on the cooling pipes (5.5 MW). The spatial distributions of neutron flux ($n/cm^2/s$), nuclear heating density (W/cm^3), neutron damage (dpa/FPY) and He – production (appm/FPY) in Eurofer with relevant contours are reported in Figure 4. A significant streaming from gaps between blanket and divertor, below pumping duct and

through the empty lower port is noteworthy in all maps. The inboard side of the cassette is better shielded compared to the outboard. The neutron fluxes vary in the range ~$5 \cdot 10^{11}$-$2.5 \cdot 10^{14}$ n/cm^2/s. The maximum nuclear heating densities are 21 W/cm^3 on W and 7.6 W/cm^3 on Eurofer liner; the maximum values in the inboard and outboard fixation systems which are not actively cooled are 0.03 and 0.08 W/cm^3, respectively. The nuclear heating in the TFC exceeds of more than two orders of magnitude the limit (5×10^{-5} W/cm^3), mainly because of lack of shield in lower port. The damage in Eurofer varies in the range 0.01- 4.9 dpa/FPY. The zones exceeding the Eurofer limit of 6 dpa over 2 FPY are below the Inner and outer vertical targets and on the liner. In the rest of the cassette body the dpa/FPY in Eurofer is below 3 dpa. The cumulated damage on VV slightly exceed the limit of 2.75 dpa FPY (max 3.3 dpa over 6 FPY). Regarding the he-production, the maximum value on the cassette is 84 appm/ FPY; considering the limit of reweldability (i.e. 1 appm over 6 FPY), the re-welding of pipes is possible in the zones protected by blanket modules (i.e. cut and re-welding feasible only outside the 0.16 appm/FPY contour).

On the basis of the present results, the main critical issues are the cumulated damage on Eurofer and on the VV shell. Under the present conditions, the lifetime of the cassette is limited to 1.22 FPY. Design optimization and thermo-hydraulic studies are needed to overcome the design limit and/or to improve the shield in plasma facing zone. The damage on VV can be mitigated by increasing shielding liner thickness and possibly reduce the pumping duct size.
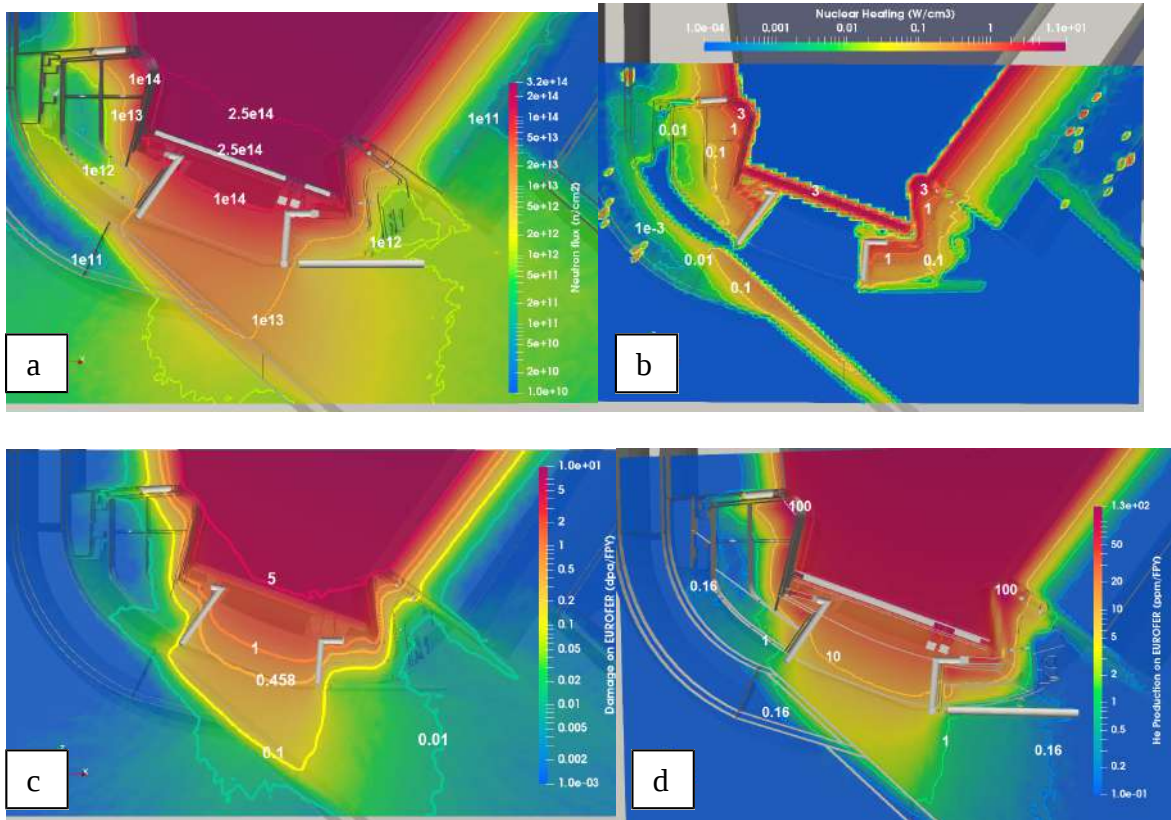
Fig.4: Poloidal-radial maps of (a) Neutron flux (n/cm^2/s), (b) Nuclear heating density (W/cm^3), (c) damage in Eurofer (dpa/FPY) and (d) He-production in Eurofer (appm/FPY).

Acknowledgement

References

[1] R. Villari, D. Flammini, Neutronic Analysis of DEMO divertor 2018, Final Report of WPDIV DIV-1-T005-D006b in preparation

[2] X-5 Monte Carlo Team: MCNP - A General Monte Carlo N-ParticleTransportCode, Version 5, Los Alamos National Laboratory, Los Alamos, New Mexico, USA, April 2003.

[3] JEFF3.3 nuclear data library, https://www.oecd-nea.org/dbdata/jeff/jeff33/index.html

[4] G. Ponti et al. The role of medium size facilities in the hpc ecosystem: the case
of the new CRESCO4 cluster integrated in the eneagrid infrastructure. In High Performance
Computing & Simulation (HPCS), 2014 International Conference on, pages 1030–1033.
IEEE, 2014.

Neutronics analysis for the design and integration of the pellet guiding tube in DEMO

Andrea Colangeli[*1], Rosaria Villari[1], Fabio Moro[1], Davide Flammini[1], Giovanni Mariano[1], Nicola Fonnesu[1]

[1]*ENEA, Department of Fusion and Nuclear Safety Technology, I-00044 Frascati (Rome), Italy[1]*

ABSTRACT. Three-dimensional nuclear analyses with MCNP5 Monte Carlo code have been performed to support design and integration of Pellet Fuelling system in DEMO reactor. Strategies to improve the pellet fuelling systems design and its shielding capability have been studied to guarantee self-sufficiency and reduce the impact of nuclear loads to other components.

1 Introduction

In the frame of this activity within EUROfusion PMI program, three-dimensional nuclear analyses with MCNP5 code [1] and JEFF3.2 nuclear data library [2] have been performed in CRESCO [3] cluster to support design and integration of Pellet Fuelling System in DEMO. In 2018 an evolution of the pellet guiding tube actively cooled have been updated and integrated in DEMO for nuclear analyses.

2 Design and integration of Pellet Fuelling Line

The in-vessel guiding tube foresees vertical pellet injection lines located behind the Inboard (IB) blanket modules (see Fig. 1&2). In order to deliver pellets as close as possible to the plasma core, a pellet Cu guiding tube is bolted to the Vacuum Vessel (VV) inner shell and located in a gap in between two adjacent blanket modules. This system has been integrated in DEMO Helium Cooled Pepple Bed (HCPB). Analyses have been performed to evaluate the nuclear heating and damage on the pellet injection lines, and radiation induced damage on the VV inner shell due to the radiation streaming through the gap. Two different configurations for the pellet guiding tube have been examined:

1. 40 cm long guiding tube
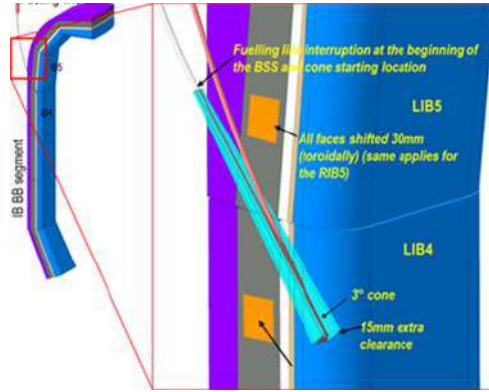2. 60 cm long guiding tube

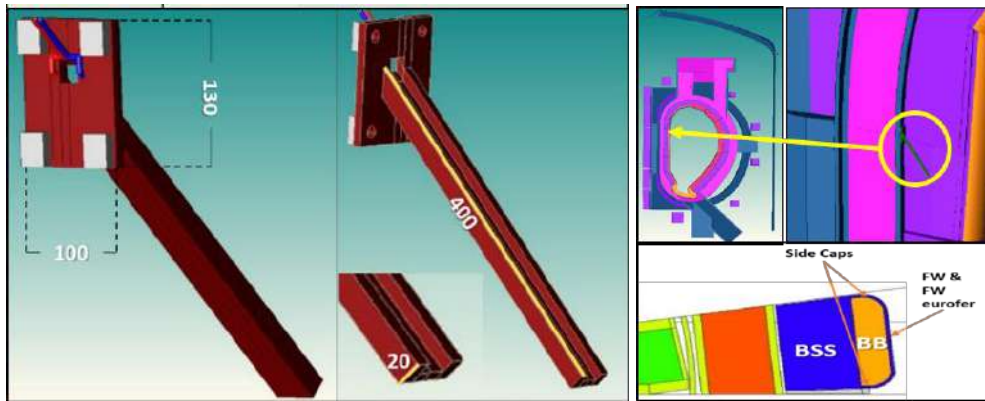---

Fig.1: Scheme of the in vessel guiding tube

Fig.2: 3D view of the 2018 pellet guiding rube configuration with the reference length (40 cm) – left and HCPB MCNP 3D model with the top viewof IB5 module with 3° blanket opening (right)

3 Results

The impact of the integration of the guiding tube on the total nuclear heating in IB blanket is marginal (Tab.1). Regarding the loads on the pellet guiding tube the maximum heating and damage in front position are 1.62 W/cm^3 (Tab. 2) and 2.1 dpa/FPY (Full Power Year) for the 40 cm configuration and 2.57 W/cm^3 and 3.2 dpa/FPY for the 60 cm one. For the water coolant the maximum heating is 1.84 and 2.83 W/cm^3 for 40 and 60 cm configurations, respectively. A major issue arises in neutron damage on the VV inner shell. Indeed, the maximum calculated damage over 6 FPY is 3.36 dpa and 3.06 dpa for 40 and 60 cm configurations, respectively (Fig. 2) The design limit for VV damage of 2.75 dpa is not achieved in both configurations considered, suggesting that further improvements in the design of the pellet injection lines are needed, e.g. extension of the connecting plate.

Table 1: Total nuclear heating in IB5 subcomponents for different configurations.

Nuclear Heating (MW)– IB5 toroidal module			
Components	**Baseline**	**2017**	**2018**
FW -W	$7.50 \cdot 10^{-2}$	$6.97 \cdot 10^{-2}$	$6.77 \cdot 10^{-2}$
FW- Eurofer	$1.92 \cdot 10^{-1}$	$1.86 \cdot 10^{-1}$	$1.87 \cdot 10^{-1}$
SIDE CAP-right	$4.38 \cdot 10^{-3}$	$4.39 \cdot 10^{-3}$	$4.39 \cdot 10^{-3}$
SIDE CAP-left*	$4.38 \cdot 10^{-3}$	$1.01 \cdot 10^{-2}$	$8.67 \cdot 10^{-3}$
Top/bottom CAPS	$3.21 \cdot 10^{-2}$	$3.08 \cdot 10^{-2}$	$3.12 \cdot 10^{-2}$
BZ	1.16	1.12	1.13
BSS	$3.28 \cdot 10^{-1}$	$3.57 \cdot 10^{-1}$	$3.50 \cdot 10^{-1}$
TOTAL	**1.78**	**1.78**	**1.78**

Table 2: nuclear heating density on Cu support for 40 cm config

Distance from VV (cm)*	**Nuclear heating density (W/cm³)**
4.82	0.81
8.82	0.84
12.83	0.87
16.83	0.94
20.83	1.00
24.82	1.01
28.82	1.19
32.82	1.28
36.83	1.44
40.83	1.62

*centre of the mesh element with respect to the VV surface at x=514
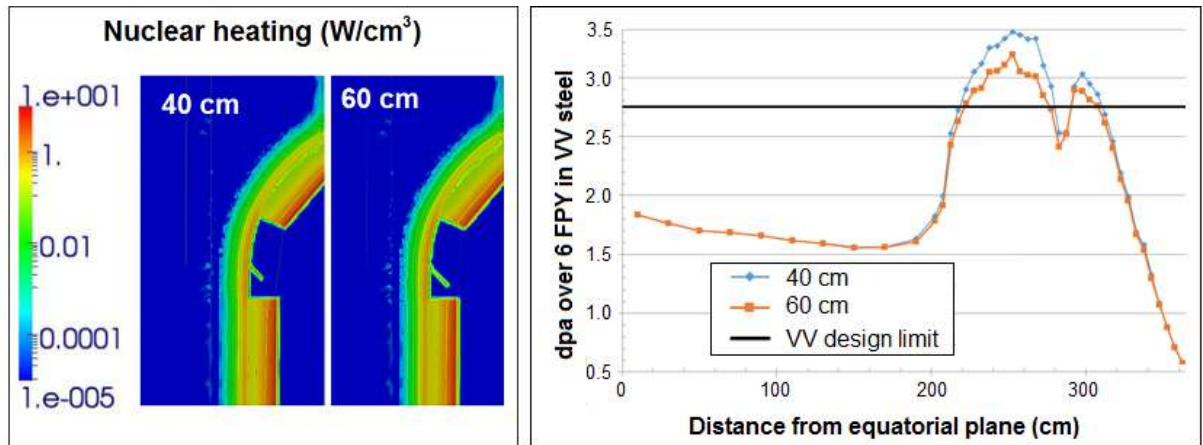
Fig. **3**: nuclear heating density distribution maps for two configuration under analysis (right), neutron damage cumulated over 6 FPY on the VV inner shell as a function of the poloidal position (left).

The reduction of the volume of the CuCrZr support from 2017 [4] and 2018 configurations allows the reduction of the nuclear heating on the Cu of about 47%. Furthermore, the active cooling allows the reduction of the maximum temperature reached by the guiding tube of one order of magnitude in the worst conditions. Moreover, the analyses highlighted the beneficial effect of a bigger connecting plate in terms of VV protection and reduction of the neutron damage (about 20% higher with respect to the DEMO design limit). It should be highlighted that the cumulated damage level is higher than the limit, but the loads on VV are overestimated taking into account the design changes in blanket and DEMO machine configuration.

References

[1]. X-5 Monte Carlo Team: MCNP - A General Monte Carlo N-ParticleTransportCode, Version 5,LosAlamosNationalLaboratory, Los Alamos, New Mexico, USA, April 2003.
[2]. JEFF3.2 nuclear data library, http://www.oecdnea.org/dbforms/data/eva/evatapes/jeff_32/.
[3]. G. Ponti, et al., The role of medium size facilities in the HPC ecosystem: the case of the new CRESCO4 cluster integrated in the ENEAGRID infrastructure. Proceedings of the 2014 International Conference on High Performance Computing and Simulation, HPCS, 6903807 (2014), pp. 1030-1033
[4]. R. Villari,A. Colangeli, D. Flammini, F. Moro, D. Trombetta. Neutron transport analysis through openings in in-vessel components, Final Report WP PMI-3-3-T007, EFDA_D_2MTM7F (2018)

COMPARATIVE STUDY OF THE NEUTRONIC PERFORMANCES OF EU-WCLL AND CHINA-WCCB BREEDING BLANKET CONCEPTS

Chiovaro P.[*1], Del Nevo A.[2], Di Maio P.A.[1]

[1]University of Palermo, Italy
[2]ENEA C.R. Brasimone, ENEA, Camugnano (BO), Italy

ABSTRACT. On the end of 2017, in the framework of EUROfusion R&D activities, a close collaboration between EU and China has started aiming at elaborating joint strategies for the development of the Water Cooled Lithium Lead (WCLL) and the Water Cooled Ceramic Breeder (WCCB) Breeding Blanket (BB) concepts. In this framework, an intense research campaign has been carried out at the University of Palermo, in close cooperation with ENEA Brasimone and ENEA Frascati, in order to compare the neutronic performances of the WCLL and WCCB BBs under irradiation in EU-DEMO. To this end, three-dimensional nuclear analyses have been performed with MCNP5 v. 1.6 Monte Carlo code. A semi-heterogeneous MCNP model of the WCLL BB in a "single module segment" lay-out has been used and an analogous semi-heterogeneous MCNP model of the WCCB BB has been set up and adapted to the reference EU-DEMO model. The nuclear responses of both the BB concepts have been compared focusing the attention mainly on global quantities as nuclear power deposition and Tritium Breeding Ratio as well as the shielding performances. The results obtained provided significant information on the different nuclear features of the two concepts, useful for the optimisation of both WCLL and WCCB BBs design.

1 Introduction

Within the framework of the Work Package International Collaboration of the EUROfusion action, a close collaboration between EU and China has been started in 2017. One of the key-points of this collaboration relies in the comparison of the nuclear performances of the Water Cooled Lithium Lead (WCLL) and Water Cooled Ceramic Breeder (WCCB) Breeding Blanket (BB) concepts. In this framework, in close cooperation with ENEA Brasimone and ENEA Frascati, the University of Palermo has launched a campaign of analyses to deeply investigate the nuclear behaviour of the two blanket concepts. The study has been performed following a computational approach based on the Monte Carlo method and adopting the Monte Carlo N-Particle (MCNP5-1.60) code [1] along with the JEFF-3.2 transport cross section libraries [2]. In particular, analysis has been carried out on the ENEA cluster CRESCO with a homogeneous operating system, by implementing the OpenMP software [3].

2 WCLL MCNP model

The MCNP model of the WCLL BB in a Single Module Segment layout has been implemented in the 2015 MCNP DEMO generic model [4, 5]. It represents a 10° toroidal slice of the whole DEMO reactor, taking into account half a sector of the machine including one inboard segment and one and half outboard segment (Fig. 1). Regarding the WCLL BB, the semi-heterogeneous MCNP model developed by ENEA-Frascati, in which a basic Breeding Unit is replicated along the poloidal direction, has been adopted for calculations. A detailed description of this model can be found in [5].
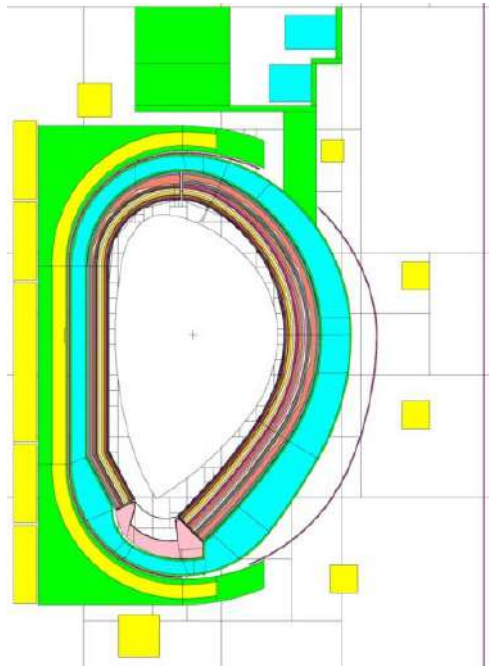
Figure 1. Poloidal radial section of the WCLL BB MCNP model.

Both the Outboard and the Inboard segments of the WCLL BB have been simulated by a layered arrangement of homogeneous volumes, with a fine segmentation in the radial direction and a rough one in the poloidal direction.

3 WCCB MCNP model

The WCCB BB layout is based on a Multi Module Segment (MMS) concept and it is composed of 10 modules (5 inboard and 5 outboard modules) [6]. In order to adapt the WCCB BB model to that of EU-DEMO BB, its equatorial outboard module has been taken as reference and its internal structure has been replicated along the EU-DEMO BB Segment poloidal direction, accordingly to the procedure already followed for the WCLL BB modelling.

Three main modelling assumptions have been made aiming at adapting the WCCB BB radial dimension to the larger WCLL one: WCCB FW and SWs have been extended to match the WCLL FW dimension, WCCB BZ has been extended to save the EU-DEMO WCLL BZ radial length, WCCB BP has been extended up to the DEMO BSS to save the EU-DEMO BB radial length and the so-modified WCCB BB layout has been directly attached to the EU-DEMO BSS.

Finally, adopting the same radial and poloidal segmentation previously described for the WCLL BB, a WCCB BB layered MCNP model has been developed and it has been integrated into the DEMO 2015 MCNP generic model.

4 Results

The radial profiles of the total neutron flux (Φ) and the volumetric density of power deposited by neutrons and photons (q''') have been evaluated in an equatorial zone of the outboard segment for both the BB concepts. In particular a superimposed mesh of 5.28E+05 voxels with pitches of 0.5 cm and 4 cm along the radial direction and the poloidal and toroidal ones respectively.

For those quantities, average values on a poloidal extension equal to that of a breeder cell (13,5 cm) and all along the toroidal range of the whole segment have been assessed (Figs. 2 - 3).
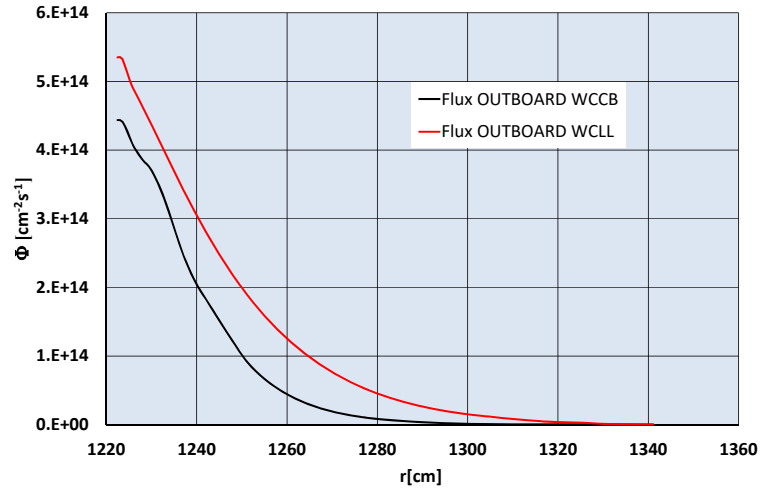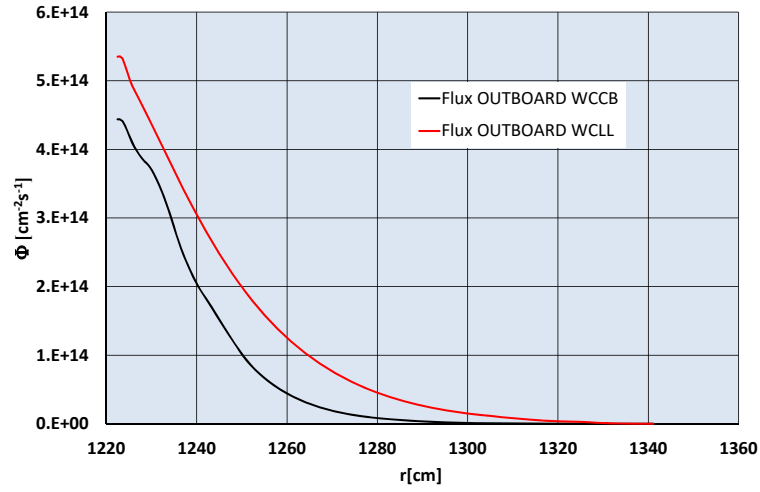
Fig. 2. Neutron flux radial profiles.

Fig. 3. Nuclear power volumetric density radial profiles.

It can be observed (Fig. 2) that the neutron flux profiles have the same trend in both the blankets and how the flux in the WCLL is always higher than in the WCCB. With regard to the volumetric density of the nuclear power radial profiles (Fig. 3), they are slightly different and the WCCB curve is above the WCLL one.

4.1. Power deposition, TBR and shielding performance*s*

The differences in the nuclear response of the two blanket concepts have been investigated taking into account also the total nuclear power and the tritium breeding performances in terms of TBR, the main outcomes of this study are shown in tables 1 and 2.

Table 1. Nuclear power deposited [MW].

	WCLL	WCCB	Δ
Outboard	$1.2744 \cdot 10^3$	$1.4761 \cdot 10^3$	13.66%
Inboard	$5.3814 \cdot 10^2$	$5.9572 \cdot 10^2$	9.67%
TOTAL	$1.8126 \cdot 10^3$	$2.0718 \cdot 10^3$	12.51%

180

Table 2. Tritium Breeding Ratio.

	WCLL			WCCB			Δ_{tot}
	Li^6	Li^7	TOTAL	Li^6	Li^7	TOTAL	
Outboard	$8.053 \cdot 10^{-1}$	$3.402 \cdot 10^{-4}$	$8.056 \cdot 10^{-1}$	1.141	$1.209 \cdot 10^{-3}$	1.142	29.46%
Inboard	$3.252 \cdot 10^{-1}$	$1.215 \cdot 10^{-4}$	$3.253 \cdot 10^{-1}$	$4.552 \cdot 10^{-1}$	$4.214 \cdot 10^{-4}$	$4.557 \cdot 10^{-1}$	28.61%
TOTAL	1.130	$4.617 \cdot 10^{-4}$	1.131	1.531	$1.503 \cdot 10^{-3}$	1.598	29.22%

It is worthwhile to observe the significant differences between the blanket responses, about the 12.5% for the total power and the 29.2% for the TBR. Such considerable gaps are due, above of all, to the geometry modification performed on the WCCB blanket to adapt it to the DEMO model. Moreover, also the different amount of water (which is a strong neutron absorber) present in the two blankets, has a not negligible influence on the different responses, being the inventory of water in the WCLL greater than in the WCCB particularly in the FW-SW system. This kind of impact of water on the tritium breeding performance has been confirmed by an analysis carried out using a dummy model of the WCCB BB whose FW, SWs and caps material compositions have been modified and set the same as the WCLL BB ones.

The results of this ad hoc analysis have shown that the differences in the nuclear response between the two BB concepts are reduced increasing the amount of water in the WCCB BB. Moreover, it is important to observe that the unrealistic TBR value assessed in the WCCB is due, in addition to the approximations assumed for modelling this BB concept, to the very large amount of beryllium which allows a very high net multiplication factor (1.75), together with the substantial Li^6 enrichment (80%) and the high packing factor of the ceramic breeder (0.8) [6].

Again, this hypothesis has been confirmed by an analysis carried out using a dummy model of the WCCB BB with a Li6 enrichment of 60% and a packing factor of 0.64, in which a TBR of 1.295 has been assessed. As far as the shielding performances are concerned both the total and the fast neutron fluxes have been evaluated at TFC. The evaluated values are similar for both the blankets as shown in table 3.

Table 3. Neutron flux at the lower part of Inboard TFC [cm^{-2} s^{-1}].

WCLL			WCCB			Δ_{Tot}
Energy range [MeV]			Energy range [MeV]			
<0.1	>0.1	Total	<0.1	>0.1	Total	
$1.31 \cdot 10^{10}$	$4.83 \cdot 10^{9}$	$1.80 \cdot 10^{10}$	$1.32 \cdot 10^{10}$	$4.84 \cdot 10^{9}$	$1.81 \cdot 10^{10}$	-0.43%

It is interesting to observe that the higher fluxes are evaluated in the lower part of the Inboard side of TFC and how these values are rather high if compared with the design limit of 10^9 cm^{-2}s^{-1}.

References

[1] X-5 Monte Carlo Team: MCNP – A General Monte Carlo N-Particle Transport Code, Version 5, LANL, Los Alamos, New Mexico, USA, 2003 (April 2003).
[2] JEFF3.2 Nuclear Data Library, (2018) http://www.oecd-nea.org/dbforms/data/eva/evatapes/jeff_32/.
[3] http://www.cresco.enea.it/
[4] F. A. Hernàndez et al., Fusion Eng. Des., 124, pp. 882-886, 2017.
[5] F. Moro, et al., Fusion Eng. Des 136, pp. 1260-1264, 2018.
[6] S. Liu. Et al., Fusion Eng. Des. 124 (2017) 865-870.

AB INITIO STUDY OF NA-ION INSERTION IN A HIGH ENERGY CATHODE FOR SODIUM BATTERIES

Michele Pavone[1*], Arianna Massaro[1], Mariarosaria Tuccillo[1], Ana B. Muñoz-García[2]

[1]*University of Naples "Federico II", Department of Chemical Sciences, Comp. Univ. Monte Sant'Angelo Via Cintia 21, 80126, Naples, Italy[1]*

[2]*University of Naples "Federico II", Department of Physics "Ettore Pancini", Comp. Univ. Monte Sant'Angelo Via Cintia 21, 80126, Naples, Italy*

ABSTRACT. In this work, we provide a first-principles study of $NaLi_{0.2}Ni_{0.25}Mn_{0.75}O_{\delta}$ as promising cathode material for Na-ion batteries. The structural, electronic and surface properties have been characterized in order to give theoretical insights into the structure-property relationships for this kind of materials. The transition metal centers are directly involved in electron conduction, while lithium only has a structural role. From preliminary results in both bulk and surface models, the lattice coordination seems to play an important role in determining the more favored path for Na adsorption and diffusion.

1 Introduction

The research carried out at the Department of Chemical Sciences of the University of Naples "Federico II" focused on the characterization of the structural, electronic and surface properties of $NaLi_{0.2}Ni_{0.25}Mn_{0.75}O_{\delta}$ (NLNMO). This material belongs to the class of transition metals (TMs)-based oxides with a peculiar layered structure and has attracted great interest as promising positive electrode for sodium ion batteries (SIBs) applications. The general formula of this kind of material can be written as $Na_{(1-x)}MO_{(2\pm\delta)}$, with x ranging between 0 and 1 during the charge/discharge process, and M representing one or more TMs. The metal atom is surrounded by six oxygen atoms in octahedral coordination with the octahedra sharing one face and forming a compact layer. The sodium ions can intercalate so that the overall structure will show alternating layers of sodium ions and transition metal oxide [1]. Among several examples, mixed Mn- and Ni-based oxides with a major amount of manganese have shown good electrochemical performances [2]. It has also been reported that the addition of Li^+ ions in the oxide lattice allows to obtain further stabilization and higher efficiency in SIB application [3]. However, many issues are still unclear, concerning the dynamics of the charge/discharge processes or the specific role of each element in determining the electronic properties and the surface chemistry of the overall material. For this reason, understanding the subtle structure-property-function relationships in this kind of materials is essential to assess their development in high-performing devices. Our aim is to investigate the properties of NLNMO that are relevant for electrochemical applications from an atomistic perspective by means of first-principles calculations.

---

[1]   Corresponding author. E-mail: michele.pavone@unina.it.

2 Methods and computational details

Mn, Ni and Li atoms are not perfectly ordered in the real material but should be randomly distributed. In order to build a reliable structural model for our system, we choose to apply a statistical method, *i.e.* the special-quasi-random-structure (SQS) approach [4] that allowed us to build a cell with a random distribution of the Li/Mn/Ni cations in the oxide that can maximize the configurational entropy within the limit of the supercell. We performed spin-polarized DFT calculations in periodic boundary conditions (PBC), using PAW potentials for core electrons and plane waves for valence electrons as implemented in the VASP code (Vienna Ab-initio Simulation Package) [5]. We used a kinetic energy cutoff of 750 eV and a 2x3x4 k-points Γ-centered grid for a 115-atoms containing cell, as obtained from convergence studies. We considered the DFT+U level of theory in order to improve the electronic structure description of our material. This method represents a possible strategy to solve the self-interaction error (SIE), arising from the Coulombic interaction of an electron with itself, that is not cancelled in DFT-based methods, as it occurs in Hartree-Fock (HF) calculations, thus leading to a bad description of electronic structure, especially for highly localized electrons in half-filled orbitals. The DFT+U approach consists of treating the strong Coulomb interaction of localized electrons with an additional effective term, *i.e.* the Hubbard term, based on the U (exchange) and J (Coulomb) parameters that can be obtained from ab initio calculations or fitting bandgap values. We used 4 eV as U-J values for both Mn and Ni d electrons. All the the computing resources and the related technical support used for this work have been provided by CRESCO/ENEAGRID High Performance Computing infrastructure and its staff [6]; CRESCO/ENEAGRID High Performance Computing infrastructure is funded by ENEA, the Italian National Agency for New Technologies, Energy and Sustainable Economic Development and by Italian and European research programmes. See: http://www.cresco.enea.it/english for information.

3 Results and discussion

We first carried out the structure optimization of the $Na_{0.83}Li_{0.2}Mn_{0.6}Ni_{0.2}O_2$ (NLMNO) cell as obtained with the SQS method, *i.e.* 115 atoms arranged in a 5x3x1 supercell compared to the NLMNO formula unit. Figure 1 depicts the minimum-energy structure obtained at the PBE+U level of theory, which predicted a volume equal to 82.5Å^3, in good agreement with $\sim80.4\text{Å}^3$ obtained from X-ray diffraction data [3].
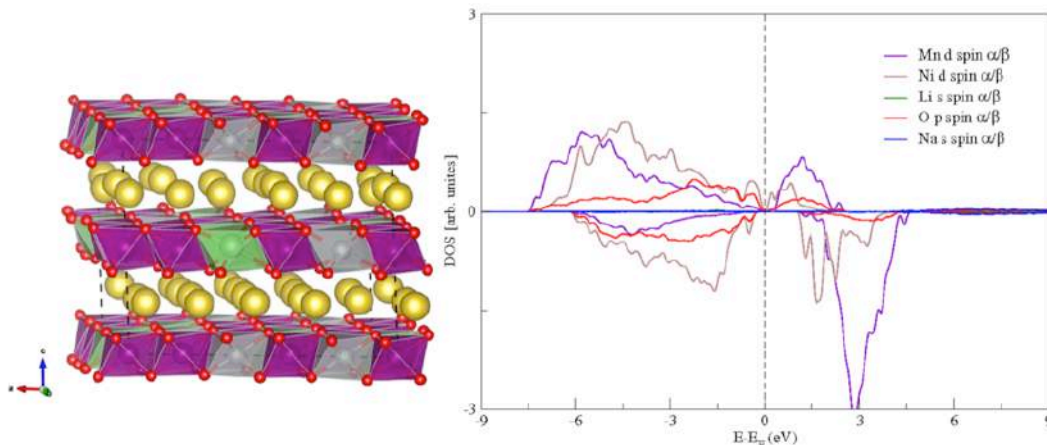

Fig.1: DFT-PBE+U minimum-energy structure of $Na_{0.83}Li_{0.2}Mn_{0.6}Ni_{0.2}O_2$ (NLMNO) 5x3x1 supercell with SQS distribution of Mn/Ni/Li cations within each oxide layer and corresponding projected density of states (PDOS). Colour code: Na, yellow; Mn, magenta; Ni, grey; Li, green; O, red.

Figure 1 also reports the electronic structure analysis that we can extract from the projected density of states (PDOS, right panel). The nature of electronic states near the Fermi Energy allows us to define which species are involved in electron conduction. The *d* states of both Ni and Mn largely hybridized with the oxygen *p* states mainly characterize the bands across the Fermi level. Analysis of the atomic magnetic moments confirms the qualitative results obtained from the PDOS: Li has magnetic moment equal to zero, Ni has an average magnetic moment of 1.14 µB and Mn has an average magnetic moment of 3.21 µB. These results match with the XANES data showing the presence of high spin Ni (II) and Mn (III) in the material [3].

In order to give further insights into the structural properties of the material, we perform the analysis of cation-oxide distances by means of pair distribution functions (PDF), as shown in Figure 2.
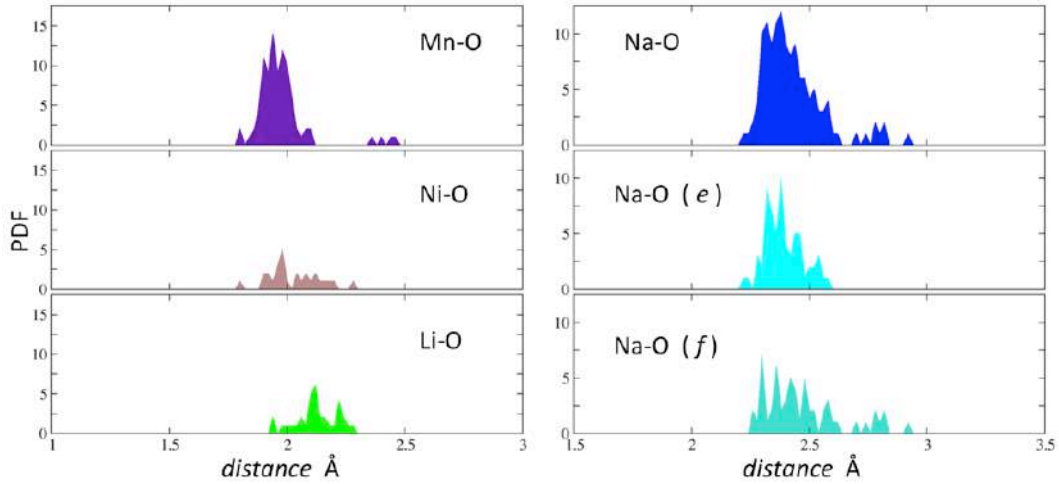
Fig. 2: Pair Distribution Functions (PDF) corresponding to the atom pairs in the legends. Na-O distances have been decomposed in contributions from Na cations at *e* and *f* positions.
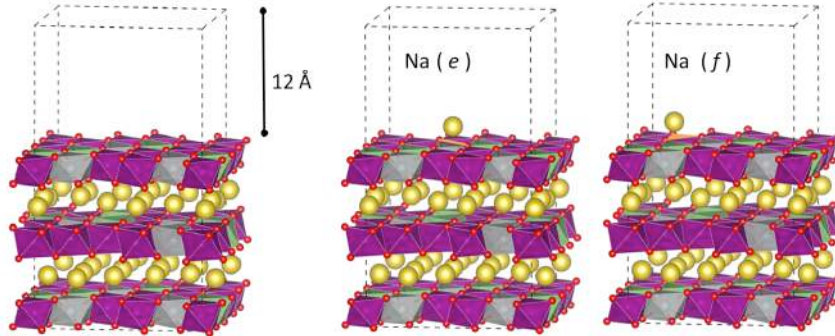
Fig. 3: Structural model of the NLMNO surface slab, highligthing the thickness of the vacuum layer (left), and DFT-PBE+U minimum-energy structures for the adsorbed Na-ion at the two possible positions, at the edge (*e* site, centre) and at the face of Mn-O_6 octahedra (*f* site, right) highligthed in orange. Color code as in Fig. 1.

The PDFs of Mn/Ni/Li-O distances are quite similar (with Li-O distances slightly higher), showing that all the three cations are localized at the center of an octahedron, thus confirming their miscibility in the oxide layer. In the case of manganese, the partial elongation of some bonds can be related to the Jahn-Teller distortion that is typical for Mn (III) with d^4 high-spin electronic configuration. For what concerns Na-O distances (Figure 2, right panel), the PDF has greater variability, with distances ranging from ~2.2 to ~2.9 Å. We decoupled the total Na-O PDF in two components, one related to

the Na coordinated at the edge of Mn-O_6 octahedra (*e* position) and the other one coordinated at the face of Mn-O_6 (*f* position). The greater variability of Na-O distances seems to be due to *f* sites, while the more compact PDF of the *e* sites suggests a more structured situation.

We also carried out the study of the NLMNO surface in order to focus on the Na adsorption. We considered the (001) termination as a starting point for our study. 12Å of vacuum are required to simulate the surface and to avoid the interaction with the replica along the c direction. From this slab model calculations we can predict the interaction of the sodium cation with the materials surface, i.e. the adsorption process occurring at the electrode/electrolyte interface. By comparing the structural parameters of surface and bulk after optimization, we observe no significant surface reconstruction in the oxide layer. We studied the adsorption of one Na cation on two possible sites, as illustrated in Figure 3, in order to determine not only the most stable and favored site, but also the metastable one that could represent an intermediate structure during the Na transport occurring along the electrode surface. From our calculations, Na adsorption seems to be more favored on the Mn-O_6 face rather than on the edge site. We found an energy difference of 0.15 eV that can be explained in terms of electrostatics. In fact, the Na cation interacts directly with three oxide ions on the *f* position, thus maximizing the Coulomb interaction between oppositely charged ions, while on the *e* position Na has only two nearby oxides. However, these are preliminary results as we aim to explore other possible Na adsorption sites, for examples on NiO_6 or LiO_6 octahedra.

4 Conclusions

The research activity at UniNa focused on the characterization of the physico-chemical properties of the NLMNO material as promising cathode material for SIBs. The first step has been the identification of a reliable structural model of the Li/Mn/Ni ordering by means of the SQS approach. The Na^+ in turn can occupy two possible positions in the lattice with different coordination, *i.e.* the octahedron face, *f*, and the octahedron edge, *e*. In the bulk, the Na ions in *f* position are less ordered with respect to the ones in *e* position. This structural variability may suggest a flatter potential energy surface at the *f* position that would allow a more favorable diffusion. The electronic structure analysis revealed that the TMs are directly involved in electron conduction, while Li has a purely structural role. From surface calculations, we showed the absence of a significant surface reconstruction, thus demonstrating the solidity of the oxide layer. The Na adsorption on the (001) surface is slightly favored on *f* sites for ~150 meV, thus suggesting that the sodiation process could start with the adsorption on *f* sites and then get the complete sodiation through the *e* sites. The results obtained so far represent a first theoretical investigation of the NLMNO material and pave the route toward the characterization of different stoichiometries (Li/Ni/Mn) and surface terminations for Na adsorption and diffusion properties.

References
[1] N. Yabuuchi, K. Kubota, M. Dahbi, S. Komaba. Research Development on Sodium-Ion Batteries. *Chem. Rev.* **114**, pp. 11636-11682, (2014).
[2] R. J. Clément, P.G. Bruce, C.P. Grey. Review-Manganese-Based P2-Type Transition Metal Oxides as Sodium-Ion Battery Cathode Materials. *J. Electrochem. Soc.* **162**, pp. A2589-A2604, (2015).
[3] D. Kim, S-H. Kang, M. Slater, S. Rood, J.T. Vaughey, N. Karan, M. Balasubramanian, C.S. Johnson. Enabling Sodium Batteries Using Lithium-Substituted Sodium Layered Transition Metal Oxide Cathodes. *Adv. Energy Mater.* **1**, pp. 333-336, (2011).
[4] a) A. Zunger, S.-H. Wei, L. G. Ferreira, J. E. Bernard. Special Quasirandom Structures. *Phys. Rev. Lett.* **65**, pp. 353-356, (1990); b) J. Mayer, E. Montroll. Statistical Mechanics of Nearest Neighbor Systems. *J. Chem. Phys.* **9**, pp. 706-721, (1941).

[5] a) G. Kresse, J. Hafner. Ab initio molecular dynamics for open-shell transition metals. *Phys. Rev. B* **48**, pp. 13115-13118, (1993); b) G. Kresse, G. Furthmüller. Efficient iterative schemes for ab initio total-energy calculations using a plane-wave basis set. *Phys. Rev. B* **54**, pp. 11169-11186, (1996).

[6] G. Ponti, F. Palombi, D. Abate, F. Ambrosino, G. Aprea, T. Bastianelli, F. Beone, R. Bertini, G. Bracco, M. Caporicci, B. Calosso, M. Chinnici, A. Colavincenzo, A. Cucurullo, P. Dangelo, M.D. Rosa, P. D. Michele, A. Funel, G. Furini, D. Giammattei, S. Giusepponi, R. Guadagni, G. Guarnieri, A. Italiano, S. Magagnino, A. Mariano, G. Mencuccini, C. Mercuri, S. Migliori, P. Ornelli, S. Pecoraro, A. Perozziello, S. Pierattini, S. Podda, F. Poggi, A. Quintiliani, A. Rocchi, C. Scio, F. Simoni, A. Vita, The role of medium size facilities in the HPC ecosystem: the case of the new CRESCO4 cluster integrated in the ENEAGRID infrastructure, *International Conference on High Performance Computing & Simulation (HPCS)*, **2014**, 1030-1033.

Polymer Physics and Computational Approaches to Investigate Genome Spatial Organization

Mattia Conte[1], Andrea Esposito[1], Luca Fiorillo[1], Carlo Annunziatella[1], Andrea Maria Chiariello[1*] and Simona Bianco[1*]

[1]*Dipartimento di Fisica, Università di Napoli Federico II, and INFN Napoli, Complesso Universitario di Monte Sant'Angelo, 80126, Naples, Italy*

Corresponding authors. Email: biancos@na.infn.it; chiariello@na.infn.it

ABSTRACT. In the last decade, novel experimental technologies from molecular biology provided us many information about the spatial organization of the chromosomes within the cell nucleus. These experiments revealed that the genome folds into an intricate, and not yet understood, three-dimensional (3D) structure, serving functional purposes, such as gene regulation. Models from polymer physics have been employed to interpret the huge quantity of experimental data related to the structural properties of the chromosomes. Our theoretical approach combines Polymer Physics and computational methods, based on standard Monte Carlo strategies and massive Molecular Dynamics simulations, in order to simulate and analyse real genomic regions. However, computational times rapidly increase with the simulated system size, which ultimately reflects its inner complexity. For this reason, an accurate model description constantly implies an efficient management of the computational resources available. In this work, we refer to the modelling of the *HoxD* genes region as an example of our computational pipeline, showing the capability of our approach to reconstruct the locus 3D structure at the single DNA molecule level and to spread light on functional architectural rearrangements occurring during cell differentiation.

1. Introduction

Novel experimental technologies have revealed a complex spatial organization of the chromosomes within the cell nucleus, deeply linked to functional processes [1]. Some of these techniques, as Hi-C [2] or GAM [3], measure, across a cell population, the average contact frequency between any pair of DNA sites. The output is typically stored in a two-dimensional matrix, in which each entry is proportional to the pairwise contact frequency. These matrices have highlighted a non-random spatial assembly of the genome, comprising a hierarchy of topological domains ranging from the sub-megabase (Mb) scale up to the range of entire chromosomes [4]. For instance, at the Mb scale, the genome folds into contact domains, called Topologically Associating Domains (TADs), which exhibit inner enrichments of interaction levels [5, 6]. Understanding the molecular mechanisms underlying contact patterns formation is currently a fascinating challenge in biology. In order to attack those riddles, theoretical and computational approaches from polymer physics have been developed in the last few years [7]. Here, we focus on the *Strings&Binders* (SBS) model [8, 9], a polymer physics approach based on a globule phase-separation mechanism and capable to explain a great variety of experimental data, as Hi-C, GAM or microscopy [3, 10–12]. In Section 2, we describe the basic aspects of the model, focusing on its computational implementation and stressing

the key role played by High-Performance-Computing (HPC) resources. In Section 3, we recall recent applications of the model to key genomic regions, focusing in particular on the *HoxD* genomic region, which undergoes a complex architectural transformation during cell differentiation, intimately linked to genes transcription [13].

2. The SBS polymer model and its computational implementation

In the SBS model a genomic region is schematized as a Self-Avoiding Walk (SAW) polymer chain, having attachment points for diffusing molecular factors, called binders. The binders interact with the chain by the standard interaction potentials stated by classic polymer physics studies [9, 14] and can bridge pair of distal sites along the polymer (**Fig. 1a**). The model undergoes a phase transition from an initial coil state, where entropic forces prevail, to a final compact globular state, obtained when binder concentration, or binder affinity, is up the transition threshold (**Fig1b**). In this way, the binders, acting as short or long-range interaction mediators, drive the fold of the polymer chain.
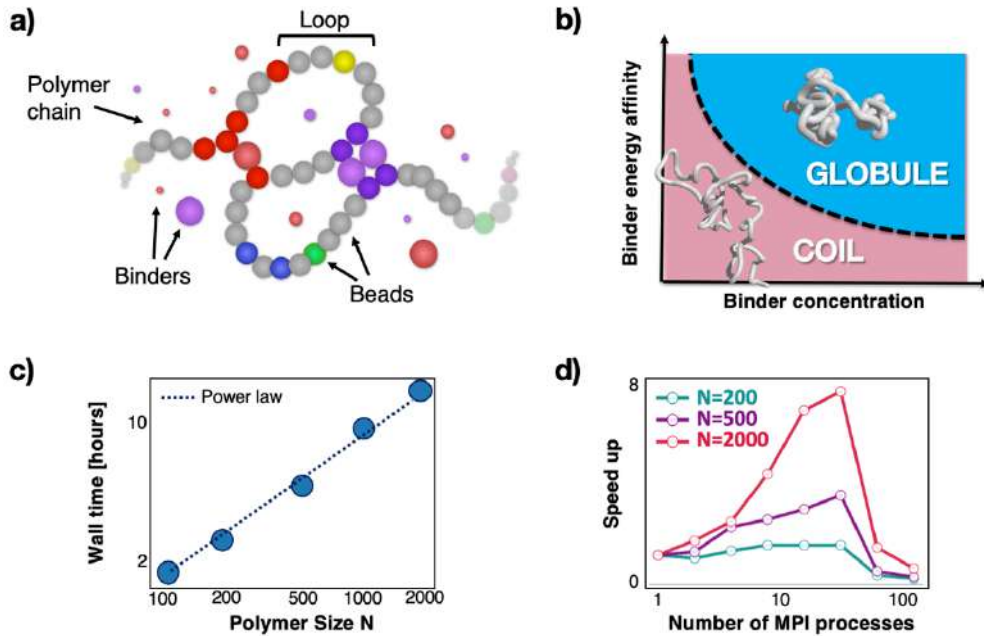
Fig.1: **SBS polymer model of chromatin and MD simulation performances.** **a)** In the SBS model, homotypic interaction between beads and cognate binders drives the folding of the polymer chain. (adapted from [12]) **b)** SBS phase diagram and coil-globule transition. (adapted from [9]) **c,d)** SBS polymer MD simulations can require heavy computational resources (adapted from [15]).

To simulate real genomic loci, having for instance specific non-trivial interaction domains in their corresponding Hi-C contact matrix, our model requires specializing the attractive interaction between the binders and the polymer. The specificity can be implemented by assign different types (colours) to the polymer sites, thus constraining the interaction only between same-coloured polymer sites and cognate binders. To this aim, we developed a computational procedure [12], called *PRISMR*, taking as input the Hi-C contact matrix of the genomic region of interest and, based on a simulated annealing Monte Carlo routine, returning as output the optimal number of different colours and their positioning along the polymer, needed to explain the input dataset within a given accuracy (**Fig.2a**).

Once obtained the optimum SBS model, we run massive Molecular Dynamics (MD) simulations to produce a thermodynamics ensemble of hundreds of polymers. To this aim, we employed the open source software LAMMPS (Large-scale Atomic/Molecular Massively Parallel Simulator) [16], an efficient MD code largely used in the field [9, 12, 17–19]. LAMMPS uses the Message Passing Interface (MPI) protocol and achieves parallelization by domain decomposition, i.e. by partition of the simulation box into sub-domains assigned to different processors. All our MD simulations were performed thanks to computer resources from ENEA CRESCO-ENEAGRID, using mainly the queue "small_h144" and the INTEL compilers with the OpenMPI library. As standard strategy in MD, we performed a prior scaling analysis to find the optimum number of MPI processes employed for the parallel running [15]. For sake of simplicity, we considered an SBS homopolymer, i.e. a polymer where all beads are of the same type. As shown in **Fig. 2c**, the speed up reaches a peak at 32 MPI processes for all the polymer lengths investigated. However, the optimal number of processes also depends on other details, such as system complexity, queuing time and resource availability. To quantify how the system complexity affects the typical running times of our MD simulations, we reported in **Fig. 2d** the total wall time required for an SBS polymer to complete 10^7 MD timesteps (when equilibrium is achieved) versus the polymer length. We observed a power-law behaviour, certifying that the computational time rapidly increases with the system complexity. Typically, more realistic SBS polymers describing real chromatin regions are quite large, with lengths ranging from hundreds to tens of thousands of beads. The amount of storage needed for ensemble simulations of such SBS polymers is of the order of tens gigabytes. In the next Section, as an example we will detail the modelling of the *HoxD* genomic region.

3. A case study: the murine *HoxD* genes region

The approach described above was successfully applied to a number of key genomic regions, including *Sox9, Epha4* and *Shh* ([9, 11, 12, 20–23] and reviews in [10, 24–26]). Here, we describe the test case of the *HoxD* region, which is involved in the formation of the animal body structures during embryo development [13, 27, 28]. We applied our polymer models in two different cell lines, embryonic stem (ESCs) and cortical neuronal (CNCs) cells, in order to explore the architectural changes occurring when the *Hoxd* genes change from a poised to a silent expression state [13]. We applied our PRISMR procedure to a 7 Mb region (chr2:71.16-78.16 Mb) around the *Hoxd* genes cluster, using as input 5kb resolution Hi-C data [29] (**Fig. 2b**). In both ESCs and CNCs, PRISMR inferred 20 different types of binding sites. Interestingly, their positions were found to correlate with combinations of epigenetic marks. We next performed MD simulations of the obtained polymer models as described above to derive ensembles of 3D conformations. In **Fig. 2b**, the comparison between the Hi-C and simulated contact maps is shown in the case of ESCs, where it is possible to appreciate that most of the experimental patterns are well reproduced by the SBS model, as also highlighted by the high Pearson correlation coefficient between them (Pearson r = 0.92 in ESCs and r=0.93 in CNCs). Such results indicate that the simulated 3D structures could represent the real 3D architecture of the region to a good extent and support a principled interpretation of the contact maps based on polymer physics. Structures like TADs can be explained within the model as regions enriched for contacts between specific types of binding sites, which biologically correspond to specific combinations of epigenetic marks. In **Fig. 2b** right panel is shown an example snapshot (produced by the POV-RAY software [30]) from our ensemble of MD simulations in ESCs and a zoom of 2Mb around the *Hoxd* genes, where the positions of surrounding genes and regulatory regions are highlighted. By analysing the obtained model ensembles, we found that the 3D organization of the region is characterised by a network of cell-type- and gene-specific many-body contacts with regulatory elements and that it undergoes deep reorganization upon differentiation from ESCs to CNCs concomitantly to genes activity and epigenetic changes. The found high specificity
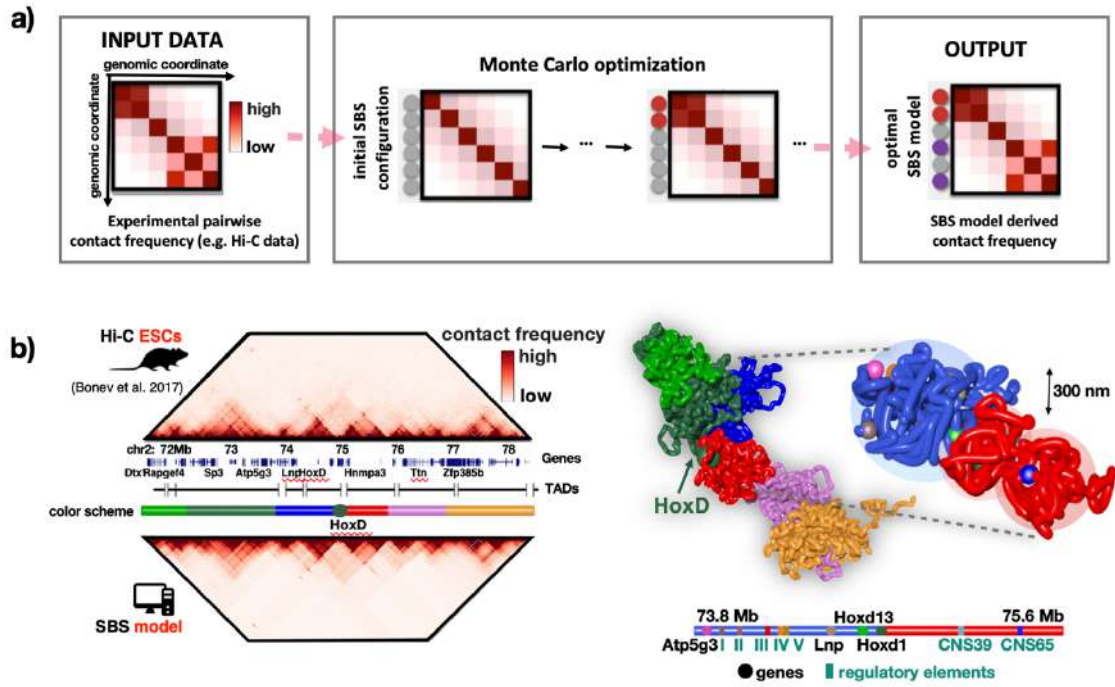
Fig.2: PRISMR computational inference of 3D genome conformations and its application on the *HoxD* genomic region. **a)** PRISMR infers the optimal SBS polymer model that best explains a given pairwise contact frequency map (adapted from [12]). **b)** PRISMR inferred SBS model describes with high accuracy Hi-C maps [29] of the *HoxD* region in mouse embryonic stem cells. On the right panel, a single-molecule time snapshot visualizes the 3D conformations corresponding to the highlighted sub-regions (adapted from [13]).

and combinatorial nature of multi-way contacts is a hint towards their key role in the control of the transcriptional program of the *HoxD* genes and contribute to spread light on the fundamental role of spatial organisation in the regulation of genes activity [13].

4. Conclusions

Polymer physics models combined with computational approaches are revealing powerful instruments to explore genome 3D organisation quantitatively and to interpret experimental contact data in a mechanistic framework. Here, we discussed the SBS model of chromatin and its MD implementation. We showed that the MD simulation time depends on several factors, in particular it scales as a power law as a function of the polymer length. Based on the SBS, we developed the PRISMR learning algorithm to infer reliable polymer models of any genomic region of interest taking as its only input an experimental pair-wise contact map of the region. In particular, here we illustrated the case of the murine *HoxD* region. We derived *HoxD* 3D structures in different cell types, shedding light on the regulatory interactions between genes and regulatory elements and their underlying molecular mechanisms. The computational resources required to model a region of the genome however strongly depend on the complexity of the model, impacted first by the size of the underlying experimental data. It will be important for future applications to improve the computational efficiency, in order to be able to deal with the increasing resolution of experiments and to pursue a deeper understanding of the genome architecture and its fundamental link with vital cell functions.

References

1. Dekker, J., Mirny, L.: The 3D Genome as Moderator of Chromosomal Communication. Cell. (2016). https://doi.org/10.1016/j.cell.2016.02.007.

2. Lieberman-Aiden, E., Van Berkum, N.L., Williams, L., Imakaev, M., Ragoczy, T., Telling, A., Amit, I., Lajoie, B.R., Sabo, P.J., Dorschner, M.O., Sandstrom, R., Bernstein, B., Bender, M.A., Groudine, M., Gnirke, A., Stamatoyannopoulos, J., Mirny, L.A., Lander, E.S., Dekker, J.: Comprehensive mapping of long-range interactions reveals folding principles of the human genome. Science (80-.). 326, 289–293 (2009). https://doi.org/10.1126/science.1181369.

3. Beagrie, R.A., Scialdone, A., Schueler, M., Kraemer, D.C.A., Chotalia, M., Xie, S.Q., Barbieri, M., De Santiago, I., Lavitas, L.M., Branco, M.R., Fraser, J., Dostie, J., Game, L., Dillon, N., Edwards, P.A.W., Nicodemi, M., Pombo, A.: Complex multi-enhancer contacts captured by genome architecture mapping. Nature. (2017). https://doi.org/10.1038/nature21411.

4. Fraser, J., Ferrai, C., Chiariello, A.M., Schueler, M., Rito, T., Laudanno, G., Barbieri, M., Moore, B.L., Kraemer, D.C., Aitken, S., Xie, S.Q., Morris, K.J., Itoh, M., Kawaji, H., Jaeger, I., Hayashizaki, Y., Carninci, P., Forrest, A.R., Semple, C.A., Dostie, J., Pombo, A., Nicodemi, M.: Hierarchical folding and reorganization of chromosomes are linked to transcriptional changes in cellular differentiation. Mol. Syst. Biol. (2015). https://doi.org/10.15252/msb.20156492.

5. Dixon, J.R., Selvaraj, S., Yue, F., Kim, A., Li, Y., Shen, Y., Hu, M., Liu, J.S., Ren, B.: Topological domains in mammalian genomes identified by analysis of chromatin interactions. Nature. 485, 376–380 (2012). https://doi.org/10.1038/nature11082.

6. Nora, E.P., Lajoie, B.R., Schulz, E.G., Giorgetti, L., Okamoto, I., Servant, N., Piolot, T., Van Berkum, N.L., Meisig, J., Sedat, J., Gribnau, J., Barillot, E., Blüthgen, N., Dekker, J., Heard, E.: Spatial partitioning of the regulatory landscape of the X-inactivation centre. Nature. 485, 381–385 (2012). https://doi.org/10.1038/nature11049.

7. Tiana, G., Luca, G.: Modeling the 3D Conformation of Genomes. (2019). https://doi.org/10.1201/9781315144009.

8. Barbieri, M., Chotalia, M., Fraser, J., Lavitas, L.-M., Dostie, J., Pombo, A., Nicodemi, M.: Complexity of chromatin folding is captured by the strings and binders switch model. Proc. Natl. Acad. Sci. (2012). https://doi.org/10.1073/pnas.1204799109.

9. Chiariello, A.M., Annunziatella, C., Bianco, S., Esposito, A., Nicodemi, M.: Polymer physics of chromosome large-scale 3D organisation. Sci. Rep. 6, (2016). https://doi.org/10.1038/srep29775.

10. Bianco, S., Chiariello, A.M.A.M., Annunziatella, C., Esposito, A., Nicodemi, M.: Predicting chromatin architecture from models of polymer physics. (2017). https://doi.org/10.1007/s10577-016-9545-5.

11. Barbieri, M., Xie, S.Q., Torlai Triglia, E., Chiariello, A.M., Bianco, S., De Santiago, I., Branco, M.R., Rueda, D., Nicodemi, M., Pombo, A.: Active and poised promoter states drive folding of the extended HoxB locus in mouse embryonic stem cells. Nat. Struct. Mol. Biol. 24, 515–524 (2017). https://doi.org/10.1038/nsmb.3402.

12. Bianco, S., Lupiáñez, D.G., Chiariello, A.M., Annunziatella, C., Kraft, K., Schöpflin, R., Wittler, L., Andrey, G., Vingron, M., Pombo, A., Mundlos, S., Nicodemi, M.: Polymer physics predicts the effects of structural variants on chromatin architecture. Nat. Genet. (2018). https://doi.org/10.1038/s41588-018-0098-8.

13. Bianco, S., Annunziatella, C., Andrey, G., Chiariello, A.M., Esposito, A., Fiorillo, L., Prisco, A., Conte, M., Campanile, R., Nicodemi, M.: Modeling Single-Molecule Conformations of the HoxD Region in Mouse Embryonic Stem and Cortical Neuronal Cells. Cell Rep. (2019). https://doi.org/10.1016/j.celrep.2019.07.013.

14. Annunziatella, C., Chiariello, A.M., Esposito, A., Bianco, S., Fiorillo, L., Nicodemi, M.: Molecular Dynamics simulations of the Strings and Binders Switch model of chromatin. Methods. 142, (2018). https://doi.org/10.1016/j.ymeth.2018.02.024.

15. Conte, M., Esposito, A., Fiorillo, L., Campanile, R., Annunziatella, C., Corrado, A., Chiariello, M.G., Bianco, S., Chiariello, A.M.: Efficient computational implementation of polymer physics models to explore chromatin structure. Int. J. Parallel, Emergent Distrib. Syst. (2019). https://doi.org/10.1080/17445760.2019.1643020.

16. Plimpton, S.: Fast parallel algorithms for short-range molecular dynamics. J. Comput. Phys. 117, 1–19 (1995). https://doi.org/10.1006/jcph.1995.1039.

17. Rosa, A., Everaers, R.: Structure and dynamics of interphase chromosomes. PLoS Comput. Biol. (2008). https://doi.org/10.1371/journal.pcbi.1000153.

18. Brackley, C.A., Taylor, S., Papantonis, A., Cook, P.R., Marenduzzo, D.: Nonspecific bridging-induced attraction drives clustering of DNA-binding proteins and genome organization. Proc. Natl. Acad. Sci. (2013). https://doi.org/10.1073/pnas.1302950110.

19. Sanborn, A.L., Rao, S.S.P., Huang, S.C., Durand, N.C., Huntley, M.H., Jewett, A.I., Bochkov, I.D., Chinnappan, D., Cutkosky, A., Li, J., Geeting, K.P., Gnirke, A., Melnikov, A., McKenna, D., Stamenova, E.K., Lander, E.S., Aiden, E.L.: Chromatin extrusion explains key features of loop and domain formation in wild-type and engineered genomes. Proc. Natl. Acad. Sci. U. S. A. 112, E6456–E6465 (2015). https://doi.org/10.1073/pnas.1518552112.

20. Annunziatella, C., Chiariello, A.M., Bianco, S., Nicodemi, M.: Polymer models of the hierarchical folding of the Hox-B chromosomal locus. Phys. Rev. E. (2016). https://doi.org/10.1103/PhysRevE.94.042402.

21. Kragesteen, B.K., Spielmann, M., Paliou, C., Heinrich, V., Schöpflin, R., Esposito, A., Annunziatella, C., Bianco, S., Chiariello, A.M., Jerković, I., Harabula, I., Guckelberger, P., Pechstein, M., Wittler, L., Chan, W.L., Franke, M., Lupiáñez, D.G., Kraft, K., Timmermann, B., Vingron, M., Visel, A., Nicodemi, M., Mundlos, S., Andrey, G.: Dynamic 3D chromatin architecture contributes to enhancer specificity and limb morphogenesis. Nat. Genet. 50, 1463–1473 (2018). https://doi.org/10.1038/s41588-018-0221-x.

22. Paliou, C., Guckelberger, P., Schöpflin, R., Heinrich, V., Esposito, A., Chiariello, A.M., Bianco, S., Annunziatella, C., Helmuth, J., Haas, S., Jerkovic, I., Brieske, N., Wittler, L., Timmermann, B., Nicodemi, M., Vingron, M., Mundlos, S., Andrey, G.: Preformed chromatin topology assists transcriptional robustness of Shh during limb development. Proc. Natl. Acad. Sci. U. S. A. 116, (2019). https://doi.org/10.1073/pnas.1900672116.

23. Fiorillo, L., Bianco, S., Chiariello, A.M., Barbieri, M., Esposito, A., Annunziatella, C., Conte, M., Corrado, A., Prisco, A., Pombo, A., Nicodemi, M.: Inference of chromosome 3D structures from GAM data by a physics computational approach. Methods, in press.

24. Esposito, A., Annunziatella, C., Bianco, S., Chiariello, A.M., Fiorillo, L., Nicodemi, M.: Models of polymer physics for the architecture of the cell nucleus. Wiley Interdiscip. Rev. Syst. Biol. Med. 11, (2019). https://doi.org/10.1002/wsbm.1444.

25. Chiariello, A.M., Esposito, A., Annunziatella, C., Bianco, S., Fiorillo, L., Prisco, A., Nicodemi, M.: A polymer physics investigation of the architecture of the murine orthologue of the 7q11.23 human locus. Front. Neurosci. 11, (2017). https://doi.org/10.3389/fnins.2017.00559.

26. Bianco, S., Annunziatella, C., Esposito, A., Fiorillo, L., Conte, M., Campanile, R., Chiariello, A.M.: Understanding chromatin structure: Efficient computational implementation of polymer physics models. (2019). https://doi.org/10.1007/978-3-030-10549-5_53.

27. Andrey, G., Montavon, T., Mascrez, B., Gonzalez, F., Noordermeer, D., Leleu, M., Trono, D., Spitz, F., Duboule, D.: A switch between topological domains underlies HoxD genes collinearity in mouse limbs. Science (80-.). 340, (2013). https://doi.org/10.1126/science.1234167.

28. Noordermeer, D., Duboule, D.: Chromatin Architectures and Hox Gene Collinearity. Curr. Top. Dev. Biol. 104, 113–148 (2013). https://doi.org/10.1016/B978-0-12-416027-9.00004-8.
29. Bonev, B., Mendelson Cohen, N., Szabo, Q., Fritsch, L., Papadopoulos, G.L., Lubling, Y., Xu, X., Lv, X., Hugnot, J.P., Tanay, A., Cavalli, G.: Multiscale 3D Genome Rewiring during Mouse Neural Development. Cell. (2017). https://doi.org/10.1016/j.cell.2017.09.043.
30. Persistence of Vision Pty. Ltd.: Persistence of Vision Raytracer, (2004).

MONTE CARLO SIMULATIONS SUPPORTING STUDIES OF PWR'S, NUCLEAR CRITICALITY SAFETY AND TAPIRO RESEARCH REACTOR SIMULATIONS

Patrizio Console Camprini[1*], Kenneth W. Burn[1]

[1]*ENEA, Fusion and Technology for Nuclear Safety and Security Department, 40129, Bologna, Italy*

ABSTRACT. In the framework of the Development of Expertise in Nuclear Safety, studies are carried out within the Project B.3.1 funded by the Italian Ministry of Economic Development – Annual Plan 2017. Monte Carlo simulations were performed by means of the MCNP6.1 code concerning nuclear safety evaluations of both PWR cores and critical configurations for the storage of fissile materials. In fact, Gen-II reactor - similar to Tihange model - and innovative Gen-III PWR's are treated as benchmarks for deep penetration problems. Ex-core responses are used to employ and test variance reduction techniques. In addition, Nuclear Criticality Slide Rule Suite and Whitesides' k_{eff}-of-the-world are studied to test deep penetration problems and stability of the fundamental distribution of the flux together with the sampling of particular responses. In addition, some simulations were performed supporting the TAPIRO research reactor, located in ENEA Casaccia center. The worth of the control rods and the insertion curves were calculated with Monte Carlo, in order to employ the latest ENDF/B-VIII.0 nuclear data set and provide updated results to the reactor staff.

1 Ex-core Calculations for Gen-II and Gen-III PWR Models

The present research activity concerned Monte Carlo simulations of Gen-II and Gen-III nuclear power plants and followed what has been carried out in the previous years. In fact, Monte Carlo MCNP6.1[1] code has been used to model and analyse benchmarks of a Gen-II system similar to the nuclear reactor at Tihange [2] and a reference Gen-III nuclear reactor core. The simulation regarding Gen-II nuclear core was about the determination of the detector response placed at 2 different positions outside the core: the first was at 45° angle and the second was at 315° (Fig. 1). Both were boron detectors and placed at about 250 cm from the axis of the core, 80 cm outside the core cylindrical region. Detector material was ^{10}B dispersed in natural boron, and the considered nuclear reaction was alpha particle production induced by a neutron absorption as (n,α).

Conversely, a Gen-III innovative nuclear system was studied through a reference benchmark [3]. Deep penetration problems considered here were neutron flux and reaction rates at a distance of 325 cm and 460 cm away from the core axis, namely about 150 cm and 280 cm in the reactor pit that is made of concrete. The response function has been selected in order to provide deep penetration problem in both the geometrical and in the energy domain. Considered nuclides are the following: ^{59}Co (n,γ), ^{151}Eu (n, γ), ^{54}Fe and ^{56}Fe for (n, γ) and (n,2n) respectively. In addition, dose rates were computed in these positions (Fig. 2).

The approach to the calculation followed different models of the neutron source inside the core. A fixed source is firstly defined by sampling the fundamental mode, treating a previous eigenvalue problem and scoring neutron production on a particular axial binning on a pin-by-pin pattern. The ex-core responses were then studied from this fundamental mode in a fixed source problem, aiming at all the specific tallies requested. In the fixed source calculation, a volumetric source has been

implemented with an isotropic angular distribution. Energy distributions considered three different possible spectra: the MCNP6.1 default fission spectrum, the ^{235}U fission spectrum and the ^{239}Pu fission spectrum both related to fission induced by thermal neutrons. Different configurations of the fixed source were sampled in order to study the impact on responses:

- homogeneous source throughout the core
- source with an axial distribution assembly by assembly
- source with a pin-by-pin resolution and a subdivision of the pin in 2 cylindrical shells

In addition, an eigenvalue direct problem was solved together with the responses of interest.

Fixed source simulations allowed also the implementation of the DSA variance reduction technique – developed at ENEA for fixed source simulations and thus extended to eigenvalue problems [4].

The DSA method produces variance reduction parameters through a minimization of the quality function – namely the maximization of the figure of merit. In fact, the adaptive multi-step iterative algorithm starts from initial sampling of a number of tracks, and thus increases knowledge of the system acting on different contribution to tally in phase space. This machine learning technique allows to avoid the utilisation of a previous direct calculation and then importance function is no longer requested. Maximization of the figure of merit for a single or a multiple response produces the variance reduction parameters that can be expressed in a weight window form to easily utilise the MCNP calculation facility. The framework of the work is the Project B.3.1 funded by the Italian Ministry of Economic Development – Annual Plan 2015 – about the Development of Expertise in Nuclear Safety. In particular Subproject A2, deliverable ID LP1-120 [5].
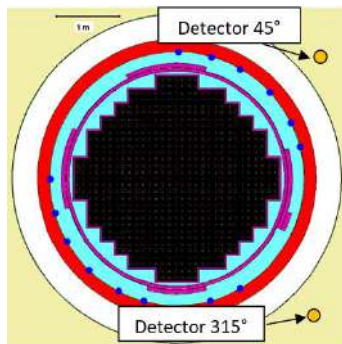
Fig.1: Gen-II model core cross-section
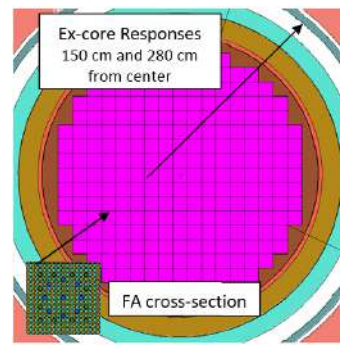
Fig.2: Gen-III PWR core cross-section
(Fuel assembly – FA – cross-section)

2 Nuclear Criticality Safety Studies

2.1 Update to Slide Rule Suite

The nuclear criticality safety studies concern the configurations of the fissile materials with respect to fuel storage pools and facilities in which the fissile compounds are treated and confined. The design needs verifications in order to prevent that the system becomes critical at any time and in any conditions. In this context, critical configurations are considered as accidental conditions.

The research activity used as a case study is the update to the benchmark of the "nuclear criticality slide rule" [6]. The geometry of the system is reported in Figure 3. The problem takes into account five fissile spheres of different compositions and sizes. The screen is present in certain configurations and has various compositions and thicknesses. The distance between the screen and the sphere is a varying parameter. The ground is either concrete or soil. In the study a uranyl fluoride sphere of about 25.55 cm radius is considered. The ground is made of concrete, the screen is 40 cm thick and is

located at 600 m from the surface of the sphere The request was to determine the prompt neutron and the gamma doses at the detector (a 40 cm radius sphere in air). Monte Carlo simulations were conducted through the MCNP6.1 code. It was used with the continuous energy ENDF/B-VII.1 cross-section set. Cell flux was calculated through a track length estimator. A two-step method was used to generate the source term and simulate the doses. The first step is a static calculation solving the eigenvalue problem to determine the distribution of fission neutron production inside the fissile assembly. The second step used the results of the first step to describe a fixed source of fission neutrons. A Watt spectrum was used for the energy distribution. The prompt gamma and neutron doses were determined in separate calculations.
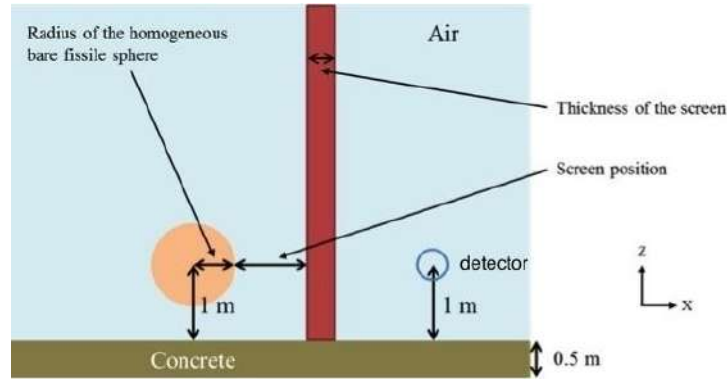
Fig.3: Slide Rule problem configuration

2.2 Whitesides' Keff-of-the-World Problem

Whitesides' well-known k_{eff}-of-the-world problem [6] was considered in order to reproduce in the domain of the criticality safety analyses the need to hold the fundamental mode while calculating responses in positions well outside the active region. The same need arises in the analysis of a Gen-III PWR core, considering the neutron flux leakage. Whitesides' problem consists of a 9x9x9 array of plutonium spheres in a void with pitch 60 cm, surrounded by a 30 cm thick layer of water. The radius of the spheres is about 4 cm in such a way that the array is subcritical. In the central position, a sphere was replaced by one with a radius of about 5 cm. This sphere is by itself slightly supercritical. The problem was then modified: the array of spheres is placed in a matrix of water, a water reflector is all around. A layer of concrete 50 cm thick is outside. An idealized ex-core neutron detector is placed in the outermost of the assembly. The whole configuration is represented in Figure 4. The density of the interstitial water and the reflector was varied in order to establish the amount of decoupling.

3 Control Rod Insertion Curves for TAPIRO Research Reactor

Within the framework of the analyses of the TAPIRO nuclear research reactor [7], Monte Carlo simulations were performed with MCNP6.1 code, in order to update the insertion curves of the control rods. TAPIRO is a fast reactor, reflected by means of a copper cylindrical volume. Since ENDF/B-VIII.0 nuclear data set introduced significant modifications for the neutron cross-sections of copper, it was necessary to evaluate the impact on the main parameters of the system. First, the substitution of only the ^{63}Cu and ^{65}Cu nuclides in the simulation yielded a change in the k_{eff} of the system of about 400 pcm. Therefore, it was worth to update the insertion curves of the control rods,

to improve the reactor knowledge and management. All these five control rods are made of copper and provide reflection when inserted. Conversely, if one or more rods are extracted some reflection is reduced and the reactor becomes subcritical. Insertions were evaluated for one Regulation Rod, two Safety Rods and two Compensation Rods. The insertion of the control rods was simulated one by one, and moving all safety rods together as well as all compensation rods.
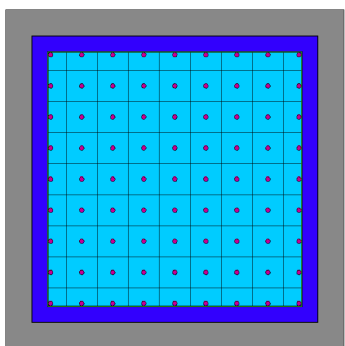

Fig. 4. Whitesides' modified k_{eff}-of-the-world
(horizontal section and detector)
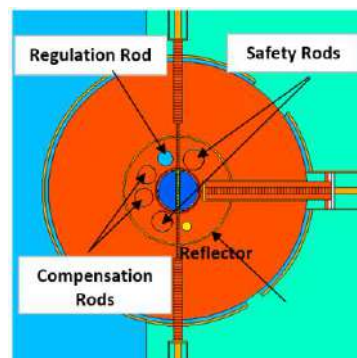
Fig. 5. TAPIRO reactor core
(core cross section and positions of the rods)

Acknowledgement

References

[1] Goorley J.T. et al., "Initial MCNP6 Release Overview - MCNP6 version 1.0", LA-UR-13-22934
[2] Brovchenko M., et al. "Neutron-gamma flux and dose calculations in a Pressurized Water Reactor (PWR)", International Conference on Radiation Shielding (ICRS13), Paris, 3-6 Oct 2016
[3] Burn K.W., et al. "Monte Carlo Methods for Core Safety Analysis: Design of Instrumentation for Monitoring PWR Core Degradation in Case of a Severe Accident". ENEA Report RdS 2014/063
[4] Burn K.W., "Optimizing variance reduction in Monte Carlo eigenvalue calculations that employ the source iteration approach", *Ann. Nucl. Energy* 73, 218-240, 2014
[5] Burn K. W. and P. Console Camprini, "Sviluppo e Applicazioni di Metodologie Monte Carlo per le Valutazioni Neutroniche in supporto alle Analisi di Sicurezza dei Reattori Nucleari in Operazione", Rapporto ENEA, PAR ADPFISS-LP1-120, (2017)
[6] K.W. Burn, P. Console Camprini, M. Duluc, "Employment of the Single Eigenvalue Monte Carlo Method to some Criticality Safety Problems; Comparison with a Standard Deterministic – Monte Carlo Approach", International Conference on Nucleare Criticality Safety (ICNC), Paris Sept (2019)
[7] CARTA M., et al. "TRIGA RC-1 and TAPIRO, ENEA Research Reactors", ENEA, Italian National Agency for New Technologies, Energy and Sustainable Economic Development C.R Casaccia, Vienna, June 10-12, 2013.

THE IMPACT OF BORON DOPING ON HYDROGEN STORAGE PROPERTIES OF MgH$_2$

Sandra Kurko, Bojana Paskaš Mamula, Jelena Rmuš, Jasmina Grbović Novaković and Nikola Novaković

University of Belgrade, VINČA Institute of Nuclear Sciences, P.O. Box 522, 11001, Belgrade, Serbia

ABSTRACT. The influence of boron doping on the kinetics of hydrogen diffusion in bulk and desorption from MgH$_2$ surface were calculated using Nudged Elastic Band (NEB) method within AbInit code. In the bulk calculation, MgH$_2$ doped with 6.25 at% of boron was used. The activation energies were calculated for the hydrogen diffusion in the vicinity of boron atom. In the slab calculations the hydrogen desorption activation energies from (110) boron doped MgH$_2$ surface were calculated. It was shown that boron significantly lowers the H-diffusion barrier, while the surface desorption energies are strongly dependent on the boron vicinity.

1 Introduction

To use hydrogen as a renewable energy vector it is essential to develop the sustainable and economical systems for its transport and storage for stationary and mobile application. The solid state hydrogen storage was shown to be the safest and the most compact method [1]. Materials that have a good balance between gravimetric and volumetric hydrogen storage capacity, price and physico-chemical properties are Mg based metal hydrides [2]. However, MgH$_2$ has high thermodynamic stability and poor hydrogen desorption kinetics at low temperatures. Nevertheless, the destabilization of its crystalline structure and introduction of various defects like impurities, vacancies and catalyst dopants can increase the reaction kinetics and improve dehydrogenation properties of MgH$_2$ [3]. To reveal the most important features governing the sorption properties of MgH$_2$, it is crucial to obtain a better understanding of the changes induced by the destabilization processes and their influence on sorption properties. Theoretical investigations of MgH$_2$ by ab initio DFT calculations provide insight into the nature of compound bonding and cohesion at the fundamental electronic level and also demonstrate the role of dopants and defects. Novaković et al. [4] found that transition metals Ti and Co interact with neighbouring hydrogen atoms and form tightly bonded 9 atoms clusters. In these clusters TM is positioned in the centre, while for surrounding H atoms are in (110) and four in (-1-10) plane with charge localisation inside the cluster around TM atoms. This leads to weakening of Mg-H bonds in the cluster vicinity and makes the overall structure less stable in proportion to the amount of charge located inside the clusters. In our calculations, we have previously shown that introduction of boron in tetragonal MgH$_2$ structure leads to destabilisation of its structure and increase in enthalpy of formation that is dependable on boron doping concentration [5]. Destabilization of MgH$_2$ by boron was confirmed experimentally, when we irradiated hydride with boron ions [6].We have also calculated that the stable phase is possible if 6.25 at% of Mg ions were substituted with boron. The reaction kinetics can be studied by employing NEB (Nudged Elastic Band) method within DFT calculations.

In rutile MgH$_2$ hydrogen desorption is the easiest from the (110) surface. Hydrogen desorption energy and activation barriers also depend on the Wyckoff positions of desorbed H atoms [7].

.

2 Details of calculations

To study hydrogen diffusion in bulk MgH_2 near boron atom and hydrogen desorption from the boron doped MgH_2 surface Abinit code and Troullier-Martins pseudopotentials were used. To calculate the MEP (minimum energy path) and activation energy for hydrogen diffusion and desorption, NEB (nudged elastic band) algorithm as implemented in Abinit was used. In NEB calculations all starting and final structures were fully relaxed. NEB-CI (climbing image) method was used with 8 images in bulk and 12 for surface calculations. Convergence parameters were the same as in the structure relaxation calculations. Diffusion of hydrogen was studied using $Mg_{15}BH_{32}$ supercell, constructed using 2x2x2 stacking of MgH_2 unit cells. For comparison, hydrogen diffusion was also studied in bulk MgH_2. Structure optimisation calculations parameters are given in [28]. Hydrogen diffusion process can be regarded as diffusion of hydrogen vacancies in the opposite direction. To comprehend the diffusion process in the boron vicinity both hydrogen vacancy formation enthalpy and activation barriers for non-equivalent hydrogen vacancies diffusion were calculated. Direction of H vacancy diffusion was from H1 to H4 position (see Fig. 1.left).

Hydrogen desorption from the boron doped MgH_2 surface was studied by slab calculations with (110) plane exposed. Slab supercell consisted of 12 parallel atomic planes along the supercell z-axis and 96 atoms (32 Mg and 64 H) with vacuum approximately 15 Å thick. At the surface, two-fold bonded hydrogen atoms denoted as H2s were exposed to vacuum. The second atomic layer consists of Mgs atoms and H3s atoms triple coordinated with Mg and the third one consists of "regular" bulk Hb atoms. In boron doped MgH_2, the same supercell was used with one Mg atom in the second atomic layer substituted with boron, so the concentration of boron is 3.125 at%. Desorption of hydrogen was modelled by successive removal of one up to four hydrogen atoms in different arrangements from surface and sub-surface layers. NEB calculations and energy barrier determination were done for different configurations presented in Figure 1.right.
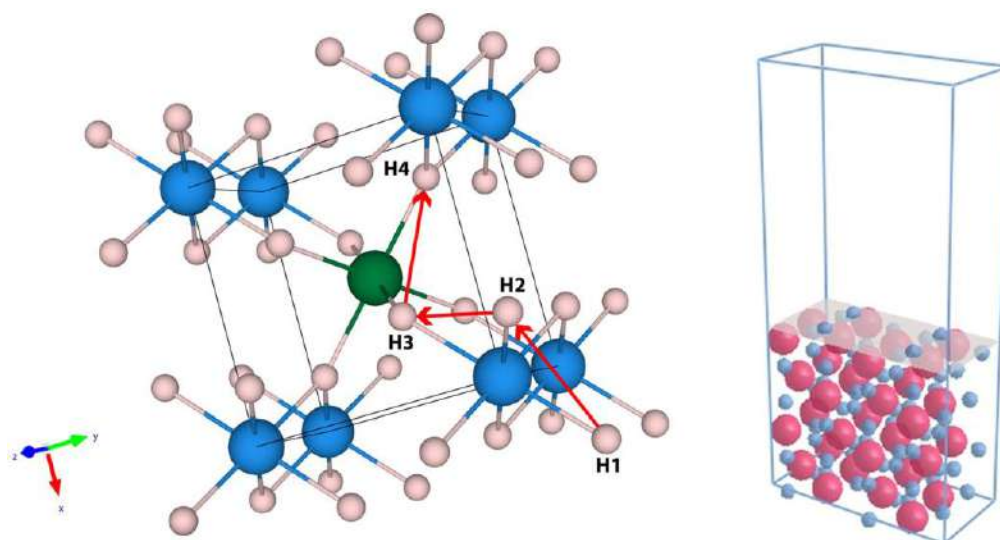
Fig. 1. Left) Part of $Mg_{15}BH_{32}$ supercell used in the vacancy diffusion calculations. H1-H4 are positions of hydrogen atoms where vacancies are formed. Red arrows show the calculated vacancy diffusion direction. Blue spheres represent Mg atoms, white hydrogen and green boron. Right) slab (2x2)(110) supercell used in surface desorption calculations. Red spheres represent Mg atoms, blue hydrogen.

3 Results

3.1 Bulk hydrogen vacancy diffusion calculations

In doped compound $Mg_{15}BH_{32}$ neutral hydrogen vacancy diffusion was considered for four non-equivalent positions presented in Figure 1.left and denoted as H1-H4. In H1 and H2 are hydrogen atoms bonded to nnMg atom (boron nearest neighbour) with Mg-H distances 1.986 Å and 1.955 Å, respectively. In positions H3 and H4 are hydrogen atoms bonded to boron with B-H distances 1.476 Å for H3 and 1.544 Å for H4.
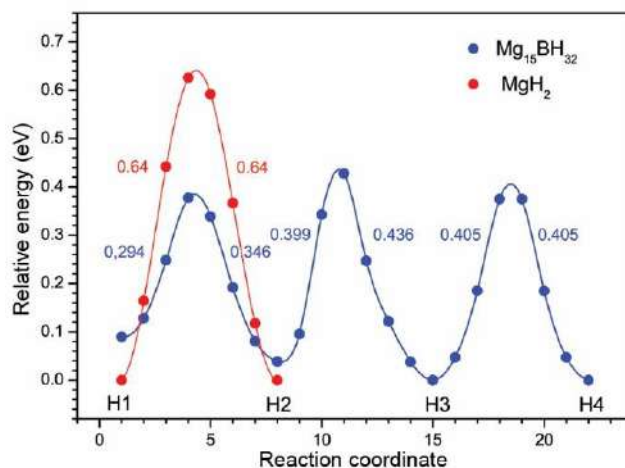

Fig. 2. Energy barriers for diffusion of hydrogen neutral vacancy in MgH_2 and $Mg_{15}BH_{32}$ as calculated by NEB method. Dots correspond to energies of particular intermediate NEB images.

In non-doped calculated MgH_2 vacancy formation energy is 1.82 eV, while activation energy for diffusion is 0.64 eV. In doped structure these energies are dependable on the position of particular vacancy, i.e. its distance from boron (see Fig. 2). Anyhow, all energies are lower in boron doped hydride. So, the boron has beneficial impact on hydrogen vacancy diffusion in its vicinity.

3.2 Surface H desorption calculations

Activation energies for H_2 desorption from H saturated surface were calculated using NEB method, both from the clean surface and in the boron vicinity. In non-doped structure two different reaction paths A and B were calculated. In A configuration, two H_{2s} (surface two-fold bonded) atoms from the surface layer were desorbed, while in B configuration one is H_{2s} and the other one is H_{3s} (surface three-fold bonded) from the second layer.

Boron doping leads to similar effects that vacancies in the surface have on the hydrogen desorption from the subsurface layers. Calculated activation energies in non-doped MgH_2 are in good agreement with other literature data and comparable with experimentally obtained values. As expected, activation energies for recombinative desorption of two H_{2s} atoms are higher than those for H_{2s} and H_{3s} atoms due to their larger initial distance. Surface boron doping causes the increase in activation energies for H_2 desorption from boron vicinity, while activation barriers for H_2 desorption further from boron are slightly lower than in non-doped hydride.
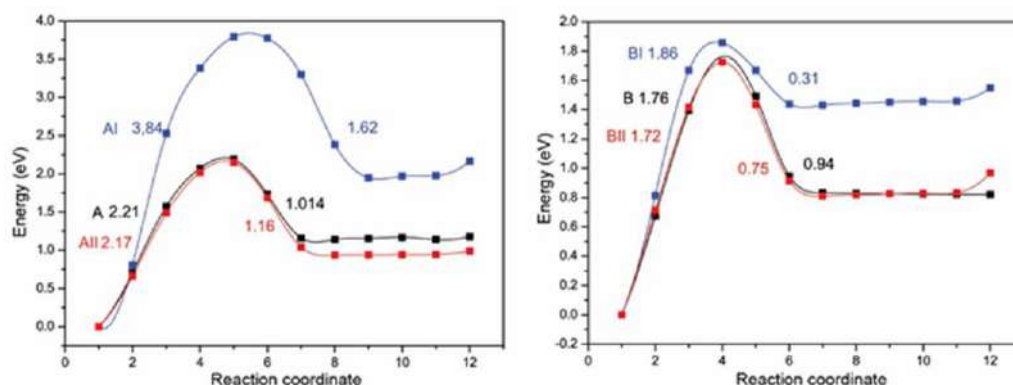
Fig. 3. Energy barriers for recombinative H_2 desorption from boron doped (110) MgH_2 surface in different surface and subsurface configurations.

Acknowledgements

References

[1] R. Varin, T. Czujko, Z.S. Wronski. Nanomaterials for hydrogen storage. (2009) doi:10.1007/s12045-007-0047-9

[2] E. Callini, K-F Aguey-Zinsou, R. Ahuja, J.R. Ares, S. Bals, N. Biliškov, et al. Nanostructured materials for solid-state hydrogen storage: A review of the achievement of COST Action MP1103. *Int J Hydrogen Energy* **41**, pp. 14404–28. (2016) doi: https://doi.org/10.1016/j.ijhydene.2016.04.025

[3] J. Grbović Novaković, L. Matović, M. Drvendžija, N. Novaković, D. Rajnović, M. Šiljegović et al. Changes of hydrogen storage properties of MgH_2 induced by heavy ion irradiation. *Int J Hydrogen Energy* **33**, pp. 1876–9. (2008) doi:10.1016/j.ijhydene.2008.02.008

[4] N. Novaković, J. Grbović Novaković, L. Matović, M. Manasijević, I. Radisavljević, B. Paskaš Mamula et al. Ab initio calculations of MgH_2, MgH_2:Ti and MgH_2:Co compounds. *Int J Hydrogen Energy* **35**, pp.598–608. (2010) doi:10.1016/j.ijhydene.2009.11.003

[5] S. Kurko, B. Paskaš Mamula, L. Matović, J.G. Novaković, N. Novaković. The Influence of Boron Doping Concentration on MgH_2 Electronic Structure, *Acta Physica Polonica* A **120**, pp. 238–41 (2011)

[6] S. Kurko, Lj. Matović, N. Novaković, B. Matović, Z. Jovanović, B. Paskaš Mamula, J. Grbović Novaković, Changes of Hydrogen Storage Properties of MgH_2 Induced by Boron Ion Irradiation, *Int J Hydrogen Energ* **36,** pp.1184-1189. (2011)

[7] S. Kurko, I. Milanović, J. Grbović Novaković, N. Ivanović, N. Novaković. Investigation of surface and near-surface effects on hydrogen desorption kinetics of MgH_2. *Int J Hydrogen Energy* **39**, pp. 862–7. (2014) doi:10.1016/j.ijhydene.2013.10.107

Study of solid molecular deuterium D_2 growth for high speed pipegun pellet injector

Simone Giusepponi[1]*, Francesco Buonocore[1], Massimo Celino[1], Antonio Frattolillo[2] and
Silvio Migliori[1]

[1] *ENEA-DTE-ICT Division, C.R. Casaccia, via Anguillarese 301, 00123 Rome, Italy*

[2] *ENEA-FSN-FUSTEC Division, C.R. Frascati, via E. Fermi 45, 00044 Frascati (RM), Italy*

Abstract. This study paves the way to design streamlined numerical procedures,
aimed at optimizing the growth conditions of high quality pellets for high-speed
pipe-gun injectors.

1 Introduction

We have set up a numerical model of solid molecular deuterium (D_2) growth, to address technological issues related to the production of high quality pellets for high-speed pipe-gun injectors [1]. The pneumatic pellet injection system is designed for DEMO refueling requirements. The technological study is dedicated to the integration of high/low speed pellet injectors in a single device equipped with steadystate extruders to provide a continuous supply of solid cryogenic pellets of hydrogen isotopes (D_2 or D-T) at low(high) speed and high(low) frequency. This system is under development in an ongoing collaboration between ORNL (Oak Ridge National Laboratory) and ENEA [2–5]. In order to reach this goal, it is necessary to explore the phase transition at very extreme conditions of temperature and pressure around the triple point: T* = 18.71 K; P* = 171.3 mbar: temperature in the range 8-20 K and pressure in the range 5-200 mbar. In these ranges, there is the transition region of molecular deuterium from solid to gas and viceversa. An atomistic model can be a very useful method to have an insight into the physics of molecular deuterium in these conditions, therefore, extensive molecular dynamics (MD) simulations represent a valid support for the formulation of this atomic model. Furthermore, since hundreds of thousands of molecules are needed, classical molecular dynamics methods are used. In this report we considered NPT-MD simulations with P = 25 mbar. Simulations with other values of pressure are in progress.

2 Computational details

The LAMMPS (Large-scale Atomic/Molecular Massively Parallel Simulator) code is used to perform MD simulations of the molecular deuterium (D_2) systems. LAMMPS [6] is a classical MD code that models an ensemble of particles in a solid, liquid, or gaseous state. It can model atomic, polymeric, biological, metallic, granular, and coarse-grained systems using a variety of force fields and boundary conditions. Firstly, the solid phase is studied by using MD simulations at constant temperature and pressure (NPT), starting from the absolute zero temperature 0 K, up to temperature and pressure below the triple point. Then, cutting the solid phase on the specific Miller directions, we set up the surface slab on which the deuterium gas is deposited or evaporate. Secondly, different gases of molecular deuterium

---

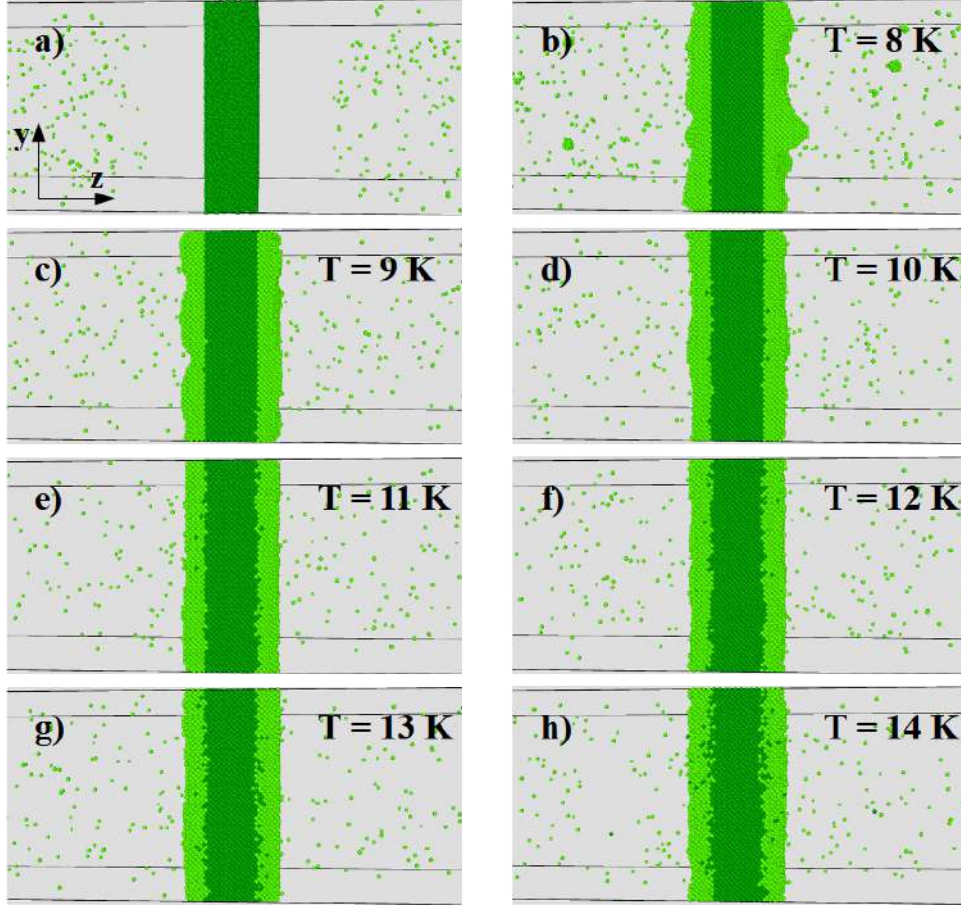*Corresponding author. E-mail: `simone.giusepponi@enea.it`.

Figure 1: a) Starting configuration of the system and b-h) snapshots of the solid phase at different temperatures in the ranges 8-14 K at the 75% of gas absorption. Dark green: molecules in solid phase at the beginning of the simulation; light green: molecules in gas phase at the beginning of the simulation.

are prepared in aforementioned ranges of temperature an pressure to be coupled with the solid surface slab and create the solid-gas interfaces that is finally studied.

The crystal structure of molecular deuterium is the face centered cubic (FCC) with experimental lattice parameter $a_{D_2} = 5.07$ Å [7]. To set up the numerical model, initially, a crystalline FCC bulk system of N = 4000 deuterium molecules D_2 is considered (10 × 10 × 10 crystal unit cells). PBC (Periodic Boundary Conditions) are imposed to mimic an infinitely extended system in x, y and z directions. LAMMPS code uses interatomic potentials to model interactions between atoms, in this case, the Lennard-Jones potential with $\epsilon = 2.29$ meV, $\sigma = 3.07$ Å is used [8]. Performing an energy minimization of the system, we found the following values for the lattice parameter and the cohesion energy: $a_{D_2} = 4.75$ Å $E_{coh} = 19$ meV/molecule of D_2. The simulation cell was cubic with: $L_0 = 47.5$ Å. Then, in order to explore the solid phase, the system was heated from the absolute zero temperature up to 16 K (in step of 1 K) by performing NPT simulations at hydrostatic constant pressure (P = 0 mbar). Then, cutting the previous relaxed solid on the (001) Miller plane, slabs with two free surfaces perpendicular to the z direction are obtained. Moreover, to increase tha area of the free surfaces, we replicate for 4 times the systems along x and y directions to have slabs of solid deuterium (40 × 40 × 10 crystal unit cell) made up of 64000 molecules D_2 with dimensions: $L_x = L_y \simeq 190$ Å and $L_z \simeq 50$ Å infinitely ex-
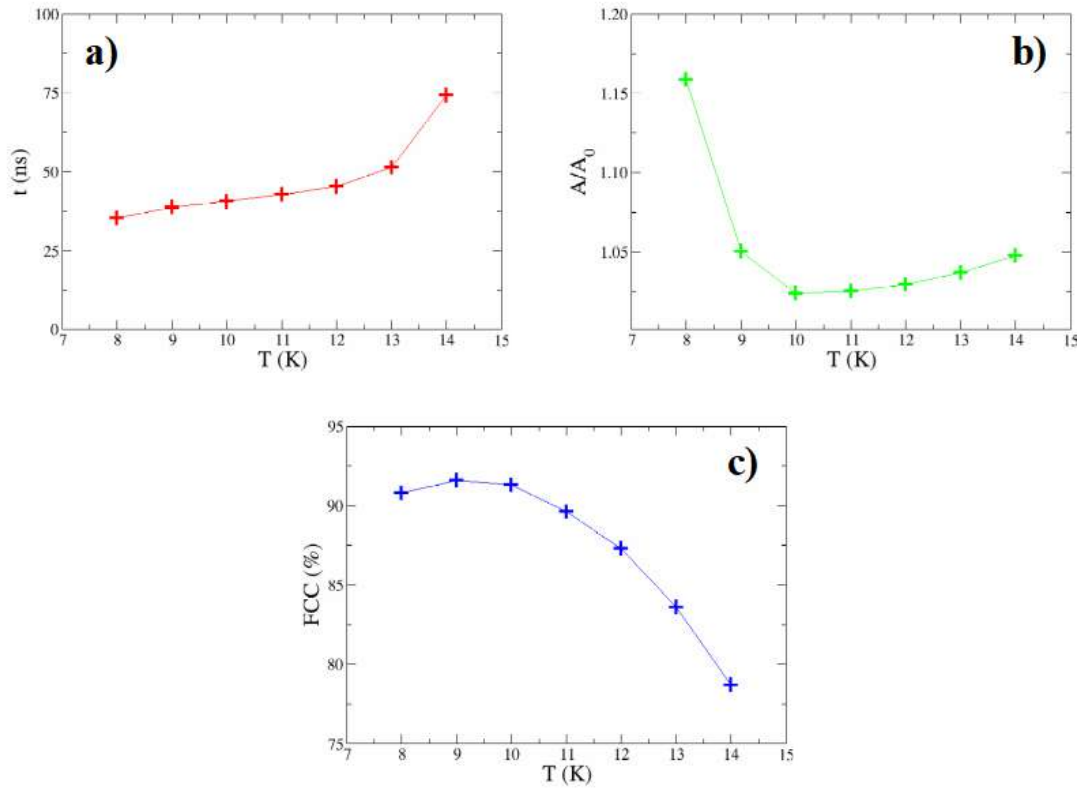
Figure 2: a) Absorption time to have +75% in the growth of the solid. b) Ratio of the area of the reconstructed surfaces to the area of the initial solid. c) Percentage of molecules of solid deuterium in FCC position.

tended in both x and y directions due to PBC. With respect of the gaseous deuterium phase, we prepare an equilibrated system of 64000 molecules D_2 at temperature T = 20 K and pressure P = 25 mbar along the z direction. Then, the gas is cooled down at T = 8 K (in step of 1 K) by performing NPT simulations, with supercell sides $L_x = L_y$ fixed at 190 Å and L_z free to change in order to satisfy the imposed values of the pressure and temperature. Finally, the two phase are coupled together (see Fig.1a) putting an empty space between the solid and gas to permit a soft relaxation of the system at the initial stages.

3   Results and discussion

The system shown in Fig.1a) is used as starting configuration for a set of very long MD simulations up to time frames of one hundred ns, at constant temperature T in the range 8-20 K and constant pressure P. The pressure along x and y directions is kept fixed at 0 mbar, instead along the z direction is kept fixed at 25 mbar. This permit to have a solid slab with a thickness of about 50 Å and two free surfaces, each one with an area of about 200×200 Å^2, in coexistence with a gas at 25 mbar. The first result is that for temperature T $\geq$ 15 K the solid phase sublimates. The molecules in solid phase tend to pass at the gas phase more easily then the opposite process, the faster this is, the higher the temperature. On the contrary, for temperature T $\leq$ 14 K, the reverse process is favorite, then the number of molecules in solid phase increases with time and the phenomenon is quickened by the decrease in temperature. Therefore, the equilibrium temperature between solid and gas at 25 mbar is within 14 and 15 K, in good

agreement with experimental value T $\simeq$ 15 K. To explore and characterize the growing process of solid molecular deuterium, we calculate the absorption rate of the gas and the quality of the reconstructed solid. In panels b-h) of Fig.1, are reported the snapshots of the reconstructed solid deuterium in the range of temperature 8-14 K, when 75% of molecules has changed their state from gas to solid. Dark (light) green spheres refer to D_2 molecules that are in solid (gas) phase at the beginning of the MD simulations. In fig.2a) are reported the required time (absorption time) to reach this level of growth of the solid (+75%) at different simulation temperatures. There is a linear increase in time until T = 12 K, then, there is a net increase in the absorption time which tends to infinity approaching to the equilibrium temperature, when the number of molecules passing from the solid to the gaseous state is equal to the number of molecules passing from the gaseous state to the solid state. Furthermore, we observe that the reconstructed solid surfaces are less smooth at low temperatures, therefore, we calculated the ratio of the area of the reconstructed surfaces to the area of the initial solid. In Fig2b), it is pointed out that, T = 10 K is the lower limit for having slightly corrugated surfaces. Finally, in Fig.2c, we report the percentage of molecules of solid deuterium in FCC position. The maximum is for temperatures around 9-10 K; for higher values of T there is a reduction in the number of molecules in the FCC position, this is due to the increased mobility of molecules, consequent to the larger thermal energy.

In conclusion, the temperature range 10-12 K, is the range in which there are the best conditions for having good quality solid deuterium. In fact, in this range, the absorption rate is not so low, the surfaces are satisfactorily smooth and the molecules form FCC lattice. This result is strongly confirmed by experimental data produced by ENEA pellet injector experts [3–5].

The scalability study with this system (128000 D_2 molecules) indicates that best speed-up is reached with 192 cores of CRESCO6 cluster. The simulations performed for this work required an overall computational cost of around 150,000 cpu hours.

References

[1] S. K. Combs and L. R. Baylor. Pellet-injector technology. brief history and key developments in the last 25 years. *Fusion Science and Technology*, 73:493–518, 2018.

[2] S. K. Combs et al. Experimental study of the propellant gas load required for pellet injection with iter-relevant operating parameters. *Fusion Science and Technology*, 68:319–325, 2015.

[3] F. Bombarda et al. State of the art and perspective of high-speed pellet injection technology. *Fusion Engineering and Design*, 124:797–800, 2017.

[4] A. Frattolillo et al. Core fueling of demo by direct line injection of high-speed pellets from the hfs. *IEEE Transactions on plasma science*, 46:1429–1435, 2018.

[5] A. Frattolillo et al. Addressing the feasibility of inboard direct-line injection of high-speed pellets, for core fueling of demo. *Fusion Engineering and Design*, 146:2426–2429, 2019.

[6] S. Plimpton. Fast parallel algorithms for short-range molecular dynamics. *J. Comp. Phys.*, 177:1–19, 1995.

[7] A. E. Curzon and A. J. Mascall. The crystal structures of solid hydrogen and solid deuterium in thin films. *Brit. J. Appl. Phys.*, 16:1301, 1965.

[8] L. A. Zepeda-Ruiz et al. Effect of wetting on nucleation and growth of d$_2$ in confinement. *J. Chem. Phys.*, 148:134708, 2018.

EXACT CALCULATION OF EXTINCTION PROBABILITIES IN GAMES OF CYCLIC DOMINANCE

Filippo Palombi[1*]

[1]*ENEA, Via E. Fermi 45, 00044 Frascati (IT)*

ABSTRACT.

Games of cyclic dominance have become very popular in the scientific debate about the origin of biodiversity and species coexistence, as they provide a natural framework to describe ecosystems that evolve with no leading species consuming all others. The simplest model with such features is the cyclic Lotka-Volterra model, where three species fight against each other according to rules derived from the Rock-Paper-Scissors game. In this model, species coexistence becomes durable in the thermodynamic limit, namely for increasingly large populations, while it is unstable for small populations, due to stochastic noise. Agent-based simulations allow computing the extinction probability with statistical uncertainty. In this report, we show that one can calculate the extinction probability exactly via recursive techniques.

1 Introduction

Cyclic competition is distinctively associated with closed relational chains, describing aspects of the struggle for life such as feeding, hunting, mating. The prototype is a system made of three different species, interacting with one another like children playing Rock-Paper-Scissors, the famous game where paper wraps rock, scissors cut paper and rock crushes scissors. Such schemes are at heart of biological systems spanning a wide range of length scales and complexity. Examples include the repressilator [1], the E. coli colicin E2 system [2], the common side-blotched lizard [3], several plant systems [4, 5, 6] and so forth.

In principle, the absence of apex predators and bottom preys in cyclic chains allows species to dominate in turn. As soon as one of them outperforms the others, it becomes itself a source of nourishment for the next one along the chain. This feature suggests that cyclic competition may serve as a fundamental mechanism facilitating coexistence and biodiversity. Experiments performed in Ref. [2] on three cyclically interacting strains of E. coli confirmed this thesis and also made it more precise: species can coexist provided ecological processes (interaction and dispersal) develop locally. In practice, to ensure coexistence in the experiments, colonies of different strains had to first grow in separate spatial domains and then be left free to invade neighboring colonies.

2 Extinction probability in the cyclic Lotka-Volterra model

The cyclic Lotka-Volterra model assumes three species A, B, C, cyclically interacting according to two-agent predation reactions

$$AB \overset{k_{AB}}{\to} BB, \qquad BC \overset{k_{BC}}{\to} CC, \qquad CA \overset{k_{CA}}{\to} AA, \tag{1}$$

---

*Corresponding author. E-mail: `filippo.palombi@enea.it`.

where k_{AB}, k_{BC}, k_{CA} are reaction rates, i.e. occurrence probabilities per unit time. These interactions (also known as *dominance replacement reactions*) leave the total number of agents invariant, namely they involve two agents and result in two agents after each interaction. We consider a system with N_A agents of species A, N_B agents of species B and N_C agents of species C in the beginning, for $N_A, N_B, N_C \geq 1$. We let (N_A, N_B, N_C) denote generically the state of the system when the number of agents of species A, B and C are respectively N_A, N_B and N_C. The state of the system evolves according to the reactions Eq. (1), occurring one after another along an infinite sequence. At each step of the evolution, a reaction is selected with probability proportional to the reaction rate and the number of possible realizations in the system at the given step. For instance, the number of possible realizations of AB $\rightarrow$ BB is $N_A N_B$. Hence, the selection probabilities are

$$P_{AB \rightarrow BB} = \frac{k_{AB} N_A N_B}{k_{AB} N_A N_B + k_{BC} N_B N_C + k_{CA} N_C N_A} \equiv p_{AB}(N_A, N_B, N_C) \,, \tag{2}$$

$$P_{BC \rightarrow CC} = \frac{k_{BC} N_B N_C}{k_{AB} N_A N_B + k_{BC} N_B N_C + k_{CA} N_C N_A} \equiv p_{BC}(N_A, N_B, N_C) \,, \tag{3}$$

$$P_{CA \rightarrow AA} = \frac{k_{CA} N_C N_A}{k_{AB} N_A N_B + k_{BC} N_B N_C + k_{CA} N_C N_A} \equiv p_{CA}(N_A, N_B, N_C) \,. \tag{4}$$

These probabilities depend only upon the state of the system. In particular, they do not depend on time. Eventually, the system reaches one of three absorbing states, viz. $(N_A + N_B + N_C, 0, 0)$, $(0, N_A + N_B + N_C, 0)$ or $(0, 0, N_A + N_B + N_C)$. When this happens, the system stops evolving. Therefore, it makes sense to define the probabilities

$$P_A(N_A, N_B, N_C; t) = \text{prob}\{(N_A, N_B, N_C) \rightarrow (N_A + N_B + N_C, 0, 0) \text{ after } t \text{ iterations}\} \,, \tag{5}$$

$$P_B(N_A, N_B, N_C; t) = \text{prob}\{(N_A, N_B, N_C) \rightarrow (0, N_A + N_B + N_C, 0) \text{ after } t \text{ iterations}\} \,, \tag{6}$$

$$P_C(N_A, N_B, N_C; t) = \text{prob}\{(N_A, N_B, N_C) \rightarrow (0, 0, N_A + N_B + N_C) \text{ after } t \text{ iterations}\} \,. \tag{7}$$

To keep the notation simple, we omit to specify t whenever it is understood that $t \rightarrow \infty$. We remark that $(N_A, 0, 0)$ is an absorbing state for all $N_A \geq 1$, in that it cannot change under Eq. (1). We also observe that a state $(N_A, N_B, 0)$ can only evolve into $(0, N_A + N_B, 0)$, hence

$$P_A(N_A, 0, N_C) = 1 \,, \quad P_B(N_A, 0, N_C) = 0 \,, \quad P_C(N_A, 0, N_C) = 0 \,, \tag{8}$$

and analogously for $(0, N_B, N_C)$ and $(N_A, N_B, 0)$. Finally, by symmetry we have

$$P_A(N_A, N_B, N_C) = P_B(N_C, N_A, N_B) = P_C(N_B, N_C, N_A) \,, \tag{9}$$

provided $k_{AB} = k_{BC} = k_{CA}$. It is possible to calculate $P_k(N_A, N_B, N_C; \infty)$ exactly for arbitrary (N_A, N_B, N_C) and for $k = $ A, B, C. To this aim, we simply need to use iteratively the relation

$$P_k(N_A, N_B, N_C; t) = p_{AB}(N_A, N_B, N_C) P_k(N_A - 1, N_B + 1, N_C; t - 1)$$

$$+ p_{BC}(N_A, N_B, N_C) P_k(N_A, N_B - 1, N_C + 1; t - 1)$$

$$+ p_{CA}(N_A, N_B, N_C) P_k(N_A + 1, N_B, N_C - 1; t - 1) \,. \tag{10}$$

The meaning of Eq. (10) is clear. There are only three possible states connected to (N_A, N_B, N_C). They are $(N_A - 1, N_B + 1, N_C)$, $(N_A, N_B - 1, N_C + 1)$ and $(N_A + 1, N_B, N_C - 1)$. The extinction probability after a time t is the sum of the probabilities to go from (N_A, N_B, N_C) to one of the states connected to

it in one iteration times the extinction probability after a time $t - 1$ from those states. As $t \to \infty$, the dependence of the probabilities on t decreases progressively, hence we obtain the consistency relation

$$P_k(N_A, N_B, N_C) = p_{AB}(N_A, N_B, N_C)P_k(N_A - 1, N_B + 1, N_C)$$
$$+ p_{BC}(N_A, N_B, N_C)P_k(N_A, N_B - 1, N_C + 1)$$
$$+ p_{CA}(N_A, N_B, N_C)P_k(N_A + 1, N_B, N_C - 1) \,. \tag{11}$$

This equation can be iterated to get the value of $P_k(N_A, N_B, N_C)$. Let us make a couple of examples under the assumption $k_{AB} = k_{BC} = k_{CA}$.

$$P_A(1, 1, 1) = \frac{1}{3} \{P_A(0, 2, 1) + P_A(1, 0, 2) + P_A(2, 1, 0)\} = \frac{1}{3} \{0 + 1 + 0\} = \frac{1}{3} \,; \tag{12}$$

$$P_A(2, 1, 1) = \frac{2}{5} P_A(1, 2, 1) + \frac{1}{5} P_A(2, 0, 2) + \frac{2}{5} P_A(3, 1, 0) = \frac{1}{5} + \frac{2}{5} P_A(1, 2, 1)$$
$$= \frac{1}{5} + \frac{2}{5} \left\{ \frac{2}{5} P_A(0, 3, 1) + \frac{2}{5} P_A(1, 1, 2) + \frac{1}{5} P_A(2, 2, 0) \right\} = \frac{1}{5} + \frac{4}{25} P_A(1, 1, 2)$$
$$= \frac{1}{5} + \frac{4}{25} \left\{ \frac{1}{5} P_A(0, 2, 2) + \frac{2}{5} P_A(1, 0, 3) + \frac{2}{5} P_A(2, 1, 1) \right\} = \frac{1}{5} + \frac{8}{125} + \frac{8}{125} P_A(2, 1, 1) \,,$$
$$\Rightarrow \ P_A(2, 1, 1) = \frac{25}{117} + \frac{8}{117} = \frac{33}{117} \,. \tag{13}$$

To compute the extinction probability for $N_A, N_B, N_C \gg 1$, we can generalize the above iterative procedure as follows. From the above examples, we notice that the expression on the right-hand side of Eq. (11) becomes more and more complicated each time we iterate the equation. In full generality, the right-hand side of Eq. (11) can be recast into the more general form

$$P_k(N_A, N_B, N_C) = \sum_{M_A, M_B, M_C} \pi_k(M_A, M_B, M_C) P_k(M_A, M_B, M_C) \,, \tag{14}$$

where $\pi_k(M_A, M_B, M_C)$ are general coefficients that we should update at each iteration step. These coefficients are defined for all M_A, M_B, M_C such that $M_A + M_B + M_C = N_A + N_B + N_C \equiv N_{tot}$. The number of possible combinations of M_A, M_B, M_C is the number of weak 3-compositions of N_{tot}, i.e.

$$\text{no. of possible combinations of } M_A, M_B, M_C = \binom{N_{tot} + 2}{N_{tot}} = \frac{1}{2}(N_{tot} + 2)(N_{tot} + 1) \,. \tag{15}$$

As can be seen, this number increases quadratically with N_{tot}. To calculate $P_k(N_A, N_B, N_C)$, we proceed as follows. We initially let

$$P_k(N_A, N_B, N_C) = 0 \,, \tag{16}$$

and

$$\pi_k(N_A - 1, N_B + 1, N_C) = p_{AB}(N_A - 1, N_B + 1, N_C) \,,$$
$$\pi_k(N_A, N_B - 1, N_C + 1) = p_{BC}(N_A, N_B - 1, N_C + 1) \,,$$
$$\pi_k(N_A + 1, N_B, N_C - 1) = p_{CA}(N_A + 1, N_B, N_C - 1) \,,$$
$$\pi_k(M_A, M_B, M_C) = 0 \text{ for all other } M_A, M_B, M_C \,. \tag{17}$$

Then we update all coefficients according to the rule

$$\pi'_k(M_A, M_B, M_C) = p_{AB}(M_A - 1, M_B + 1, M_C)\pi_k(M_A - 1, M_B + 1, M_C)$$

$$+ p_{BC}(M_A, M_B - 1, M_C + 1)\pi_k(M_A, M_B - 1, M_C + 1)$$

$$+ p_{CA}(M_A - 1, M_B, M_C + 1)\pi_k(M_A - 1, M_B, M_C + 1), \tag{18}$$

for all M_A, M_B, M_C. Then, we let

$$\pi'_k(0, M_B, M_C) = \pi'_k(M_A, M_B, 0) = 0 \quad \text{if } k = A, \tag{19}$$

$$\pi'_k(M_A, 0, M_C) = \pi'_k(0, M_B, M_C) = 0 \quad \text{if } k = B, \tag{20}$$

$$\pi'_k(M_A, M_B, 0) = \pi'_k(M_A, 0, M_C) = 0 \quad \text{if } k = C. \tag{21}$$

This step is needed to ensure that all contributions from $P_A(0, M_B, M_C)$ and so forth never contaminate other terms at the subsequent steps. Then, we let

$$P'_k(N_A, N_B, N_C) = P_k(N_A, N_B, N_C) + \sum_{M_A, M_C} \pi'_k(M_A, 0, M_C) \quad \text{if } k = A,$$

$$P'_k(N_A, N_B, N_C) = P_k(N_A, N_B, N_C) + \sum_{M_A, M_B} \pi'_k(M_A, M_B, 0) \quad \text{if } k = B,$$

$$P'_k(N_A, N_B, N_C) = P_k(N_A, N_B, N_C) + \sum_{M_B, M_C} \pi'_k(0, M_B, M_C) \quad \text{if } k = C. \tag{22}$$

Finally, we let

$$P_k(N_A, N_B, N_C) = P'_k(N_A, N_B, N_C),$$

$$\pi'_k(M_A, 0, M_C) = 0 \quad \text{if } k = A,$$

$$\pi'_k(M_A, M_B, 0) = 0 \quad \text{if } k = B,$$

$$\pi'_k(0, M_B, M_C) = 0 \quad \text{if } k = C, \tag{23}$$

and

$$\pi_k(M_A, M_B, M_C) = \pi'_k(M_A, M_B, M_C), \tag{24}$$

for all M_A, M_B, M_C. To stop the iteration we need to introduce a stopping criterion. To this aim, we notice that after infinite iterations, the recursion becomes exact, hence it follows

$$\sum_{\substack{M_A + M_B + M_C = N_{tot} \\ M_A, M_B, M_C \neq N_A, N_B, N_C}} \pi_k(M_A, M_B, M_C) = 0. \tag{25}$$

Therefore, we introduce a parameter $\epsilon > 0$ and we stop the iteration as soon as

$$\sum_{\substack{M_A + M_B + M_C = N_{tot} \\ M_A, M_B, M_C \neq N_A, N_B, N_C}} \pi_k(M_A, M_B, M_C) < \epsilon. \tag{26}$$

Fig. 1 shows that the number of iterations needed to have Eq. (26) fulfilled increases quadratically in N_{tot} for fixed ϵ and decreases logarithmically in ϵ for fixed N_{tot}. In particular, Fig. 1 corresponds to $k_{AB} = k_{BC} = k_{CA} = 1$ and $N_A = N_B = N_C = N_{tot}/3$.
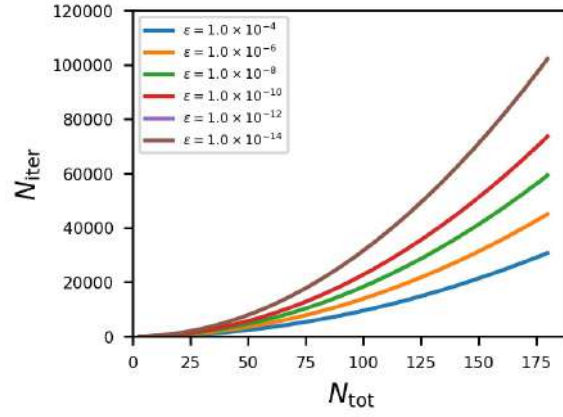
Figure 1: Number of iterations vs. N_{tot} for various values of ϵ.

3 Geometry

In order to code the iteration, we need an ordering for the triplets $(N_{\text{A}}, N_{\text{B}}, N_{\text{C}})$. In other words, we need a function

$$\phi : \{(N_{\text{A}}, N_{\text{B}}, N_{\text{C}}) \in \mathbb{N}_0^3 \ : \ N_{\text{A}} + N_{\text{B}} + N_{\text{C}} = N_{\text{tot}}\} \to \mathbb{N}_0 . \tag{27}$$

To define this function, we first let $N_{\text{A}} = 0$ and run all possible values of $N_{\text{B}}, N_{\text{C}}$. Then, we let $N_{\text{A}} = 1$ and run all possible values of $N_{\text{B}}, N_{\text{C}}$, etc. For each value of N_{A}, we let $N_{\text{B}} = 0$ and run all possible values of N_{C}. Then, we let $N_{\text{B}} = 1$ and run all possible values of N_{C} and so forth. In this way, we produce a sequence of blocks of triplets such as

$$(N_{\text{A}}, N_{\text{B}}, N_{\text{C}}) = (0, 0, N_{\text{tot}}), (0, 1, N_{\text{tot}} - 1), \ldots, (0, N_{\text{tot}}, 0) \to (N_{\text{tot}} + 1) \text{ triplets}$$

$$(N_{\text{A}}, N_{\text{B}}, N_{\text{C}}) = (1, 0, N_{\text{tot}} - 1), (1, 1, N_{\text{tot}} - 2), \ldots, (1, N_{\text{tot}} - 1, 0) \to N_{\text{tot}} \text{ triplets}$$

$$(N_{\text{A}}, N_{\text{B}}, N_{\text{C}}) = (2, 0, N_{\text{tot}} - 2), (2, 1, N_{\text{tot}} - 3), \ldots, (2, N_{\text{tot}} - 2, 0) \to (N_{\text{tot}} - 1) \text{ triplets}$$

$$\ldots$$

$$(N_{\text{A}}, N_{\text{B}}, N_{\text{C}}) = (N_{\text{tot}}, 0, 0) \to 1 \text{ triplet} . \tag{28}$$

From this sequence it is clear that to assign an ordering number to each triplet it is sufficient to count the number of complete blocks and to count then the number of triplets within the first incomplete block up to the current triplet. The latter number is N_{B}. Hence, we have

$$\phi(N_{\text{A}}, N_{\text{B}}, N_{\text{C}}) = \psi(N_{\text{A}}) + N_{\text{B}} , \tag{29}$$

where

$$\psi(N_{\text{A}}) = \sum_{k=N_{\text{tot}}+2-N_{\text{A}}}^{N_{\text{tot}}+1} k = \sum_{k=0}^{N_{\text{tot}}+1} k - \sum_{k=0}^{N_{\text{tot}}+1-N_{\text{A}}} =$$

$$= \frac{1}{2}(N_{\text{tot}} + 2)(N_{\text{tot}} + 1) - \frac{1}{2}(N_{\text{tot}} + 2 - N_{\text{A}})(N_{\text{tot}} + 1 - N_{\text{A}})$$

$$= \frac{N_{\text{A}}}{2}(2N_{\text{tot}} + 3 - N_{\text{A}}) . \tag{30}$$
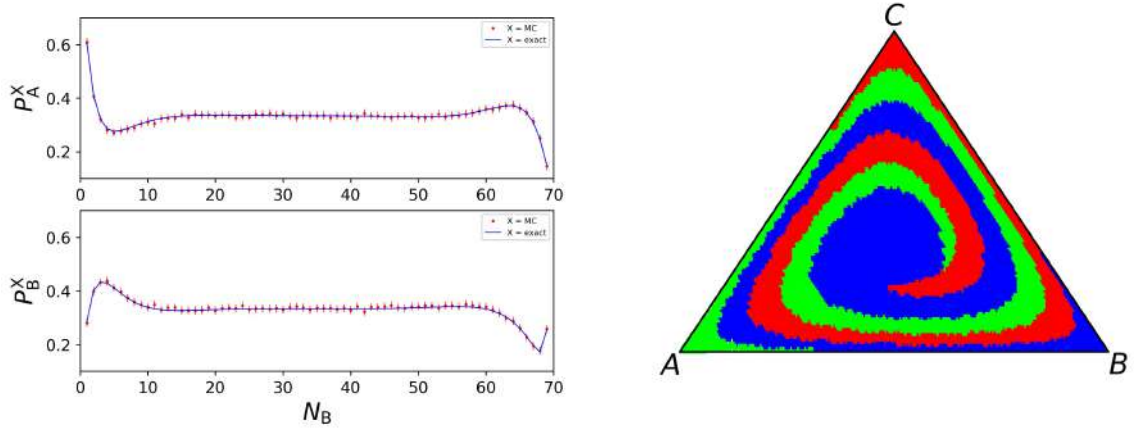
Figure 2: (left) Extinction probability from recursive techniques and Gillespie simulations for $N_{\text{tot}} = 100$ and $N_A = 70$; (right) attraction basins of species extinction for $N_{\text{tot}} = 240$.

Therefore

$$\phi(N_A, N_B, N_C) = \frac{N_A}{2}(2N_{\text{tot}} + 3 - N_A) + N_B \,. \tag{31}$$

In particular, the last triplet has ordering number $\phi(N_{\text{tot}}, 0, 0) = (N_{\text{tot}}^2 + 3N_{\text{tot}})/2$. This is in agreement with Eq. (15) as the number of possible triplets is given by $\phi(N_{\text{tot}}, 0, 0) + 1$.

The inverse formulas express $N_A(\phi)$, $N_B(\phi)$, $N_C(\phi)$ as functions of ϕ. To obtain $N_A(\phi)$, we assume for a moment that we know ψ. Eq. (30) can be recast into $N_A^2 - (2N_{\text{tot}} + 3)N_A + 2\psi = 0$. It yields

$$N_A(\psi) = \frac{(2N_{\text{tot}} + 3) - \sqrt{(2N_{\text{tot}} + 3)^2 - 8\psi}}{2} \,. \tag{32}$$

Unfortunately, we do not know ψ. Nevertheless, since $\phi > \psi$ it follows that $[(2N_{\text{tot}} + 3) - \sqrt{(2N_{\text{tot}} + 3)^2 - 8\psi}] < [(2N_{\text{tot}} + 3) - \sqrt{(2N_{\text{tot}} + 3)^2 - 8\phi}]$. Hence,

$$N_A(\phi) = \left\lfloor \frac{(2N_{\text{tot}} + 3) - \sqrt{(2N_{\text{tot}} + 3)^2 - 8\phi}}{2} \right\rfloor , \qquad N_B(\phi) = \phi - \frac{N_A}{2}(2N_{\text{tot}} + 3 - N_A) \,. \tag{33}$$

In Fig. 2 (left) we compare the estimate of the extinction probability obtained for $N_{\text{tot}} = 100$ and $N_A = 30$ from numerical simulations with the one obtained from the above recursive technique. As can be seen, the agreement is very good. In Fig. 2 (right) we show the attraction basins for $N_{\text{tot}} = 240$. Each point on the ternary diagram corresponds to a triplet (N_A, N_B, N_C). It is colored in red, green or blue depending on whether $P_A > \{P_B, P_C\}$, $P_B > \{P_C, P_A\}$ or $P_C > \{P_A, P_B\}$. As can be seen, the attraction basins generate a spiral pattern.

4   Parallel Computing

Computing $P_k(N_A, N_B, N_C)$ for all possible (N_A, N_B, N_C) is demanding, even for moderate values of N_{tot}. In order to speed up the computation, the simplest possibility is to use multi-threding techniques. Specifically, we coded the algorithm described in sect. 2 in C with OpenMP directives. Each thread computes $P_k(N_A, N_B, N_C)$ for a given choice of (N_A, N_B, N_C). A global counter shared by all parallel threads represents the variable ϕ introduced in sect. 3. As soon as a thread completes the calculation of P_k, the counter is increased by one and the thread starts a new computation of P_k. In this project we submit computations on the parallel queues of CRESCO6 and CRESCO4F.

5   Conclusions

We have discussed a recursive technique that allows the exact calculation of extinction probabilities in the cyclic Lotka-Volterra model. The recursion yields results perfectly comparable with numerical simulations based on the Gillespie algorithm. The technique can be extended to games of cyclic dominance featuring more complex reactions. We are currently studying possible generalizations to spatially structured models, where the extinction probability undergoes phase transitions occurring for critical values of agent mobility.

References

[1] M. B. Elowitz and S. Leibler. A synthetic oscillatory network of transcriptional regulators. *Nature*, 403:335, 2000.

[2] B. Kerr, M. A. Riley, M. W. Feldman, and B. J. M. Bohannan. Local dispersal promotes biodiversity in a real-life game of rock–paper–scissors. *Nature*, 418:171–174, 2002.

[3] B. Sinervo and C. M. Lively. The rock-paper-scissors game and the evolution of alternative male strategies. *Nature*, 380:240–243.

[4] D. R. Taylor and L. W. Aarssen. Complex competitive relationships among genotypes of three perennial grasses: Implications for species coexistence. *Am. Nat.*, 136:305–327, 1990.

[5] D. D. Cameron, A. White, and J. Antonovics. Parasite–grass–forb interactions and rock–paper–scissor dynamics: predicting the effects of the parasitic plant Rhinanthus minor on host plant communities. *J. Ecol.*, 97(6):1311–1319, 2009.

[6] R. A. Lankau and S. Y. Strauss. Mutual Feedbacks Maintain Both Genetic and Species Diversity in a Plant Community. *Science*, 317(5844):1561–1563, 2007.

Evolution of the Internet at the Autonomous Systems Level During a Decade

Agostino Funel[1*]

[1]*ENEA, DTE-ICT-HPC, P.le E. Fermi, 1, Portici (NA), Italy*

ABSTRACT. We empirically study the evolution of the Internet at the Autonomous Systems (ASes) level examining how many properties of its undirected graph change during the decade 2008-2017. In order to analyze local as well as global properties we consider three classes of metrics related to structure, connectivity and centrality. We find that the Internet almost doubled its size and became more connected. The Internet has a small internal nucleus, composed of high degree ASes, much more stable and connected than external components. There are indications of an underlying hierarchical organization where a small fraction of big ASes are connected to many regions with high internal cohesiveness containing low and medium degree ASes and these regions are poorly connected among them. The overall trend of the average shortest path length of the Internet is a slight decrease over time. Betweenness centrality measurements suggest that during its evolution the Internet became less congested.

1 Introduction

The Internet is a highly engineered communication infrastructure continuously growing over time. It consists of Autonomous Systems (ASes) each of which can be considered a network, with its own routing policy, administrated by a single authority. ASes peer with each other to exchange traffic and use the Border Gateway Protocol (BGP) [1] to exchange routing and reachability information in the global routing system of the Internet. Therefore, the Internet can be represented by a graph where ASes are nodes and BPG peering relationships are links. The structure of the Internet has been studied by many authors and the literature on the subject is vast. One of the most used methods is the statistical analysis of different metrics characterizing the AS graph [2], [3], [4], [5]. There are not many studies concerning the evolution of the Internet over time [6],[7] and because the amount of data to analyze tends to grow dramatically often only a limited number of properties are considered. The purpose of this work is to study the evolution of the Internet considering features related to both its topology and data traffic. To achieve this goal we consider for each year of the period 2008-2017 a snapshot of the undirected AS graph, introduce three classes of metrics related to structure, connectivity, centrality and analyze how they change over time. In this report, after introducing the used datasets and metrics, we summarize the main results published in [8].

---

*Corresponding author. E-mail: `agostino.funel@enea.it`.

2 Data sets

The ASes graphs have been constructed from the publicly available IPv4 Routed /24 AS Links Dataset provided by CAIDA [9]. AS links are derived from traceroute-like IP measurements collected by the Archipelago (Ark) [10] infrastructure, a globally distributed hardware platform of network path probing monitors. The association of an IP address with an AS is based on the RouteViews [11] BGP data and the probed IP paths are mapped into AS links. We exclude multi-origin ASes and AS sets because they may introduce distortion in the association process. The sizes of the ASes graphs analyzed in this work are shown in Tab. 1.

Year	2008	2009	2010	2011	2012	2013	2014	2015	2016	2017
# Nodes	28838	31892	35149	38550	41527	47407	47581	50856	51736	52361
# Edges	135723	152447	184071	213870	281596	282939	298355	347518	379652	414501

Table 1: Sizes of the ASes undirected graphs.

3 Description of metrics

The metrics chosen for this analysis are reported Tab. 2. We use the notation $G = (N, E)$ to indicate an AS graph which has N nodes and E edges.

Metric	Relevance	Importance
Degree distribution	Structure	Scale-free, global properties.
k-core decomposition		Nested hierarchical structure of tightly interlinked subgraphs.
Clustering coefficient	Connectivity	Neighbourhood connectivity. Hierarchical structure.
Shortest path length		Reachability (minimum number of hops between two ASes).
Closeness centrality	Centrality	Indicates the proximity of an AS to all others.
Node betweenness centrality		Related to node traffic load.
Edge betweenness centrality		Related to link traffic load.

Table 2: Metrics used to study the evolution of the Internet at the AS level over time.

4 Results

In this section we compare the measurements of the metrics concerning the Internet AS graphs obtained for each year of the decade 2008-2017 and report the corresponding results.

4.1 Degree distribution

In Fig. 1 are shown the node probability degree distributions and their complementary cumulative functions (CCDF). For all data sets the peak of the degree distribution is for $k = 2$, a result already reported in [12] where it is claimed that it is due to the AS number assignment policies. While the edge density is around $\delta \approx 3 \times 10^{-4}$ during the decade 2008-2017, the general trend is a growth over time for both $\hat{k}$ and k_{max} as shown in Tab. 3. This means that the Internet has become more connected preserving its

sparse nature. All degree distributions have a similar form. In order to verify the statistical plausibility of the power law model we perform a goodness of fit test based on the Kolmogorov-Smirnov statistic [13] which provides a p-value. The power law has statistical support if $p > 0.1$. From Tab. 3 we see that even if the best fit exponent is always around the value $\alpha \approx 2.1$ the power law can be considered a reliable model only for the distributions of the years 2008, 2010 and 2011. Since for the majority of the most larger data sets $p \leq 0.1$ we could say that at the AS level the evolution of the Internet can not be explained by models which predict a pure power law degree distribution.

Year	2008	2009	2010	2011	2012	2013	2014	2015	2016	2017
$\delta \times 10^{-4}$	3.3	3.0	3.0	2.9	3.3	2.5	2.6	2.7	2.8	3.0
$\hat{k}$	9.4	9.6	10.5	11.1	13.6	11.9	12.5	13.7	14.7	15.8
k_{max}	5430	6430	7684	8416	11179	9838	10682	11739	18110	13725
k_{min}^{PL}	23	8	44	30	16	15	17	17	14	14
α	2.12 ± 0.03	2.13 ± 0.01	2.08 ± 0.03	2.07 ± 0.03	2.20 ± 0.02	2.10 ± 0.01	2.10 ± 0.02	2.11 ± 0.01	2.10 ± 0.01	2.14 ± 0.01
$p \pm 0.01$	0.67	0.04	0.60	0.93	0	0	0	0	0	0

Table 3: In the table are shown: the edge density δ, the average degree $\hat{k}$, the maximum degree k_{max}. The best fit power law cut off and exponent are k_{min}^{PL} and α. The condition $p > 0.1$ indicates statistical plausibility of the power law model.
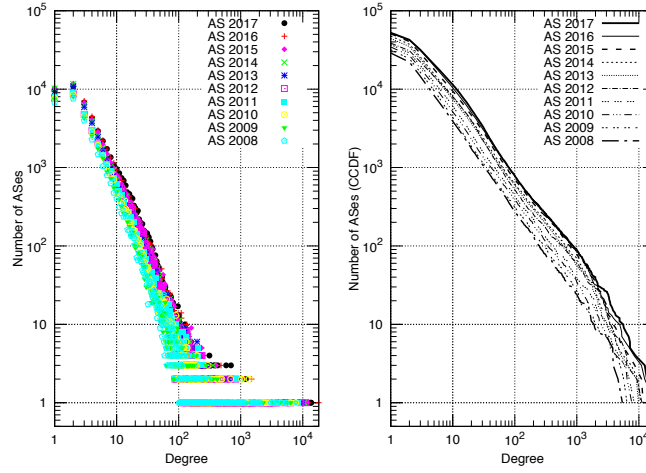
Figure 1: Node degree probability distributions (left) and their CCDF (right).

4.2 K-core decomposition

On the left if Fig. 2 are shown for each year of the decade 2008-2017 the distribution of ASes and edges in each k-core. We observe that in general for each k-core both the number of ASes and edges increase over time. The evolution of the Internet nucleus is shown on the right of Fig. 2. The coreness of the nucleus increases over time (in 2016 and 2017 it has the same value). The fraction of ASes in the nucleus is quite stable over time although in absolute value $\mathcal{N}_n$ increases from 2008 to 2013, decreases in 2014 and 2015 and then increases again until 2017. We observe the same trend also for the number of edges in the nucleus. On average the nucleus contains $\sim$0.4% of all ASes and $\sim$4% of all edges. Compared to the evolution of the nucleus the periphery evolves with a different dynamics [8].
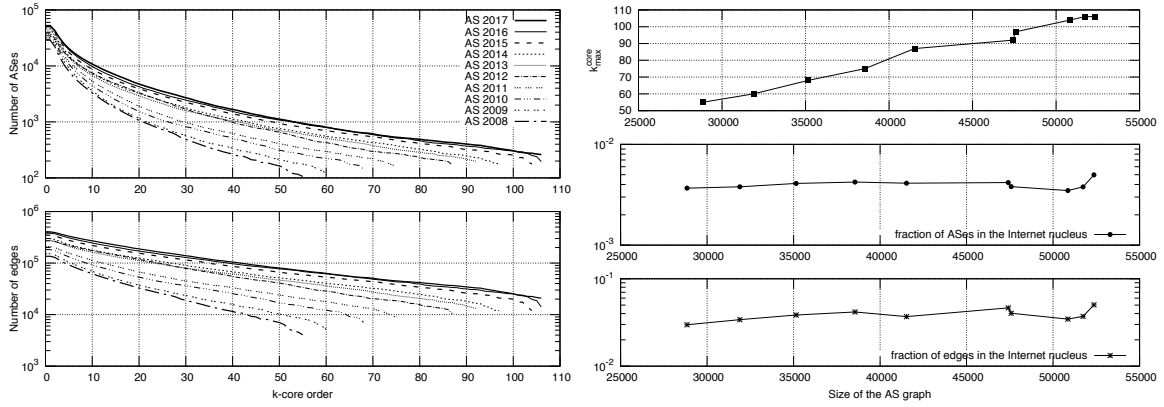
Figure 2: Left: Number of ASes and edges in each k-core during the decade 2008-2017. Right: For each year of the decade 2008-2017 are shown, as a function of the size of the AS graph: the highest coreness k_{max}^{core} (top); the percentage of ASes (middle) and edges (bottom) in the Internet nucleus.

4.3 Clustering coefficient

The clustering coefficient has been used to investigate the hierarchical organization of real networks. The hierarchy could be a consequence of the particular role of the nodes in the network. A stub AS does not carry traffic outside itself and is connected to a transit AS that, on the contrary, is designed for this purpose. The hierarchy of the Internet is rooted in its geographical organization in international, national backbones, regional and local areas. It is reasonable to suppose that this hierarchical structure introduces correlations in the connectivity of the ASes. A. Vázquez *et al* [2] showed that the hierarchical structure of the Internet is captured by the scaling $C(k) \sim k^{-\gamma}$ and found $\gamma = 0.75$. Ravasz and Barabasi [14] proposed a deterministic hierarchical model for which $C(k) \sim k^{-1}$ and using a stochastic version of the model showed that the hierarchical topology is again well described by the scaling $C(k) \sim k^{-\gamma}$ even if the value of γ can be tuned by varying other network parameters.
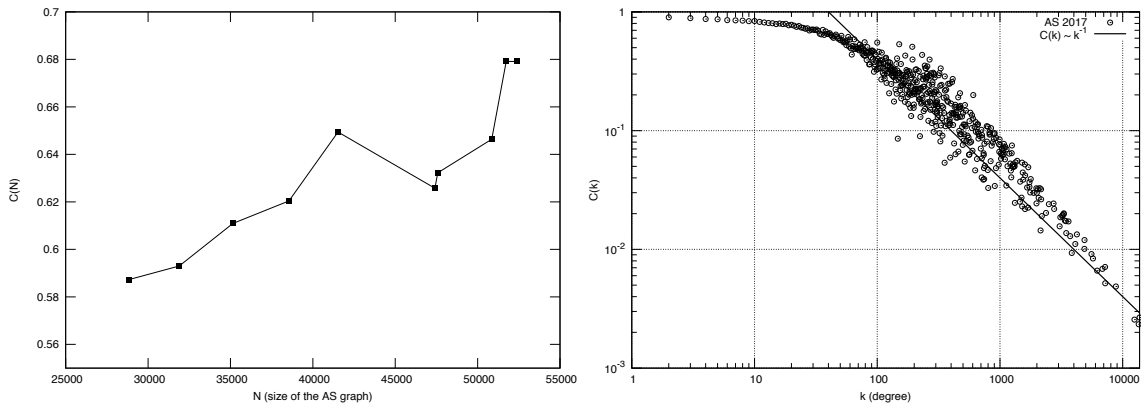
Figure 3: Left: Average clustering coefficient as a function of the size of the AS graph during the decade 2008-2017. Right: Average clustering coefficient as a function of the node's degree for the AS graph of the year 2017. The solid line shows the slope $C(k) \sim k^{-1}$.

On the left of Fig. 3 is shown the average clustering coefficient as a function of the size of the AS graph. For the deterministic hierarchical model studied in [14] C is independent of N. The weak dependence of C on N might indicate the presence of a hierarchical organization in the structure of the Internet. To

further investigate on this point we study $C(k)$. On the right of Fig. 3 we plot $C(k)$ for the AS graph only for the year 2017 because for all other years the plots are almost overlapping. The best fit with the power law $k^{-\gamma}$ provides for all the years values of γ which differ only by $\sim 0.1\%$ obtaining, on average, $\gamma = 1.08 \pm 0.01$. In Fig. 3 is also shown the slope of the function $C(k) \sim k^{-1}$ and even if it nicely follows the slope of the experimental points the goodness of fit test does not give any statistical support to the scaling $C(k) = k^{-\gamma}$. However, data show that $C(k)$ decreases with k especially for $k > 100$. Low degree ASes have high neighbourhood connectivity and, on the contrary, neighbours of big hub ASes are slightly connected among them. This is consistent with a hierarchical organization in which big ASes are connected to many regions with high internal cohesiveness and composed of low or medium degree ASes, and these regions are poorly connected among them.

4.4   Shortest path length

In Fig. 4 are shown the shortest path length distributions $s(h)$ for all the years 2008-2017. We observe that the overall trend is a slight decrease of S over time with an average of ~ 3.0. Zhao *et al* [15] analyzed BGP data from the Route-Views Project [11] in the period 2001-2006 and observed a very weak decreasing of S. They measured a decreasing rate of $\sim 2.5 \times 10^{-4}$ and found $S(2001) = 3.4611$ and $S(2006) = 3.3352$. They noticed that simple power law and small world models, which predict a growth of S with the size of the Internet, fail to explain the overall slight decrease of S over time and argued that this might be due to the fact that the Internet expands according to many factors not considered by simple models like competitive and cooperative processes (like commercial relationships), policy-driven strategy and other human choices. From the comparison of our result with that of Zhao *et al* there are indications the S has been slightly reduced during the period 2001-2017.
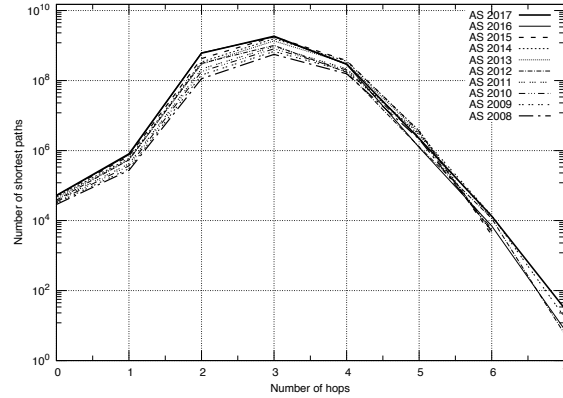
Figure 4: Shortest path distributions $s(h)$ for the AS graphs during the decade 2008-2017.

4.5   Closeness centrality

The closeness centrality Γ as a function of the node's degree k is shown in Fig. 5 for the years 2008 and 2017. The plots of the other years have similar slope. Their curves lie in between of those plotted and are not shown in the figure for better readability because they overlap in the region $100 < k < 1000$. We observe that Γ increases with the degree which means that big hub ASes are in the center of the Internet while low degree ASes are peripheric. We consider Γ in three regions: $k \leq 100$, $100 < k \leq 1000$ and $k > 1000$ corresponding respectively to low, medium and high degree and we find that

within errors it is almost constant over the period 2008-2017 with average values of 0.392 ± 0.007, 0.434 ± 0.004 and 0.484 ± 0.004.
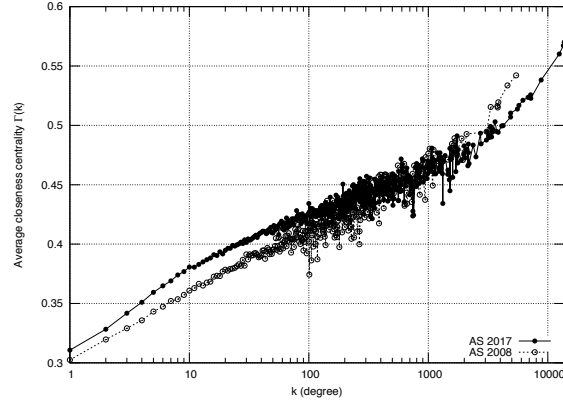
Figure 5: Average closeness centrality $\Gamma(k)$ as a function of the degree k for the AS graphs of the years 2008 and 2017.

4.6 Betweenness centrality

The average node betweenness centrality $B_n(k)$ as a function of the degree k is shown in Fig. 6 for the AS graphs of the years 2008 and 2017. As in the case of the closeness centrality, we do not plot the curves of the other years for readability reasons. However, for all the years the average node betweenness centrality increases with the degree which means that the higher is the degree of an AS the more is the number of shortest paths passing through it. There is evidence of an overall slight decrease of $B_n(k)$ during the evolution of the Internet from 2008 to 2017. The overall average values of B_n calculated in 2008 and 2017 are $\sim 7.1 \times 10^{-5}$ and $\sim 3.6 \times 10^{-5}$ respectively. In Tab. 4 are reported the average values of $B_n(k)$ calculated in the degree regions $k \leq 100$, $100 < k \leq 1000$ and $k > 1000$.
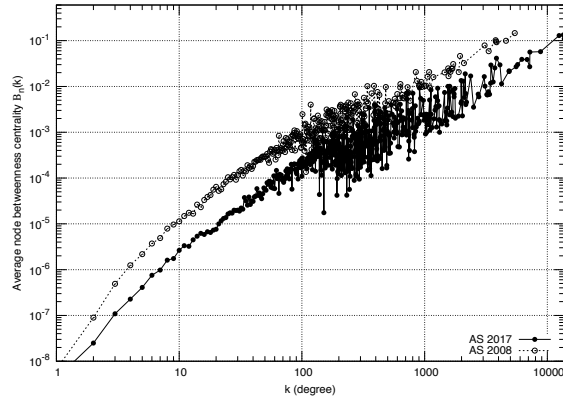
Figure 6: Average node betweenness centrality $B_n(k)$ as a function of the degree k for the AS graphs of the years 2008 and 2017.

In order to study the edge betweenness centrality B_e we represent an edge as a point of the xy plane whose coordinates (k_x, k_y) are the degrees of the nodes it connects. In Fig. 7 is shown, for each year of the decade 2008-2017, the colored 3D map of the average B_e. The highest B_e is associated to edges

$B_n(k)$	2008	2009	2010	2011	2012	2013	2014	2015	2016	2017
$k \leq 100$	3.3×10^{-4}	3.0×10^{-4}	2.2×10^{-4}	1.8×10^{-4}	1.2×10^{-4}	1.2×10^{-4}	1.2×10^{-4}	8.9×10^{-5}	7.7×10^{-5}	7.3×10^{-5}
$100 < k \leq 1000$	3.0×10^{-3}	2.8×10^{-3}	2.2×10^{-3}	2.0×10^{-3}	1.5×10^{-3}	1.6×10^{-3}	1.5×10^{-3}	1.3×10^{-3}	1.0×10^{-3}	0.9×10^{-3}
$k > 1000$	4.5×10^{-2}	4.0×10^{-2}	3.1×10^{-2}	2.9×10^{-2}	1.9×10^{-2}	2.0×10^{-2}	1.8×10^{-2}	1.5×10^{-2}	1.4×10^{-2}	1.4×10^{-2}

Table 4: Average node betweenness centrality B_n in the degree regions $k \leq 100$, $100 < k \leq 1000$ and $k > 1000$.
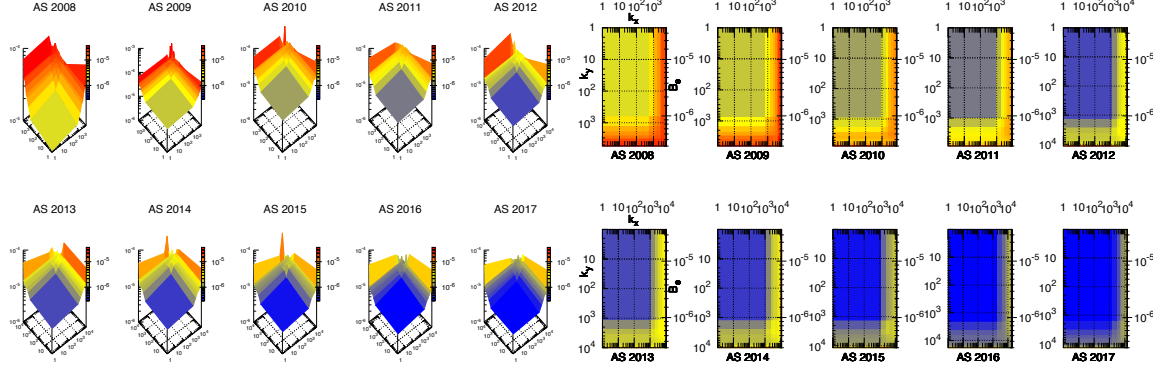
Figure 7: Average edge betweenness centrality B_e for the AS graphs of the years 2008-2017. Left: color mapped 3D plots of B_e. To each edge is associated a point of the xy plane whose coordinates (k_x, k_y) are the degree of the nodes it connects. Right: colored contour maps of the figures on the left.

which have at least a high degree ($k > 1000$) AS as a terminal. Edges connecting low or medium degree ASes have lower B_e. This is what one would expect considering that high degree ASes are the backbone of the Internet and the most part of the shortest routes should cross them. We also observe a slight decrease of B_e over time. The overall average B_e was $\sim 2.2 \times 10^{-5}$ in 2008 and $\sim 0.7 \times 10^{-5}$ in 2017, indicating that somehow the Internet has become less congested although it has expanded. By looking at the colored contour maps shown on the right side of Fig. 7 we infer that during its evolution the lowering of B_e affected first the part of the Internet containing low and medium degree ASes ($k < 1000$) and subsequently the backbone.

5   Conclusion

We studied the evolution of the Internet at the AS level during the decade 2008-2017. For each year of the decade we considered a snapshot of the AS undirected graph and analyzed how a wide range of metrics related to structure, connectivity and centrality varies over time. During the decade 2008-2017 the Internet almost doubled its size and became more connected. The study of the k-core decomposition shows that the number of ASes and edges in each core increases over time. The Internet has a small internal nucleus composed of high degree ASes. The fraction of nodes and edges in the nucleus is quite stable over time and is $\sim 0.4\%$ and $\sim 4\%$, respectively. We analyzed the first external cores from order 2 to 10 and we found that the fraction of nodes and edges they contain exhibits much more large fluctuations. This result indicates that the external cores evolve differently from the nucleus. We found that the ASes in the nucleus are much more connected than those in the periphery. We investigated the hierarchical organization of the Internet by studying the average clustering coefficient C. There are indications of an overall hierarchical organization of the Internet where a small fraction of big

ASes ($k > 1000$) are connected to many regions with high internal cohesiveness containing low and medium degree ASes and these regions are slightly connected among them. The average shortest path length S of the Internet slightly decreased during the decade 2008-2017 form ~3.1 to ~2.9 measured in 2008 and 2016-2017 respectively. Regardless of the analyzed year, the closeness centrality Γ of an AS increases with its degree. Hence, big ASes are in the center of the Internet and low degree ASes are in the periphery. It is reasonable to assume that the traffic load of an AS or carried by an edge is proportional to the number of shortest paths passing through the AS and containing the edge. These measurements can be quantified by the average node and edge betweenness centrality B_n and B_e. We found that B_n increases with the degree indicating that big ASes manage much more traffic than small ASes. There is evidence of an overall slight decrease of both B_n and B_e during the decade 2008-2017. The overall average values of B_n calculated in 2008 and 2017 are $\sim7.1\times10^{-5}$ and $\sim3.6\times10^{-5}$ respectively, and those of B_e are $\sim2.2\times10^{-5}$ and $\sim0.7\times10^{-5}$. This is an indication that during the evolution of the Internet the traffic load somehow decreases. This may be due to the adoption of more efficient routing policies and to infrastructural upgrades with more advanced network devices.

6 Acknowledgments

References

[1] T. Li Y. Rekhter and S. Hares. A border gateway protocol 4. rfc 4271. Internet Engineering Task Force, January 2006.

[2] A. Vázquez, R. Pastor-Satorras, and A. Vespignani. Internet topology at the router and autonomous system level. *arXiv:cond-mat/0206084 [cond-mat.dis-nn]*, 2002.

[3] Beichuan Zhang, Raymond Liu, Daniel Massey, and Lixia Zhang. Collecting the internet as-level topology. *SIGCOMM Comput. Commun. Rev.*, 35(1):53–61, January 2005.

[4] Priya Mahadevan, Dmitri Krioukov, Marina Fomenkov, Xenofontas Dimitropoulos, k c claffy, and Amin Vahdat. The internet as-level topology: Three data sources and one definitive metric. *SIGCOMM Comput. Commun. Rev.*, 36(1):17–26, January 2006.

[5] Damien Magoni and Jean Jacques Pansiot. Analysis of the autonomous system network topology. *SIGCOMM Comput. Commun. Rev.*, 31(3):26–37, July 2001.

[6] B. Edwards, S. Hofmeyr, G. Stelle, and S. Forrest. Internet topology over time. *arXiv:1202.3993 [cs.NI]*, 2012.

[7] Guo-Qing Zhang, Guo-Qiang Zhang, Qing-Feng Yang, Su-Qi Cheng, and Tao Zhou. Evolution of the internet and its cores. *New Journal of Physics*, 10(12):123027, 2008.

[8] A. Funel. The graph structure of the internet at the autonomous systems level during ten years. *Journal of Computer and Communications*, 7(8):17–32, 2019.

[9] CAIDA. Center for applied internet data analysis. `http://www.caida.org/data/active/ipv4_routed_topology_aslinks_dataset.xml`.

[10] CAIDA. Archipelago measurement infrastructure. `http://www.caida.org/projects/ark/`.

[11] UOREGON. University of Oregon Route Views Project. `http://www.routeviews.org/`.

[12] Priya Mahadevan, Dmitri Krioukov, Marina Fomenkov, Xenofontas Dimitropoulos, k c claffy, and Amin Vahdat. The internet as-level topology: Three data sources and one definitive metric. *SIGCOMM Comput. Commun. Rev.*, 36(1):17–26, January 2006.

[13] A. Clauset, C. R. Shalizzi, and M. E. J. Newman. Power law distributions in empirical data. *SIAM Rev.*, 51(4):661–703, November 2009.

[14] E. Ravasz and A. Barabasi. Hierarchical organization in complex networks. *Phys. Rev.*, E 67:026112, February 2003.

[15] Jinjing Zhao, Peidong Zhu, Xicheng Lu, and Lei Xuan. Does the average path length grow in the internet? In Teresa Vazão, Mário M. Freire, and Ilyoung Chong, editors, *Information Networking. Towards Ubiquitous Networking and Services*, pages 183–190, Berlin, Heidelberg, 2008. Springer Berlin Heidelberg.

[16] F. Iannone et al. CRESCO ENEA HPC clusters: a working example of a multifabric GPFS Spectrum Scale layout. *Proceedings of the 2019 International Conference on High Performance Computing & Simulation, HPCS 2019*.

CRESCO ENEA HPC CLUSTERS: A WORKING EXAMPLE OF A MULTIFABRIC GPFS SPECTRUM SCALE LAYOUT

F.Iannone[1*], F.Ambrosino[1], G.Bracco[1], M.De Rosa[1], A.Funel[1], G.Guarnieri[1], S.Migliori[1], F.Palombi[1], G.Ponti[1] and G.Santomauro[1]

[1]*ENEA- Energy Technologies Department – ICT Division – HPC laboratory – Lungotevere Thaon de Ravel, Rome, Italy*

ABSTRACT. ENEA is the Italian National Agency for New Technologies, Energy and Sustainable Economic Development. ENEA operates in many sectors among which the most important are: energy technologies, materials physics, life sciences and climate. In the framework of its institutional mission, the ICT Division provides computing and storage resources integrated into ENEAGRID/CRESCO, an infrastructure distributed over 6 sites, whose main facilities are the HPC CRESCO clusters. The bulk of all storage is based on IBM Spectrum Scale (GPFS) since many years. The access to data, even over WAN, is managed by GPFS clusters. In May 2018 the new cluster CRESCO6 was inaugurated. CRESCO6, a 1.4 Pflops based on Intel Xeon X86_64 SkyLake CPU ranked at 420th of TOP 500 Nov.2018 list. While the interconnection of CRESCO6 is based on Intel Omni-Path (OPA) (100 Gbps), the previous CRESCO4 and CRESCO5 clusters have a network based on InfniBand QDR Truescale fabric (40 Gbps). Hence, in order to provides storage to all CRESCO clusters a GPFS multifabric layout has been implemented after dedicated tests. The work describes the ENEAGRID/CRESCO infrastructure and in particular the solution adopted to implement the GPFS multifabric, and the next future developments.

1 Introduction

A new cluster named CRESCO6 has been installed at the ENEA Research Center of Portici since Oct. 2018. The effort was made possible thanks to an agreement signed in 2015 between ENEA with CINECA [1], the main provider of HPC services in Italy, aimed at providing supercomputing and data storage services to EUROfusion, the European consortium for the Development of Fusion Energy. The agreement signed with ENEA aims at promoting the joint development of research activities in the field of HPC and was the basis for the deployment of CRESCO6, as TIER1 cluster at the Portici ENEA Research Centre. CRESCO6 has the objective to offer a computational resource of high-level to the scientific community and industry, by providing the user to exploit advanced systems of high performance computing system for modelling, integrated in a distributed architecture and accompanied by tools for advanced graphics. It supports multiple Research & Development activities (including those defining the institutional mission of the Agency), carried on in collaboration with national and international governmental institutions and with Italian private industrial partners. The new supercomputer refreshes the complex computational infrastructure of ENEA, granting a performance increase of a factor 10 compared with so-far available resources.

At beginning the storage infrastructure of the CRESCO data center [2], mainly composed of DDN raid systems, was based on Infiniband Qlogic Truescale in order to provide the high performance filesystem GPFS also to the HPC clusters CRESCO4/5, they too on the same fabric. When the cluster CRESCO6 was designed, a new fabric technology, named Omni-Path, was available by Intel, so it arose the problem to integrate different fabrics in order to access the same storage infrastructure.

This paper shows the technical specifications of the new cluster CRESCO6 including comparison of two different network topologies of Omni-Path as well as the technical details of how to implement a multi-fabric layout able for working Infiniband and Omni-Path on a single GPFS cluster using the same storage systems.

2 CRESCO6 Technical Specification

CRESCO6 is a high performance computing system (HPC) consisting of 434 nodes for a total of 20832 cores. It is based on Lenovo ThinkSystem SD530 platform, an ultra-dense and economical two-socket server in a 0.5 U rack form factor inserted in a 2U four-mode enclosure. Each node is equipped with:

- 2 Intel Xeon Platinum 8160 CPUs, each with 24 cores with a clock frequency of 2.1 GHz;
- A RAM of 192 GB, corresponding to 4 GB/core;
- A low-latency Intel Omni-Path 100 Series Single-port PCIe 3.0 x16 HFA network interface.

The nodes are interconnected by an Intel Omni-Path network with 21 Intel Edge switches 100 series of 48 ports each, bandwidth equal to 100 GB/s, latency equal to 100ns. The connections between the nodes have 2 tier 2:1 no-blocking tapered fat-tree topology (Fig.1). The consumption of electrical power during massive computing workloads is amounts to 190 kW.
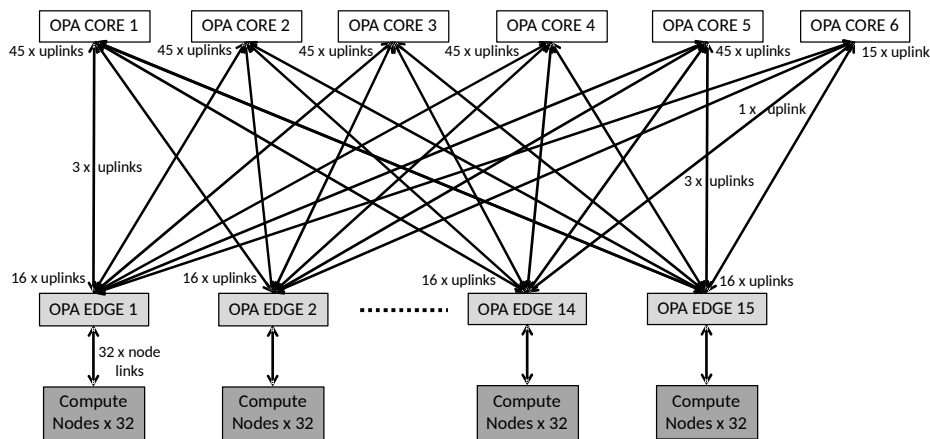
Fig.1: CRESCO 6 Omni-Path network topology: 2 tier 2:1 no-blocking tapered fat-tree.

The CRESCO data center is composed of 2 rooms of ~90m^2 with 2 different air free cooling systems but ready for water free cooling. Actually three HPC clusters are in operations: CRESCO4: 100 Tflops, CRESCO5: 25 Tflops, both with Infiniband QDR low latency network, and CRESCO6: 1.4 Pflops with Omni-Path. A special nodes section with large memory and accelerator cpus (Intel Xeon PHI KNC and Nvidia GPU Tesla K40) are available within the Infiniband QDR network.
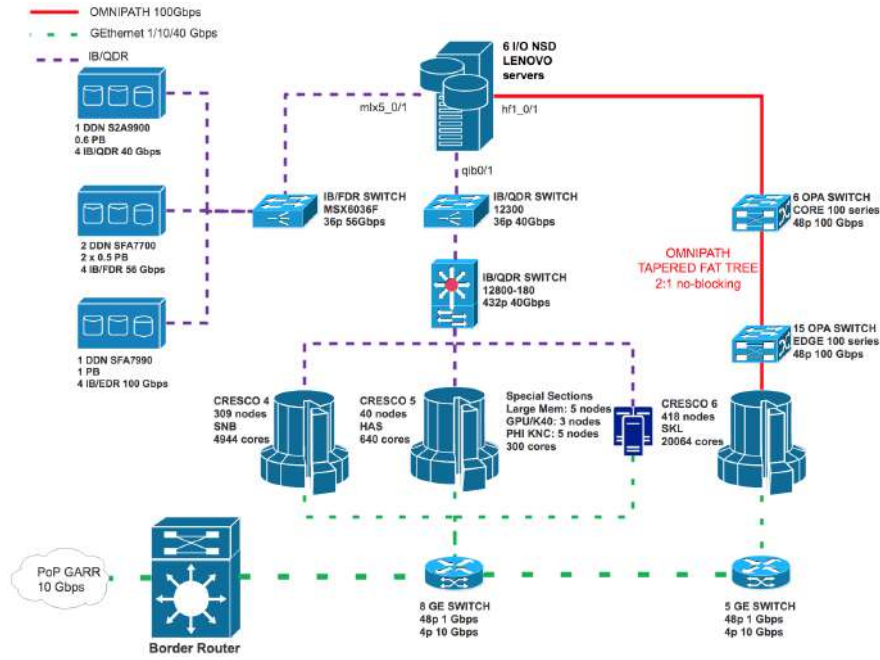
Fig.2: CRESCO CED layout.

The storage systems are based on DDN solutions with a network based on Infiniband. The technical specifications are as follow:

- 1 DDN S2A9900, size 600 TB raw, IB/QDR, I/O bandwidth:6 GB/s;
- 2 DDN SFA7700, size 1 PB raw, IB/FDR, I/O bandwidth: 11 GB/s;
- 1 DDN SFA7990, size 1 PB raw, IB/EDR, I/O bandwidth:20 GB/s.

The high performance filesystem is based on GPFS Spectrun Scale with 6 NSD nodes able to provide parallel I/O at all.

3 Multifabric GPFS layout

The main challenge, to deploy CRESCO6 HPC cluster into the CRESCO data center infrastructure, has been to design and implement a layout on which: the old Infiniband QDR (40 Gbps) fabric of the CRESCO 4/5 clusters, including high performance storages DDN equipped with Infiniband FDR (56 Gbps), the new Omni-Path (100 Gbps) fabric of CRESCO6 cluster and the high performance filesystem Spectrum Scale (GPFS), work all together into a single infrastructure.

The main hardware components of the layout solution, depicted also in fig.2, is as follow:

- The high performance storage systems based on DDN Infiniband QDR/FDR/EDR as dscripted in the par. II;
- 6 NSD servers for GPFS based on 2U Lenovo ThinkSystem SR650, 96 GB RAM, 2 Intel Xeon Gold 5518 CPU @2.3 GHz 12 cores, 1 QLogic IBA7322 QDR Infiniband HCA (rev 02), 1 Mellanox MCX454A-FCAT DUAL FDR Infiniband HCA, 1 Intel Omni-Path HFI Silicon 100 Series;

- 1U switch Mellanox MSX6036F - 36 ports FDR Infiniband for linking the NSD servers to the storage DDN systems;
- 1 U switch Qlogic 12300 – 36 ports QDR Infiniband for linking the NSD servers to the CRESCO 4/5 clusters.

The main software stack including operating system, Infiniband and Omni-Path frabric, RDMA, SRP, Multipath packages and finally Spectrum Scale GPFS.

3.1 Operating System

The CRESCO6 cluster is based on Linux Centos 7.3 but early tests with Centos 7.3 as NSD OS have shown that no clean configuration was obtained as many diagnostic messages by SRP service resulted in */var/log/messages*. The update to Centos 7.4 has fixed these issues thanks to improve the RDMA Infiniband support by RedHat[xx]. Hence the Linux kernel version for the NSD OS is *3.10.0-693.21.1.el7.x86_64.*

3.2 RPMs software stack

The Centos 7.4 RPM packages required for the stack of the NSD servers are as follow:

- *Device Mapper Multipath:* allows to configure multiple I/O paths between server nodes and storage systems into a single device. The RPMs are : *Device-mapper-multipath* and *Device-mapper-multipath-libs* version*: 0.49-111.3l7;*
- *Infiniband support:* the packages ship with Centos 7.4 are earlier versions of Mellanox OFED that in our first tests didn't work. So the version 13-7 of the Infiniband package group of Centos 7.4 repos are used in the layout. It includes the packages: *libibverbs*, *libibverb-utils, librdmacm, rdma-core, rdma-core-devel*, *srp_daemon*. Furthermore the package *Infiniband-diags-1.6.7-1* has been installed in order to use infiniband diagnostic command tools;
- *Omni-Path driver*: the Centos 7.4 packages for the Omni-Path driver version 10.3.1.0-11 are: *opa-basic-tools* and *opa-fastfabric.*

The services to configure on the NSD servers are: *i) RDMA:* set *SRP_LOAD=yes* in the file */etc/rdma/rdma.conf. ii) SRP daemon*: modify the file */usr/sbin/srp_daemon.sh* in order to limit the initiator search only to the used HCA mlx5 interface. *iii)MULTIPATH*: set the devices (DDN storage systems) and map the *wwid* of the Logical Unit (LUN) of the DDN systems.

A last configuration set is on the storage side to define the *GUIDs* of the HCA interface of the all NSD servers into the DDN controllers. In our case the command: *ibstat mlx5 | grep GUID* find it for Mellanox HCA.

3.3 Spectrum Scale GPFS

The high performance filesystem installed on CRESCO is Spectrum Scale (GPFS) version 4.2.3-2 [3]. The six NSD servers have to provide RDMA service on both fabric: Infiniband for the GPFS client nodes of CRESCO4/5 and Omni-Path for the GPFS client nodes of CRESCO6. To make that, a list of RDMA enabled devices, ports, and subnets must be defined into GPFS configuration for all the

class of nodes. In a single fabric configuration, such as IB/QDR with Truescale, GPFS has no *nodeclass* definition and the default value of the variable *verbsPorts* is : *qib0/1/1*. It means that only the GPFS client nodes with QDR HCA *qib0* can use RDMA to access NSD disks. To set the multifabric layout, two classes have to be defined with specific properties, for example:

- *nodeclass crescoOPA* with *verbsPorts hfi1_0/1/2* for all client nodes of CRESCO6*;*
- *nodeclass crescoQDROPA* with both *verbsPorts qib0/1/1* and *hfi1_0/1/2* for the six NSD servers.

The GPFS commands are: *mmcrnodeclass* and *mmchconfig verbsPorts*. These definition can be made any time but they become active only when GPFS is restarted on the nodes.

The I/O performance of the Spectrum Scale in multifabric layout shows transfer rates in R/W of ~1.5 GB/s for the IB/QDR client nodes and ~2.5 GB/s for Omni-Path client nodes.

4 Conclusions

The new HPC facility, CRESCO6, is in operation at ENEA data center. Several benchmarks were made in order to test the performances. The high performance storage systems have been integrated in a multifabric layout mixing different technologies: Qlogic/TrueScale, Mellanox and Intel Omni-Path on which the high performance filesystem Spectrum Scale (GPFS) works with excellent I/O throughput.

5 Acknowledgment

References

[1] Consorzio Interuniversitario del Nord est Italiano Per il Calcolo Automatico (Interuniversity Con-sortium High Performance Systems) http://www.cineca.it (accessed 5 July 2018).
[2] S. Migliori, G. Bracco, et al. Architecture and performances of the CRESCO HPC system. International Supercomputing Conference, Dresden 17-19/6/2008.
[3] IBM Spectrum Scale. https://www.ibm.com/us-en/marketplace/scale-out-file-and-object-storage.
[4] G. Ponti et al., "The role of medium size facilities in the HPCecosystem: the case of the new CRESCO4 cluster integrated in the ENEAGRID infrastructure", Proceedings of the 2014 International Conference on High Performance Computing and Simulation, HPCS 2014, art.no. 6903807, 1030-1033

PARALLEL TEXT MINING OF LARGE CORPORA IN GRID ENVIRONMENT - TaLTaC IN ENEAGRID INFRASTRUCTURE

Silvio Migliori[1], Daniela Alderuccio[1], Fiorenzo Ambrosino[1], Antonio Colavincenzo[1],
Marialuisa Mongelli[1], Samuele Pierattini[1], Giovanni Ponti[1], Andrea Quintiliani[1],
Sergio Bolasco[2], Francesco Baiocchi[3], Giovanni De Gasperis[4]

[1]ENEA – DTE-ICT Division – Roma, Italy
[2]Sapienza Università di Roma, Italy
[3] Staff TaLTac, Roma, Italy
[4]Dip. DISIM Università dell'Aquila, Italy

ABSTRACT.   In this work we presented an ENEAGRID approach toward Parallel Text Mining of Big Data in massive cultural Textual Corpora.
ENEAGRID provides computation, storage resources and services for Text Mining Communities in a ubiquitous and remote way.
ENEA distributed e-Infrastructure and cloud services enable the management of research process in Economic-Social Sciences, Digital Humanities and Cyber-security, providing technology solutions and tools to academic departments and research institutes.
With these research activity ENEA opens to collaborations with other Research Communities interested in Parallel Text Mining of Massive Volume of Text Data (PB &TB-sized corpora) in e-Humanities, Heritage Science, Social Sciences, Big Data, Web Mining, Business Intelligence, Open Source Intelligence, Artificial Intelligence, etc.
Keywords: Text Mining Software, Cloud Computing, Digital-Humanities, Socio-Economic Sciences, Big Data, Artificial Intelligence, Cybersecurity, Business Intelligence, AltaGamma.

1 Introduction

Researchers in Economic and Social Sciences and e-Humanities use computational resources in ENEAGRID to perform their researches regardless of the location of the specific machine or of the employed hardware/ software platform.
ENEAGRID integrates a cloud computing environment and exports: i) remote software; ii) Virtual Labs (accessible via web, where researchers can find set of software and documentation regarding specific research areas); iii) remote storage facilities (with OpenAFS file system). [6]
In this virtual environment, Text Mining software evolve from a uniprocessor software toward a multiprocessor design, integrated in an ICT research e-infrastructure. Accessing these software in Windows and Linux version exploits the high computational capacity (800 Teraflops) of the e-infrastructure, to which users access as a single virtual supercomputer.
These research activities on the integration of Language Technologies (Multilingual Text Mining Software and Lexical Resources) in the ENEA distributed digital infrastructure provide a "community Cloud" approach in a digital collaborative environment and on an integrated platform of tools and digital resources, for the sharing of knowledge and analysis of textual corpora in Economic and Social Sciences and e-Humanities.

2 TaLTaC in Cloud

"TaLTaC in CLOUD" is a joint ENEA-TaLTaC project [1] for the set-up of an ICT portal on the ENEA distributed e-Infrastructure [4] hosting TaLTaC Software [2][3] [9]. Users will access TaLTaC software (Windows and Linux versions) in a remote and ubiquitous way, and the computational power (800 Teraflops) of ICT ENEA distributed resources, as a single supercomputer. The aim of this joint ENEA-TaLTaC project is to enable the TaLTaC User Community and Digital Humanists to have remote access to TaLTaC software through ENEAGRID Infrastructure, integrating ICT inside Digital Cultural Research.

In this Project ENEA is both technological partner and TALTAC User.

As Technological Partner ENEA offers ENEAGRID, the digital infrastructure providing:

- computing power and data storage,
- Saas (Software as a Service) running Text Mining Tasks in a parallel & distributed environment,
- Collaborative research environments[7].

ENEAGRID is open to qualified users. ENEA Partners access Collaborative research environment via credentials (username and password) to Supercomputers & ICT services

As Taltac User ENEA:

i) accesses TaLTaC software: both via remote desktop and via user interfaces to ENEAGRID,

ii) shares TaLTaC results via Virtual Laboratories,

iii) stores TaLTaC data in user environment in AFS user folder.

ENEAGRID offers a digital collaborative environment and an integrated platform of tools and resources assisting research collaborations, for sharing knowledge and digital resources and for storing textual data. In this virtual environment, TaLTaC software evolves from a stand-alone uniprocessor software toward a multiprocessor design, integrated in an ICT research e-infrastructure. Furthermore, it evolves towards implementing ancient language lexical and semantic knowledge and e-resources, facing research needs and implementing solutions also for Digital Humanities communities.

3 TaLTaC Software

The TaLTaC software package, conceived at the beginning of the 2000s, has been progressively developed to date in three major releases: T1 (2001), T2 (2005) and T3 (2016); it is widespread among the text analysis community in Italy and abroad with over 1000 licenses, including two hundred entities between university departments, research institutions and other organizations.

The 2018 release of the software, T3, implemented the following priority objectives: i) the processing of big data (around of a billion words), achieving the independence from the dimensions of the text corpora, limited only by hardware resources; ii) the automatic extraction on multiple layers of results from text parsing (tokenization): layer zero (text in the original version), layer 1 (recognition of words with automatic corrections of the accents), layer 2 (pre-recognition of most common Named Entities), layer 3 (reconstruction of pre-defined multiwords); iii) computing speed, taking advantage of the power of the multi-core processing readily available on current computers (personal or cloud).

Table 1 shows the processing times of three parsing, up to layer 2, for larger corpora on PC (1-core and 8-cores) and on ENEAGRID. Preliminary results on ENEAGRID (1core-CRESCO) show that with increasing corpus size there is an even greater saving of time.

TALTAC was installed in ENEAGRID infrastructure, but the computational capabilities of the HPC system are not yet exploited because the current version of the software does not support multi-core. Therefore, the present ENEAGRID capabilities allow only multi-users access and computation; future versions of the software will be tested for multi-core capabilities to exploit the real power of ENEA ICT High Performance Computing.

Table 1: Preliminary results of processing times of three parsing on PC and on ENEAGRID.

	tokens	size of file	MAC i7 (7th generation)			ENEAGRID
			1 core	8 cores	8core /1core	1 core (CRESCO)
	millions	GB	in minutes		in %	in minutes
1 "*La Repubblica*" (100 th Artic.)	74	0,41	3,4	1,1	0,33	3,5
2 "*La Repubblica*" (400 th Artic.)	284	1,55	13,0	3,8	0,29	13,2
3 Italian and French Press	535	2,89	37,4	8,8	0,24	41,3
4 Various Press Collection	1.138	6,18	88,2	14,0	0,16	54,7

For the characteristics of the technological architecture of the TaLTaC3 platform, see previous works (Bolasco et al. 2016, 2017), that can be summarized here as: a1) HTML 5 for the GUI and jQuery with its derived Javascript frameworks to encapsulate the GUI user interaction functions for the MAC and Cloud solution; a2) Windows native DotNET desktop application; b) JSON (JavaScript Object Notation): as an inter-module language standard, with a structured and agile format for data exchange in client/server applications; c) Python / PyPy: advanced script/compiled programming language, mostly used for textual data analysis and natural language processing at the CORE back end; d) No-SQL: high performance key/value data structure storage server Redis adopted for vocabularies/linguistic resources persistence; e) RESTful: interface standard for data exchange over the HTTP web protocol; f) MULTI-PROCESSING: exploiting in the best possible way multi-core hardware, distributing processing power among different CPU cores.

The choice of the Python language allowed to develop a cross-platform computational core running on Windows, Linux, macOS. In particular, the overall system of software processes runs smoothly over a linux-based cloud computing facility, like the ENEAGRID. Furthermore, the Python code compiled through the 64bit PyPy just-in-time-compiler allows very efficient macro operations over a large set of data, stored as hash dictionaries, so that the upper limits of performance and capacity is only due to the physical limit of the host machine, in terms of RAM and number of cores and OS kernel scheduler. In our test each node in the ENEAGRID infrastructure hosted a single Redis instance and a number of 24 logic cores, with 16GB of RAM.

4 ENEAGRID Infrastructure

ENEA activities are supported by its ICT infrastructure, providing advanced services as High Performance Computing (HPC), Cloud and Big Data services, communication and collaboration tools. Advanced ICT services are based on ENEA research and development activities in the domains of HPC, of high performance networking and data management, including the integration of large experimental facilities, with a special attention to public services and industrial applications. As far as High Performance Computing is concerned, ENEA manages and develops ENEAGRID, a computing infrastructure distributed over 6 ENEA research centers for a total of about 16000 cores and a peak computing power of 800 Tflops (for more info: ENEA ICT https://ict.enea.it/ - CRESCO https://www.eneagrid.enea.it/CRESCOportal/)

5 TaLTaC in ENEAGRID Infrastructure

5.1 Software Installation and Access on ENEA e-Infrastructure

The software TaLTaC is available on Windows and Linux through ENEAGRID via AFS in a geographically distributed file system, which allows remote access to each computing node of the HPC CRESCO systems and Cloud infrastructure from anywhere in the world.

This provides three capabilities: i) data mining, sharing and storage; ii) ICT services necessary for the efficient use of HPC resources, collaborative work, visualization and data analysis; iii) the implementation of software and its settings for future data processing and analysis. Moreover, the availability of the software on the ENEA ICT infrastructure can benefit of the advantages of AFS such as scalability, redundance, backup and so on.

Through the ACL rules it can be possible to manage the accessibility of the software to the community of users in compliance of the license policies that will be put in place. The following two options are provided for TaLTaC running: the first one is to use the applications installed in the windows system and the second one is to use FARO2 – Fast Access to Remote Objects (the general purpose interface for hardware and software capabilities by web access) to directly access the applications installed in the Linux environment and that refer to the data in AFS.

5.1.1. TaLTaC2 (Windows) on Remote Desktop Access

The software TaLTaC2 is available on "Windows Server 2012 R2" by remote desktop access to a virtual machine that can be reached by the ThinLinc general-purpose and intuitive interface. All the users involved in the project activities can access the server but only the person in charge of developing and installing the application can obtain administrator privileges. For this reason, AFS authentication is always required. Every TaLTaC2 user with AFS credentials can access ENEAGRID to run the software and to manage data on AFS own areas via web and from any remote location. In the AFS environment, an assigned disk area with a large memory capacity is defined. This area is mainly used for storage and sharing of large amounts of data (less than 200 MB) (analysis, reports and documents) that come from running the software on a single processor, in serial mode, or for future parallel data mining applications.

5.1.2. TaLTaC3 (Linux) on CRESCO System

On the CRESCO systems, that is accessible from ENEAGRID infrastructure, TaLTaC3 is available on CentOS Linux nodes and then it is possible to leverage the overall computing power dedicated to the activities of TaLTaC and Digital Humanists communities. Every user can start own work session allocating a node with a reserved Redis instance and as many computing core as needed.

Performance improvements are obtainable through the parallelization so that a single user can use the full capacity of the assigned node, in terms of number of computing cores. The TaLTaC3 package is automatically started as the user login to the node by a shell script. The opensource Mozilla Firefox web browser makes the user interface in the current beta version. The access to the TaLTaC3 portal use the ThinLinc remote desktop visualization technology that allows an almost transparent remote session on the HPC system, including the graphical user interface, thanks to the built-in features such as load-balancing, accelerated graphics and platform-specific optimisations. Input and output data can be accessed through the ENEAGRID filesystems and therefore easily uploaded and downloaded.

5.2 Case Studies

ENEA distributed infrastructure and cloud services enable the management of research process in Economic-Social Sciences and Digital Humanities, providing technology solutions and tools to academic departments and research institutes: building and analyzing collections to generate new intellectual products or cultural patterns, data or research processes, building teaching resources, enabling collaborative working and interdisciplinary knowledge transfer. ENEA adopts a collaborative-research-community approach able to lead to a community-driven software design, tailor-made on specific research community needs and to community cloud computing.

Text Mining in GRID environment will provide :

i) collecting Open Data from Social and Web;

ii) on-line access «always and anywhere ON»,

ii) ubiquitous access to software and computational resources in ENEAGRID, regardless of the location of the specific machine, of the employed hardware/software platform and regardless of the corpus size (from Gigabytes to Terabytes),

iv) a simple user interface for users (web access) of: TALTAC2 windows version and of TALTAC3 linux version for large corpora on ENEAGRID;

v) Data and computing capacity;

vi) Virtual Research Environments (virtual labs) & Collaboration tools (network management, video conferencing and voip services, cloud computing, ecc.);

vii) Data storage facilities;

viii) Parallel Text/Data Mining & Analysis (data & task parallelism).

5.2.1. TaLTaC User Community

The current (2018) community of TaLTaC over the years aggregated users from the computer laboratories of automatic analysis of texts and text mining, also carried out within the institutional courses of bachelor and magistral degrees, plus Ph.D. students from doctoral degree courses at the universities of Rome "La Sapienza" and "Tor Vergata", of Padua, Modena, Pisa, Naples and Calabria (a total estimate of over 1300 students over the last eight years); furthermore, there is another set of users that subscribed to specific tutorial courses dedicated to TaLTaC (more than 60 courses for a total number of 750 tutorial participants).

A call about the opportunity of using "remotely" the software via the ENEA distributed computing facilities, received the manifestation of interest by 40 departments and other research institutes.

5.2.2. Digital Humanities Community as TaLTaC user

In collaboration with academic experts, ENEA focused on Digital Humanities projects in Text Mining & Analysis in Ancient Writings Systems of the Near East and used TaLTaC2 to perform quantitative linguistic analysis in cuneiform corpora (transliterated into latin alphabet) [5] .

Cuneiform was used by a number of cultures in the ancient Near East to write 15 languages over 3,000 years. The cuneiform corpus was estimated to be larger than the corpus of Latin texts but only about 1/10 of the extant cuneiform texts have been read even once in modern times. This huge cuneiform corpus and the restricted number of experts lead to the use of Text Mining and Analysis, clustering algorithms, social network analysis in the TIGRIS Virtual Lab for Digital Assiriology[8] , a virtual research environment implemented in ENEA research e-infrastructure. In TIGRIS V-Lab researchers perform basic tasks to extract knowledge from cuneiform corpora. (i.e. dictionaries extraction with word list of toponyms, chrononyms, theonyms, personal names, grammatical and semantic tagging, concordances, corpora annotation, lexicon building, grammar writing, etc.).

6 Conclusion

This project leads to the TaLTaC software evolution: i) from a uniprocessor software toward a multiprocessor design, integrated in an ICT research e-infrastructure; ii) from a stand-alone software (allowing Text Mining & Analysis to search for linguistic constructions in textual corpora, showing results in a table or concordance list) to a software "always and anywhere on", that also can be accessed via web, providing an interface where you can visualize results, create interpretative models, collaborate with others, combine different textual representations and storing data, co-developing research practices. Furthermore, this project reflects the shift from the individual-researcher-approach to a collaborative research community-approach, leading to a community-driven software design, tailor-made on specific research community needs and to Community Cloud Computing. This interdisciplinary knowledge transfer enables creating and activating new knowledge from big (cultural and socio-economic) data, both in modern and ancient languages.

ENEAGRID offers to researchers computation and storage resources and services in a ubiquitous and remote way. ENEAGRID integrates a cloud computing environment and exports: a) remote software

(i.e. TaLTaC); b) Virtual Labs: thematic areas accessible via web, where researchers can find set of software and documentation regarding specific research areas; c) remote storage facilities (with OpenAFS file system).

All these activities are based in ENEA e-Infrastructure, collecting Open Data extracted from Open Sources and will be described in a specific publication.

With these researches ENEA opens to collaborations with Research Communities interested in Parallel Text Mining of Massive Volume of Text Data (PB & TB-sized corpora) in: e-Humanities, Heritage Science, Social Sciences, Big Data, Web Mining, Business Intelligence, Open Source Intelligence, Artificial Intelligence, Cybersecurity, etc.

References

[1] D. Alderuccio, S. Migliori, A. Quintiliani, F. Ambrosino, A. Colavincenzo, M. Mongelli, S. Pierattini , G. Ponti, S. Bolasco, F. Baiocchi, G. De Gasperis. TaLTaC in ENEAGRID Infrastructure in *Proceedings JADT 2018 (Journées Internationales d'Analyses statistique des Données Textuelles) 14th Int. Conference on Statistical Analysis of Textual Data)-* pp. 501-508 - Roma 15.6.2018 c/o CNR, (2018)

[2] S. Bolasco, F. Baiocchi, A. Canzonetti, G. De Gasperis (2016). TaLTaC3.0, un software multi-lessicale e uni-testuale ad architettura web, in D. Mayaffre, C. Poudat, L. Vanni, V. Magri, P. Follette (eds.), *Proceedings of JADT 2016,* CNRS University Nice Sophia Antipolis, Volume I, pp. 225-235. (2016).

[3] S. Bolasco, G. De Gasperis (2017). TaLTaC 3.0 A Web Multilevel Platform for Textual Big Data in the Social Sciences" in C. Lauro, E. Amaturo, M.G. Grassia, B. Aragona, M. Marino. (eds.) *Data Science and Social Research - Epistemology, Methods, Technology and Applications (series: Studies in Classification, Data Analysis, and Knowledge Organization)* Springer Publ., pp. 97-103. (2017).

[4] G. Ponti et al. (2014). The Role of Medium Size Facilities in the HPC Ecosystem: The Case of the New CRESCO4 Cluster Integrated in the ENEAGRID Infrastructure In: *Proceedings of the International Conference on High Performance Computing and Simulation,* HPCS (2014), ISBN: 978-1-4799-5160-4. (2014).

[5] G. Ponti, D. Alderuccio, G. Mencuccini, A. Rocchi, S. Migliori, G. Bracco, P. Negri Scafa (2017). Data Mining Tools and GRID Infrastructure for Text Analysis in *"Private and State in the Ancient Near East" Proceedings of the 58th Rencontre Assyriologique Internationale,* Leiden 16-20 July 2012, edited by R. De Boer and J.G. Dercksen, Eisensbrauns Inc. - LCCN 2017032823 (print) | LCCN 2017034599 (ebook) | ISBN 9781575067858 (ePDF) | ISBN 9781575067841. (2017).

[6] ENEAGRID http://www.ict.enea.it/it/hpc -

[7] Laboratori Virtuali http://www.ict.enea.it/it/laboratori-virtualixxx/virtual-labs

[8] TIGRIS Virtual Lab http://www.afs.enea.it/project/tigris/indexOpen.php

[9] TaLTaC: www.taltac.it

Author Index